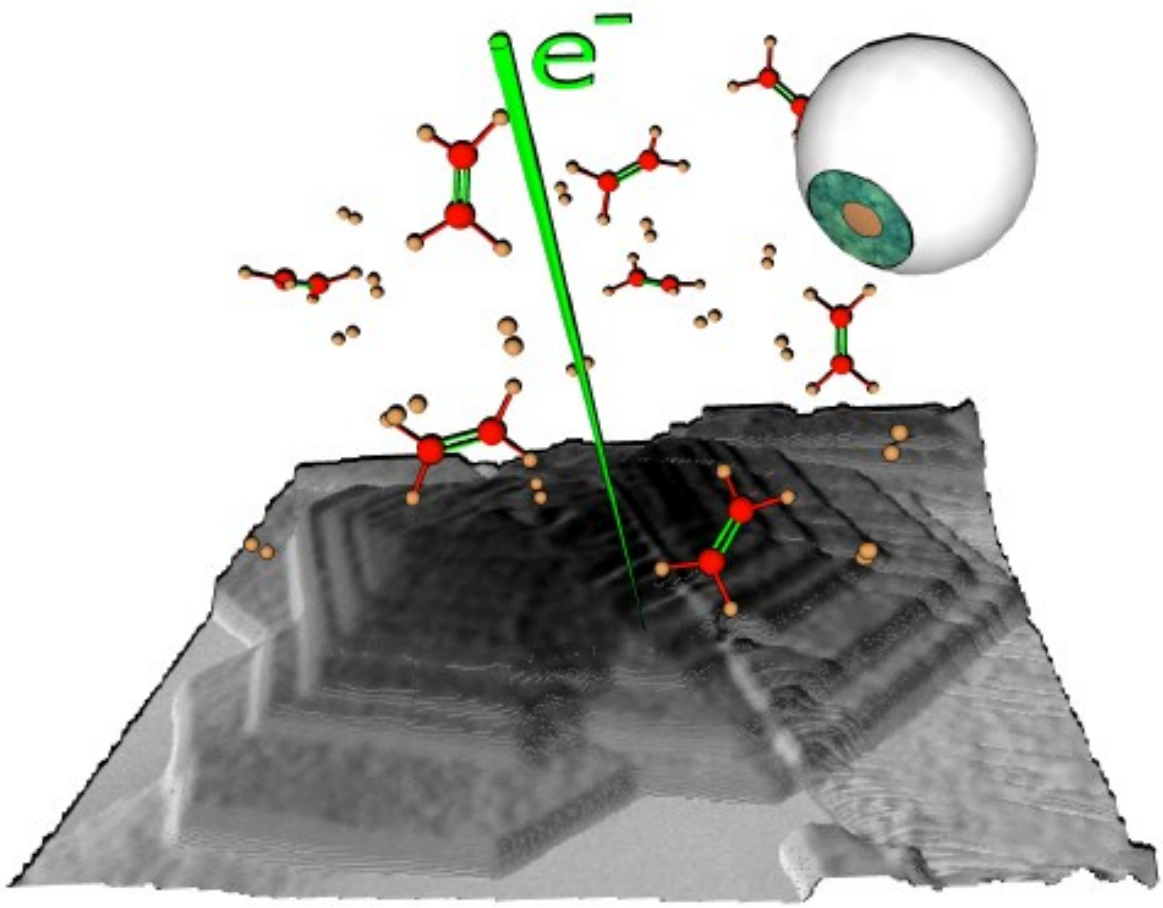
e⁻

In situ scanning electron microscopy studies on the dynamics of metal-catalyzed CVD growth of graphene

vorgelegt von
M.Sc.
Zhu-Jun Wang
geb. in Xi'an, China

von der Fakultät II – Mathematik und Naturwissenschaften
der Technischen Universität Berlin
zur Erlangung des akademischen Grades

Doktor der Naturwissenschaften
- Dr.-rer.-nat.

genehmigte Dissertation

Promotionsausschuss:

Vorsitzender: Prof. Dr. Reinhard Schomäcker

Gutachter: Prof. Dr. Robert Schlögl
Prof. Dr. Michael Lehmann
Prof. Dr. Thomas Risse

Tag der wissenschaftlichen Aussprache: 15. Dezember 2016

Berlin 2017

TABLE OF CONTENTS

Publications

Peer reviewed journal articles by the author

Articles included in the thesis:

1. **Zhu-Jun Wang**, et. al. "Adlayer Graphene Formation and a Processing Window for Self-terminating single-layer Graphene Growth" (draft). (refers to chapter 8)

2. **Zhu-Jun Wang**, Jichen Dong, Yi Cui, Gyula Eres , Olaf Timpe, Qiang Fu, Feng Ding, Robert Schlögl "Stacking sequence and interlayer coupling in few layer graphene revealed by in situ imaging" *Nature Comm*., **2016**, Article number: 13256(2016), DOI: 10.1038/NCOMMS13256. (refers to chapter 7)

3. **Zhu-Jun Wang**, Gisela Weinberg, Qiang Zhang, Thomas Lunkenbein, Achim Klein-Hoffmann, Michalina Kurnatowska, Milivoj Plodinec, Qing Li, Lifeng Chi, R. Schlöegl, Marc-Georg Willinger "Direct Observation of Graphene Growth and Associated Copper Substrate Dynamics by *in Situ* Scanning Electron Microscopy" *ACS Nano*., **2015**, 9, 1506–1519, DOI: 10.1021/nn5059826. (refers to chapter 5)

Articles related in the thesis:

1. Robert S. Weatherup, Ashwin J. Shahani, **Zhu-Jun Wang**, Ken Mingard, Andrew J. Pollard, Marc-Georg Willinger, Robert Schlögl, Peter W. Voorhees, Stephan Hofmann "In Situ Graphene Growth Dynamics on Polycrystalline Catalyst Foils" *Nano Lett.*, **2016**, 16, 6196–6206, DOI: 10.1021/acs.nanolett.6b02459. (refers to Figure 6-3 and Figure 6-4 in chapter 6)

2. Raoul Blume, Piran R. Kidambi, Bernhard C. Bayer, Robert S. Weatherup, **Zhu-Jun Wang**, Gisela Weinberg, Marc-Georg Willinger, Mark Greiner, Stephan Hofmann, Axel Knop-Gericke, Robert Schlögl "The influence of intercalated oxygen on the properties of graphene on polycrystalline Cu under various environmental conditions" *Phys. Chem. Chem. Phys*., **2014**,16, 25989–26003, DOI: 10.1039/C4CP04025B. (refers to Figure 3-6 in chapter 3)

3. Piran R. Kidambi, Bernhard C. Bayer, Raoul Blume, **Zhu-Jun Wang**, Carsten Baehtz, Robert S. Weatherup, Marc-Georg Willinger, Robert Schlögl, and Stephan Hofmann "Observing

Graphene Grow: Catalyst–Graphene Interactions during Scalable Graphene Growth on Polycrystalline Copper" *Nano Lett.*, **2013**, 13, 4769–4778, DOI: 10.1021/nl4023572. (refers to Figure 3-4 and Figure 3-5 in chapter 3)

Remarks:

In the chapter 3, Figure 3-4 and Figure 3-5 are reproduced with permission from [Piran R. Kidambi, Bernhard C. Bayer, Raoul Blume, Zhu-Jun Wang, Carsten Baehtz, Robert S. Weatherup, Marc-Georg Willinger, Robert Schloegl, Stephan Hofmann. Nano Lett., 2013, 13, 4769–4778. DOI: 10.1021/nl4023572] Copyright [2013] American Chemical Society.

The chapter 5 is reproduced with permission from [Zhu-Jun Wang, Gisela Weinberg, Qiang Zhang, Thomas Lunkenbein, Achim Klein-Hoffmann, Michalina Kurnatowska, Milivoj Plodinec, Qing Li, Lifeng Chi, R. Schloegl, Marc-Georg Willinger. ACS Nano, 2015, 9 (2), 1506–1519. DOI: 10.1021/nn5059826] Copyright [2015] American Chemical Society.

In the chapter 6, Figure 6-3 and Figure 6-4 are reproduced with permission from [Robert S. Weatherup, Ashwin J. Shahani, Zhu-Jun Wang, Ken Mingard, Andrew J. Pollard, Marc-Georg Willinger, Robert Schloegl, Peter W. Voorhees, Stephan Hofmann. Nano Lett., 2016, 16, 6196–6206. DOI: 10.1021/acs.nanolett.6b02459] Copyright [2016] American Chemical Society.

The chapter 7 is reproduced from [Zhu-Jun Wang, Jichen Dong, Yi Cui, Gyula Eres , Olaf Timpe, Qiang Fu, Feng Ding, Robert Schlögl. Nature Comm., 2016, Article number: 13256. DOI: 10.1038/NCOMMS13256]. This work is licensed under a Creative Commons Attribution 4.0 International License. https://creativecommons.org/licenses/by/4.0/

Other articles:

1. Christin Büchner, **Zhu-Jun Wang**, Kristen M. Burson, Marc-Georg Willinger, Markus Heyde, Robert Schloegl, and Hans-Joachim Freund "A Large-Area Transferable Wide Band Gap 2D Silicon Dioxide Layer" *ACS Nano.*, **2016**, 10, 7982–7989, doi: 10.1021/acsnano.6b03929

2. Xing Huang, Yongqiang Yu, Travis Jones, Hua Fan, Lei Wang, Jing Xia, **Zhu-Jun Wang**, Li-

Dong Shao, Xiang-Min Meng, and Marc-Georg Willinger "In Situ Formation of Crystallographically Oriented Semiconductor Nanowire Arrays via Selective Vaporization for Optoelectronic Applications" *Advanced Materials*, **2016**, 21, 7603–7612, doi: 10.1002/adma.201602867

3. Xing Huang, **Zhu-Jun Wang**, Gisela Weinberg, Xiang-Min Meng, Marc-Georg Willinger "In Situ Scanning Electron Microscopy Observation of Growth Kinetics and Catalyst Splitting in Vapor–Liquid–Solid Growth of Nanowires" *Adv. Funct. Mater.,* **2015**, 25, 5979–5987, doi: 10.1002/adfm.201502619

4. Mark. T. Greiner, T. E. Jones, B. E. Johnson, T. C. R. Rocha, **Zhu-Jun Wang**, M. Armbrüster, Marc-Georg Willinger, A. Knop-Gerickea, R. Schlögl "The oxidation of copper catalysts during ethylene epoxidation" *Phys. Chem. Chem. Phys.,* **2015**, 17, 25073–25089, doi: 10.1039/C5CP03722K

5. Narendar Nasani**, Zhu-Jun Wang**, Marc-Georg Willinger, Aleksey A. Yaremchenko, Duncan P. Fagg "*In situ* redox cycling behaviour of Ni–$BaZr_{0.85}Y_{0.15}O_{3-\delta}$ cermet anodes for Protonic Ceramic Fuel Cells" *International Journal of Hydrogen Energy*, **2014**, 39, 19780–19788, doi: 10.1016/j.ijhydene.2014.09.136

Dedication

This thesis is submitted for the doctor of natural sciences at Faculty II - Mathematics and Natural Sciences of the Technical University of Berlin.

The contents of this dissertation are the result of my original work except where clear references are made, or where the contribution from others has been clearly acknowledged.

This thesis is dedicated to my father, Ding-Yuan Wang, who has given me strength and courage to achieve my goals; and without his devotion and inspiration I would not be the person I am today.

Zhu-Jun Wang, September, 2016, Berlin

Acknowledgments

I would like to express my sincere gratitude to my supervisor Dr. Marc Georg Willinger for the continuous support of my Ph.D study and related research, for his patience, motivation, immense knowledge, many sleepless nights experiment, and for all the fun we have had in the last five years. His guidance helped me in all the time of research and writing of this thesis. I could not have imagined having a better supervisor and mentor for my Ph.D study.

Besides my supervisor, special thanks to Gisela Weinberg for all the help associated with modified the experimental setup. A large part of this work would not have been possible without her enthusiastic, patience and meticulous technical support.

My sincere thanks also go to Prof. Robert Schlögl and Prof. Dangsheng Su who provided me an opportunity to join Fritz Haber Institute and who gave access to the top level electron microscopy and research facilities. Without they precious support it would not be possible to conduct this research. Besides, I special thank Dr. Raoul Blume for *in situ* XPS measurements.

During my Ph.D., I have had the privilege and pleasure of collaborating with many researchers from outside Fritz Haber Institute. I am grateful to Jichen Dong (Hong Kong Polytechnic University) for the theoretical simulations and scientific discussions, Dr. Gyula Eres (Oak Ridge National Laboratory) for stimulating discussions, Dr. Yi Cui (Suzhou Institute of Nano-Tech and Nano-Bionics, CAS) and Prof. Qiang Fu (Dalian Institute of Chemical Physics, CAS) for collaborative work on STM measurements, and Dr. Milivoj Plodinec (Ruđer Bošković Institute) for help with on Raman measurements. In particular, I am grateful to Prof. Feng Ding (Hong Kong Polytechnic University) for enlightening me and boarding my scientific view.

I would like to thank and gratefully acknowledge Mr. Yi Hu from Shaanixi Stargate Investment Holding Group Co. Ltd. for supporting me throughout my education and writing this thesis without his help I could not have made it this far.

Last but not the least; I would like to thank the rest of my thesis committee: Prof. Robert Schlögl, Prof. Michael Lehmann, Prof. Dr. Thomas Risse and Prof. Reinhard Schomäcker for their insightful comments and encouragement, but also for the hard question which incented me to widen my research from various perspectives.

Abstract

Electron microscopy has contributed tremendously to our understanding of catalysis. Scanning- and transmission electron microscopes are used to investigate the structure and composition of catalytically active materials. They provide guiding feedback during synthesis of catalyst precursors and are used to study reaction induced modifications on spent catalysts. Electron microscopy delivers local information that is complementary to the information provided by spatially averaging spectroscopy or diffraction based tools. However, since the observations in electron microscopy are generally performed under vacuum and close to room temperature, the obtained structural, compositional and atomistic details concern an equilibrium state that is of limited value when the active state of a catalyst is in the focus of the investigation. Since the early attempts of Ruska in 1942, in situ microscopy has demonstrated its potential and, with the recent availability of commercial tools and instruments, led to a shift of the focus from ultimate spatial resolution towards observation of relevant dynamics. In view of the most recent developments in *in situ* transmission electron microscopy, it appears that the potential of scanning electron microscopy has slightly been overlooked.

Within the framework of this thesis, the experimental set-up of an environmental scanning electron microscopy (ESEM) has been modified and improved. The aim was to implement *in situ* SEM as a technique for the observation of surface dynamics of active catalysts. A laser heating system was developed for imaging at temperatures up to 1000°C at reduced thermal drift, reduced thermal inertia and contamination-free imaging under reactive atmosphere. Furthermore, the gas feeding and vacuum system have been improved and a mass spectrometer for gas phase analysis has been implemented. The set-up is now versatile and allows real-time observations during a wide range of *in situ* experiments under different atmospheres, pressures and temperatures.

This thesis demonstrates the effectiveness of *in situ* scanning electron microscopy (SEM) for studying the mechanistic details of graphene growth by metal catalysed chemical vapour deposition (CVD) on Ni, Cu and Pt. Using this instrument, the formation of

graphene could be observed in real-time during chemical vapour deposition experiments inside the chamber of the microscope. Complete CVD cycles, ranging from substrate annealing to graphene growth and subsequent cooling, can be monitored without interruption of the process. Hence, it is possible to obtain a complete and undisturbed picture of the involved dynamics without the need for sample transfer. The latter is important for the validation of mechanistic models that are derived on the basis of post-growth observation. On the basis of feedback from *in situ* SEM, graphene growth conditions could be optimized towards the production of high quality large area single-layer graphene. *In situ* SEM is not only suitable for the observation of CVD graphene growth, but can be extended to study the formation and growth of other atomically thin 2 dimensional nano materials and to directly reveal surface dynamics of active catalysts in reactive environments. Due to the applicable pressure and temperature range, the instrument is capable of providing visual information about the state of a surface that can be related to spectroscopic data obtained by *in situ* near ambient pressure (NAP) X-ray photoemission experiments under similar conditions.

Zusammenfassung

Elektronenmikroskopie spielt eine wichtige Rolle in der Katalyseforschung und hat wesentlich zum Verständnis der Katalyse beigetragen. Raster- und Transmissionselektronenmikroskope werden verwendet, um die Struktur und Zusammensetzung katalytisch aktiver Materialien zu untersuchen. Dabei liefern die analytischen Untersuchungen zum einen wichtige Rückschlüße für die Optimierung der Synthese neuer Katalysatoren, zum anderen werden die Mikroskope eingesetzt um reaktionsinduzierte Modifikationen an gebrauchten Katalysatoren zu untersuchen. Die Elektronenmikroskopie liefert lokale Informationen und ist somit komplementär zu integralen, spektroskopischen oder beugungsbasierten Methoden. Da elektronenmikroskopische Beobachtungen generell unter Vakuum und meist bei Raumtemperatur durchgeführt werden, betreffen die erhaltenen morphologischen, strukturellen, und atomistischen Details einen Gleichgewichtszustand, der dann von begrenztem Wert ist, wenn der aktive Zustand eines Katalysators im Fokus der Untersuchung steht. Seit den frühen Versuchen von Ruska im Jahr 1942 hat die *in situ* Mikroskopie ihr Potenzial unter Beweis gestellt. Mit der Verfügbarkeit von kommerziellen Instrumenten und speziellen Probenhaltern hat sich in den letzten Jahren der Fokus auf dem Gebiet der Elektronenmikroskopie etwas von der ultimativen Auflösung in Richtung Beobachtung relevanter Dynamik erweitert. Angesichts der jüngsten Entwicklungen in der *in situ* Transmissionselektronenmikroskopie scheint allerdings das Potenzial der *in situ* Rasterelektronenmikroskopie noch etwas unterbewertet.

Im Rahmen dieser Arbeit wurde der experimentelle Aufbau eines Niederdruck-Rasterelektronenmikroskops (REM) modifiziert und verbessert. Ziel war es, *in situ* REM als Methode zur Beobachtung der Oberflächendynamik von aktiven Katalysatoren zu implementieren. Ein Laser-Heizsystem wurde für Untersuchungen bei Temperaturen bis 1000 ° C bei reduzierter thermischen Drift und Trägheit entwickelt. Weiterhin wurde die Gaszufuhr und das Vakuumsystem verbessert und ein Massenspektrometer für die Gasphasenanalyse implementiert. Der Aufbau ist nun vielseitig und ermöglicht Echtzeit-Beobachtungen von dynamischen Prozessen unter definierten Bedingungen.

Diese Arbeit demonstriert das Potential der *in situ* Rasterelektronenmikroskopie anhand von Untersuchungen zum Wachstum von Graphen auf katalytisch aktiven Substraten unter chemischer Gasphasenabscheidung. Komplette Wachstumszyklen, angefangen von der

Probenvorbehandlung durch Ausheizen in Wasserstoff, gefolgt vom Graphenwachstum in einer Kohlenwasserstoffhaltigen Atmosphäre und schließlich, der Abkühlung der Probe, können nun in einem Instrument verfolgt werden. Dadurch ist es möglich, ein vollständiges und ungestörtes Bild der involvierten Dynamik zu erhalten. Letzteres ist wichtig für die Validierung von mechanistischen Modellen, die bisher vorwiegend auf Basis von *ex situ* Beobachtungen erstellt worden sind. Mit Hilfe der *in situ* Beobachtungen konnten die Wachstumsbedingungen für die Produktion von qualitativ hochwertigem Graphen optimiert werden. Das modifizierte *in situ* REM eignet sich nicht nur für die Beobachtung des Wachstums von Graphene und anderen zweidimensionalen Strukturen, sondern wird inzwischen auch für die Untersuchung der Oberflächendynamik aktiver Katalysatoren eingesetzt. Dabei liefert das Gerät komplementäre und lateral aufgelöste Informationen, die mit rein spektroskopischen Daten anderer *in situ* Methoden kombiniert werden können.

Abbreviations

AFM Atomic force microscope/-microscopy

AGV Auxiliary gas valve

BLG Bilayer graphene

BPV By pass valve

BTG Bara tron gauge

CCG Compact cold cathode gauge

CIV Column cathode gauge

CVD Chemical vapor deposition

DFT Density functional theory

EBSD Electron backscatter diffraction

EBV Environmental backing valve

EG Epitaxial graphene

FEG Field emission gun

FWHM Full width at half maximum

GNR Graphene nano ribbon

GSED Gaseous secondary electron detector

HOPG Highly oriented pyrolytic graphite

IGP Ion getter pump

LEED Low energy electron diffraction

LFD Large a field detector

MBE Molecular beam epitaxy

MLG Monolayer graphene

PVP Pre vacuum pump

QFBLG Quasi-freestanding bilayer graphene

QMS Quadrupole mass spectrometer

Rad-OM Radiation-mode optical microscopy

sccm Standard cubic centimeter per minute

SLG Single layer graphene

STM Scanning tunnelling microscopy

TEM Transmission electron microscope/-microscopy

UHV Ultra-high vacuum

vdW van-der-Waals

XPS X-ray photo electron spectroscopy

1. Introduction

After a short introduction to graphene, this chapter summarizes the main methods for graphene synthesis and provides a short review on *in situ* techniques that have been used for the direct observation of graphene growth.

1.1. Graphene

Graphene, corresponding to single layer graphite, is made of hexagonal arrays of carbon atoms. Each carbon atom has four bonds, three in-plane σ bonds with its three neighbours and one out-of-plane π-bond. Due to graphene's 2D structure, the π-bonds hybridize to form the π- and π∗-bands. The electrons can freely move in this half-filled band and are responsible for most of graphene's outstanding electronic properties. At room temperature, the electron mobility in graphene exceeds 15000 $cm^2 \cdot V^{-1} \cdot s^{-1}$. The resistivity of graphene is around 10^{-6} Ω·cm and thus the lowest value at room temperature presently known.[1] Due to the intersection of graphene's conduction and valence bands at the Dirac points, graphene is a zero-gap semiconductor.[2] Moreover, it's absorption of visible light is only 2.3%.[3] This feature makes it applicable as a unique transparent conductor with high transmittance and conductivity. Based on its extraordinary physical and electronic properties, graphene attracts widespread attention, for example by application-oriented researches who try to achieve next-generation high frequency electronic devices and eventually, to find a replacement for silicon-based electronics.

Besides, graphene was also identified as a new allotrope of carbon material.[2] Due to its simple structure, graphene plays an important role as a model system in the study of the electronic properties of other carbon allotropes, including graphite, charcoal, carbon nanotubes and fullerenes. Thus graphene forms the basis for the understanding of carbon materials.

Based on the role graphene plays in material science and the high potential for practical applications, this material has drawn enormous attention during the last decade. Indeed, the development of the number of papers published on graphene during the last years (see **Figure 1-1**) reflects its impact. To date, it remains to be seen if the praised properties of this wonder material will finally find applications in future technology and will have an impact on our society. In fact, controlled large scale growth of high quality graphene remains the bottle neck for its widespread application. This work contributes to the understanding of CVD growth of graphene by revealing mechanistic insights on the growth dynamics.

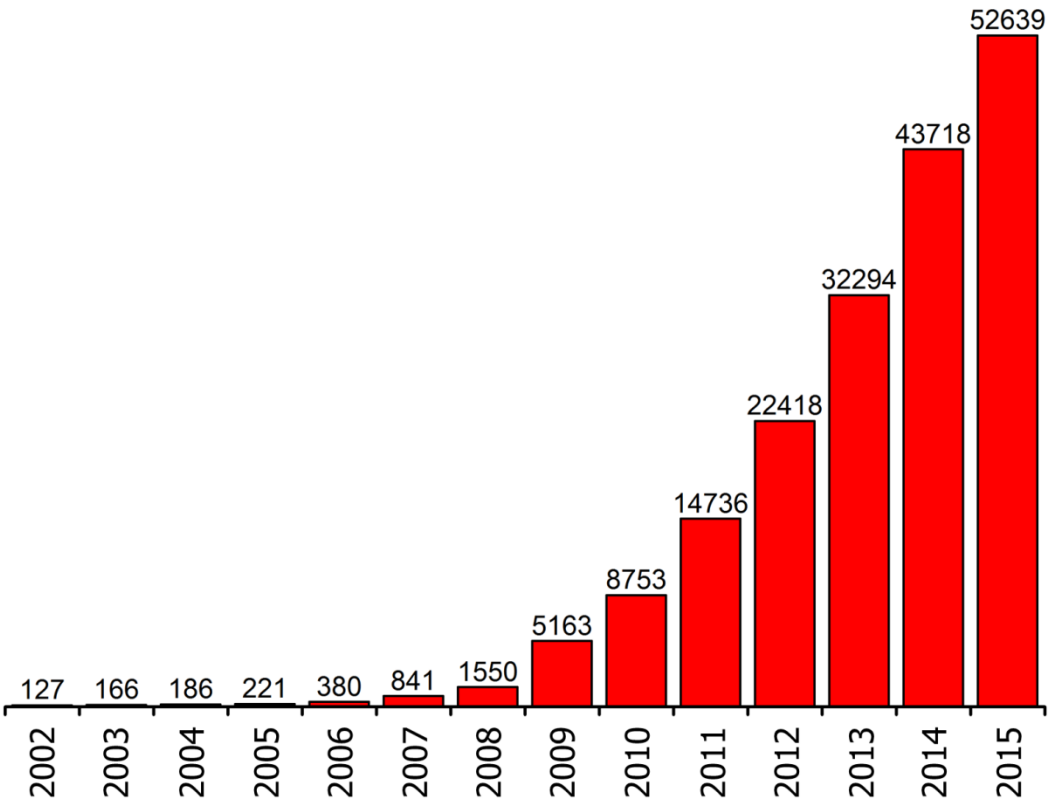

Figure 1-1. The number of scientific papers published on graphene from 2002. The data was obtained from the Web of Sience™ for the topic word 'graphene'.

1.2.Graphene synthesis

After the discovery of graphene's exceptional physical properties by Novoselov,[4] mechanical exfoliation was mainly used to obtain high quality graphene. In this process, graphene is peeled off from graphite and thinned by repeated application of adhesive tape. In order to achieve single layer graphene, multiple exfoliation steps are required. After the exfoliation, acetone is typically used to remove the adhesive tape and to transfer it onto arbitrary substrates, such as a silicon wafer. The exfoliation for producing graphene is reliable and can be applied to other 2-D materials, such as h-BN and MoS_2.[5] However, the size of the obtained sheets is generally small and only around 1 mm^2. It is a time-consuming process with low yield and can thus not be applied for graphene mass production.

A method based on chemical vapour deposition (CVD) synthesis has emerged as dominant route for the production of high-quality graphene since 2006-2009.[6-8] So far, graphene growth by metal catalysed CVD over various metal catalysts is the most widely applied method for the production of large-area, single-crystal graphene.[9-14] Generally two strategies have been followed in order to grow large-area single-crystal domains. One strategy is to depress the graphene nucleation density, thereby offering sufficient space for a limited number of graphene islands to growth on the catalyst surface.[9] The nucleation density can be limited for instance by reducing the hydrocarbon partial pressure, or the number of catalyst surface defects,[15] by growth-etching-regrowth[16] or by local feeding.[17] Nevertheless, in order to maintain continued graphene growth without the appearance of new nucleation events, a fine control of the growth processes is needed. An alternative route to large grain sizes relies on the merging of aligned islands without formation of grain boundaries. In a recent report, Nguyen *et. al.* demonstrated that large domain sizes can be realized by seamless stitching of smaller graphene domains.[18] They observed that a seamless stitching can only happen when merging domains are co-oriented. However, it remains difficult to control the in-plane orientation of graphene islands and to achieve seamless coalescence of a large number of domains. Currently, the technology of growing wafer-scale single crystal graphene remains a bottleneck for

industrial mass production. Thus, it remains a great challenge to find process conditions for scalable synthesis of continuous single layer graphene with large grain size on metal catalyst. So far, growth optimization was mostly based on feedback obtained by post-growth characterizations. In order optimize graphene growth more efficiently and to overcome the present limitations, a fundamental understanding of the underlying mechanisms is required. For this, direct observation of graphene formation on different metal catalysts in real-time and as a function of growth conditions is required.[19]

1.3. *In situ* observation techniques for graphene CVD growth

Real-time observation of graphene growth has been realized by several *in situ* techniques. Based on the working principle, these *in situ* methods can be grouped into imaging- and spectroscopic techniques.

1.3.1. *In situ* imaging

The inception of real-time imaging methods that provide spatially- and time-resolved details has dramatically accelerated the understanding of the growth of 2D materials. The value of real-time imaging for deducing the details of graphene growth has been demonstrated for a number of transition metal catalysts such as Ni, Cu, Ru, Rh, and Ir using low-energy electron microscopy (LEEM),[12,20-25] scanning tunnelling microscopy (STM),[26-28] and Radiation-mode optical microscopy.[29]

1.3.1.1. Low-energy electron microscopy

Low-energy electron microscopy (LEEM) is a surface sensitive technique for the observation of surfaces and thin films.[30] In LEEM, a low-energy electron beam (1-100eV) is used to image the sample surface. A high-energy electron beam (15-20keV) is generated by an electron gun. The beam is focused by a series of electromagnetic lens (illumination optics) and then deflected towards the sample by a beam deflector. (see **Figure 1-2**) After deflection, the high-energy beam first passes through an objective lens,

which is grounded, and then enters a retarding electric field in which the kinetic energy of the electron beam is decreased to 1-100 eV before it finally reaches the sample surface. The incoming low-energy beam emits backscattered electrons from the sample surface. The backscattered electrons pass through the retarding field between the sample and the objective lens in reverse direction and get accelerated. Afterwards, the beam goes back over the same route until the deflector, which acts as a beam separator. The backscattered electron beam is deflected in the direction of the projector lenses and finally reaches the imaging plane, where an image is produced. Besides imaging the sample surface, LEEM also allows to observe low-energy electron diffraction (LEED) pattern by changing the excitation of the intermediate lens.

Compared with SEM, which uses a focused electron probe to scan across the sample and collects locally generated signals to produce images, in LEEM, all pixels are recorded simultaneously. Based on the image formation principle, LEEM is ideally suited for *in situ* observation of dynamic processes at surfaces. Therefore, several *in situ* studies aimed on deducing details of graphene growth either through CVD growth or via precipitation from the bulk were reported for a number of transition metal substrates such as Cu, Ru, Rh and Ir using LEEM.[12,21,25,31]

However, due to the high scattering amplitude of low-energy electrons in atmosphere, LEEM is limited to high vacuum operation. [22] So far, *in situ* observation under real CVD conditions at controllable atmosphere or ambient pressure has not been realized by LEEM. (see **Figure 1-3**)

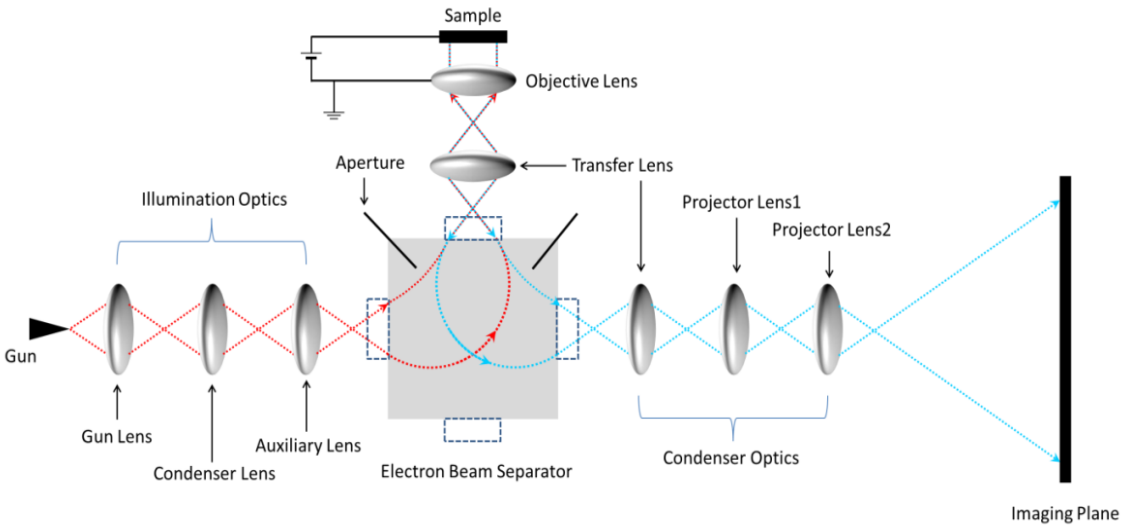

Figure 1-2. Scheme showing the optics and path of electrons in a LEEM.

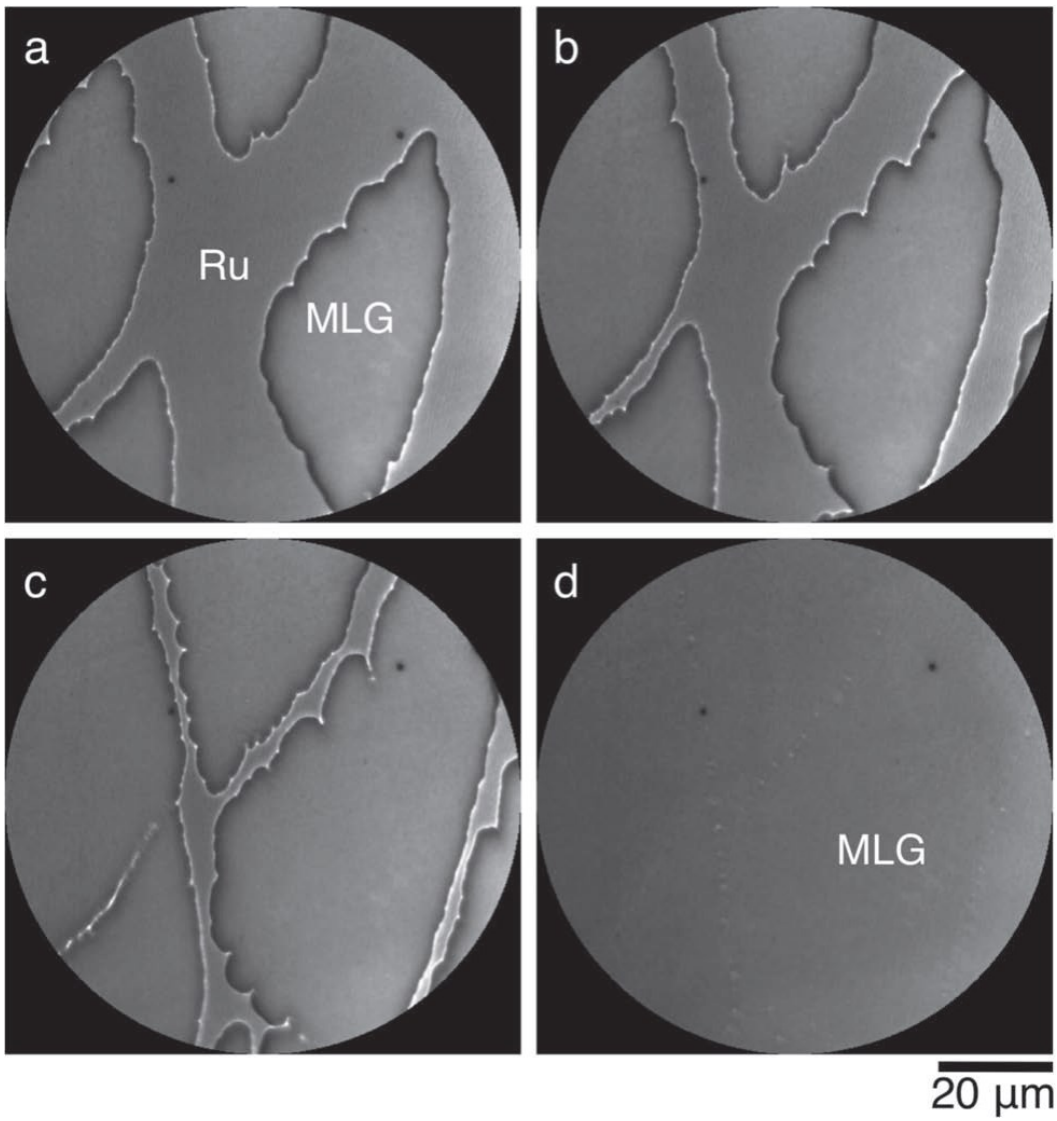

Figure 1-3. ***In situ*** **LEEM images of mono layer graphene (MLG) growth on Ru(0001) at 3×10^{-8} Torr ethylene at 830 °C. Elapsed time: (a) 800 s; (b) 880 s; (c) 1040 s; (d) 1490 s. Reproduced from** ***Small.*** 2012**, 8. 2250-2257.**[12]

Due to pressure limitation of LEEM, the carbon precursor for graphene is generally provided either through surface segregation or by direct hydrocarbon feed, without the addition of hydrogen. Hydrogen, however, plays an important role in controlling the quality of CVD graphene and is known to reduce the nucleation density of graphene or

even suppresses its nucleation. It is further involved in graphene healing due to its preferential etching of defects.[16]

1.3.1.2.Radiation-mode optical microscopy

In optical microscopy, a series of lenses and reflected or transmitted visible light is used to generate magnified images of a sample. At the temperatures required for graphene growth (above 900°C on Cu), the substrate radiates in the visible light regime. Therefore, sufficient contrast for imaging graphene growth on metal substrates could not be obtained using reflected light. (see **Figure 1-4**) However, the emissivity of graphite and Cu is quite different at high temperature.[32,33] Thus it is possible to image graphene on Cu with radiation-mode optical microscopy, which utilizes light that is radiated from the surface to produce the image. Terasawa & Saiki demonstrated the possibility to observe graphene growth by radiation-mode optical microscopy (Rad-OM).[29](see **Figure 1-5**)

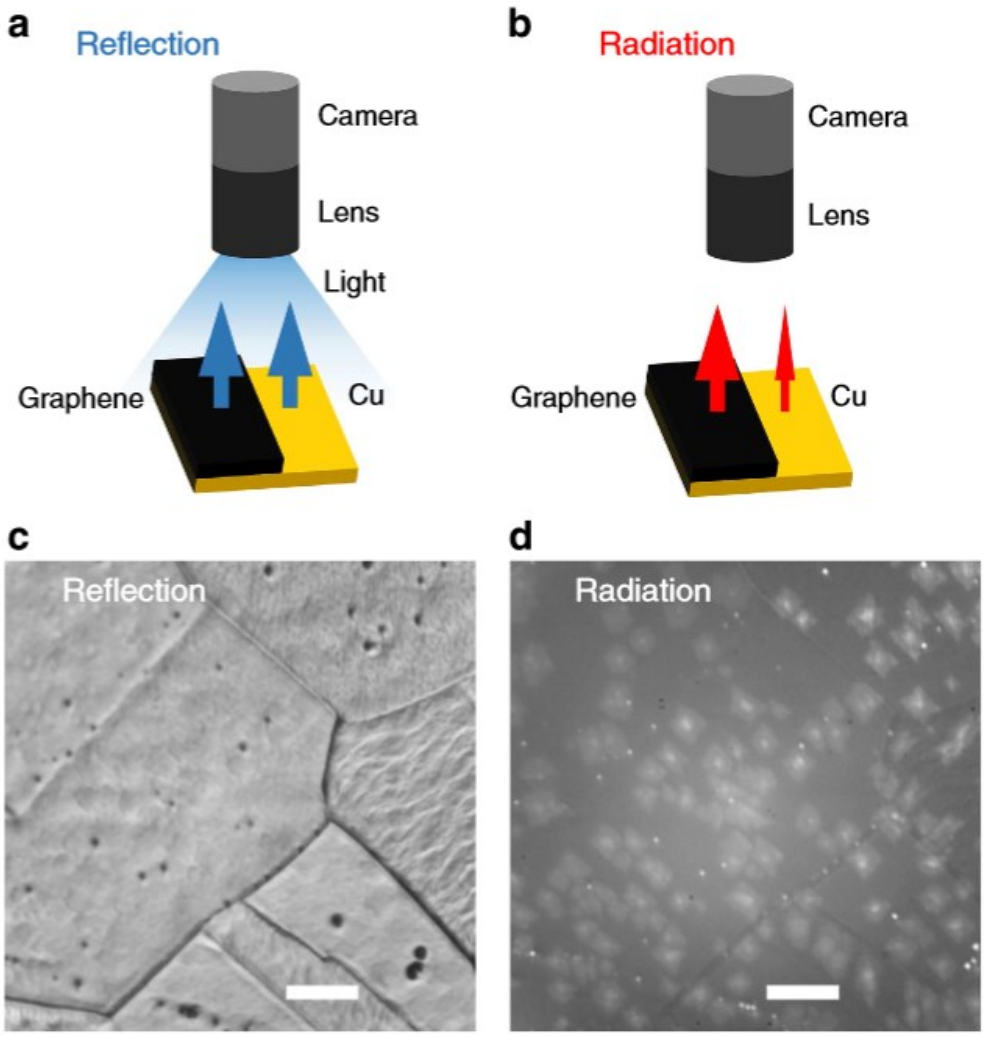

Figure 1-4. (a,b) Schematic illustrations. Due to the high transparency of graphene, the reflected light intensity from graphene on Cu is very similar to that of a bare Cu substrate (a). In contrast, the thermal radiation emitted from graphene at high temperatures is much larger than from copper, owing to the significant difference in their emissivity (b). (c) Reflection mode optical microscopy image obtained for graphene on Cu at 900°C. (d) Rad-OM image obtained for graphene on Cu at 750°C for the same area as (c). Scale bars measure 50µm. [29]

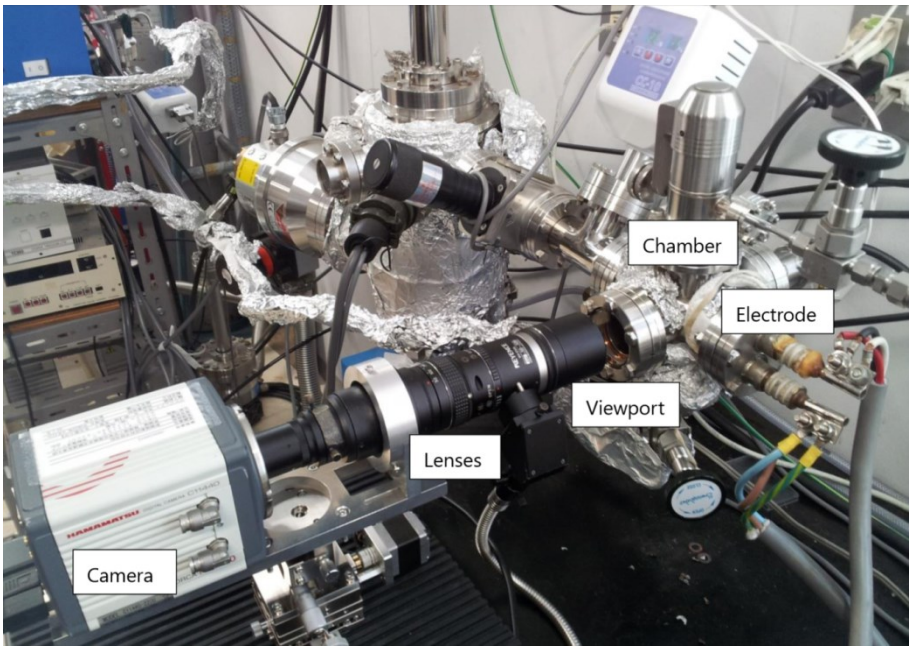

Figure 1-5. Image of the radiation-mode optical microscopy system used by Terasawa, T et al.[29]

The radiation-mode imaging technique enables observation of dynamic processes during growth at high temperature and atmospheric pressure at micrometer to millimeter resolution. (**Figure 1-6**)

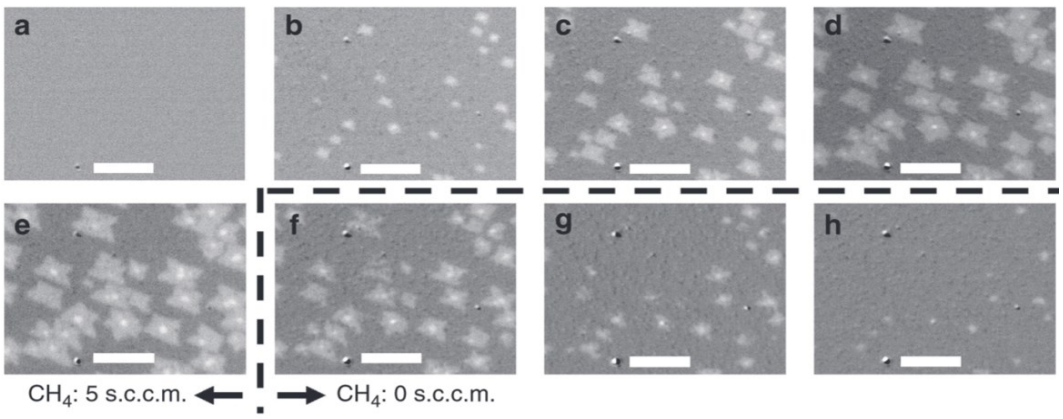

Figure 1-6. Rad-OM images of graphene growth and shrinkage. (a–e) The growth at 0, 100, 200, 300 and 380 s with a CH_4 flow rate of 5 sccm (f–h) The shrinkage at 500, 600 and 700s with that of 0 sccm in hydrogen plus Ar. The black dashed line indicates the change of the CH_4 flow rate. Scale bar measures 50 µm. Reproduced from Nat. Commun. 2015, 6, 6. [29]

1.3.1.3.Isotope labelling and micro-Raman mapping

Isotope labelling is a technique that enables to study the reaction pathway. It allows tracking the path of a reaction by substituting one atom kind of the reactant by an isotope. The labelled isotope can be traced in the products and helps to deduce the route of reaction.

Li, et. al. reported a study of adlayer graphene growth and stacking sequence of multilayer graphene using isotopic labelling of the methane precursor.[34] They dosed isotopically labelled methane periodically into a quartz tube furnace for graphene growth. After growth, micro-Raman mapping was used to study the distribution of the isotope in the formed graphene. The ex-situ observation provided valuable insights into the mechanism of adlayer formation (see **Figure 1-7**). Besides, Hao, et. al. used isotope labelling to study the growth detail of single crystal graphene on Cu.[9] (see **Figure 1-8**)

However, due to limited spatial resolution of Raman mapping, isotope labelling can only provide information down to the micrometre scale. Moreover, since growth processes cannot be directly captured by isotope labelling, details of the dynamic behaviour are missed and possible surface modifications during sample cooing and transfer remain undetected.

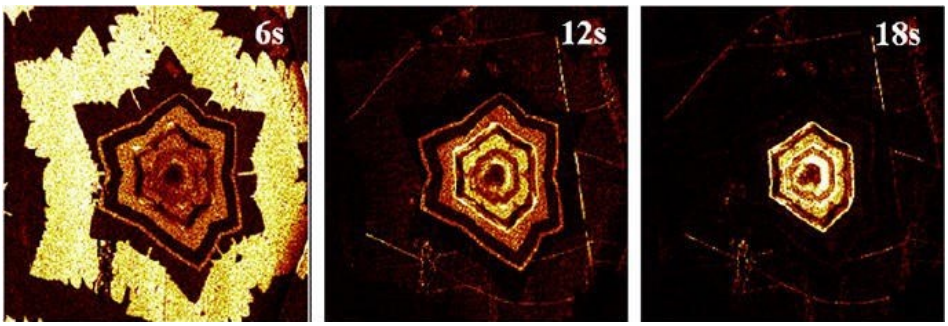

Figure 1-7. Raman mapping of isotopically labelled multilayer graphene. Optical image of the graphene grain transferred onto the 300 nm SiO_2/Si substrate. Schematic of growth mechanism shows the adlayer graphene form underneath the first layer. Figure taken from *Nano Letters* 2013, 13, 486. [34]

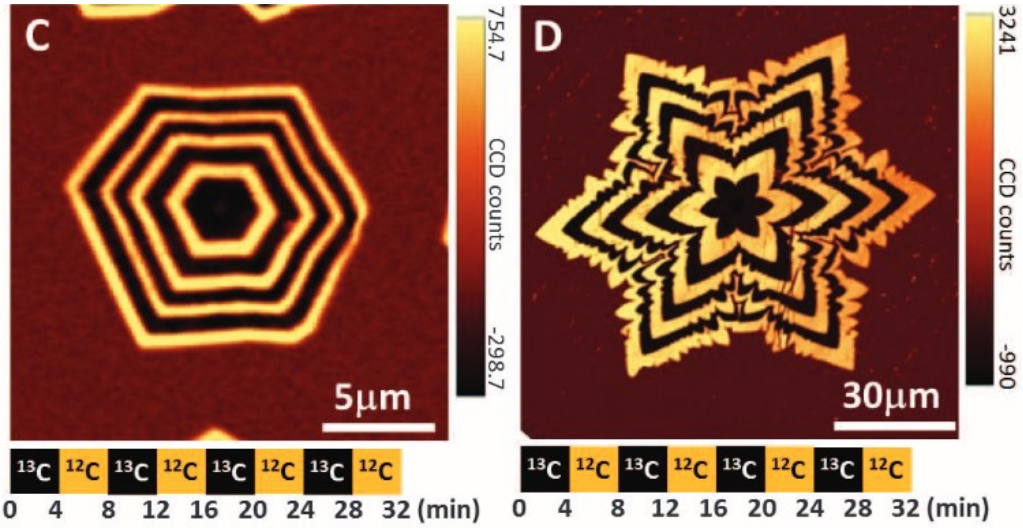

Figure 1-8. Raman mapping of isotopically labelled single crystal graphene indicates attachment limitation growth (left) and diffusion limitation growth (right). Figure taken from Science 2013**, 342, 720** [9]

1.3.1.4. *In situ* scanning tunnelling microscopy

Scanning tunnelling microscopy (STM) is a technique that uses the tunnelling of electrons over small distances to image surfaces at the atomic level.[35] The image is recorded by recording the height of the tip which is maintained with a constant current between the tip and the surface (in constant current mode). A plot of the tip height at all measurement positions on the surface provides the topography.

STM is a versatile technique that allows observation under ambient atmosphere over a wide range of temperatures.[36] Thus, the STM can be employed to investigate formation of graphene at the atomic scale. Atomic resolution STM imaging requires extremely clean

surfaces, a fine tip, excellent vibration control, and a stable electromagnetic environment. Therefore, STM is a challenging technique for *in situ* observation of graphene growth and has so far only been realized under UHV condition.

Dong, et. al reported *in situ* STM to study details of graphene growth on Rh.[27,37] They found that the edge kink creation is the rate-limiting step during graphene growth and that kink creation at concave corners during graphene coalesce of co-oriented domains shows a lower barrier (see **Figure 1-9**). Using STM, Günther et. al showed that the graphene-metal interaction can induce metal surface reconstruction and formation of large terraces with high steps, leading to much better ordered graphene layers.[38] (see **Figure 1-10**)

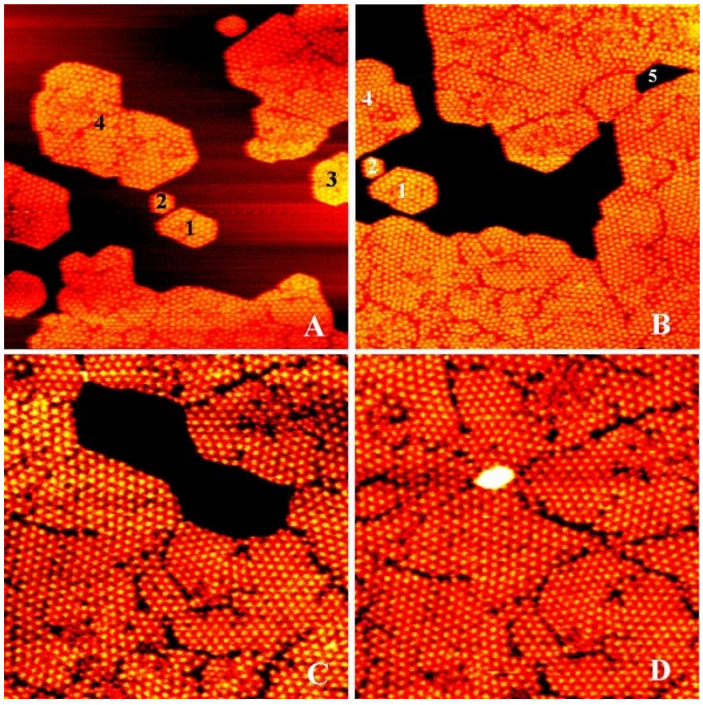

Figure 1-9. Four snap shots from a STM movie. Frame to frame analysis was performed for the 865s period between panels A and B and the 524 s period between C and D. Sample voltage: 1.84 V. Tunnelling current: 50 pA. Image sizes: 160×160 nm^2 for A and B; 100×100 nm^2 for C and D. Reproduced from *ACS Nano*. 2013**, 7. 7028-7033.**

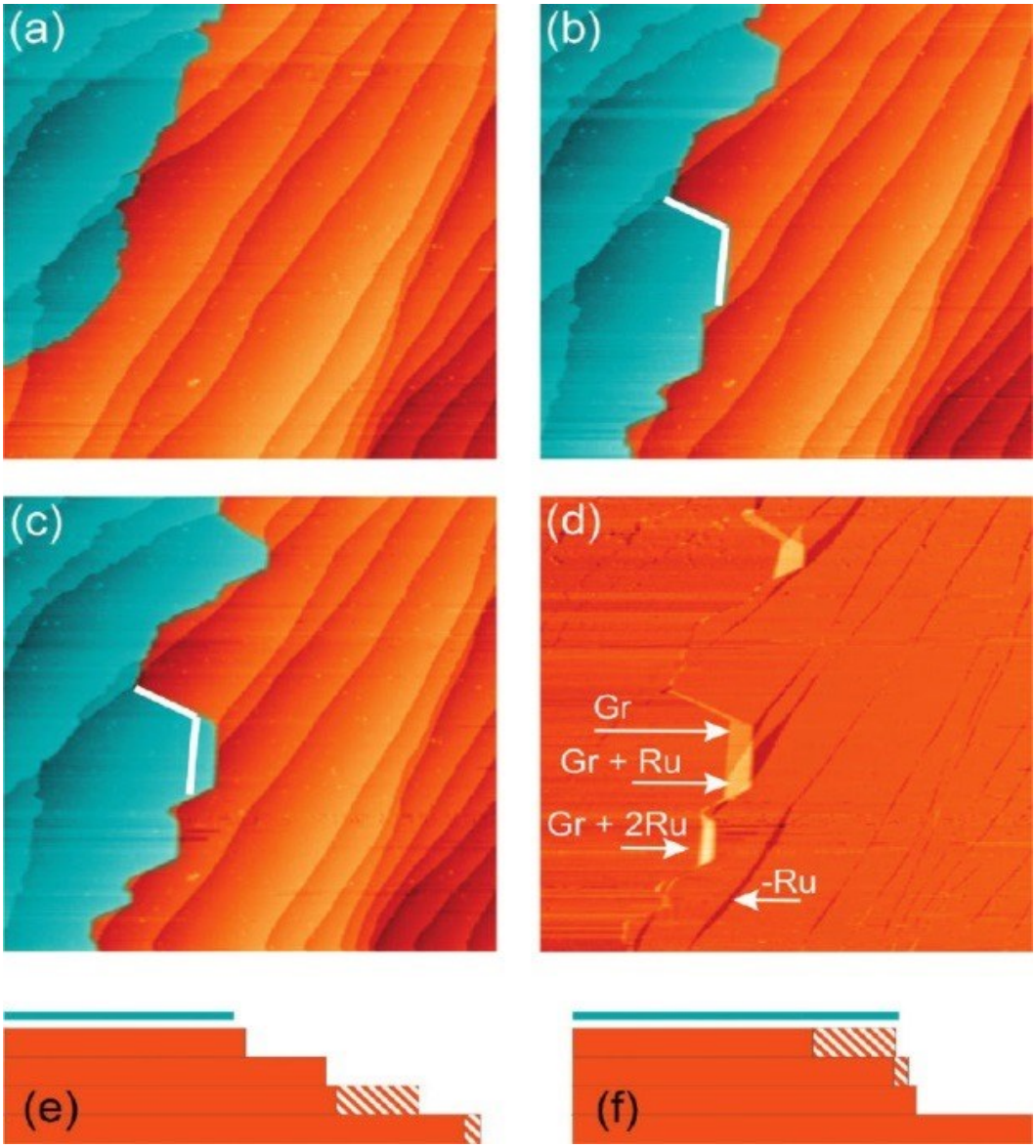

Figure 1-10. In situ STM scans from a series of images recorded at 665°C. (a) After dosing 4.5 L of C_2H_4 at 2×10^{-8} mbar the ethylene valve was closed. (b,c) Ru(0001) terraces grow and steps are no longer over grown. (d) Differential image of (b) and (c), showing areas where Ru atoms were removed (dark) and areas were graphene has grown and one or two layers of Ru atoms were deposited (bright). (e,f) Growth mechanism; the shading indicates reshuffled Ru layers. Figure taken from *Nano Letters*. 2011**, 11. 1895-1900.**

1.3.2. *In situ* spectroscopy

In order to better understand graphene CVD growth on metal catalyst, it is necessary to complement imaging techniques with *in situ* techniques that are capable of providing chemical information about the state of the surface during the CVD processes.

1.3.2.1. *In situ* X-ray photoelectron spectroscopy (XPS)

XPS is a surface sensitive chemical characterization technique that has been widely used in catalysis, materials science and microelectronics. Especially in the field of heterogeneous catalysis, XPS plays an important role and offers detailed information about the composition and electronic structure of catalyst surfaces.[39] However, due to the low mean free path of photoelectrons in atmosphere, XPS is conventionally carried out *ex situ* in a UHV chamber, where chemical information can only be measured before and after catalytic experiments. Real-time information about the actual state of the surface in the active state is missed. To reveal the nature of a catalytically active surface during a reaction, differentially pumped photoelectron detectors have been developed. These near-ambient pressure XPS (NAP-XPS) systems enable to measure the composition and state of a surface at pressures in the few mbar regime .[40]

By combining *in situ* XPS with real-time imaging under relevant reaction atmosphere, we were able to acquire detailed information about the electronic structure of the surface and the coupling between graphene and the copper substrate.[41] We found that the Cu catalyst surface is in the metallic state during the CVD process and that the C_{1s} XPS core level signatures for isothermally growing graphene are shifted to higher binding energies (BEs) compared to previously reported peak positions for isolated graphene. The observed BE upshift is indicative of an electronic coupling between the Cu catalyst and the growing graphene. The higher BE is retained after hydrocarbon exposure and cooling, but lost during air/oxygen exposure. It was found that oxygen intercalation gives rise to a decoupling of Cu and graphene. (see **Figure 1-11**). Interestingly, graphene coupling and oxygen induced decoupling can also be followed as contrast variations in the secondary electron images recorded in the ESEM (This will be discussed in chapter 3).

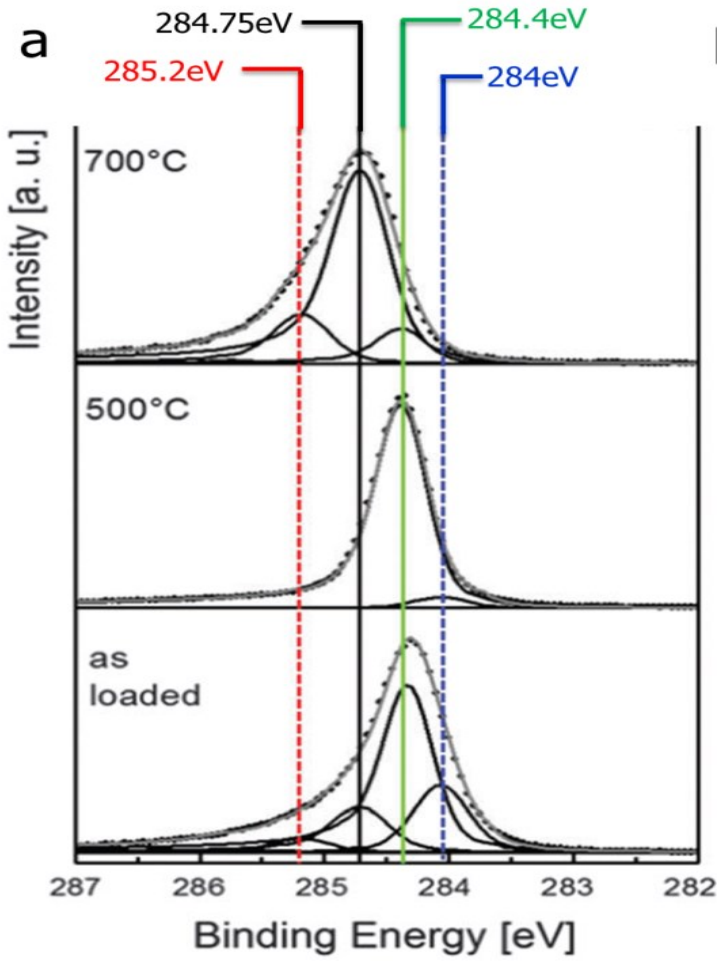

Figure 1-11. Coupling and decoupling of graphene on Cu via oxygen intercalation as measured using in situ XPS for the C1s.

As summarized above, *in situ* techniques are powerful and fundamentally important methods for the studying of graphene CVD growth. In the following chapters, I will elaborate the effectiveness of *in situ* SEM for studying the mechanistic details of graphene CVD on metal catalyst. Finally, using *in situ* SEM, we find a simple recipe for a potential scale-up process for the controlled growth of single-layer graphene.

1.4. References

1. Chen, J. H.; Jang, C.; Xiao, S. D.; Ishigami, M.; Fuhrer, M. S. *Nat. Nanotechnol*. **2008**, 3, 206.

2. Castro Neto, A. H.; Guinea, F.; Peres, N. M. R.; Novoselov, K. S.; Geim, A. K. *Reviews of Modern Physics* **2009**, 81, 109.

3. Nair, R. R.; Blake, P.; Grigorenko, A. N.; Novoselov, K. S.; Booth, T. J.; Stauber, T.; Peres, N. M. R.; Geim, A. K. *Science* **2008**, 320, 1308.

4. Novoselov, K. S.; Geim, A. K.; Morozov, S. V.; Jiang, D.; Zhang, Y.; Dubonos, S. V.; Grigorieva, I. V.; Firsov, A. A. *Science* **2004**, 306, 666.

5. Novoselov, K. S.; Jiang, D.; Schedin, F.; Booth, T. J.; Khotkevich, V. V.; Morozov, S. V.; Geim, A. K. *Proc. Natl. Acad. Sci. U. S. A*. **2005**, 102, 10451.

6. Yu, Q.; Lian, J.; Siriponglert, S.; Li, H.; Chen, Y. P.; Pei, S.-S. *Appl. Phys. Lett*. **2008**, 93.

7. Kim, K. S.; Zhao, Y.; Jang, H.; Lee, S. Y.; Kim, J. M.; Kim, K. S.; Ahn, J.-H.; Kim, P.; Choi, J.-Y.; Hong, B. H. *Nature* **2009**, 457, 706.

8. Somani, P. R.; Somani, S. P.; Umeno, M. *Chemical Physics Letters* **2006**, 430, 56.

9. Hao, Y. F.; Bharathi, M. S.; Wang, L.; Liu, Y. Y.; Chen, H.; Nie, S.; Wang, X. H.; Chou, H.; Tan, C.; Fallahazad, B.; Ramanarayan, H.; Magnuson, C. W.; Tutuc, E.; Yakobson, B. I.; McCarty, K. F.; Zhang, Y. W.; Kim, P.; Hone, J.; Colombo, L.; Ruoff, R. S. *Science* **2013**, 342, 720.

10. Gao, L. B.; Ren, W. C.; Xu, H. L.; Jin, L.; Wang, Z. X.; Ma, T.; Ma, L. P.; Zhang, Z. Y.; Fu, Q.; Peng, L. M.; Bao, X. H.; Cheng, H. M. *Nat. Commun*. **2012**, 3, 7.

11. Chen, S. S.; Ji, H. X.; Chou, H.; Li, Q. Y.; Li, H. Y.; Suk, J. W.; Piner, R.; Liao, L.; Cai, W. W.; Ruoff, R. S. *Advanced Materials* **201**3, 25, 2062.

12. Sutter, P. W.; Flege, J. I.; Sutter, E. A. *Nat. Mater*. **2008**, 7, 406.

13. Pan, Y.; Zhang, H. G.; Shi, D. X.; Sun, J. T.; Du, S. X.; Liu, F.; Gao, H. J. *Advanced Materials* **2009**, 21, 2777.

14. Iwasaki, T.; Park, H. J.; Konuma, M.; Lee, D. S.; Smet, J. H.; Starke, U. *Nano Letters* **2011**, 11, 79.

15. Geng, D. C.; Wu, B.; Guo, Y. L.; Huang, L. P.; Xue, Y. Z.; Chen, J. Y.; Yu, G.; Jiang, L.; Hu, W. P.; Liu, Y. Q. *Proc. Natl. Acad. Sci. U. S. A.* **2012**, 109, 7992.

16. Ma, T.; Ren, W.; Liu, Z.; Huang, L.; Ma, L.-P.; Ma, X.; Zhang, Z.; Peng, L.-M.; Cheng, H.-M. *Acs Nano* **2014**, 8, 12806.

17. Wu, T.; Zhang, X.; Yuan, Q.; Xue, J.; Lu, G.; Liu, Z.; Wang, H.; Wang, H.; Ding, F.; Yu, Q.; Xie, X.; Jiang, M. *Nat. Mater*. **2016**, 15, 43.

18. Van Luan, N.; Shin, B. G.; Dinh Loc, D.; Kim, S. T.; Perello, D.; Lim, Y. J.; Yuan, Q. H.; Ding, F.; Jeong, H. Y.; Shin, H. S.; Lee, S. M.; Chae, S. H.; Quoc An, V.; Lee, S. H.; Lee, Y. H. *Advanced Materials* **2015**, 27, 1376.

19. Wang, Z.-J.; Weinberg, G.; Zhang, Q.; Lunkenbein, T.; Klein-Hoffmann, A.; Kurnatowska, M.; Plodinec, M.; Li, Q.; Chi, L.; Schloegl, R.; Willinger, M.-G. *ACS nano* **2015**, 9, 1506.

20. Nie, S.; Walter, A. L.; Bartelt, N. C.; Starodub, E.; Bostwick, A.; Rotenberg, E.; McCarty, K. F. *Acs Nano* **2011**, 5, 2298.

21. Nie, S.; Wofford, J. M.; Bartelt, N. C.; Dubon, O. D.; McCarty, K. F. *Phys. Rev. B* **2011**, 84, 7.

22. Sutter, P.; Ciobanu, C. V.; Sutter, E. *Small* **2012**, 8, 2250.

23. Sutter, P.; Hybertsen, M. S.; Sadowski, J. T.; Sutter, E. *Nano Letters* **2009**, 9, 2654.

24. Sutter, P.; Sutter, E. *Adv. Funct. Mater*. **2013**, 23, 2617.

25. Wofford, J. M.; Nie, S.; McCarty, K. F.; Bartelt, N. C.; Dubon, O. D. *Nano Letters* **2010**, 10, 4890.

26. Kwon, S. Y.; Ciobanu, C. V.; Petrova, V.; Shenoy, V. B.; Bareno, J.; Gambin, V.; Petrov, I.; Kodambaka, S. *Nano Letters* **2009**, 9, 3985.

27. Dong, G. C.; Frenken, J. W. M. *Acs Nano* **2013**, 7, 7028.

28. Patera, L. L.; Africh, C.; Weatherup, R. S.; Blume, R.; Bhardwaj, S.; Castellarin-Cudia, C.; Knop-Gericke, A.; Schloegl, R.; Comelli, G.; Hofmann, S.; Cepek, C. *Acs Nano* **2013**, 7, 7901.

29. Terasawa, T. O.; Saiki, K. *Nat. Commun*. **2015**, 6, 6.

30. Bauer, E. *Reports on Progress in Physics* **1994**, 57, 895.

31. Loginova, E.; Nie, S.; Thuermer, K.; Bartelt, N. C.; McCarty, K. F. *Phys. Rev. B* **2009**, 80.

32. Kwiecinska, B.; Scott, E. *Journal of Microscopy-Oxford* **1977**, 109, 289.

33. Ramanathan, K. G.; Yen, S. H. *Journal of the Optical Society of America* **1977**, 67, 32.

34. Li, Q.; Chou, H.; Zhong, J.-H.; Liu, J.-Y.; Dolocan, A.; Zhang, J.; Zhou, Y.; Ruoff, R. S.; Chen, S.; Cai, W. *Nano Letters* **2013**, 13, 486.

35. Binnig, G.; Rohrer, H. Ibm *Journal of Research and Development* **1986**, 30, 355.

36. Feltz, A.; Memmert, U.; Behm, R. *J. Surf. Sci*. **1994**, 314, 34.

37. Dong, G. C.; van Baarle, D. W.; Rost, M. J.; Frenken, J. W. M. *New J. Phys*. **2012**, 14, 15.

38. Guenther, S.; Daenhardt, S.; Wang, B.; Bocquet, M. L.; Schmitt, S.; Wintterlin, J. *Nano Letters* **2011**, 11, 1895.

39. Venezia, A. M. *Catalysis Today* **2003**, 77, 359.

40. Blume, R.; Kidambi, P. R.; Bayer, B. C.; Weatherup, R. S.; Wang, Z.-J.; Weinberg, G.; Willinger, M.-G.; Greiner, M.; Hofmann, S.; Knop-Gericke, A.; Schloegl, R. *Physical Chemistry Chemical Physics* **2014**, 16, 25989.

41. Kidambi, P. R.; Bayer, B. C.; Blume, R.; Wang, Z.-J.; Baehtz, C.; Weatherup, R. S.; Willinger, M.-G.; Schloegl, R.; Hofmann, S. *Nano Letters* **2013**, 13, 4769.

2. Equipment and modification

The ESEM is a versatile instrument for investigating the micro/nano-structure and chemical composition of samples in a gaseous environment.[1] However, commercial ESEM's were primarily designed to observe a large range of different samples under different atmospheres, ranging from investigation of biological or non-conductive samples to dynamic experiments.[2,3] Versatility is an important design criterion for a commercial instrument that should fulfil the needs of customers from different fields. For specific applications, there is still room for improvements. In order to achieve controllable and reliable conditions that are relevant for the investigation of gas-phase induced catalyst dynamics and reactions, the set up needed to be modified. In this chapter, the equipment modifications are described.

2.1.The vacuum system of the ESEM

The ESEM (FEI Quantum 200F FEG) is equipped with a turbo molecular pump and pre-vacuum pumps for generating the vacuum in the chamber and additional ion getter pumps to pump the upper part of the column and the electron gun with the field emitter.[1,2] To separate areas with different vacuum levels, two pressure limiting apertures (PLA) are used;[4] one PLA which separates the UHV region of the gun chamber from the column region (intermediate cavity), and one PLA separating the intermediate column vacuum from the chamber (see **Figure 2-**). The working pressure in the chamber of the ESEM can be set using the manufacturer's software to several modes, which correspond to different pumping configurations: the “High Vacuum” (High-Vac), “Low Vacuum” (Low-Vac) and ESEM mode. Each mode is determined by the setting of the automatic environmental backing valve (EBV) and the valve connecting the chamber with the main turbo molecular pump (ChIV). The automatic EBV is closed for High-Vac and is open for low vacuum and ESEM mode (see **Figure 2-2**). While the chamber is directly pumped by the

main TMP in High-Vac mode, the ChIV valve is closed during Low-Vac and ESEM mode. The background pressure of the ESEM chamber reaches values of around 8.8×10^{-6} Pa after pumping for 3-5h. With the addition of a water-cooled heating stage, the vacuum level only reached values of around 9×10^{-5} Pa. The loss of vacuum quality due to the circulating cooling water in the chamber is attributed to the quick-connectors connecting the water hoses of the heating stage to the water in- and outlet at the sidewall of the chamber.

In order to improve the quality of the vacuum and to eliminate possible sources of carbon contamination, the pre-vacuum pumps were replaced by oil-free scroll pumps. Moreover, prior to CVD growth experiments, the chamber of the ESEM was routinely cleaned using a N_2+O_2 plasma generator.

In order to achieve a better control of the vacuum at different gas flow rates and to avoid the use of the in-built pressure regulator, a second turbo molecular pump (TMP2) was connected to the differential line via a manually regulated valve (RV) to vacuumize. Using this additional pump and valve, it is now possible to control the chamber pressure either by changing gas flow into the chamber or by adjusting pumping rate via the manual valve. Since the internal tubing for the imaging gases did not fulfil our requirement of vacuum quality, the inbuilt imaging gas inlet was blocked (see **Figure 2-**). Gases used during the experiments were directly guided into the chamber using a home-built flange with a gas-feed-through.

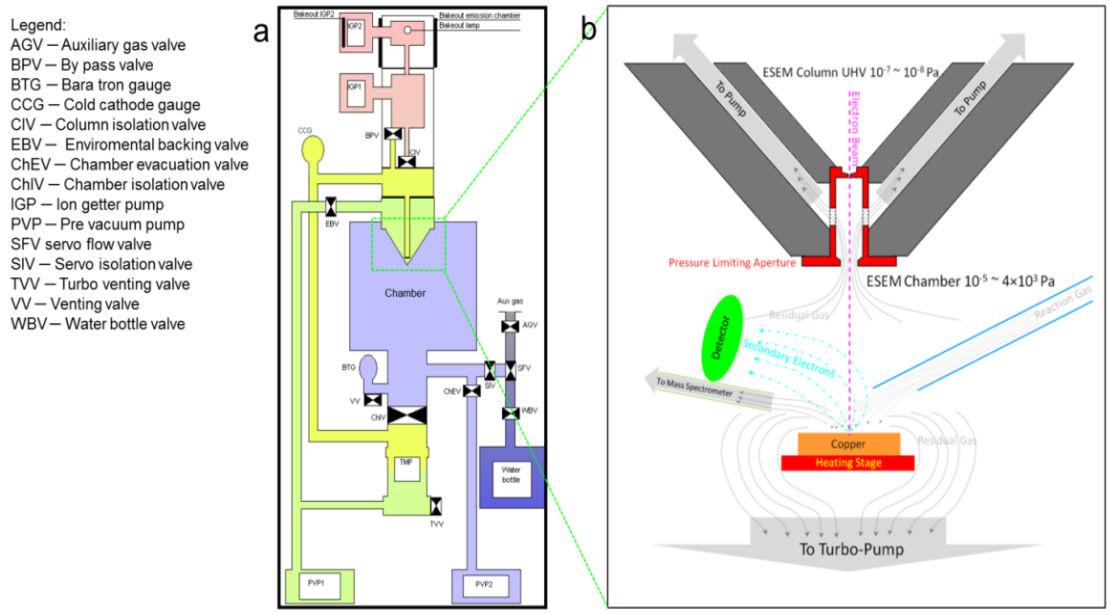

Figure 2-1. Schematic representation of the differential pumping system of the ESEM. (a) Differential pumping system of ESEM (FEI quanta 200F). (b) Schematic illustration showing pressure limiting aperture that separates the specimen chamber and the intermediate cavity (column).

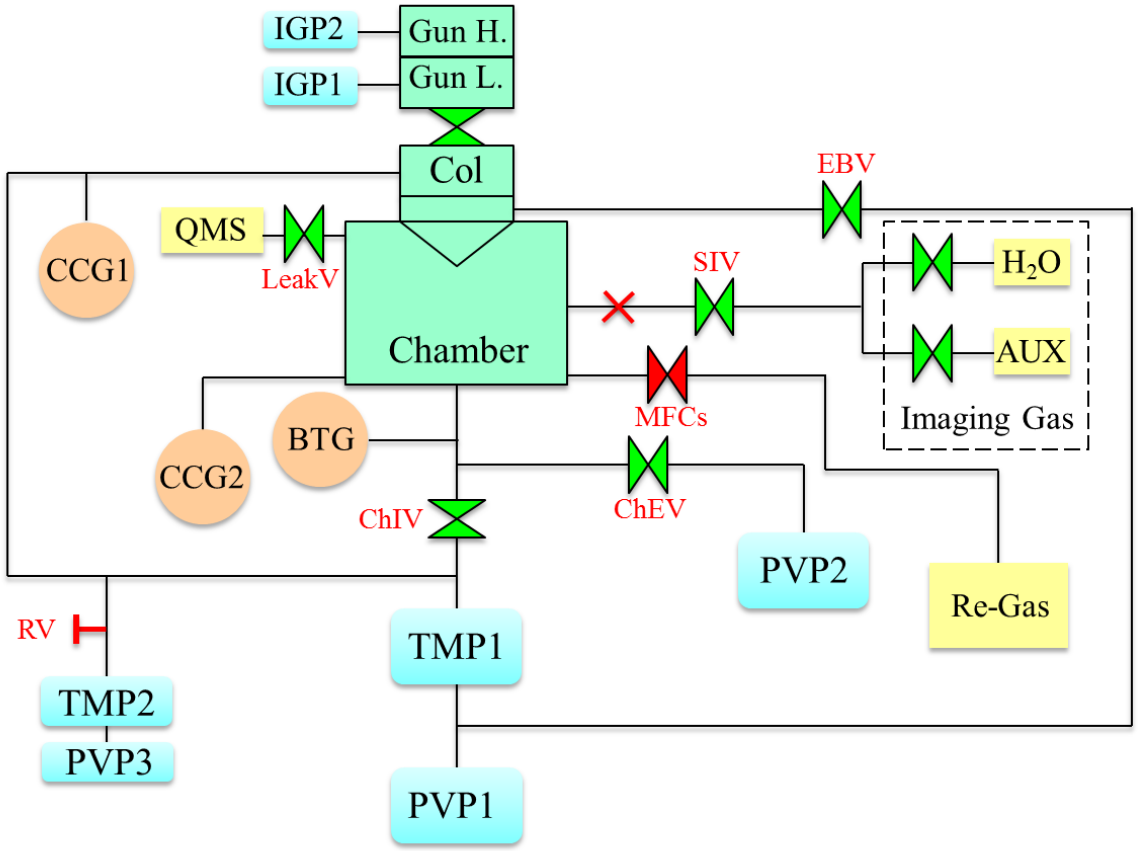

Figure 2-2. Schematic showing modified ESEM Vacuum system.

2.2.Imaging and detectors

The conventional SEM applies an Everhart-Thornley detector to collect secondary electrons (SE), which primarily carry information about sample topography.[5,6] The SE are generated when the high energy electron beam interacts with the sample and ejects electrons from the atoms of the sample.[7] These emitted electrons travel through the material and scatter inelastically along the way. Due to their low kinetic energies, SE can escape only from a very shallow region near the sample surface, providing topographic

information. They escape the surface with low kinetic energies (around 10eV).[8] To generate an image of a sample's topography, the electron beam is scanned along the surface while the emitted SE signal is detected and registered for each point. In order for the detector to collect enough SE signals to construct an image, a sufficiently good vacuum in the range below $5E^{-2}$ Pa is required. Otherwise the slow SE would be scattered by gas molecules in the atmosphere.[9] The Everhart-Thornley detector is not designed to image at higher pressure conditions and due to the internally applied high voltage, would lead to plasma discharges.[10]

Under Low-Vacuum conditions (0.05 to 200 Pa) and ESEM conditions, the collision of SE with gas molecules leads to gas ionization, and generation of a cascade of low-energy electrons.[11,12] These slow electrons can be detected, but a special detector is required.[1] Such a detector utilizes a positive potential, to generate a strong enough electric field in which slow electrons are attracted toward the detector. In this way, the ionized gas acts as medium and transfers the discharge current to the detector. The discharge current is related to the generated electrons from the sample. At same time, the electric field force drags positive ions toward the sample surface and suppresses static charging. After collection of the ionized SE, the signal is sent to an electron amplifier and mapped to an image. (see **Figure 2-3**) This imaging method suppresses surface charging and enables nonconductive samples to be observed by SEM without conductive coatings.[11]

The ESEM (FEI Quanta 200F) is equipped with two kinds of detectors, which can work at different pressure ranges. The so called “large a field detector” (LFD) is for imaging at low vacuum (1.0×10^{-2} Pa to 200 Pa). The other is a gaseous secondary electron detector (GSED), which allows imaging at pressures up to 2600 Pa.[13]

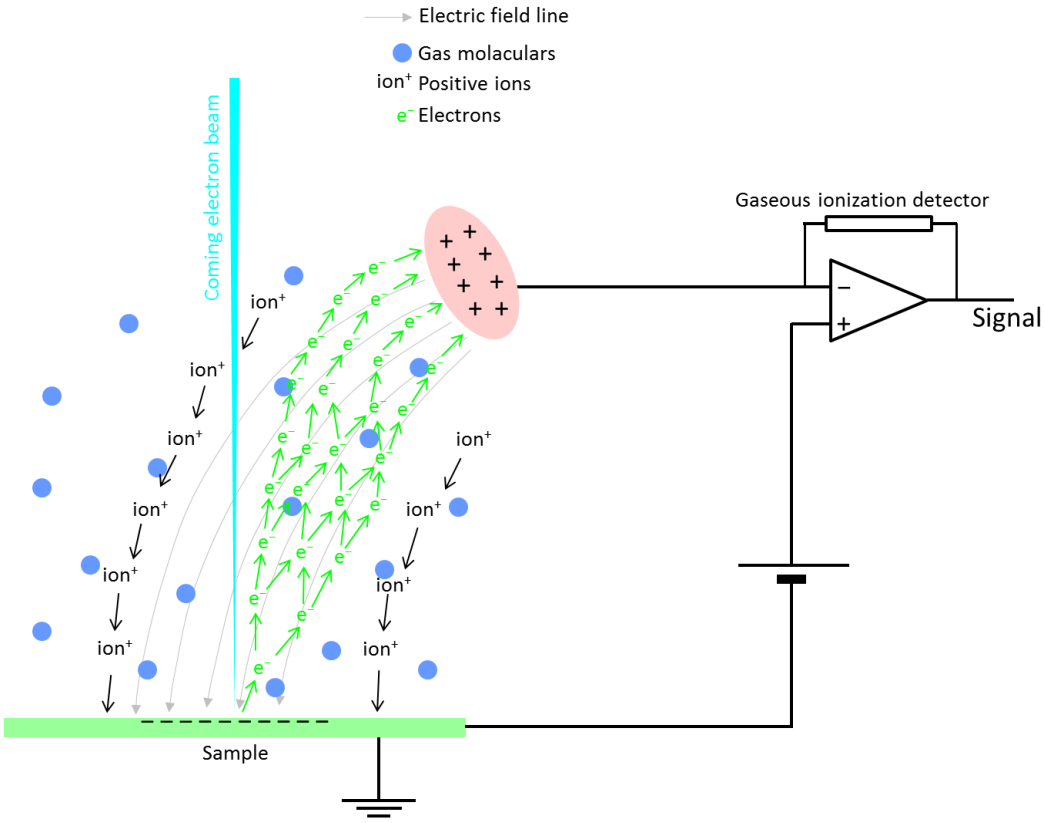

Figure 2-3. A schematic drawing, showing how gas ionization is used to amplify the secondary electron signal detected by the large field detector.

With increasing chamber pressure, electrons from the electron beam collide with gas molecules, thereby degrading the incident electron flux. Due to scattering of electrons by gas molecules, a gradual loss of electrons from the direction of the initial beam will occur in the ESEM chamber. The electrons are scattered over a peplum-shaped volume cantered around the beam focus.[14] Since the width of the scattering region is orders of magnitude larger than the width of beam, the scattered electrons only contribute to background noise

(see **Figure 2-4**). The remaining focused electron beam contains only a fraction of the intensity of the original beam but is sufficient for imaging the specimen.[1]

The optimal working distance, accelerating voltage and beam spot size varies with chamber pressure, atmosphere and sample composition, and has to be chosen in view of the required information and obtainable resolution. Often, the optimal setting corresponds to the best compromise between resolution and image quality.[9]

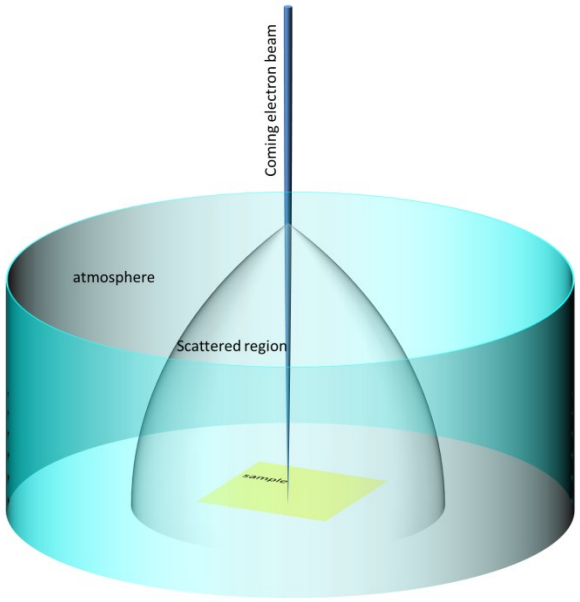

Figure 2-4: Simple sketch of electron scattering in gaseous environment

2.3. Heating stage

There are two basic requirements for the heating system of the ESEM.[15] 1. The CVD graphene growth experiments required temperatures up to 1100 °C. 2. The lifetime of the heating system needed to be long, in order to enable routine, long-duration experiments at high temperature. The commercial ESEM is equipped with a heating stage that is able to heat up to 1000 °C. However, this heating stage has a few disadvantages. 1. Heating and cooling rates are relatively slow and show undesired hysteresis during temperature regulation, especially at high temperatures (800-1000 °C). 2. The volume of the heating unit is relatively big, resulting in large thermal inertia. Furthermore, the temperature of a conventional heater is always higher than the sample that is heated by heat flow from the heater to the sample, 3. The life time of the heating unit is relatively short (<100 h). In order to avoid these problems, we have developed a novel laser heating stage for ESEM that enables fast heating to temperatures of up to 1000 °C. The heating stage uses a commercial infrared laser to provide heating power. Direct heating of the sample reduces the amount of thermal radiation and heated mass compared to Joule heating with the conventional heating stages. Since only the sample is hot and the surrounding components of the heating stage are water-cooled, catalytic background activity during experiments in reactive atmosphere is minimized.

The laser heating stage is composed of three basic components: 1. optical path unit, 2. cooling unit, 3. heating plate and laser generator. The main structure of the laser heating stage is shown in **Figure 2-5.** The optical path unit includes an optical fiber, a collimator and a prism. The incident laser light is introduced into the ESEM chamber by an optical fiber feed-through. The laser beam is divergent after exiting the optical fiber. Hence, a collimator is needed to form a parallel beam of desired diameter. In order to illuminate the heating plate or backside of the sample, a prism is added to change the light path. (see **Figure 2-5e**) Due to the relatively high power of the laser radiation (up to 40 W), the collimator and prism need to be actively cooled. Thus a cooling unit was developed. (see **Figure 2-6, Figure 2-7**, **Figure 2-8**) The cooling unit consists of the stage chiller (aluminium block, **Figure 2-6**), laser adapter cooling unit (aluminium block, **Figure 2-7**) and a prism and collimator cooling unit (copper, **Figure 2-8**). All the cooling parts are cooled by mechanical contact to the stage frame, which is cooled by a closed loop water circulation unit.

For accurate temperature measurements, thermocouple wires were directly spot-welded on the sample. The temperature was controlled by adjustment of the laser power output.

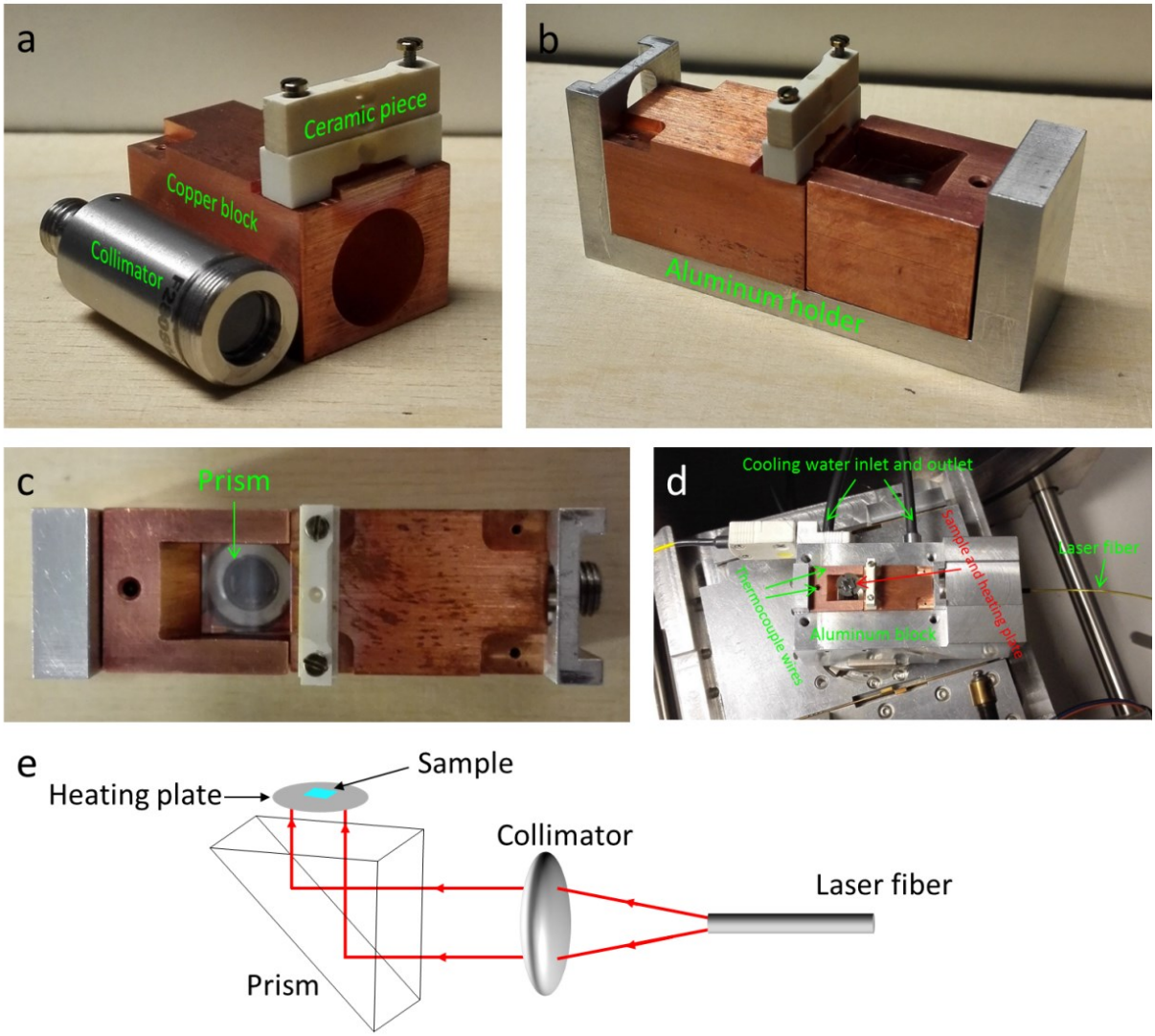

Figure 2-5. Components of the laser heating stage. (a) Collimator, copper block and ceramic sample holder. (b) Optical path unit and cooling unit. (c) Top view of optical path unit and cooling unit. (d) The laser heating stage in working state. (e) Scheme of the optical path.

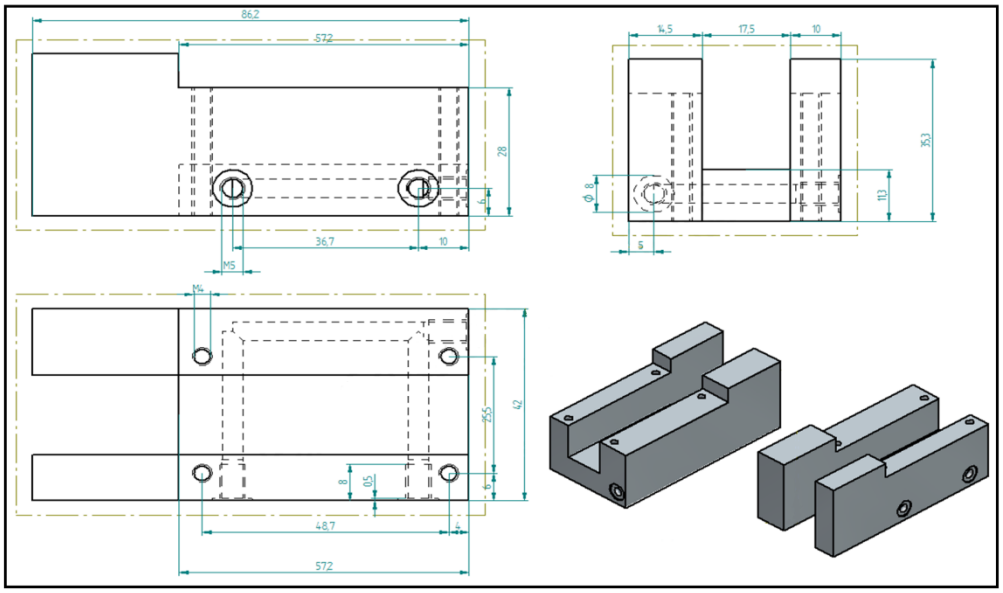

Figure 2-6. Three-view drawings of the stage chiller unit.

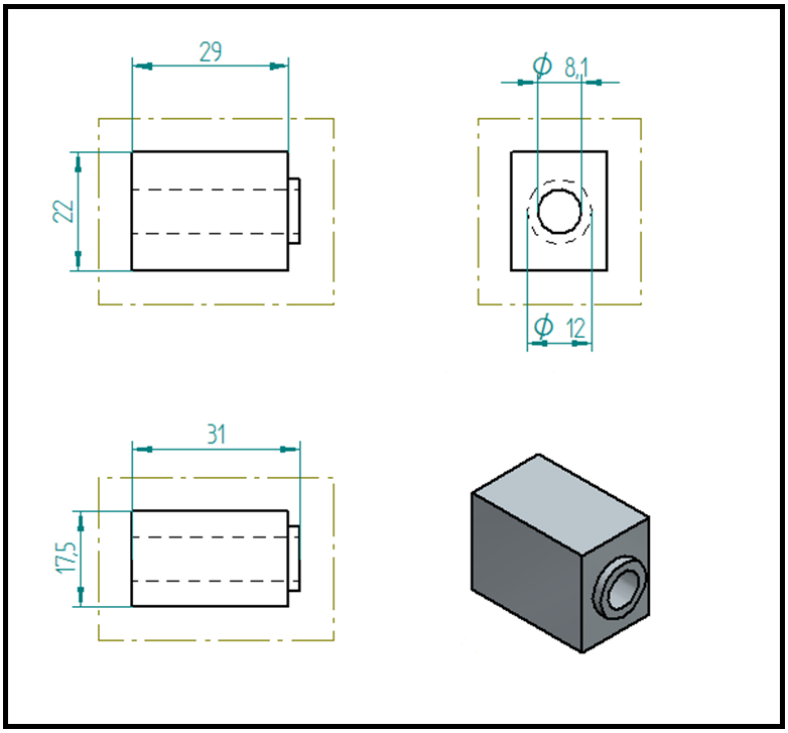

Figure 2-7. Three-view drawings of the laser adapter cooling unit.

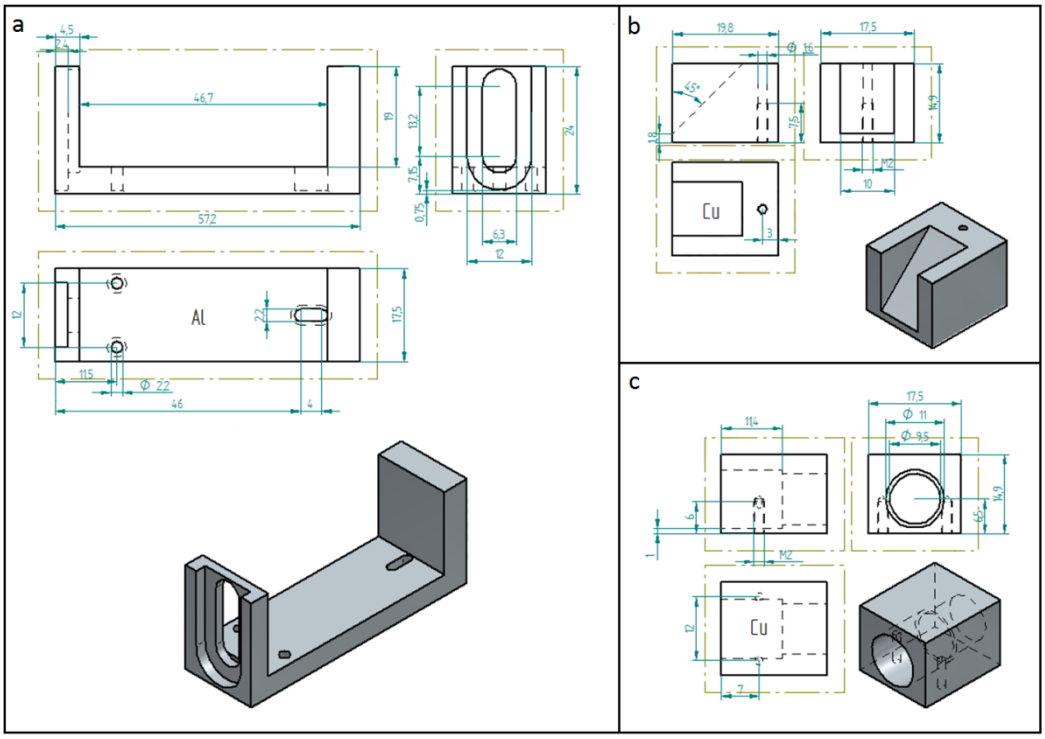

Figure 2-8. Three-view drawings of the cooling unit for the prism and collimator. (a) Aluminium holder. (b) Prism cooling unit. (c) collimator cooling unit.

2.4.Mass spectrometer

In order to identify the residual gas composition in the chamber, a quadruple mass spectrometer (Pfeiffer OmniStar) was attached to the chamber of the ESEM. The quadrupole mass spectrometer (QMS) is pumped by a separate turbo molecular pump, and connected to the chamber via a leak valve. The pressure drop between the ESEM chamber and the QMS enables the gas in the ESEM chamber to be sucked into mass spectrometer (see **Figure 2-9**).

In the FEI Quanta ESEM, some of the vacuum tubings and components are interconnected by KF-flanges (Klein Flange) with circular clamp and elastomeric O-ring. Furthermore, the chamber and vacuum components cannot be baked-out. The ESEM is thus not an ultra-high-vacuum capable instrument. The vacuum level that can be reached is limited and the

corresponding residual gas pressure is around 3.2×10^{-5} Pa (ESEM chamber is connect to gas feeding tubes), with a rest-gas composition mostly comprising water, N_2 and O_2 (see MS data **Figure 2-10**). Indeed, when the working pressure is set to "high vacuum" mode (2×10^{-5} Pa), the main peak in the MS signal is due to water. (see **Figure 2-10**). Assuming that the background pressure is due to air leaks, the O_2 net partial pressure is around 5×10^{-6} Pa. Although it is not much, it might, depending on the metal substrate, play a role during the catalytic CVD growth of graphene and has therefore to be taken into account. Under Low−vac mode, hydrogen annealing at a chamber pressure of 25 Pa, partial pressure of air is further diluted. (see **Figure 2-11**) So far, we have so far not calibrated it for different pressures. For the moment, the MS mainly serves us to monitor the quality of the vacuum and the growth atmosphere, without providing quantitative numbers about the amount of O_2 and H_2O.

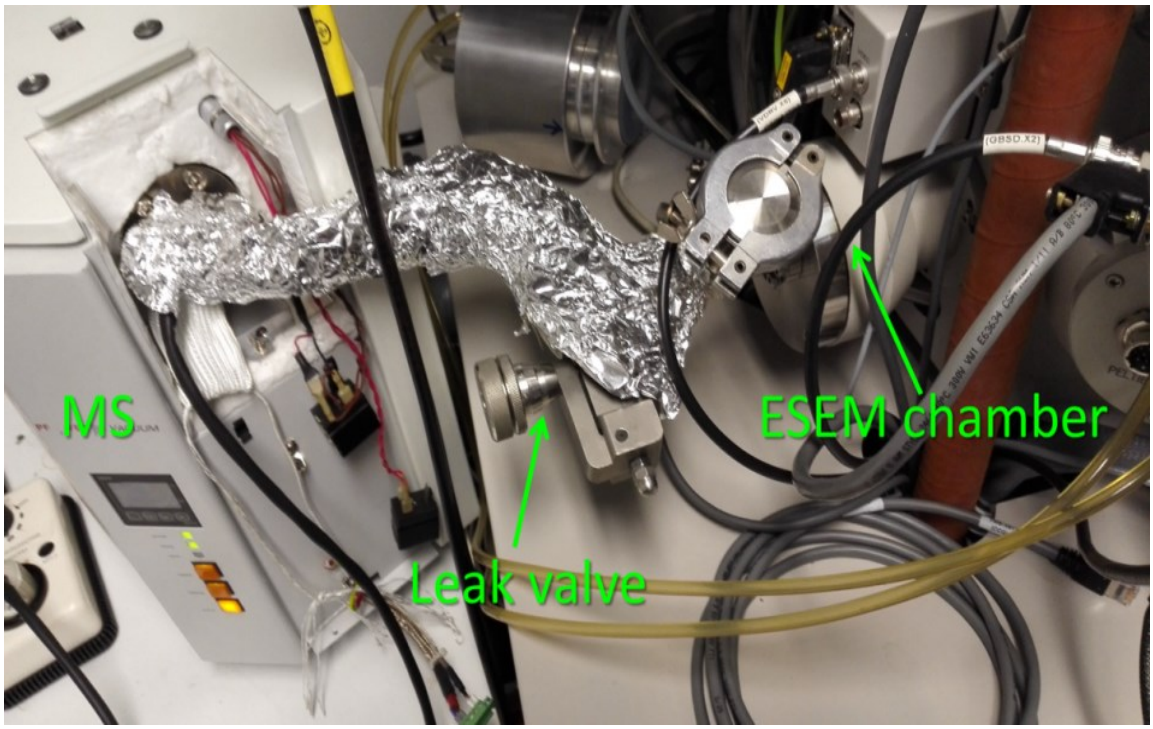

Figure 2-9. Photo of the connection between the mass spectrometer and ESEM chamber.

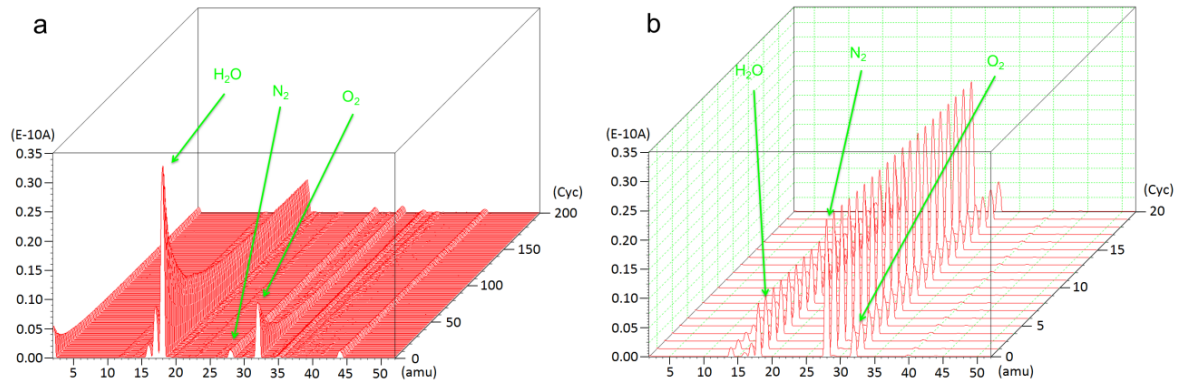

Figure 2-10. Residual gas composition in the ESEM chamber shown in the form of a continuously varying electrical signal (analog scan) where the measured ion current is indicative for the concentration of molecules of a certain mass. (a) MS data recorded during the baking of the quadrupole spectrometer. The H_2O signal and the portion of O_2 that is related to fragmentation of H_2O decrease with time. During this process, the N_2 intensity remains constant. (b) MS spectrum when the spectrometer is connected to the ESEM chamber (leak valve fully opened), showing increased N_2 and O_2 signals. The ratio between the two confirms the presence of air leaks.

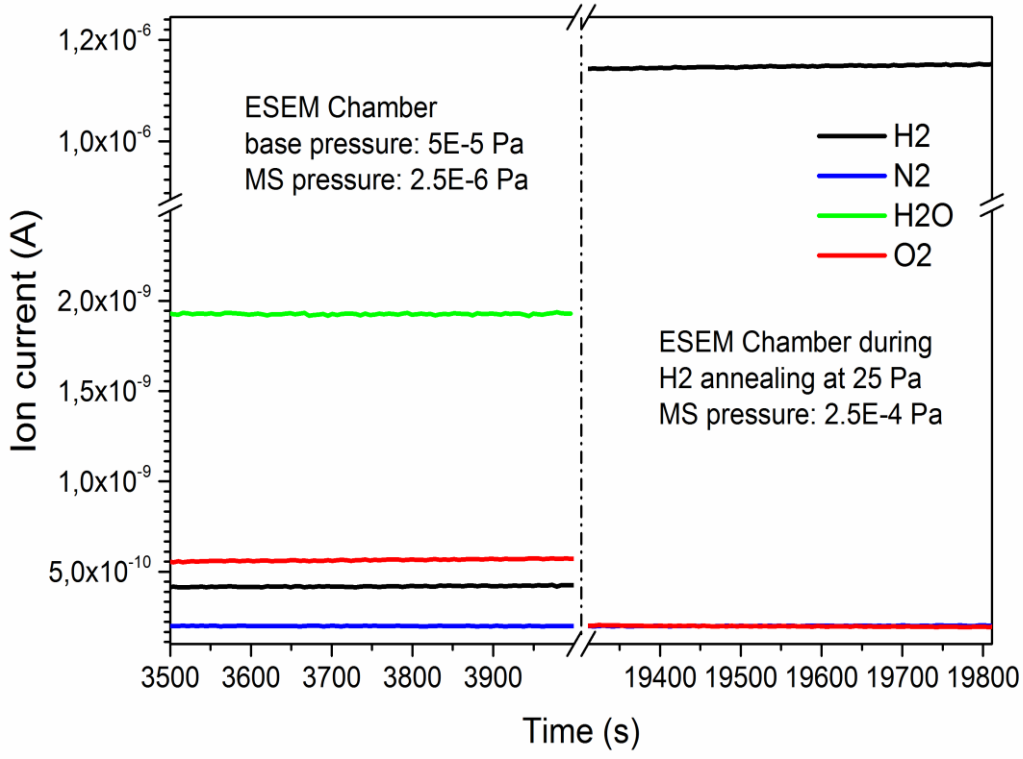

Figure 2-11. Residual gas composition in the chamber of the ESEM after blockage of the internal lines for imaging gases, measured at a base pressure of ~5E^{-5} Pa shows the presence of mainly water, oxygen, hydrogen and nitrogen. The oxygen signal is higher than the nitrogen signal due to contributions from

fragmentation of water by electron impact ionization. Under hydrogen annealing at a chamber pressure of 25 Pa, the gas flow to the MS was restricted by a leak valve to $2.5E^{-4}$ Pa.

The modifications of the vacuum system and the blockage of the internal gas-lines for imaging gas resulted in an improved base-pressure and reduced oxygen signal in the chamber.

Based on modified ESEM, directly observing surface processes at nanoscale during a reaction under controlled temperature and atmosphere can be realized. The experimental data, such as morphology, temperature and pressure, can be record and related in real-time. Thus, this technique serves as a general framework for design and optimizing the experiment condition. In brief, *in situ* SEM provides an efficient method for generating feedback for the understanding relevant reaction process at nanoscale.

2.5. References

1. Danilatos, G. D. *Environmental scanning electron microscope: Some critical issues*, 1994.

2. Donald, A. M. *Nat. Mater.* **2003**, *2*, 511.

3. Nedela, V. In *Emag: Electron Microscopy and Analysis Group Conference 2007*; Baker, R. T., Mobus, G., Brown, P. D., Eds. 2008; Vol. 126.

4. Danilatos, G. D. *Microscopy and Microanalysis* **2000**, *6*, 21.

5. Grigoryev, A. Y. *Scanning* **1990**, *12*, 87.

6. Everhart, T. E.; Thornley, R. F. M. *Journal of Scientific Instruments* **1960**, *37*, 246.

7. Chung, M. S.; Everhart, T. E. *Journal of Applied Physics* **1974**, *45*, 707.

8. Shih, A.; Yater, J.; Hor, C.; Abrams, R. *Applied Surface Science* **1997**, *111*, 251.

9. Toth, M.; Uncovsky, M.; Knowles, W. R.; Baker, F. S. *Appl. Phys. Lett.* **2007**, *91*.

10. Kim, K. H.; Akase, Z.; Suzuki, T.; Shindo, D. *Materials Transactions* **2010**, *51*, 1080.

11. Danilatos, G. D. *Advances in Electronics and Electron Physics* **1988**, *71*, 109.

12. Meredith, P.; Donald, A. M.; Thiel, B. *Scanning* **1996**, *18*, 467.

13. Phillips, M. R.; Toth, M.; Drouin, D. *Appl. Phys. Lett.* **1999**, *75*, 76.

14. Zoukel, A.; Khouchaf, L.; Martino, J. D.; Ruch, D. *Micron* **2013**, *44*, 107.

15. Ubhi, H. S.; Parsons, J.; Othen, N.; Campbell, S.; Poole, R.; Gholinia, A. In *Electron Microscopy and Analysis Group Conference 2013*; Nellist, P. D., Ed.; Iop Publishing Ltd: Bristol, 2014; Vol. 522.

3. Observation of graphene

3.1. Abstract

During imaging in scanning electron microscopy (SEM), sample contamination is a common problem that affects the quality of results unfavourably. Sample contamination refers to the deposition of carbonaceous molecular on the sample surface. During normal imaging processes in SEM, electron beams induce that residual carbonaceous molecular are bombarded on sample surface. The build-up of deposited carbon layer often appears in SEM images as the well-known “black box.” This process is known as electron beam induced carbon deposition. In this point of view, the secondary electron (SE) signal that enables to image thin deposited carbon layer on sample surface. This raise the question — Does sensitivity of the SE signal that enables the observation of atomically thin carbon surface layers? Indeed, single layer graphene can be imaged by SE detector and the number of graphene layers can be measured by SEM. In this chapter, we combine *in situ* XPS with *in situ* SEM to study the relation between SE contrast of graphene on Cu substrate. We find high sensitivity of SE signal even can image graphene-substrate coupling status.

3.2. Introduction

Generally, different interactions between the electron beam and the sample can give rise to signals that can be detected. The most important signals for image generation in the ESEM originate from secondary electrons and backscattered electrons and additional electrons that are produced by the interaction of these electrons with the imaging gas.[1] Due to the low kinetic energy and an associated low mean free path, secondary electrons originate from a region close to the surface of the sample.[2] In contrast, backscattered electrons can also originate from a volume below the surface up to a depth that depends on the density and mean atomic number, channelling condition and acceleration voltage.

Graphene-substrate interactions play an important role in graphene applications. On one hand, the graphene-substrate interaction can induce a band gap, which is crucial for the application of graphene in semi-conductor devices.[3] Therefore, graphene-substrate interaction has attracted a lot of research interest in bandgap engineering of graphene and surface science.[4,5]

Since we are dealing with atomically thick sheets, the properties of graphene on substrates should be characterized by conventional surface sensitive techniques, such as LEEM, XPS, STM, Raman and AFM.[6-11] Due to the discrete intensity of SE, the number of graphene layers can be identified by SEM.[12,13] Hence, we investigate use SEM as surface sensitive imaging tool to interpret graphene-copper interaction information.

The aim of this investigations was to gain insight into the connection between SE contrast of graphene and graphene-copper coupling status. For this purpose, using *in situ* XPS characterizations as reference, we compared the contrast changes of *in situ* SEM observed during re-heating decoupled graphene on Cu. We confirm that changes in the coupling between copper and graphene can be identified as slight changes in the SE image contrast.

3.3.Result and discussion

Using complementary *in situ* SEM and XPS we capture the evolution of graphene on Cu surface, the state of the surface during growth and the graphene-Cu interactions at each stage of graphene CVD growth and after exposure to ambient air. Graphene growth was performed by CVD growth at 900°C (C_6H_6, vapour pressure ~10^{-2} Pa, 99.2% purity, after ~10^{-2} Pa H_2 pretreatment) in SEM and XPS chamber. The thickness of polycrystalline Cu foil is 25μm (Alfa Aesar Puratronic, 99.999% purity). The experimental process is shown in **Figure. 3-1**. After growth and cooling, the as-grown sheets were furthermore characterized by Raman. On the basis of the Raman spectra the grown sheets can be identified as high-quality single-layer graphene.[14]

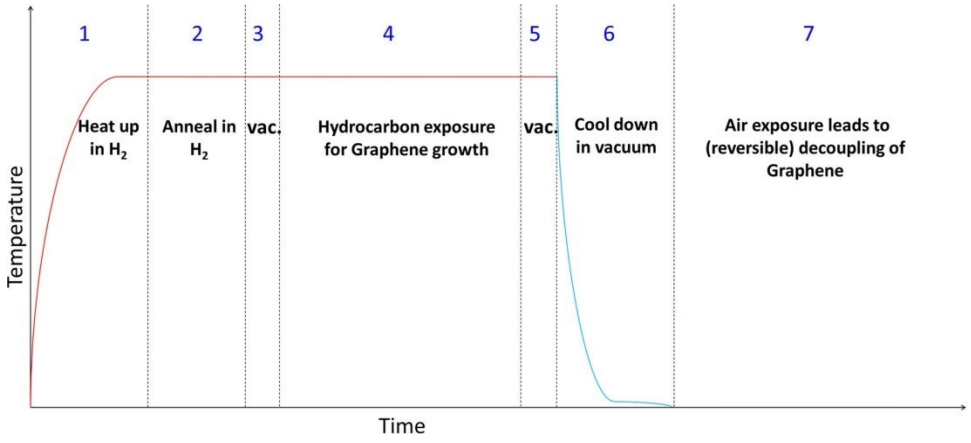

Figure. 3-1. Schematic process diagram illustrating the salient stages of graphene CVD on polycrystalline Cu.

In situ SEM images capturing the appearance and growth of carbon sheets on Cu at 900°C is presented in **Figure 3-2a, b**. We note, in the SEM images, due to channelling contrast and differences in the work function, the Cu surface exhibits contrast differences arising from different Cu grains.[15] But graphene covered regions are always darker than bared catalyst surface on same Cu grain. (see **Figure 3-2**) Thus graphene sheets still can be identified by SE contrast in SEM image.

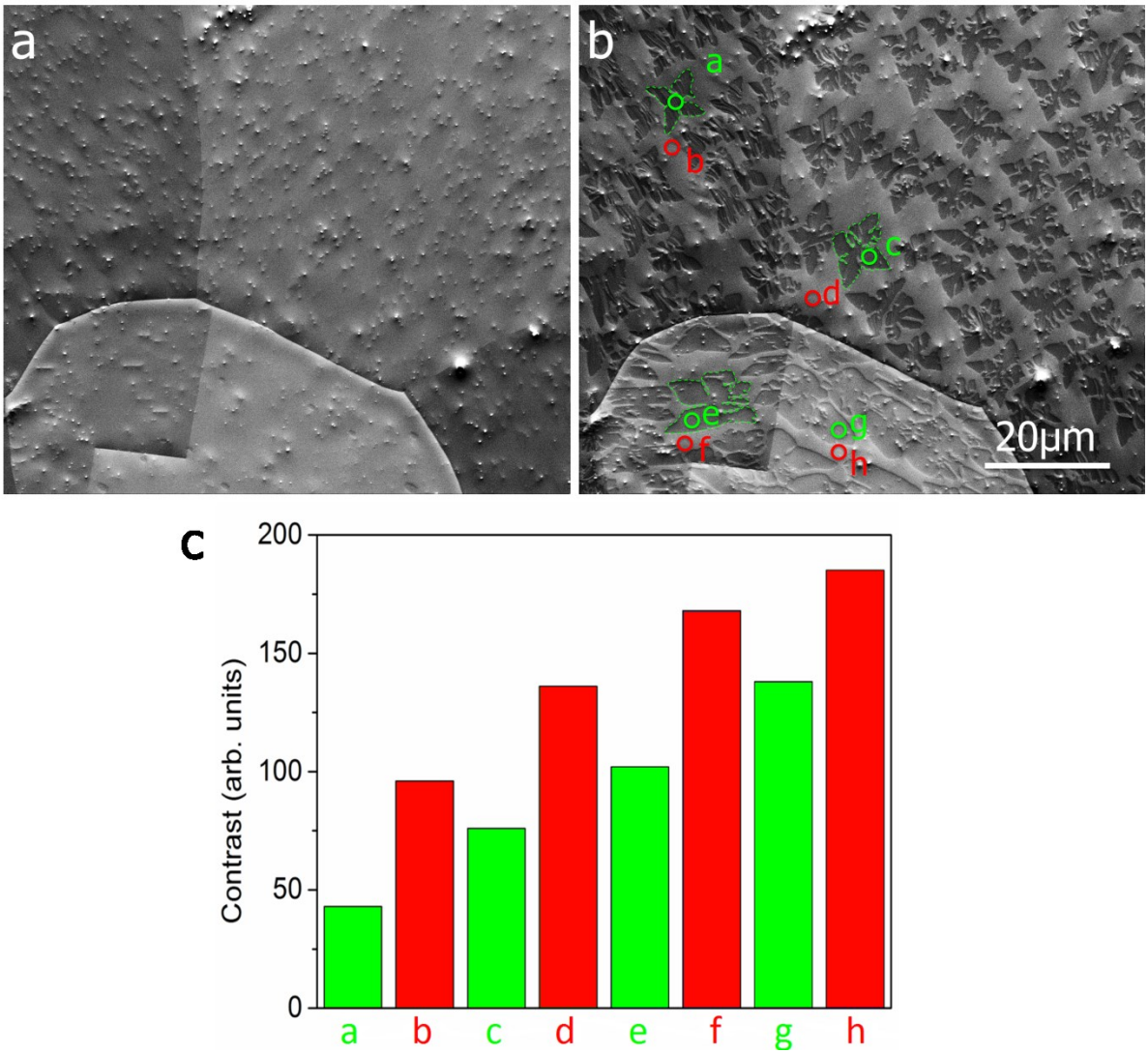

Figure 3-2. Characterization of graphene-Cu contrast. The *in situ* SEM image (a) showing Cu grain contrast at 900°C. Differences in contrast for different Cu grains are due to electron channelling and variations in the grain orientation dependent work function. (b) showing the graphene covered Cu grain at 900°C and the corresponding column diagram (c) showing that graphene can be distinguished by the SE contrast. The green and red circles in (c) designate the contrast of graphene and uncovered Cu on different grain substrate. Note that the graphene contrast is always darker than Cu.

However, when samples after graphene growth were exposed to ambient air and then re-investigated by SEM, changes in the contrast were observed. (see **Figure 3-3**). We note the change of graphene contrast is grain dependent. Compared with contrast during growing, after exposure in air, the graphene contrast in SEM changes from "dark" into "white" on some Cu grains. (see upper half plane of **Figure 3-3 a**) On the contrary, some graphene contrast does not change on specific Cu grains. (half bottom of **Figure 3-3 a**) To better

compare the contrast of graphene on different Cu grain, the contrast of graphene and Cu grain were designated in **Figure 3-3a** are plotted in **Figure 3-3b**.

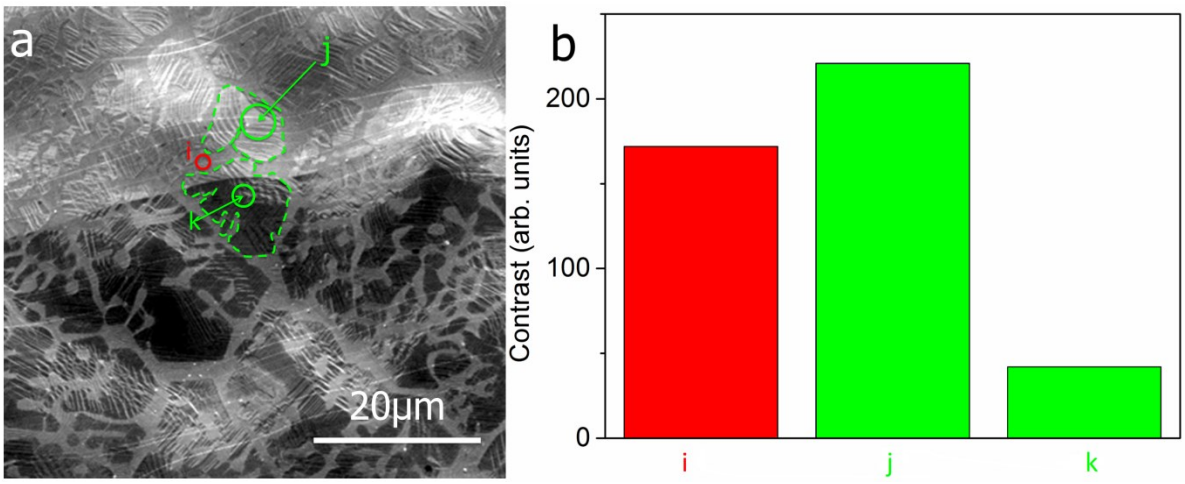

Figure 3-3. (a) showing the air exposure graphene on different Cu grains and the corresponding column diagram (b) showing that the SE contrast of graphene on different Cu grain. The green and red circles in (a) designate the contrast of graphene and uncovered Cu substrate. The edge of graphene domains are highlighted by green dotted lines in (a).

As known, graphene Cu interaction is relatively weak.[7] So During exposing to air, oxygen can intercalate the graphene-Cu interface and lead to a weakening of the coupling strength between graphene and the Cu substrate.[7] So the graphene contrast changing could be related to oxygen intercalation. Furthermore, strength of graphene-Cu interaction is grain dependent.[5] This may explain why the change of graphene contrast upon air exposure is grain dependent.

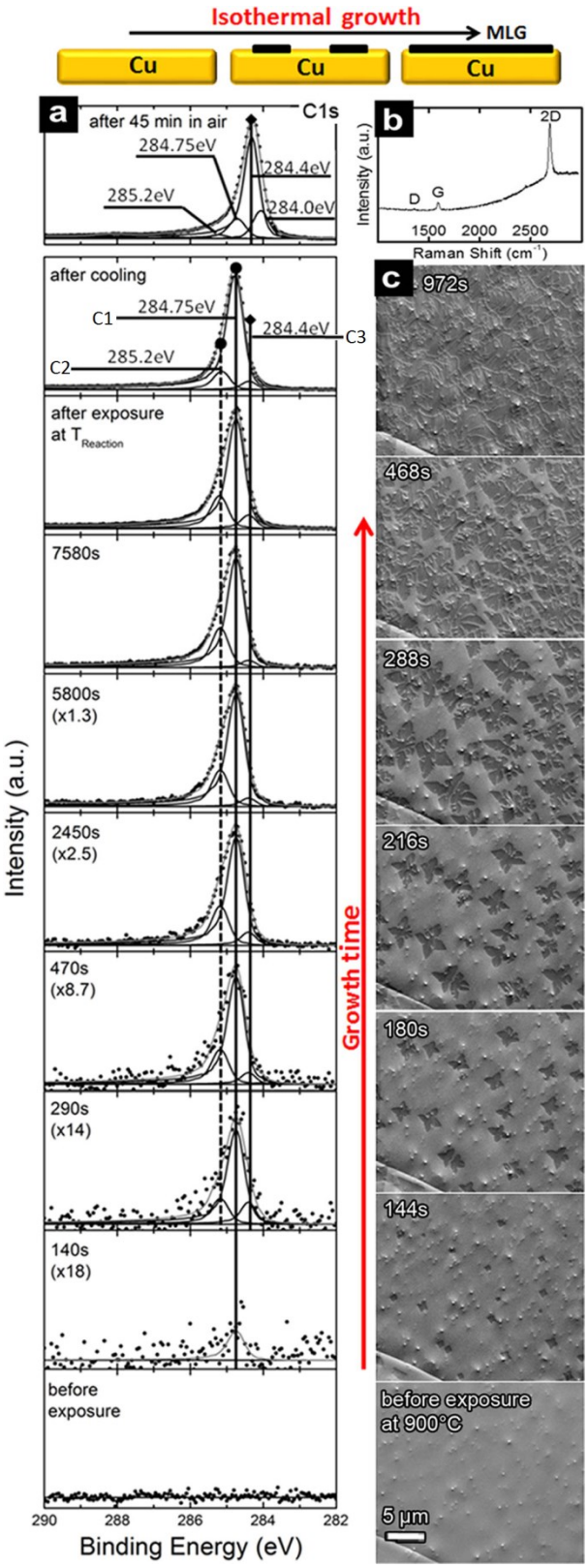

Figure 3-4. Isothermal graphene growth on Cu: (a) *in situ* time-resolved XPS C1s core level scans at 900°C during graphene growth and cooling, and after air exposure. (b) Raman spectrum obtained from the in situ grown graphene in part a, typical for all *in situ* grown graphene. (c) Corresponding time-

resolved *in situ* SEM image sequence for graphene growth on Cu at 900°C. Time stamps in (a) and (c) refer to time elapsed after hydrocarbon introduction.

In order to understand the contrast changing on graphene covered Cu, we use surface sensitive XPS technique to *in situ* characterize graphene growth and air exposure behaviour. The corresponding growth process in XPS, we observe the rise of a small intensity in the C1s XPS spectra centred at 284.75 eV (labelled C1). Two additional components appear at binding energies of 285.2 (labelled C2) and 284.4 eV (labelled C3) after~470 s. (see **Figure 3-4a**) C1, C2, and C3 reflect the presence of several distinct carbon binding arrangements on the Cu surface during growth. All peaks increase with prolonging C_6H_6 exposure time, keeping approximately the same intensity ratio to each other, which imply that the graphene coverage is increasing. Intensity ratio of C1s peaks remains largely unchanged upon C_6H_6 removal at 900°C and during subsequent cooling in vacuum. (see **Figure 3-4a**) Grown samples ambient air exposure at room temperature for ~45 min, re-measurements XPS show a shift in the dominating C1s peak component toward C3 at 284.4 eV, along with an increase in the oxygen O1s signal (see **Figure 3-5**). We note however that our observed shifted BE, that is, the C1 at 284.75 eV, could also be rationalized by exchange interactions between the Cu valence electronic structure and the C1s core hole, that is, spectroscopically a final state effect rather than a ground state effect. In any case, the recovery of the quasi free-standing graphene signal post air exposure to C3 at 284.4 eV and concurrent appearance of an O1s signal (see **Figure 3-5**) is clearly indicative of oxygen intercalation. Therefore, we assign C1 (284.75 eV) to graphene growing in a coupled state and C3 (284.4eV) to graphene in a decoupled or quasi free-standing state (i.e., oxygen intercalated between graphene and Cu, see **Figure 3-4 a**). We emphasize that the terms “coupled” and “decoupled” are here used as relative descriptions for graphene in direct contact with Cu and graphene with intercalated oxygen on Cu, respectively. Based on *in situ* XPS results, we confirm at room temperature after grown sample exposure in air, oxygen can intercalate graphene and Cu and create quasi-free-standing graphene.[14,16]

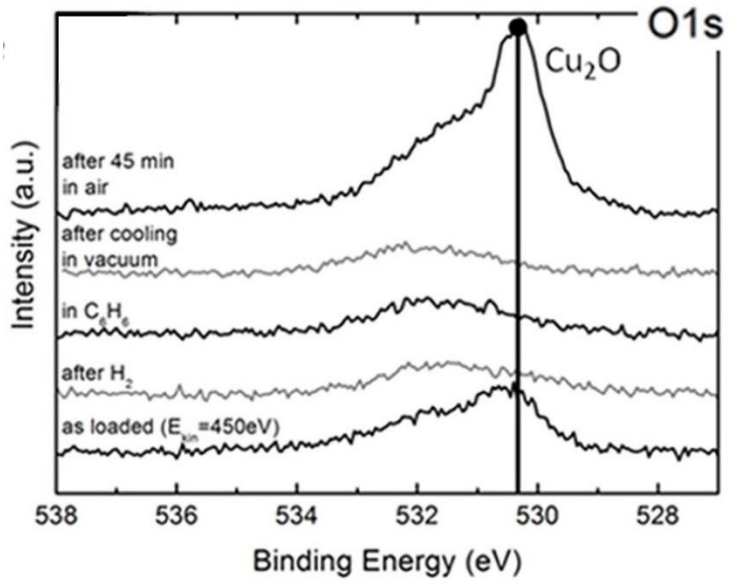

Figure 3-5. Surface chemistry of O1s spectra on the Cu substrate as loaded (before step 1), after H_2 anneal, during hydrocarbon exposure, after cooling in vacuum, and after ambient air exposure using *in situ* XPS.

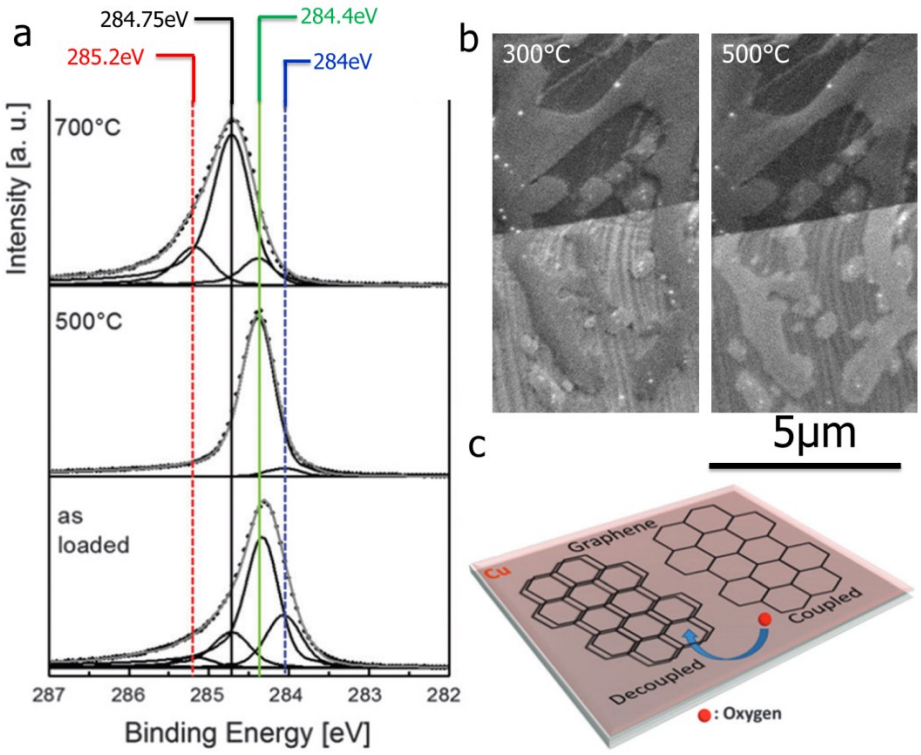

Figure 3-6. Coupling and decoupling of graphene on Cu via oxygen intercalation as measured using in situ XPS for the (a) C1s and in situ SEM for (b). in situ SEM images show air transferred graphene

islands on Cu during annealing in vacuum. (c) a schematic picture of coupled and decoupled graphene on Cu.

Re-annealing in vacuum can release oxygen from graphene-Cu interface and make intercalated graphene coupled on Cu surface again.[14,16] Hence, we also performed *in situ* experiments to follow the process of re-annealing of air-exposed graphene. As loaded, the air-exposed sample exhibits a well-defined decoupled C3 component at ~284.4 eV, accompanied by three minor peaks at 285.2, 284.75, and 284.0 eV. (see **Figure 3-6**) This peak feature is consistent with the spectrum after air exposure in **Figure 3-4a**.

With increasing temperature, the C1s components at 285.2, 284.75, and 284.0 eV disappear, and the remaining majority component is C3 at 284.4 eV, corresponding to decoupled graphene. With further heating to 700°C the C1s spectrum changes dramatically: The C1s main component shifts to 284.74 eV, that is, recovers the C1 position corresponding to coupled graphene, and a small shoulder at C2 (285.2 eV) emerges (see **Figure 3-6a**). According to the *in situ* XPS results, vacuum annealing leads to a recovery of the graphene-substrate coupling. Interestingly, we find that the SE contrast of graphene domains changes from “bright” to “dark” during annealing in vacuum. (**Figure 3-6 b** and **Figure 3-7**). On the basis of the *in situ* XPS observations, we attribute the change in the contrast observed by *in situ* SEM during vacuum annealing to a change in the interaction strength as a consequence of the de-intercalation of oxygen.

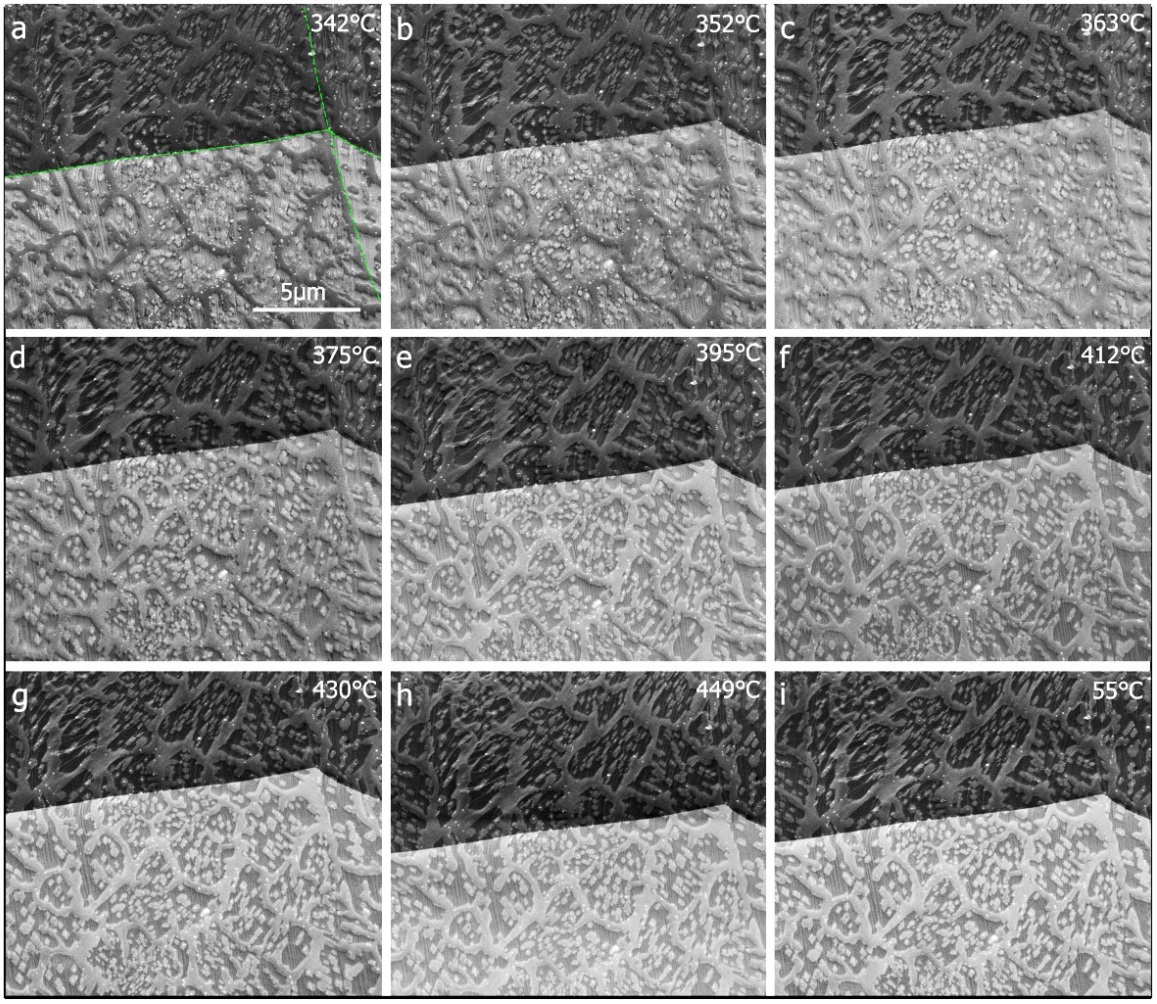

Figure 3-7. ***In situ*** **SEM image sequence of air transferred graphene domains on Cu during annealing in vacuum showing the oxygen intercalated graphene re-couple on Cu (characterized by darker contrast). Grain boundaries in the Cu substrate are highlighted by green dotted lines in (a).**

Further analysis in situ SEM images, we note again that the graphene SE contrast changing is grain dependent. This feature clearly indicates that the oxygen intercalation and the graphene-Cu coupling strength is grain dependent.[7] This is a detail that remains undetected by laterally averaging *in situ* XPS measurements on polycrystalline substrates.

3.4.Conclusion

In this chapter, we use reversible oxygen intercalation between graphene and polycrystalline Cu to confirm the degree of coupling between graphene and copper can be judged by SE contrast – although at the moment not quantitatively, but at least qualitatively by the contrast in SEM images. The results demonstrate the potential of the *in situ* SEM technique as surface-science tool and the advantage of obtaining laterally resolved information. It furthermore demonstrates the advantage of combining complementary *in situ* techniques where one provides chemical, spectroscopic information and the other one visual information. One technique supports the interpretation of findings obtained by the other and together they deliver more complete, consistent information.

In following chapters, we will use *in situ* SEM technique as surface-science tool to study detail of graphene growth behaviour on different metal catalyst.

3.5.Methods

In situ CVD growth. *In situ* CVD growth experiments were performed inside the chamber of a commercial ESEM (FEI Quantum 200). The instrument is equipped with a heating stage (FEI), a gas supply unit (mass flow controllers from Bronkhorst) and a mass spectrometer (Pfeiffer OmniStar) for the analysis of the chamber atmosphere. The vacuum system of the ESEM was upgraded with oil-free pre-vacuum pumps. Polycrystalline copper foils from Alfa Aesar were used as substrate (99.999% purity). Prior to CVD growth experiments, the chamber of the ESEM was plasma cleaned. Cu foils were annealed at 1000°C under a hydrogen flow of 8 sccm at a pressure of around 4.4×10^{-2} Pa for 50 min inside the chamber. The temperature was measured *via* a K-type thermocouple that was spot-welded onto the substrate. CVD growth was performed at ~1000°C using a flow of 4 sccm H_2 and leak valve dosing C_6H_6 at a total chamber pressure of $2\text{-}4\times10^{-2}$ Pa. During the experiments, the

microscope was operated at an acceleration voltage of 5.0kV. Images were recorded using the secondary electron signal collected by a standard Everhart Thornley detector (ETD) during sample annealing, CVD growth.

In situ XPS measurements during C_6H_6 CVD were performed at the BESSY II synchrotron at the ISISS end station of the FHI-MPG.70 A differentially pumped XPS system allows CVD at pressures up to 1 mbar while measuring in situ XPS (base pressure < 10^{-7}mbar). Cu catalyst foils were clamped with SiC clips onto SiO_2(300 nm)/Si wafers and heated via an IR laser focused onto the backside of the wafer. Temperature readings were taken via a pre-calibration with a thermocouple and cross-checked with pyrometer measurements during CVD (±30°C of reported temperature). The reaction atmosphere composition was continuously monitored using a mass spectrometer (Prisma).

3.6.References

1. Danilatos, G. D. *Advances in Electronics and Electron Physics* **1988**, *71*, 109.

2. Everhart, T. E.; Thornley, R. F. M. *Journal of Scientific Instruments* **1960**, *37*, 246.

3. Khomyakov, P. A.; Giovannetti, G.; Rusu, P. C.; Brocks, G.; van den Brink, J.; Kelly, P. J. *Phys. Rev. B* **2009**, *79*, 12.

4. Sutter, P.; Hybertsen, M. S.; Sadowski, J. T.; Sutter, E. *Nano Letters* **2009**, *9*, 2654.

5. Wintterlin, J.; Bocquet, M. L. *Surf. Sci.* **2009**, *603*, 1841.

6. Nilsson, L.; Andersen, M.; Bjerre, J.; Balog, R.; Hammer, B.; Hornekaer, L.; Stensgaard, I. *Surf. Sci.* **2012**, *606*, 464.

7. Frank, O.; Vejpravova, J.; Holy, V.; Kavan, L.; Kalbac, M. *Carbon* **2014**, *68*, 440.

8. Zhao, H.; Lin, Y.-C.; Yeh, C.-H.; Tian, H.; Chen, Y.-C.; Xie, D.; Yang, Y.; Suenaga, K.; Ren, T.-L.; Chiu, P.-W. *Acs Nano* **2014**, *8*, 10766.

9. Sutter, P.; Sadowski, J. T.; Sutter, E. *Phys. Rev. B* **2009**, *80*, 10.

10. Coraux, J.; N'Diaye, A. T.; Engler, M.; Busse, C.; Wall, D.; Buckanie, N.; Heringdorf, F.; van Gastel, R.; Poelsema, B.; Michely, T. *New J. Phys.* **2009**, *11*, 22.

11. Land, T. A.; Michely, T.; Behm, R. J.; Hemminger, J. C.; Comsa, G. *J. Chem. Phys.* **1992**, *97*, 6774.

12. Park, M.-H.; Kim, T.-H.; Yang, C.-W. *Surf. Interface Anal.* **2012**, *44*, 1538.

13. Hiura, H.; Miyazaki, H.; Tsukagoshi, K. *Applied Physics Express* **2010**, *3*.

14. Kidambi, P. R.; Bayer, B. C.; Blume, R.; Wang, Z.-J.; Baehtz, C.; Weatherup, R. S.; Willinger, M.-G.; Schloegl, R.; Hofmann, S. *Nano Letters* **2013**, *13*, 4769.

15. Wendt, U.; Nolze, G. *Praktische Metallographie-Practical Metallography* **2007**, *44*, 236.

16. Blume, R.; Kidambi, P. R.; Bayer, B. C.; Weatherup, R. S.; Wang, Z.-J.; Weinberg, G.; Willinger, M.-G.; Greiner, M.; Hofmann, S.; Knop-Gericke, A.; Schloegl, R. *Physical Chemistry Chemical Physics* **2014**, *16*, 25989.

4. Graphene growth by chemical vapour deposition on metal surfaces

4.1.Abstract

Chemical vapour deposition (CVD) is the most promising and versatile method for graphene production. There have been numerous recent reports of high quality graphene growth on Ni, Cu and Pt. Three metal catalysts that show characteristic differences in terms of their catalytic activity, graphene-surface interaction and carbon solubility have been considered.

Ni and Ni-based catalysts, which have a relatively high solubility limit of carbon and plays an important role as catalyst in the reaction of dry reforming of methane (DRM) with CO. However, during the reaction Ni-based catalysts suffer from fast deactivation by carbon coking. This disadvantage of Ni-based catalysts shows signs of potential application prospect for carbon films growth on Ni. On the contrary, due to low carbon solubility and very weak graphene-surface interaction, Cu is mostly used by the graphene community. Besides, it is well-known that Pt is very active in hydrocarbon dissociation reaction. Thus Pt is also good catalyst for graphene CVD growth.

In this chapter, in order to evaluate the effect of the performance of graphene growth on these metal catalysts, we use *in situ* SEM investigate carbon film formation and screen for better candidate catalyst which is capable to produce high quality single layer graphene for further study in following chapters.

4.2.Introduction

Graphene CVD growth was first reported in 2008 and 2009, using Ni, Cu and Pt.[1-3] Afterwards a lot of research attention are attracted to explore graphene growth behaviour on a variety of transition metal substrates.[4-7] During CVD growth process, the metal substrate not

only plays a role as catalyst to lower the energy barrier of hydrocarbon dissociation, but also determines the mechanism of graphene formation.

Based on the long-time experience, three metal catalysts – Cu, Pt, Ni – have shown remarkable ability to assist graphene growth. In 2013, Hao. et al. reported the high quality large-area single-layer single-crystal graphene can be fabricated on polycrystalline Cu catalyst.[8] Due to advantages such as good control of graphene nucleation density, low cost, and ability to transfer, graphene growth on Cu has attracted a lot of research activities.[9-14]Pt offers a quite large error-tolerant window for graphene growth, and a much higher catalytic activity for hydrocarbon dissociation than Cu. Besides the high activity for hydrocarbon dissociation, Pt also exhibits a relatively weak metal-graphene interaction.[15,16] This characteristic has the advantage that the synthesized graphene can be easily transferred onto other substrates without being damaged, and substrate can repeat to be used.[3,17,18] Thus Pt also can be used for large-area single-crystal graphene.[17,19]

Therefore, currently Cu and Pt are considered as the most prevalent metal catalyst for high quality graphene growth at high temperatures (>900°C). In contrast to Cu and Pt, Ni (111) surface offers a perfect lattice match up with graphene in theory,[15,20] and a graphitic lattice can form on its surface at low temperatures (<600°C). Hence the formation of graphene can be achieve at low temperatures range (600 ~400°C).[2,21,22]

In this chapter, to better understand formation of graphene, we employ *in situ* SEM to observe the details of graphene CVD growth on Ni, Cu and Pt. We find single layer graphene can be easily grown on Cu and Pt surface (this will be discussed in detail in following chapters). On the contrary, due to high carbon solubility of Ni and a bulk reservoir effect, carbon precipitation during can occur, making SLG growth difficultly. Furthermore, in order to study influence of Ni catalyst morphology, such as specific surface area and thickness, to carbon formation, we carry out in situ observation on Ni film and Ni foil. In our condition, no matter what kind of Ni catalyst, SLG hardly grow on Ni-based substrate.

4.3.Results and discussion

Ni foil and film were annealed at 300-600°C under a hydrogen flow of 8 sccm at a pressure of 4.4×10^{-2} Pa inside the ESEM chamber. The initial polycrystalline Ni foil surface shows small grain and Ni film surface shows a homogeneous contrast in the SE image (see **Figure 4−1** and **4−2**). Due to contributions from electron channelling to contrast in the secondary electron image, different orientations of grains can still be detected. Regarding Ni foil, above 500 °C, the onset of morphological changes on the surface can be observed. Regarding Ni film above 300 °C, surface grain growth appears. Surface reconstructions lead to the appearance of a pronounced electron channelling contrast pattern due to differently oriented crystalline grains as shown in **Figure 4−**1 and **Figure 4−2**. Above certain temperature, which is high enough for abnormal grain growth and migration, causing expansion of grains that expose low energy faces at the expense of energetically less favourable ones. As a consequence of surface reconstruction, processing-induced artefacts from foil rolling start to disappear. With rising temperature, the grain size of the polycrystalline surface further increases. After annealing, the grain size depends on the thickness of Ni. As shown in **Figure 4−**1 and **Figure 4−2**, the grains sizes of Ni foil are bigger than Ni films.

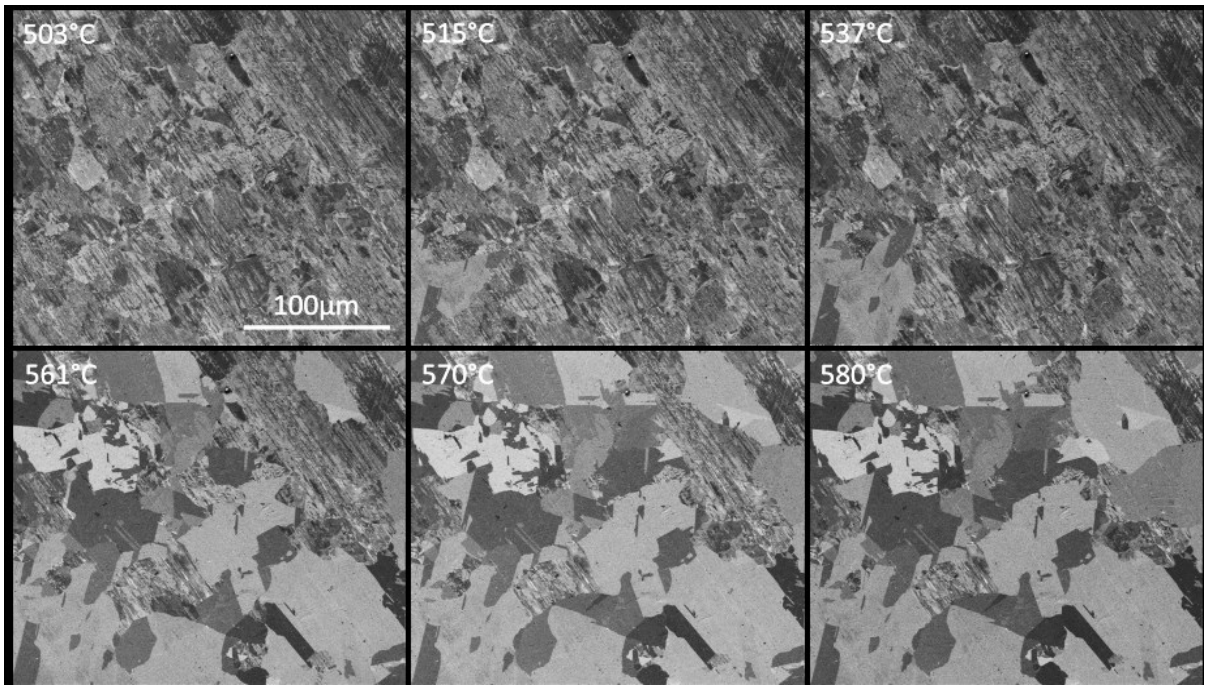

Figure 4−1. Ni foil surface modifications can be seen in snapshots taken during an annealing process under 4.4×10-2 Pa H2 atmosphere.

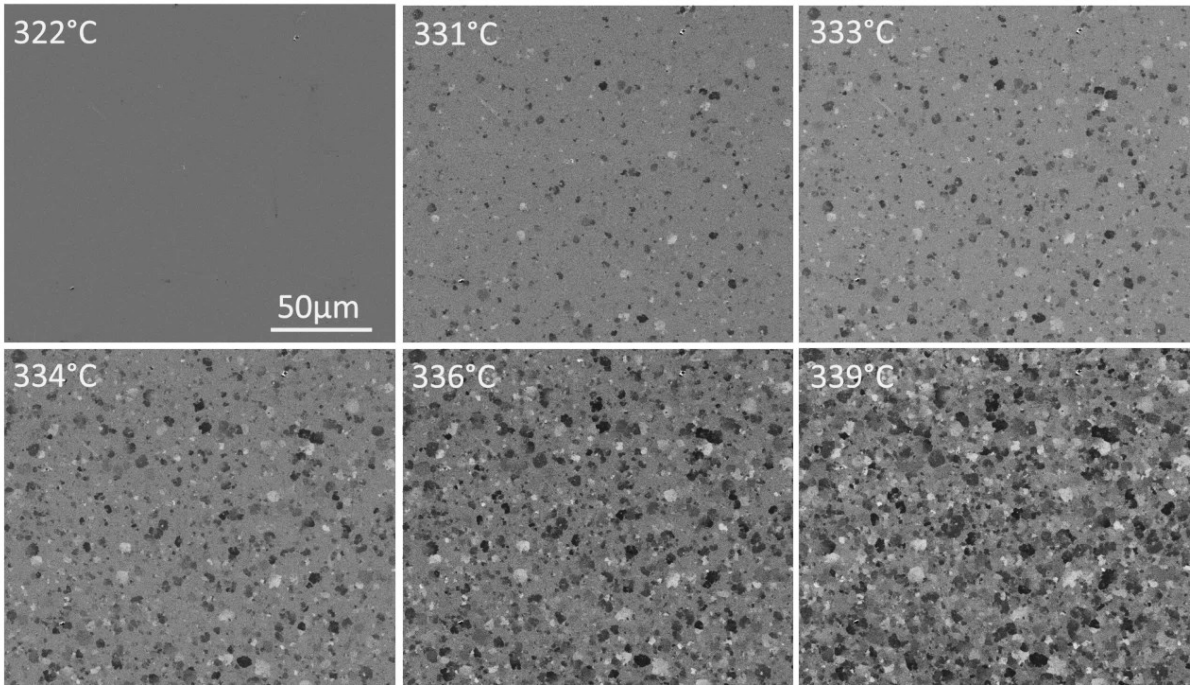

Figure 4−2. Ni film grain growth can be seen in snapshots taken during an annealing process under 4.4×10^{-2} H2 atmosphere. (Sample courtesy: University of Cambridge)

After annealing for around 1 hour H_2 under flow of 8 sccm at 4.4×10^{-2} Pa, the hydrogen flow was reduced to 0.2 sccm and 0.5 sccm of C_2H_4 were added. Formation of carbon deposits can generally be observed after a dosing C_2H_4. A series of *in situ* SEM images capturing the appearance and growth of carbon sheets on Ni foil and film is presented in **Figure 4−3** and **Figure 4−4**. Accordingly, the resulting product obtained in the ESEM ranges from graphitic carbon deposits to graphitic layers on Ni surface. In **Figure 4−3** and **Figure 4−4**. snapshots taken during metal catalysed CVD growth in the chamber of the ESEM are shown for the case of polycrystalline nickel foil and film, respectively. In the case of Ni foil, carbon layer growth involves diffusion into substrate during growing, and precipitation from the bulk during cooling. (see **Figure 4−5**) Thus the high quality SLG cannot be precisely grown on thick Ni catalyst, and graphitic layers are generally formed on Ni foil. (see **Figure 4−5 d**)

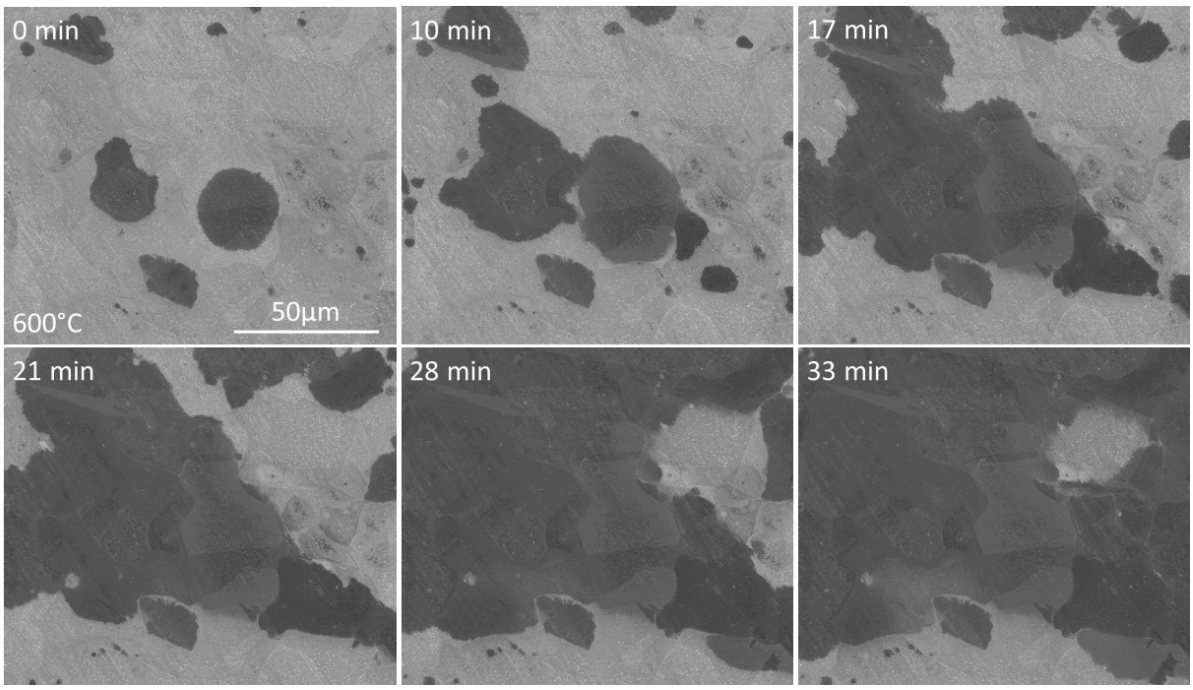

Figure 4−3. ***In situ*** **SEM images recorded at 600 °C during LP-CVD growth showing the growth of graphitic layers (characterized by darker contrast).**

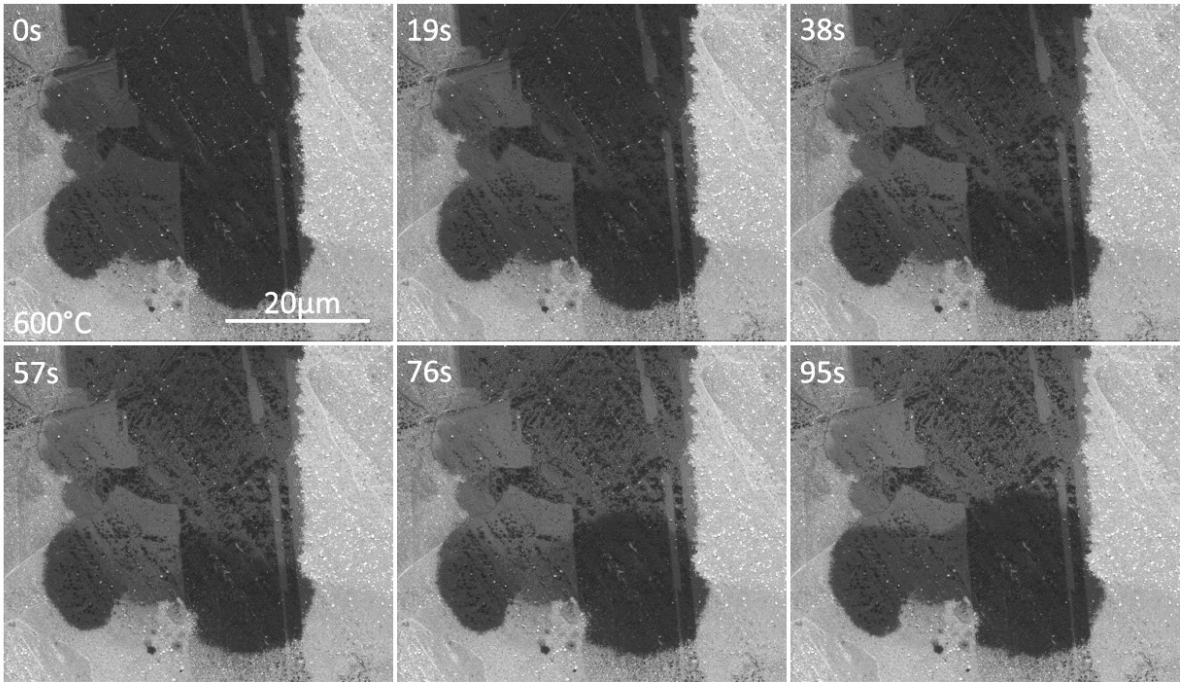

Figure 4−4. ***In situ*** **SEM images recorded at 600 °C during LP-CVD growth showing the diffusion of carbon into bulk. (Characterized by darker contrast).**

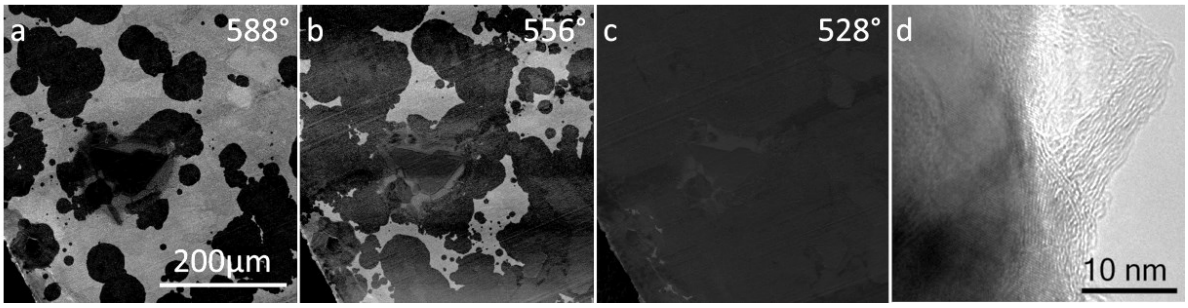

Figure 4−5. Carbon precipitation upon Ni foil surface during cooling step. (a-c) Snapshots taken during cooling step are shown graphitic layers form on Ni surface during cooling. (d) TEM image show graphitic layers.

Due to high carbon solubility of Ni and a bulk reservoir effect, carbon diffusion into bulk and precipitation upon surface is hardly controlled during growth and SLG growth is difficultly to be maintained. In order to decrease bulk reservoir effect and carbon precipitation, we carry out *in situ* carbon layer growth on Ni film (100nm thickness Ni layer on SiO_2). (see **Figure 4−6**).

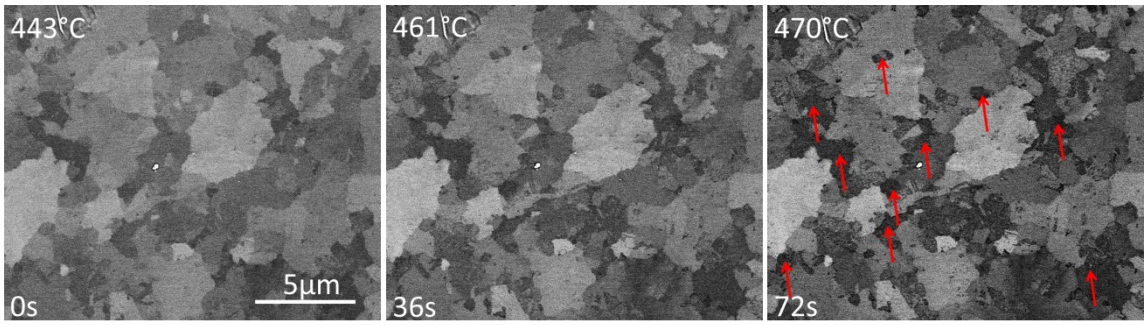

Figure 4−6. *In situ* SEM images recorded during LP-CVD growth showing the growth of carbon layers on Ni film (highlighed by arrows).

As shown in **Figure 4−6**, in case of Ni film, although bulk diffusion and surface precipitation are restricted, carbon layer can only be grown on special grain and catalyst surface are not fully covered by carbon layers. Furthermore, the contrast of carbon layers is not homogenous which means the layer grown on Ni are not SLG.(see **Figure 4−7**) In **Figure 4−7b** we show

the element distribution from sputtered Ni film, where the corresponding EDX line scans profiles taken through the white line in Figure 3 a.

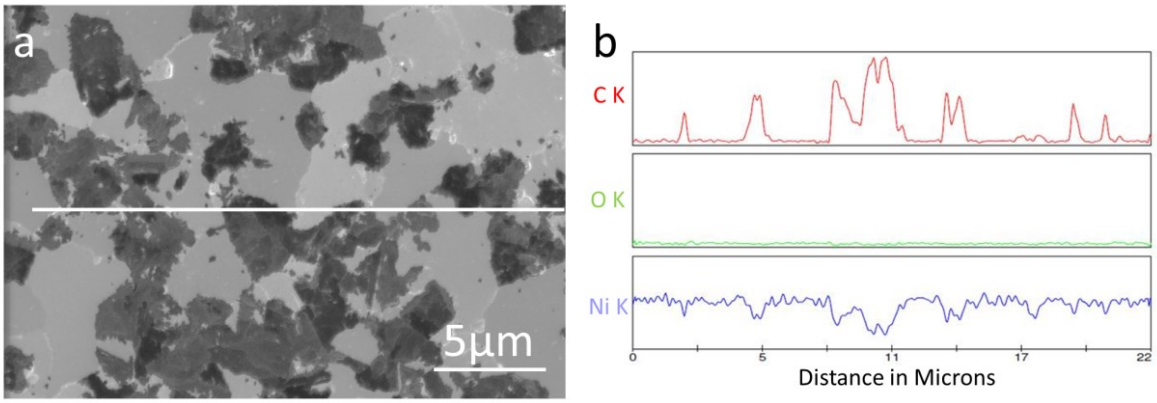

Figure 4−7. SEM image and EDX line-scan (a) SEM image show graphene covered special surface grain of Ni film. (b) EDX line-scan profile through white line in (a). The EDX line-scan profiles were taken with an electron probe size of 1-3 nm diameters.

In our experiments, when we started with the graphene growth on Ni based catalyst, there were still some unresolved issues about the vacuum quality in the chamber. In some experiments, we faced problems with oxygen leakage until the problem was finally resolved.(see **Figure 4−8**) However, SLG still cannot be well grown on Ni based catalyst in ESEM chamber. Overall, due to the difficulty of obtaining well defined SLG, the focus was shifted to other metal catalyst.

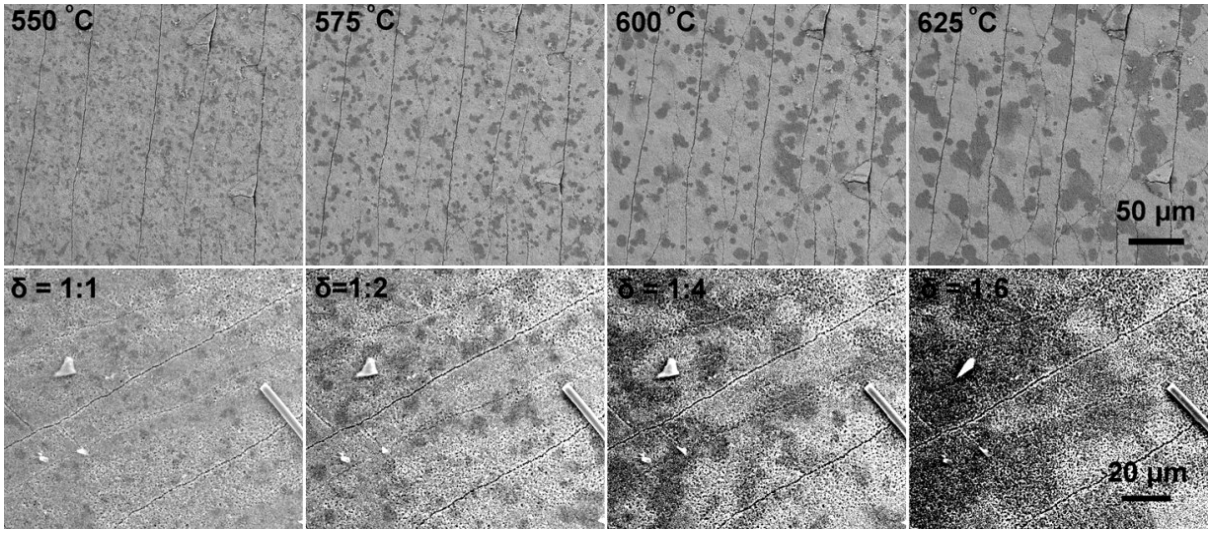

Figure 4−8. Dynamic contrast variations due to formation and etching of graphene are observed under oxygen leakage condition.

Because of high carbon solubility and a bulk reservoir effect, carbon precipitation is not very well controlled during cooling step and SLG formation is hardly maintained. On the contrary, as shown in **Figure 4−9**, SLG can be nicely controlled growth on Cu and Pt (this will be discussed in chapter 5 and 6).

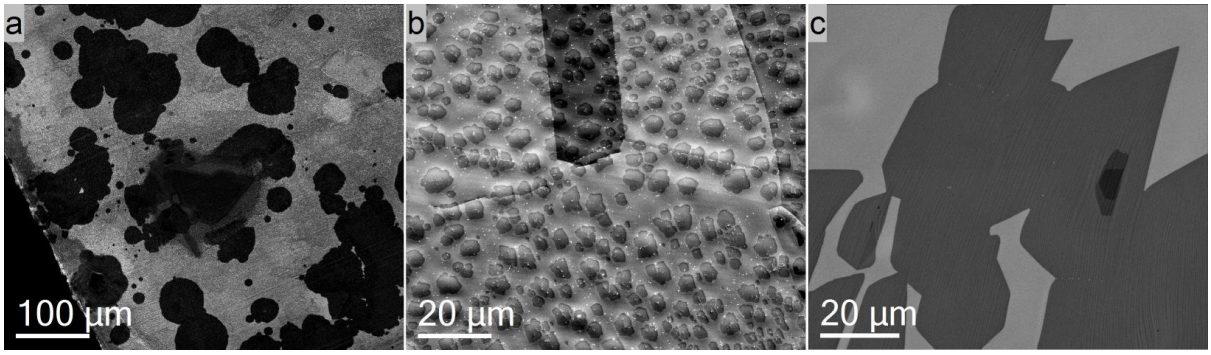

Figure 4−9: Snapshots taken during CVD growth in the chamber of the ESEM for the case of Ni, Cu and Pt are shown in (a), (b) and (c), respectively. Dark contrast is due to carbon deposits, which were identified by post growth characterization as mostly single layer graphene in the case of Cu and Pt.

4.4.Conclusion

The different catalytic properties of the metal catalysts are reflected by different growth modes on the respective catalysts. Diffusion of carbon species is purely confined to the surface in the case of copper. The bulk solubility of carbon in platinum lies in between the two extreme forms of Ni, with a high solubility and copper, with practically no solubility. Accordingly, graphene growth on Pt can be surface mediated or due to precipitation from the bulk, depending on the growth conditions (this will be discussed in detail in chapter 7 and 8). The different catalytic properties of the metal catalysts are reflected in the nucleation behaviour, growth speed and dominance of diffusion versus attachment-limited growth. We conclude graphene can easily happen on Cu and Pt surface (this will be discussed in detail in following chapters). However, due to high carbon solubility of Ni and a bulk reservoir effect, carbon precipitation during cooling making SLG growth difficultly. In our condition, SLG hardly grow on Ni-based substrate. Therefore, our following work focus on graphene growth on Cu and Pt.

4.5. References

1. Li, X. S.; Cai, W. W.; An, J. H.; Kim, S.; Nah, J.; Yang, D. X.; Piner, R.; Velamakanni, A.; Jung, I.; Tutuc, E.; Banerjee, S. K.; Colombo, L.; Ruoff, R. S. *Science* **2009**, *324*, 1312.

2. Addou, R.; Dahal, A.; Sutter, P.; Batzill, M. *Appl. Phys. Lett.* **2012**, *100*.

3. Gao, L. B.; Ren, W. C.; Xu, H. L.; Jin, L.; Wang, Z. X.; Ma, T.; Ma, L. P.; Zhang, Z. Y.; Fu, Q.; Peng, L. M.; Bao, X. H.; Cheng, H. M. *Nat. Commun.* **2012**, *3*, 7.

4. Loginova, E.; Nie, S.; Thuermer, K.; Bartelt, N. C.; McCarty, K. F. *Phys. Rev. B* **2009**, *80*.

5. Starodub, E.; Maier, S.; Stass, I.; Bartelt, N. C.; Feibelman, P. J.; Salmeron, M.; McCarty, K. F. *Phys. Rev. B* **2009**, *80*, 8.

6. Nie, S.; Walter, A. L.; Bartelt, N. C.; Starodub, E.; Bostwick, A.; Rotenberg, E.; McCarty, K. F. *Acs Nano* **2011**, *5*, 2298.

7. Dong, G. C.; Frenken, J. W. M. *Acs Nano* **2013**, *7*, 7028.

8. Hao, Y. F.; Bharathi, M. S.; Wang, L.; Liu, Y. Y.; Chen, H.; Nie, S.; Wang, X. H.; Chou, H.; Tan, C.; Fallahazad, B.; Ramanarayan, H.; Magnuson, C. W.; Tutuc, E.; Yakobson, B. I.; McCarty, K. F.; Zhang, Y. W.; Kim, P.; Hone, J.; Colombo, L.; Ruoff, R. S. *Science* **2013**, *342*, 720.

9. Bae, S.; Kim, H.; Lee, Y.; Xu, X. F.; Park, J. S.; Zheng, Y.; Balakrishnan, J.; Lei, T.; Kim, H. R.; Song, Y. I.; Kim, Y. J.; Kim, K. S.; Ozyilmaz, B.; Ahn, J. H.; Hong, B. H.; Iijima, S. *Nat. Nanotechnol.* **2010**, *5*, 574.

10. Li, X. S.; Magnuson, C. W.; Venugopal, A.; An, J. H.; Suk, J. W.; Han, B. Y.; Borysiak, M.; Cai, W. W.; Velamakanni, A.; Zhu, Y. W.; Fu, L. F.; Vogel, E. M.; Voelkl, E.; Colombo, L.; Ruoff, R. S. *Nano Letters* **2010**, *10*, 4328.

11. Chen, S. S.; Cai, W. W.; Piner, R. D.; Suk, J. W.; Wu, Y. P.; Ren, Y. J.; Kang, J. Y.; Ruoff, R. S. *Nano Letters* **2011**, *11*, 3519.

12. Vlassiouk, I.; Regmi, M.; Fulvio, P. F.; Dai, S.; Datskos, P.; Eres, G.; Smirnov, S. *Acs Nano* **2011**, *5*, 6069.

13. Wu, B.; Geng, D. C.; Guo, Y. L.; Huang, L. P.; Xue, Y. Z.; Zheng, J.; Chen, J. Y.; Yu, G.; Liu, Y. Q.; Jiang, L.; Hu, W. P. *Advanced Materials* **2011**, *23*, 3522.

14. Yan, K.; Peng, H. L.; Zhou, Y.; Li, H.; Liu, Z. F. *Nano Letters* **2011**, *11*, 1106.

15. Wintterlin, J.; Bocquet, M. L. *Surf. Sci.* **2009**, *603*, 1841.

16. Preobrajenski, A. B.; Ng, M. L.; Vinogradov, A. S.; Martensson, N. *Phys. Rev. B* **2008**, *78*, 4.

17. Ma, T.; Ren, W.; Liu, Z.; Huang, L.; Ma, L.-P.; Ma, X.; Zhang, Z.; Peng, L.-M.; Cheng, H.-M. *Acs Nano* **2014**, *8*, 12806.

18. Ma, T.; Ren, W. C.; Zhang, X. Y.; Liu, Z. B.; Gao, Y.; Yin, L. C.; Ma, X. L.; Ding, F.; Cheng, H. M. *Proc. Natl. Acad. Sci. U. S. A.* **2013**, *110*, 20386.

19. Sun, J.; Nam, Y.; Lindvall, N.; Cole, M. T.; Teo, K. B. K.; Park, Y. W.; Yurgens, A. *Appl. Phys. Lett.* **2014**, *104*, 4.

20. Eizenberg, M.; Blakely, J. M. *Surf. Sci.* **1979**, *82*, 228.

21. Weatherup, R. S.; Dlubak, B.; Hofmann, S. *Acs Nano* **2012**, *6*, 9996.

22. Peng, Z. W.; Yan, Z.; Sun, Z. Z.; Tour, J. M. *Acs Nano* **2011**, *5*, 8241.

5. Graphene growth on copper

5.1. Abstract

In this chapter, it is shown *in situ* SEM can improve understanding of graphene growth on copper via metal catalyzed CVD. It enables the observation of a complete CVD process from substrate annealing through graphene nucleation and growth and finally, substrate cooling at real-time and nanometer scale resolution without the need of sample transfer. A strong dependence of surface dynamics such as sublimation and surface pre-melting on grain orientation is demonstrated and the influence of substrate dynamics on graphene nucleation and growth is presented. Insights on the growth mechanism are provided by a simultaneous observation of the growth front propagation and nucleation rate. Furthermore, the role of trace amounts of oxygen during growth is discussed and related to graphene induced surface reconstructions during cooling.

5.2.Introduction

The breakthrough of graphene-based technology depends on the ability of producing high quality graphene sheets on industrial scale.[1] Among the various strategies currently followed,[2-7] the catalytic CVD process on polycrystalline copper foils has demonstrated potential for a cost-effective, controllable synthesis of few- or single-layer graphene.[2] So far, alterations and improvements of growth conditions have led to various morphologies of graphene domains[8-12] and successful growth of graphene single crystals up to several millimeters.[9, 13] To date, the optimization of process conditions on the basis of feedback from ex-situ characterization of the product is still very much state of the art. However, growth models that rely on ex-situ observations are in principle incapable of providing a complete picture about the dynamics of a CVD process. As a consequence, the understanding of the CVD growth dynamics on copper remains limited and empirical. Indeed, many assumptions

about the growth mechanisms that were postulated from ex-situ studies await confirmation by direct observation.

From heterogeneous catalysis we learn that a mechanistic insight can only be obtained on the basis of *in situ* techniques that are capable of capturing the interaction of a catalyst with the gas phase while the product is formed.[14-16] The value of *in situ* studies in deducing details of graphene growth either through CVD growth or via precipitation from the bulk was documented for a number of transition metal substrates such as Ni, Ru, Rh and Ir using low-energy electron microscopy (LEEM),[17-20] photoemission electron microscopy (PEEM),[21] scanning tunnelling microscopy (STM)[22, 23] and near ambient pressure X-ray photoelectron spectroscopy (NAP-XPS).[24] However, due to the low dehydrogenation activity of copper and the required high temperature, only spatially integrated spectroscopic data is available from *in situ* XPS and X-ray diffraction (XRD) on polycrystalline films under LP-CVD growth conditions.[25] Surface imaging during graphene growth on copper has so far only been realized under ultrahigh vacuum (UHV) conditions using LEEM and the deposition of elemental carbon,[26, 27] and by *in situ* SEM on graphene growth on Ni via segregation of bulk dissolved carbon.[28] To date, there is no visual and spatially resolved information available regarding the state of the surface and details of graphene growth dynamics on copper under relevant catalytic CVD conditions.

As a consequence, temperature, pressure and atmosphere related substrate dynamics and their effect on graphene nucleation and growth are still unclear.

Here we show that *in situ* observation under conditions of cold wall, low pressure (LP)-CVD is possible by utilizing a modified ESEM.

Using this instrument, we are able to follow a complete CVD cycle from substrate annealing to graphene growth and subsequent cooling. Hence, we obtain a complete and undisturbed picture of the involved dynamics without the need for sample transfer. The latter is important for the validation of mechanistic models that are derived on the basis of post-growth observation, i.e., under the premise that sample transfer and changes in temperature and atmosphere do not induce relevant modifications of the graphene-substrate interaction.[29, 30]

In the ESEM, visualization of graphene growth is enabled by the high sensitivity of the secondary electron (SE) signal to changes in the work function, the low cross section of graphene for secondary electron generation and the attenuation of secondary electrons emitted from the Cu substrate by the covering graphene layer.[31-33]

Since the investigations are made inside a microscope, a simultaneous observation of graphene as the reaction product and associated morphological changes of the catalyst is possible over a large range of magnifications. Detailed nanometer scale information can therefore easily be embedded in a global picture that is obtained at low magnifications. The *in situ* experiments presented here reveal the dynamic nature of the process in an unparalleled way and provide important insights on the growth kinetics and the substrate-film interactions at the micron to nanometer scale. Furthermore, it is one of the few cases in catalysis, where the dynamics of a working catalyst can be observed while at the same time, the product of the reaction can directly be seen.

5.3. Result

In the following, we present observations made during several complete processes of graphene growth via metal catalysed LP-CVD inside the chamber of an ESEM. Each of the experiments involved substrate annealing, graphene nucleation and growth and finally, substrate cooling. In the second part of this chapter, the observations are analyzed, discussed and related to findings of post-growth studies that are reported in the literature.

5.3.1. Copper annealing

All samples were annealed at 1000°C under a hydrogen flow of 8 sccm at a pressure of 4.4×10^{-2} Pa for 50 min inside the ESEM chamber. The initial polycrystalline copper foil shows a homogeneous contrast in the SE image (**Figure 5-1**a). With increasing temperature, small changes in contrast indicate desorption of adsorbed surface species and removal of contaminants from the Cu surface. Above 380 °C, the onset of morphological changes on the surface of the Cu foil can be observed. Surface reconstructions lead to the appearance of a

pronounced electron channelling contrast pattern due to differently oriented crystalline grains as shown in **Figure 5-1**b and the Online Movie (M1). Above 400 °C, the temperature is high enough for abnormal grain growth and migration, causing expansion of grains that expose low energy faces (mainly <100>, <110> and <111>)[34] at the expense of energetically less favourable ones. As a consequence of surface reconstruction, processing-induced artefacts from foil rolling start to disappear. Above 600 °C, contrast changes indicate desorption of remaining carbonaceous deposits. With rising temperature, the grain size of the polycrystalline foil further increases. At around 800 °C (**Figure 5-1**c) small particles of bright contrast start appearing at the surface. They measure around 10-200 nm in diameter and are mostly due to segregation of silicon contamination from the bulk to the surface (see **Figure 5-2**). Similar particles were reported by others and can frequently be observed in post-growth SEM images in the literature. [2, 8-11, 29, 30, 35, 36] Above 850 °C, these particles become mobile and start drifting across the surface in more or less random directions. Their drifting speed increases with temperature and is in the range of 10-50 nm/second at 1000 °C (see **Online Movie M1**). The movement in random directions indicates an increased mobility of the copper surface and the onset of surface pre-melting.[37, 38] As a consequence, remaining features due to foil production and signs of a crystalline surface such as steps and grain faceting disappear. However, due to contributions from electron channelling to contrast in the secondary electron image, different orientations of grains below the pre-melted surface can still be detected.

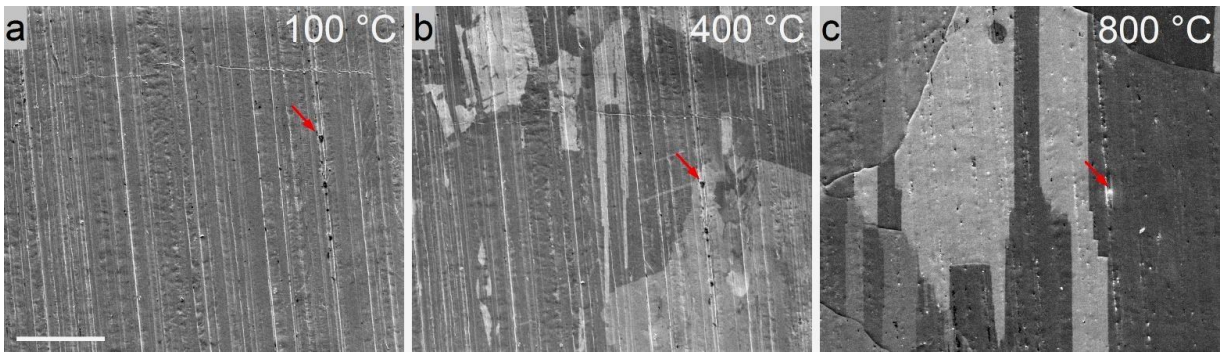

Figure 5-1 Surface modifications can be seen in snapshots taken during an annealing process at 100 °C (a), 400 °C (b) and 800 °C (c), respectively. A complete annealing process is shown in movie M1. Red arrows reference identical positions on the foil. Sample movement is due to thermal drift. The scale bar measures 20 µm.

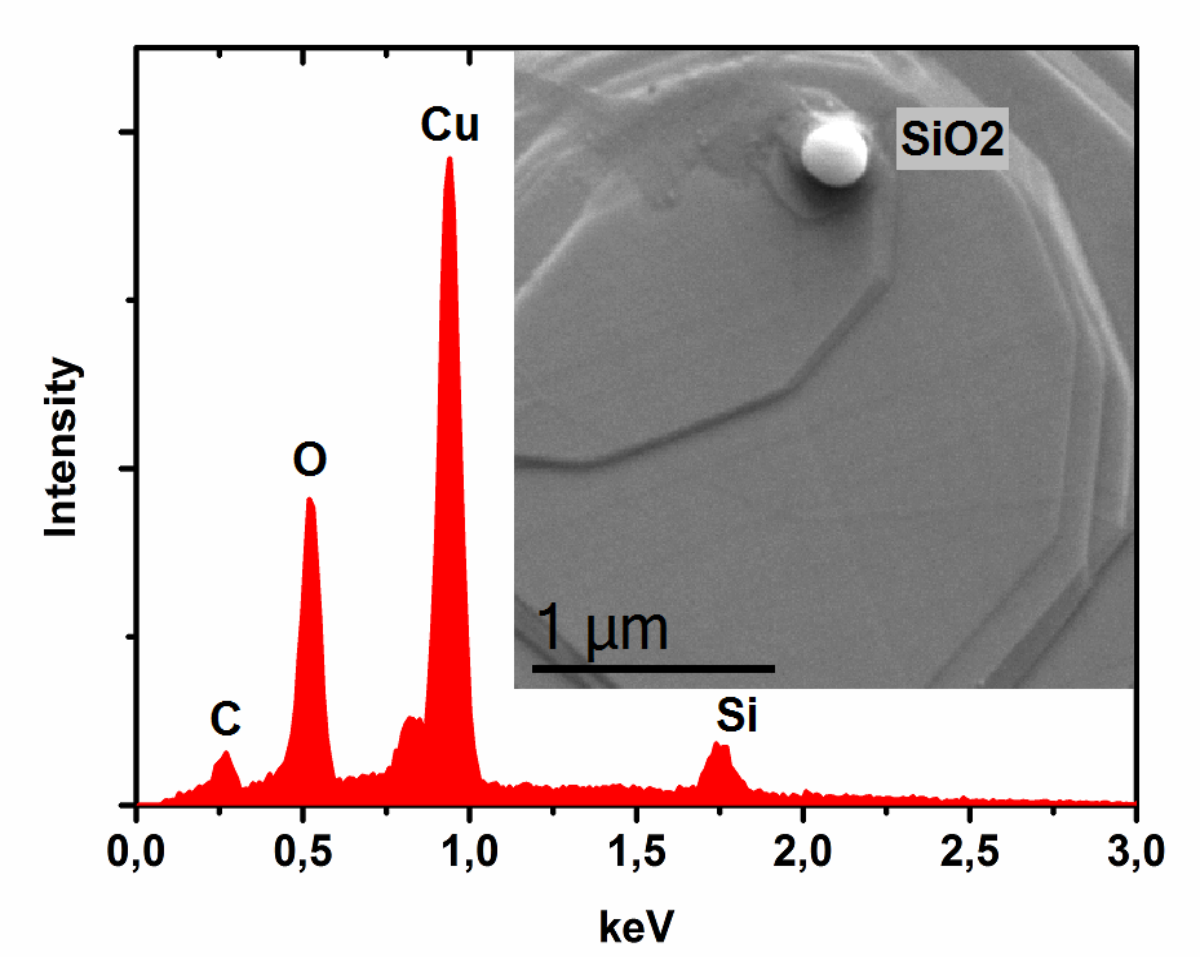

Figure 5-2 EDX confirms that the white particles correspond to SiO_2. The spectrum was recorded at 4keV acceleration voltage from the particle shown in the inset after CVD growth.

5.3.2. Graphene nucleation and growth

Typically after annealing for 50 min at 1000 °C, the hydrogen flow was reduced to 4 sccm and 0.1 sccm of C_2H_4 were added. The introduction of C_2H_4 can be detected as a change in SE image contrast, a slight increase of the chamber pressure, and further confirmed with a mass spectrometer that is attached to the microscope. Formation of carbon deposits can generally be observed after an induction period of around 10 min, when spots of darker contrast start to appear on the surface of the copper film. A series of SEM images capturing the appearance and growth of carbon sheets on Cu at 1000 °C is presented in **Figure 5-3** (and **Online Movie M2**). Although the resolution of the ESEM is not sufficient to detect the

actual nucleation event, new flakes can be observed as soon as they reach a size of around 3 nm.

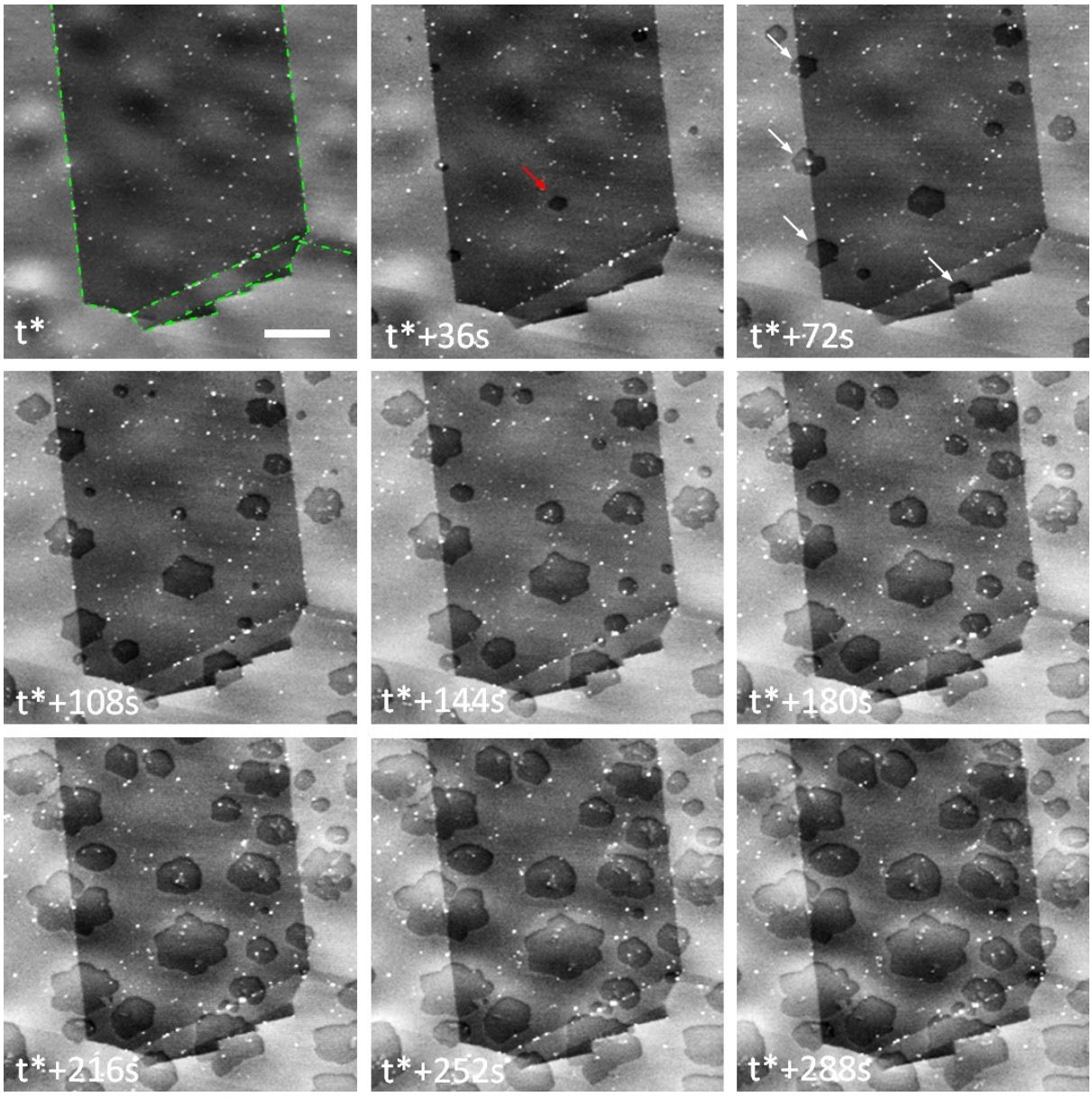

Figure 5-3 *In situ* SEM images recorded at 1000 °C during LP-CVD growth showing the nucleation and growth of carbon sheets (characterized by darker contrast). White arrows highlight nucleation events at grain boundaries. t* corresponds to the induction period from C_2H_4 dosing until the first nucleation events can be detected. Growing graphene sheets are characterized by a dark contrast. Smooth contrast of the copper surface is due to a sublimation induced surface buckling. Grain boundaries in the copper foil are highlighted by green dotted lines in the top left image. Differences in contrast for different grains are due to electron channelling. The scale bar measures 5 µm.

As a result of the high temperature and the substantial loss of copper due to sublimation,[39] the topography of the surface changes with growth time. Graphene covered regions start to show up as hills between valleys of uncovered copper (see **Figure 5-4**).

With time, the growth speed of graphene flakes decreases until finally, growth terminates although ethylene and hydrogen are delivered at constant rate and the temperature remains constant. In agreement with earlier reports on LP-CVD, growth termination occurs regardless of the fact that the copper surface is not completely covered by graphene.[29, 30]

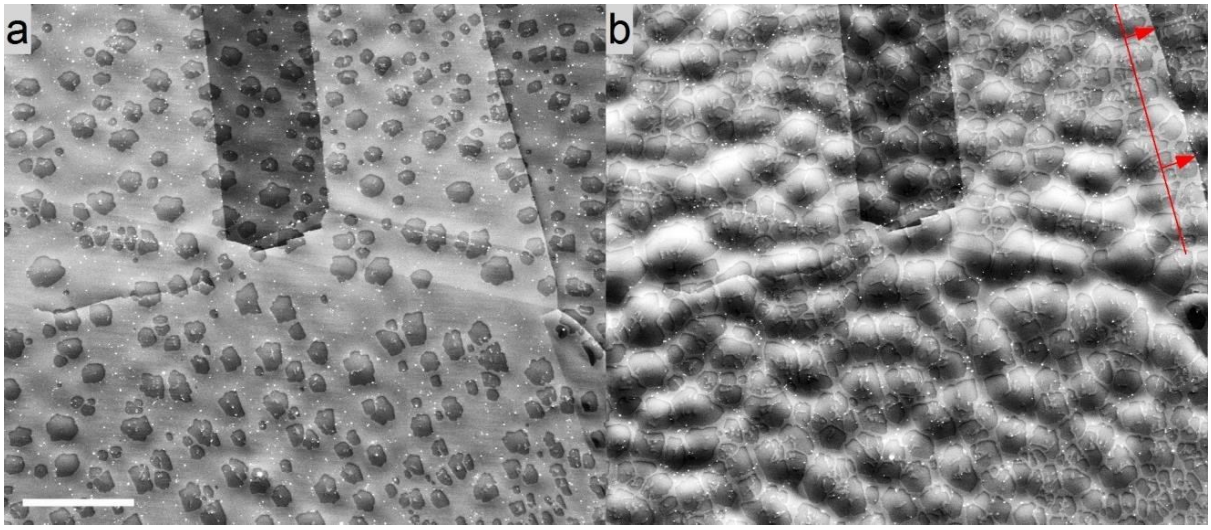

Figure 5-4 Change of the surface morphology due to sublimation during graphene growth. The shown region was used to abstract the nucleation and growth behaviour presented in Figure 5-3. The scale bar measures 20 µm. The arrows and red line indicate the propagation of a grain boundary during growth.

5.3.3. Substrate cooling

After termination of the growth process, the temperature of the substrate was decreased at a rate of 20 °C per min, while the flow of hydrogen and ethylene was kept constant. Snapshots taken during cooling are displayed in **Figure 5-5** and provided as Online Movie (M3). During cooling inside the ESEM, a copper surface reconstruction and the evolution of surface faceting is observed in the temperature range between 750 °C and 520 °C. Remarkably, the reconstruction underneath the carbon sheets is distinct and can easily be differentiated from the reconstruction of uncovered copper.

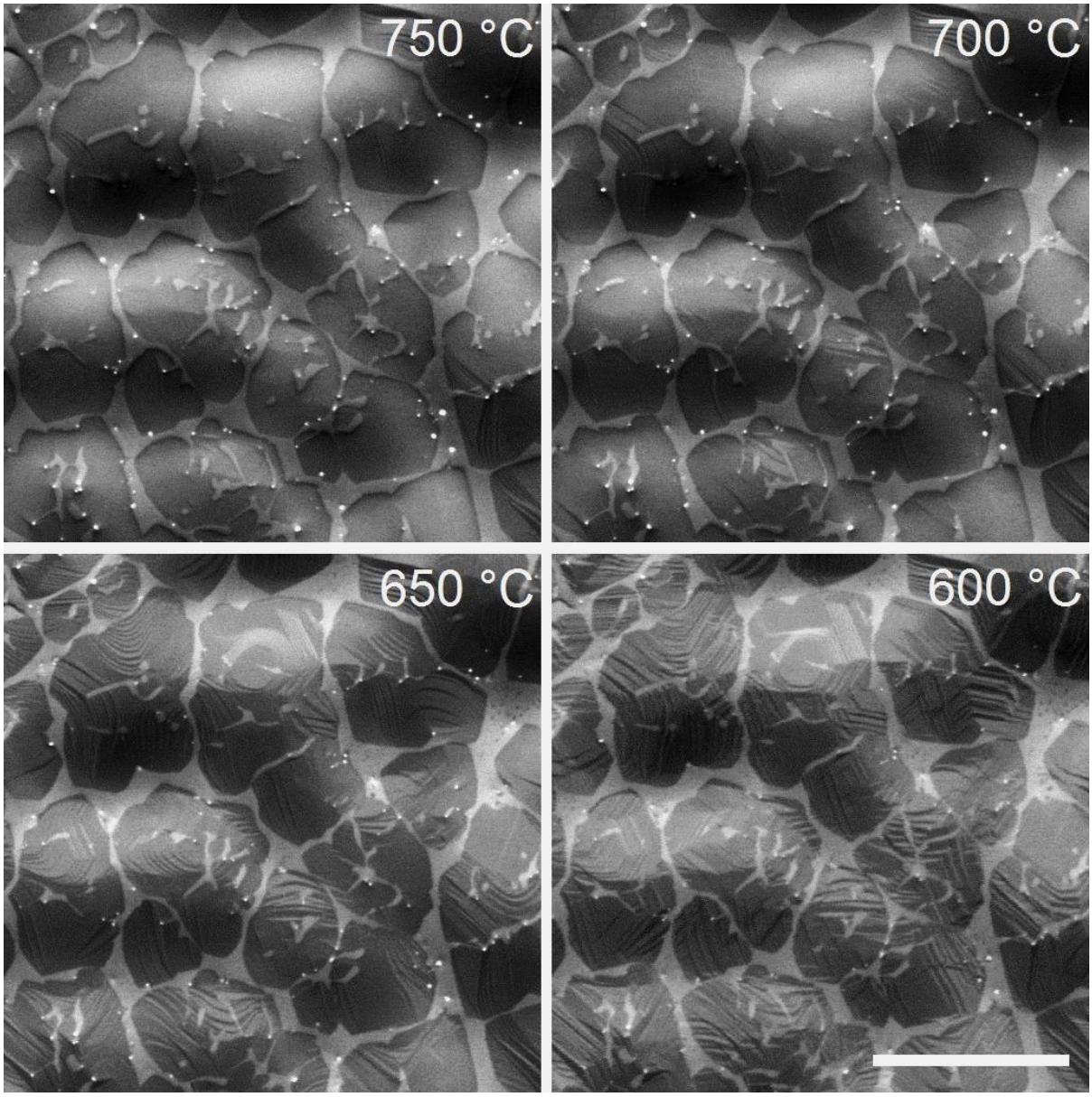

Figure 5-5 *In situ* SEM images recorded during cooling, showing distinct morphological changes of the Cu surface underneath carbon sheets during cooling. The scale bar measures 10 µm.

5.3.4. Characterization

After growth and cooling, the microscope was set to high-vacuum mode for optimized imaging conditions and post growth structural investigation. The as-grown sheets were furthermore characterized by Raman, AFM, STM and TEM. Based on the Raman spectra and

STM data, the grown sheets can be identified as high quality single layer graphene[40-42] (see **Figure 5-6**).

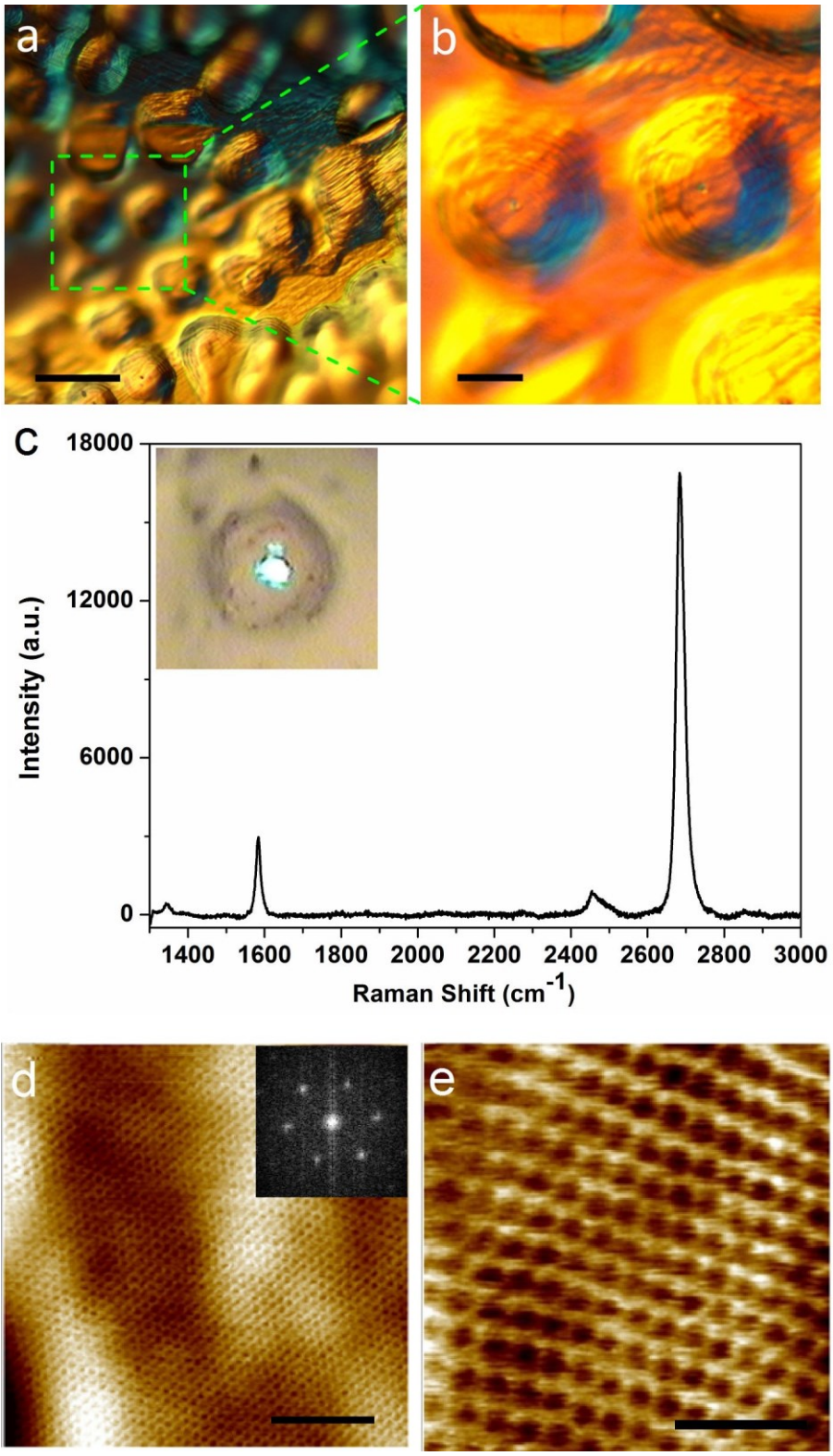

Figure 5-6 Characterization of graphene after CVD growth. (a, b) Aspect of the Cu surface as seen through an optical microscope. (c) Raman spectrum of graphene on Cu. The spectrum shows the characteristic features due to single layer graphene. The inset in panel (c) shows the laser spot on a graphene covered "hillock". (d) STM image of graphene on copper, the corresponding FFT pattern shows the symmetry of the graphene lattice. (e) High-resolution STM image from a region in (d) showing the carbon honeycomb lattice. Scales bars are 20µm (a), 5µm (b), 5 nm (d) and (e), respectively.

5.4.Discussion

5.4.1. Graphene growth behaviour

The nucleation and growth behaviour can directly be extracted from the *in situ* recorded image sequences. **Figure 5-7**a shows the percentage of the graphene covered copper surface area together with the change of the nucleation rate with time. Here, the nucleation rate is defined as the number of new graphene flakes that are detected per each recorded image frame. Values have been abstracted from an area measuring 9000 μm^2, in which a total of 507 nucleation events were registered (see **Figure 5-4**). The observed induction period and subsequent nucleation behaviour strongly indicate an initial building up of carbon growth-species on the substrate surface until super saturation is reached and nucleation is initiated. The behaviour is therefore similar to what was found by *in situ* LEEM[19] in the case of graphene growth on Ru and Ir. However, this is the first direct observation of an induction period in the case of CVD growth on copper. It confirms previous findings that were obtained *ex-situ* on the basis of time dependent growth studies.[10, 30] With the ESEM data it is now possible to relate the nucleation behaviour to the evolution of growth. During the initial phase (region I in **Figure 5-7**a), the radial growth of graphene sheets is roughly constant (central region in **Figure 5-7**b). Hence, the square functions-like onset of the integrated areal growth curve. The consumption of carbon building blocks due to nucleation and growth quickly leads to desaturation, which explains the drop in nucleation rate in the transition to the second growth phase (region II in **Figure 5-7**a). The fact that super saturation cannot be uphold demonstrates that, under the chosen experimental conditions, the production rate of carbon growth species by catalysed ethylene decomposition is lower than their total rate of consumption - either in nucleation and growth, or by recombination and desorption from the surface.

As a result of the shortage in building blocks, the growth mode changes from attachment limited towards surface diffusion-limited growth.[8] Some of the observed sheets reflect this change in growth mode by a slight change in the growth shape (**Figure 5-7**b, in the transition from the first to the second phase). The accumulation of defects and partial etching of defective carbon from growing flakes by hydrogen[9] as well as differences in growth mechanisms at corners *versus* edges furthermore play a role in the shape transformation and the change of the growth front from a straight line into a corrugated pattern (**Figure 5-7**b).[43, 44]

Although the nucleation rate drops significantly after the initial growth phase, some nucleation events are still observed during the second phase. Delayed nucleation events can be related to local inhomogeneity on the copper surface and variations in the time needed to reach the required super saturation. As shown in **Figure 5-7**c, sheets nucleating at a later time show similar initial growth behaviour as early ones.

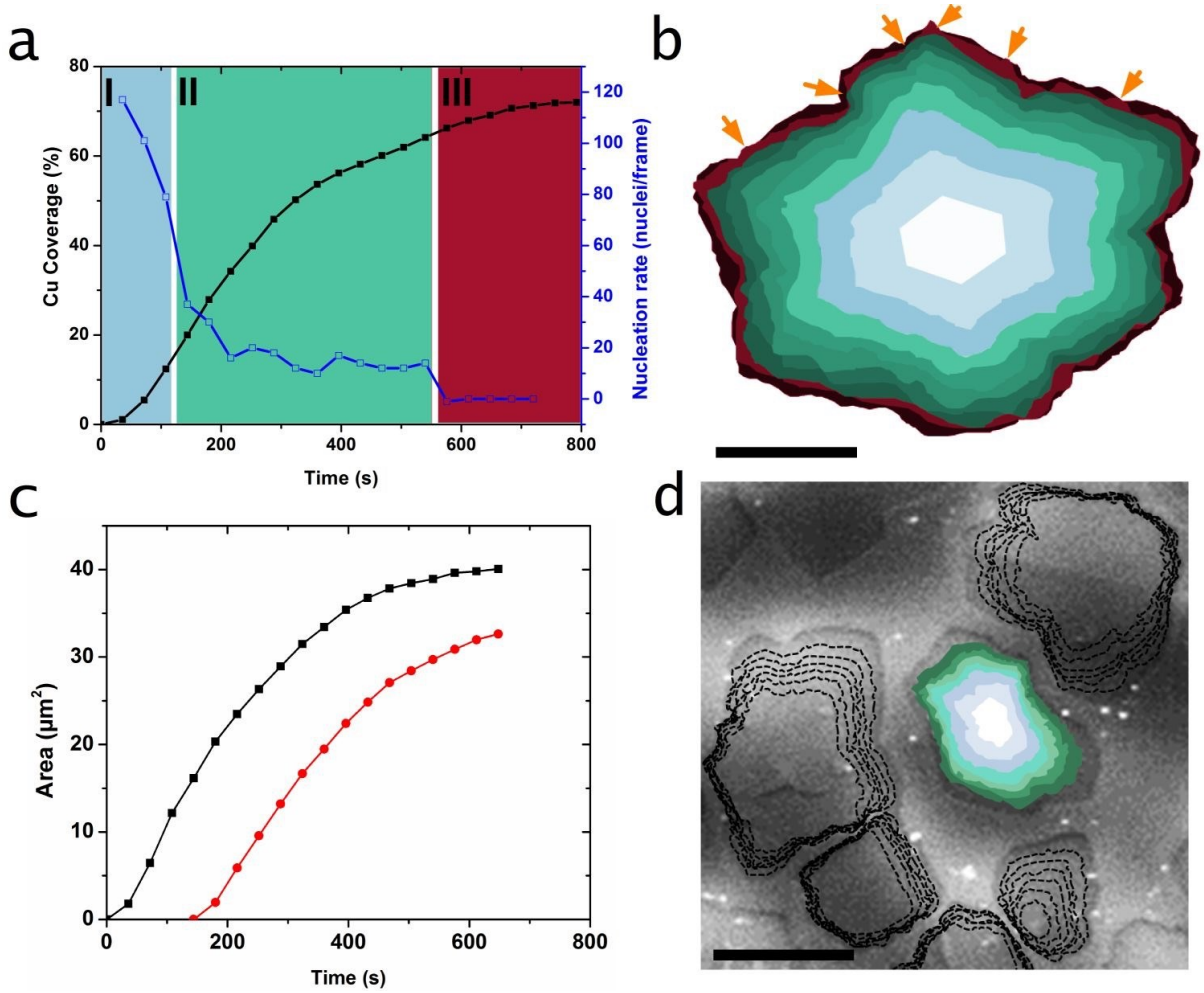

Figure 5-7 (a) Plot showing the increase of the graphene covered Cu surface area with time (black curve). The nucleation rate (blue curve) is given as the number of new graphene flakes observed per recorded image frame during *in situ* ESEM imaging. The analysed region is shown in Figure 5-4. (b) shows a superposition capturing the areal growth of a single flake (the one that is marked by a red arrow in Figure 5-3). Arrowheads indicate some places where etching is evident (see also Figure 5-10). (c) shows the areal growth of two flakes that appeared at different times (the black curve corresponds to the flake shown in (b), the red curve was abstracted from the coloured sheet in (d)). (d) shows the shape evolution of neighbouring graphene flakes in a superposition of seven image frames. The interval between subsequent image frames in (b) and (d) was 36 s. The scale bars in (b) and (d) measure 2 µm and 5 µm, respectively.

Direct observation of individual sheets reveals that the growth speed decreases faster when growth fronts of neighbouring sheets approach each other. Indeed, it was found that, under the chosen experimental conditions, growing sheets generally do not merge, even if they nucleate close to one another (**Figure 5-7**d and **Figure 5-8**). The effect of the distance and location of neighbouring graphene sheets on the growth front propagation is exemplified for different configurations of neighbours in **Figure 5-8** a-d and f. The obvious mutual influence between growing sheets is indicative for the existence of a capture zone at the growth front. The capture zone is characterized by the lifetime of carbon growth species and their associated diffusion length on the copper surface. (see **Figure 5-9**)

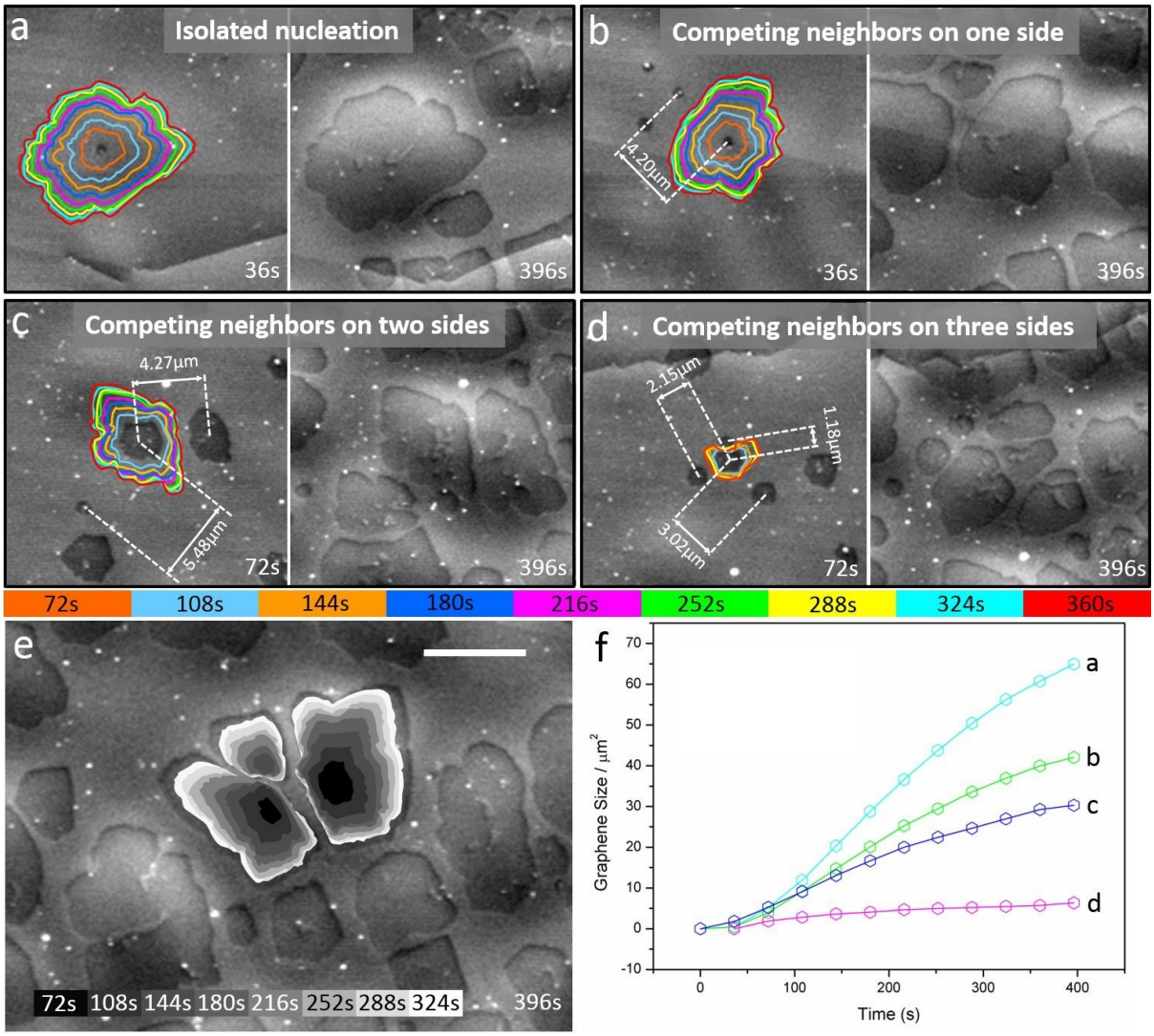

Figure 5-8 (a), (b), (c) and (d) show the shape evolution of growing graphene sheets as a function of the local surrounding. The outlines of growing sheets are colour coded according to the growth time provided in the colour legend. Surface diffusion and growth competition within the capture layer influence growth shape and rate as shown in (e) and (f). Scale bar in (e) measures 5µm.

Growth of individual sheets after nucleation in a locally supersaturated environment can therefore be described as follows. During the first phase, in which the radial growth rate is approximately constant, a newly formed nucleus grows in attachment-limited mode whilst building up a depletion zone at the growth front. Once this depletion zone has grown to its full size, which is determined by the diffusion length of growth species, the second phase of growth is entered. In this phase, growth is limited by capturing of growth species that diffuse through the diffusion layer and those that are produced by catalytic decomposition within the

diffusion layer. Hence, growth follows a typical 2D film growth behavior.[45, 46] Similarly to the Cu surface dynamics, the diffusion length of growth species depends on growth conditions and substrate grain orientation. Furthermore, depending on the degree of surface pre-melting, the grain orientation can influence the growth shape through anisotropic surface diffusion.[47] The third phase of growth is reached once the capture/diffusion zones of neighbouring sheets start to overlap. Under the present growth conditions, this happens when the distance between growth fronts gets below about 3µm. Growth at the corresponding growth fronts diminishes until balance is reached between carbon attachment and etching. A scheme of the discussed phases of graphene growth is shown in **Figure 5-9**.

This description of LP-CVD growth has several consequences for models derived on the basis of *ex-situ* determined growth curves and will help to refine existing growth models.[48] Firstly, there is not only one nucleation phase right after the induction period, which is followed by a phase of growth. Instead, substrate inhomogeneity combined with the limited diffusion length of carbon species can result in delayed nucleation events. Due to this, an integrated growth curve corresponds to a superposition of many individual growth curves starting at different times (see **Figure 5-7**c and **Figure 5-8**f). Secondly, the growth shape of individual sheets is not only influenced by surface dynamics and diffusion processes on a substrate grain, but also by capture zones of nearby growing sheets, such as demonstrated in **Figure 5-8**f. Overall, the availability of growth species at the growth front determines which of the three described phases dominates growth. Growth models should therefore be built on the basis of individual sheets under consideration of their local surrounding. Furthermore, cross talk over extended distances can happen through the atmosphere. Differences in the gas phase and boundary layer chemistry could have an effect on the growth process on neighbouring copper grains and thus influence the local kinetics of growth. It might therefore be of interest to study growth on single crystals.

The above description of growth is in concordance with previous results that showed that an extension of the linear growth regime is possible through an increase of the hydrocarbon partial pressure.[13] It results in a higher production rate of growth species, which delays the building up of fully developed depletion zone at the growth front. Consequently, at sufficiently high hydrocarbon pressure, even complete copper coverage can be achieved.[49]

Alternatively, the choice of a hydrocarbon source that shows a higher decomposition rate, can lead to higher surface coverage under otherwise similar conditions[25].

Direct observation of the growth front propagation further reveals the competition between graphene etching and growth at the beginning of phase three. Due to the reduced availability of growth species, carbon attachment can locally (*i.e.*, at defective regions) no longer counter balance the etching (see arrowheads in **Figure 5-7**b and **Figure 5-10**). However, growth can proceed after etching (**Figure 5-10**), indicating a possible repairing mechanism for defect free growth. This detail, which is missed in post-growth observation,[13] probably plays an important role in the production of large, defect free graphene sheets. Considering the many possible forms of carbon bonds, it is indeed possible that selective etching during growth controls the formation of two-dimensional graphene *versus* alternative three-dimensional forms of carbon, such as soot.

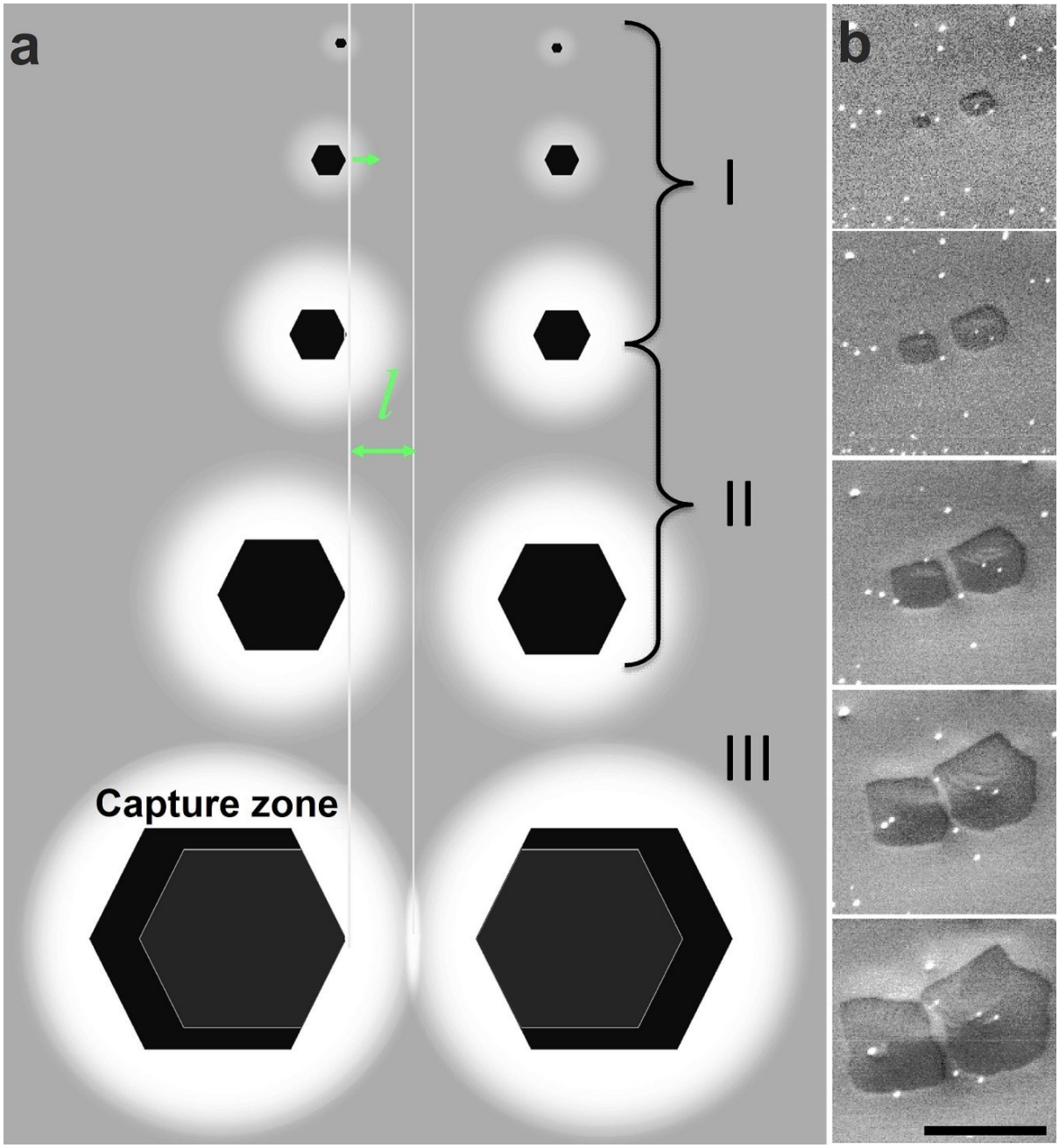

Figure 5-9. Three phases of growth. Different stages of graphene growth under LP-CVD: (a) show a scheme of the different growth phases. Phase I: building up of depletion zone. Phase II: the depletion zone has reached its full size according to the diffusion length of growth species. It can now be referred to as capture layer. Phase III: overlap of capture layers diminishes growth until a balance between etching and growth is reached. (b) *in situ* SEM images recorded during CVD growth of graphene flakes at 1000 °C. The sequence shows that growth stops once growth fronts approach each other, while it continues along other directions. The scale bar measures 5 µm.

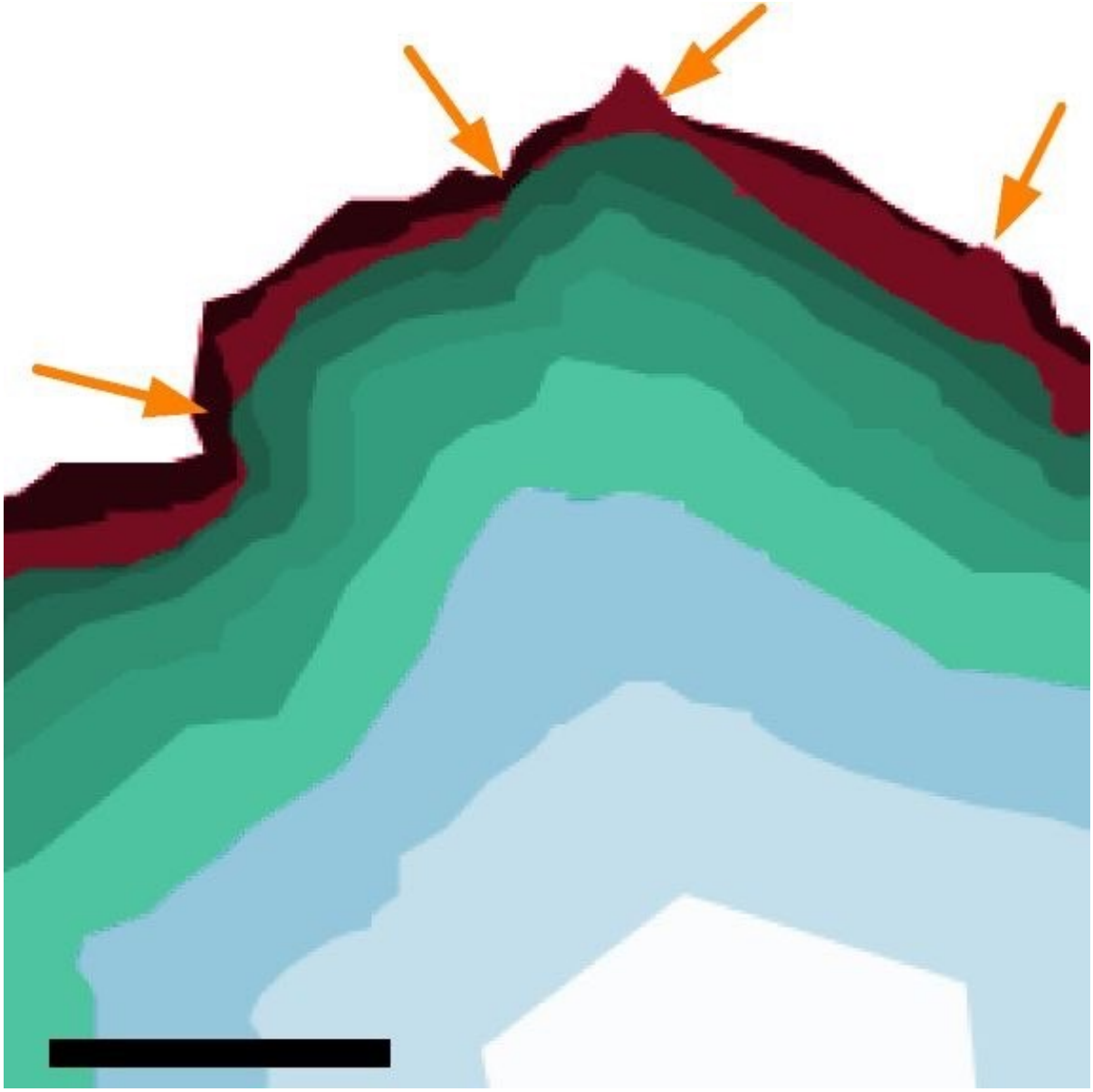

Figure 5-10. Magnified region of Figure 5-7b in the main manuscript, showing graphene etching. Arrows indicate regions where the outline in an earlier image frame exceeds the one of a later frame due to etching. The scale bar measures 1 µm.

5.4.2. Cu surface dynamics

In situ SEM experiments reveal substrate morphological changes during annealing and pronounced surface dynamics under conditions of growth. Under LP-CVD growth at 1000 °C, the loss of exposed Cu due to sublimation is substantial[39] and more pronounced than under elevated pressures. However, imaging of the surface during growth demonstrates that the growing graphene sheets provide a barrier against sublimation.

As a consequence, the lateral expansion of the growing sheets leads to the formation of graphene covered hills with valleys of uncovered copper in between them (see **Figure 5-3**, **Figure 5-4**, Online Movie M2, M4 and M5). The observed grain dependent degree of hill-and-valley formation demonstrates that the sublimation rate is related to the crystallographic orientation of a grain (**Figure 5-11** a – d). As confirmed by EBSD measurements shown in **Figure 5-11** e and f, the hill-and-valley aspect is more pronounced and characteristic for graphene growth on <100> and <110> oriented grains, while relatively flat graphene sheets are formed on <111> grains. The extent of hill and valley formation furthermore depends on growth conditions. It increases with increasing growth time and is therefore more pronounced at low hydrocarbon flow rates. In case of growth below 1000°C, the effects of sublimation are far less pronounced (see **Figure 5-12**). For our growth conditions (4.4×10^{-2} Pa, 1000 °C and 800 s of growth time), concave hills reached heights of up to 1.5 µm at a lateral expansion of a few 100 μm^2 for <110> and <100> grains.

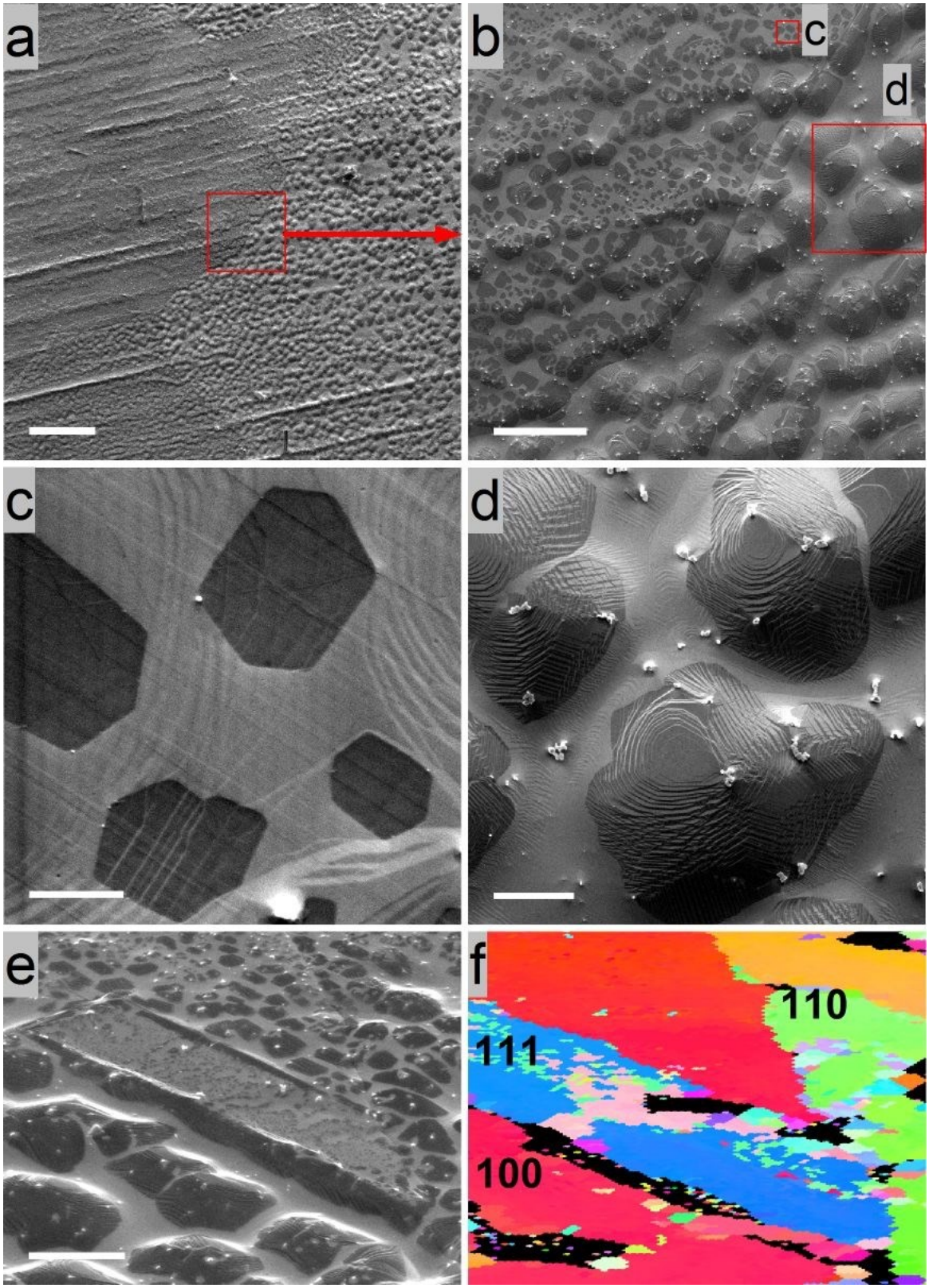

Figure 5-11 (a – d). Post-growth SEM images showing relatively flat or convex shaped graphene coated regions. (a) and (b) show overview images, (c) and (d) representative details of the morphology on the respective grains. The EBSD map recorded from a region in (e) is shown in (f). Image (e) was recorded at

a tilting angle of 70° as required for the EBSD measurement. Scale bars in (a) to (e) measure, respectively, 200 µm, 20 µm, 1 µm, 5 µm and 10 µm.

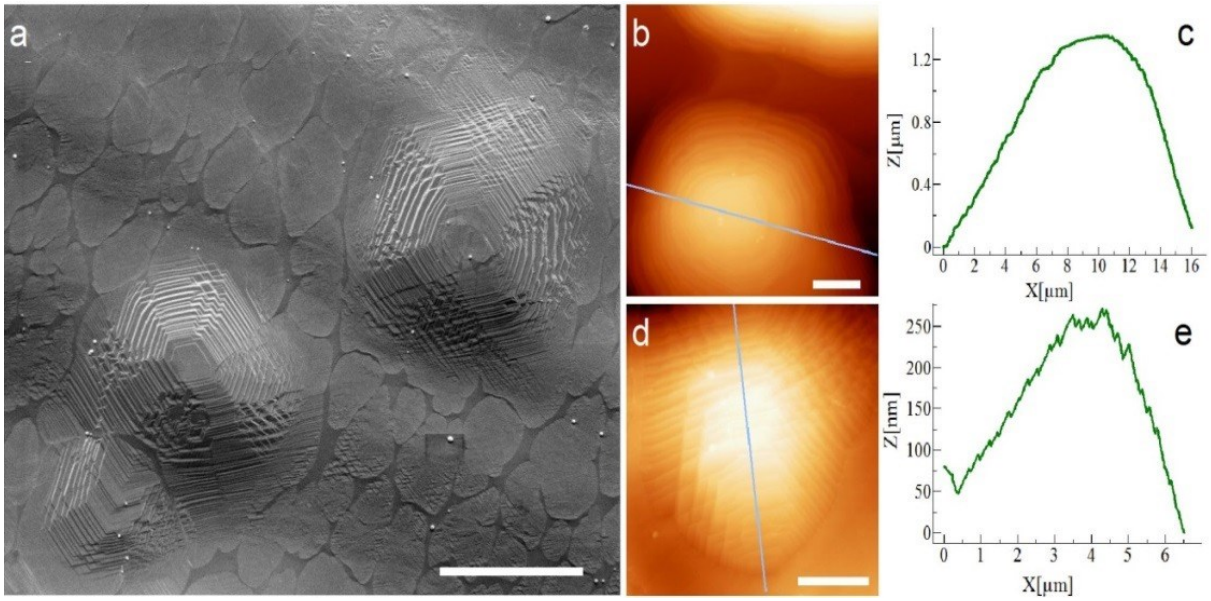

Figure 5-12 (a) Post-growth SEM image, showing sublimation induced hill-and-valley formation at high temperature (1000 °C) next to flat sheets grown subsequently at lower temperature (820-850°C). (b-e) AFM height profiles recorded over hills on [100] and [110] oriented grains. Scale bars measure 10 µm in (a) and 2 µm in (b, d), respectively.

Besides the effects of sublimation, the *in situ* observations also reveal a pre-melted and highly dynamic copper surface under conditions of LP-CVD at temperatures above 900 °C. The existence of a pre-melted surface layer on copper at this temperature is in agreement with the literature, according to which the first signs of surface pre-melting on copper can be detected at around 800 °C.[37, 38] In fact, the pre-melting at the surface can be viewed as a wetting of the solid-vapour interface by its own liquid as temperature approaches the melting point.[50] This quasi liquid exhibits structural, dynamic, and transport properties that are intermediate between those of the solid and liquid[51] and it is affected by the underlying solid substrate. The degree and onset of pre-melting follows the order in the packing density, *i.e.*, the most open <110> face disorders at the lowest temperature, followed by the <100>, while the <111> is more stable and shows weak pre-melting effects until the bulk melting temperature.[52] This is reflected in the different nucleation density observed for the <111> *versu*s the other low index surfaces: In agreement with I. Vlassiouk *et al.*,[39] we observe a higher nucleation density on the <111> compared to the <100> and <110> faces (see **Figure**

5-11a, b and e). It is a consequence of the higher degree of surface melting on the <100> and <110> surfaces, which causes a smoothening of the surface. Due to the absence of steps and edges, the number of nucleation sites is reduced as compared to the more stable <111> oriented surfaces. At lower temperatures, in the absence of surface pre-melting, we observe a similar nucleation density on <110>, <100> and <111> grains (see **Figure 5-13**). Besides pre-melting, sublimation might also play a role in grain orientation dependent nucleation and growth, as it influences the lifetime and diffusion of growth species on the surface.[30]

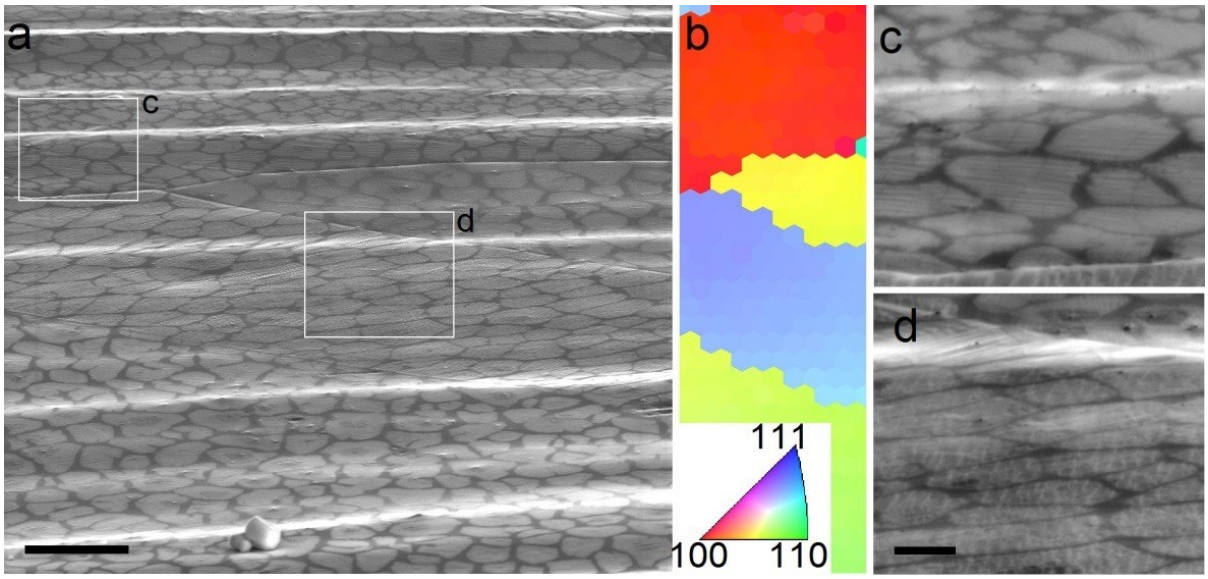

Figure 5-13 A similar nucleation density is observed on different grains for growth at temperatures where no surface melting can be detected (820-850 °C). In this temperature range, sublimation induced hill-and-valley formation is suppressed. The scale bars measure 10 µm (a) and 2 µm (d).

Due to surface pre-melting, the actual graphene growth can be decoupled from the crystalline order in the bulk. Under LP-CVD conditions on polycrystalline Cu it is therefore possible to simultaneously observe graphene sheets that grow with or without evident orientation alignment on differently oriented grains.[36, 43] For growth at 900°C, grain orientation dependent graphene shapes[36] and orientation alignment of grown sheets is dominant [39] (see **Figure 5-14**a). With increasing temperature, the wetting layer thickens and processes on the surface start to decouple from the atomic arrangement in the underlying grain. At 1000°C, growth proceeds largely decoupled from the bulk crystalline order and neither evident alignment of growth directions nor grain dependent shapes are observed for most of the

grains (**Figure 5-14**b). At this temperature, the migration of grain boundaries below growing sheets does not lead to significant disturbance in the growth behaviour (**Figure 5-15**, and Online Movie M2). Only some shapes of hexagonal symmetry are observed, which is due to growth on Cu <111> grains with a higher stability against pre-melting and better lattice matching[53] (see **Figure 5-3** and **Figure 5-11**c).

Finally, at and above the Cu melting point, in the absence of crystalline order, graphene grows in hexagonal shapes as can be seen in **Figure 5-14**c. Growth of graphene on liquid copper was firstly demonstrated by Geng *et al*.,[54] who found perfectly hexagon shaped graphene flakes. As can be seen in **Figure 5-14**c, local orientation alignment can even be observed on liquid copper. This could be indicative for the existence of a close packed structural ordering within the surface layer of the copper melt.[55] It is important to mention here that the atmosphere in the chamber has an influence on the surface mobility. Indeed, we have observed that hydrogen increases the mobility of the copper surface, confirming the findings of Sidorenko *et al*.[56]

In summary, the existence of a surface pre-melted layer has several implications: Firstly, it leads to a partial decoupling of the growth from the copper atomic arrangement in the bulk even below the copper melting point (see schematic drawing in **Figure 5-14**d). Secondly, it provides locally an atomically flat and electronically homogeneous support for allowing carbon atoms to assemble and self-organize with a minimum of interference from the support. Furthermore, due to the absence of steps and kinks, the nucleation density on pre-melted copper is strongly reduced as compared to low temperature growth.

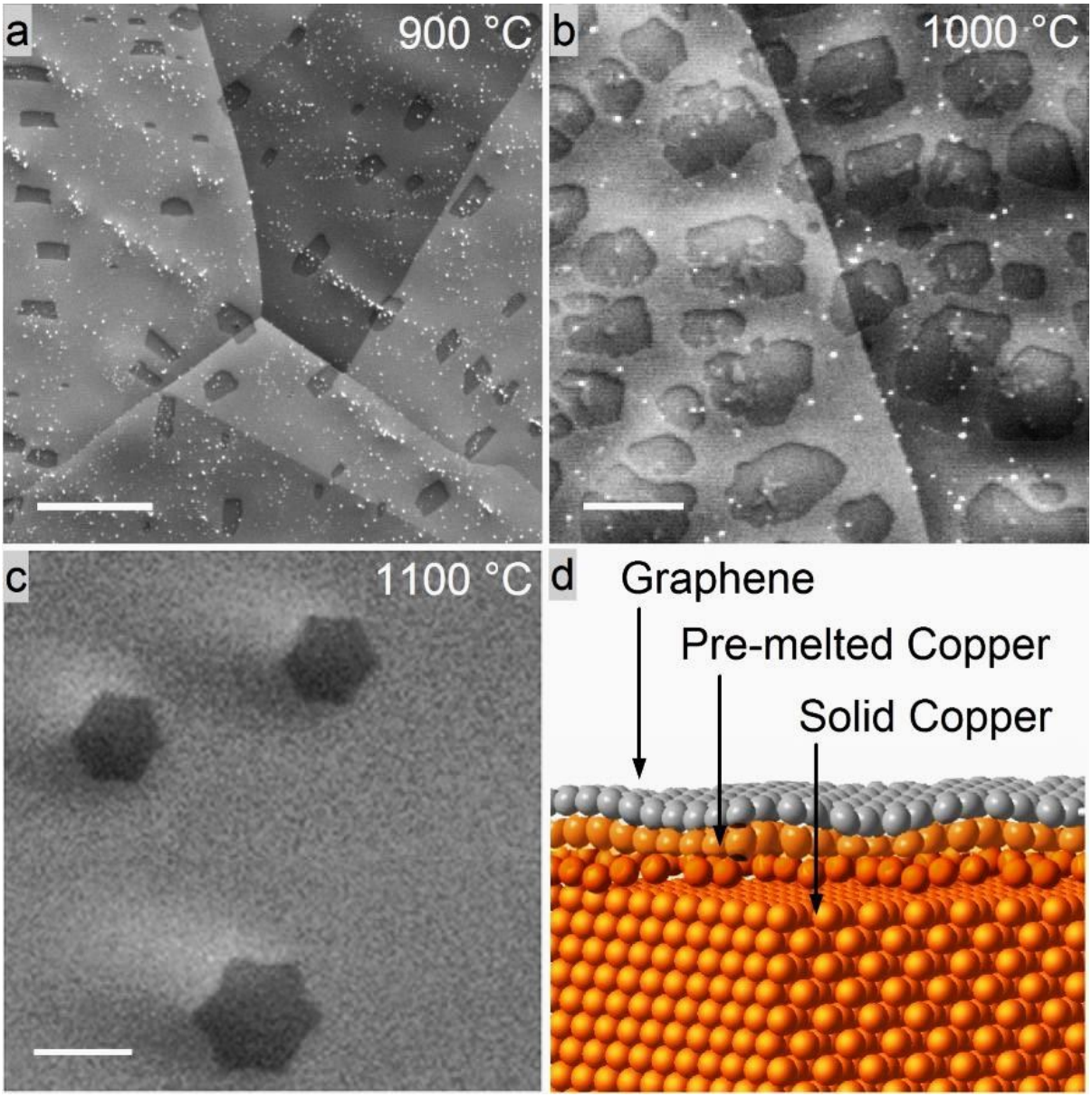

Figure 5-14. ***In situ*** **images recorded during growth at different temperature. With increasing temperature, the surface processes start to decouple from the crystalline order in the bulk of the grain due to increased thickness of the surface melt layer. (a): growing sheets at 900 °C show a grain orientation dependent shape and orientation alignment, (b) no clear shape and orientation relation is detected in the case of growth at 1000 °C. (c) above the melting point, hexagon shaped graphene sheets grow locally in concordance. (d) shows a schematic picture of graphene on a surface pre-melted Cu layer. The scale bars measure 10, 5 and 1 µm in (a), (b) and (c), respectively.**

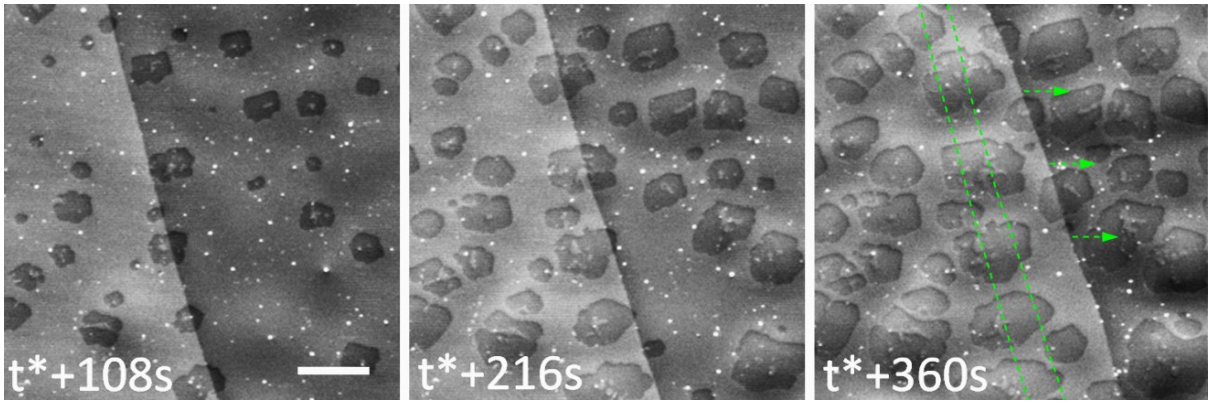

Figure 5-15. Cut out from *in situ* movie M1 showing grain migration underneath growing sheets. The scale bar is 5 µm. t* corresponds to the induction period from C_2H_4 dosing until the first nucleation events can be detected. Green dotted lines show grain boundary former position.

5.4.3. Surface reconstruction during cooling

The ESEM reveals that the covering graphene layer induces a distinct recrystallization of the surface melted layer during cooling, which can lead to preferential exposure of specific planes. This is evidenced by the appearance of crystallographic identical facets underneath different graphene sheets within single copper grains such as shown in **Figure 5-16** a, b and particularly, in c. Similar grain dependent surface step bunches have been observed by Kim *et al.*[57], who attributed their formation to strain relaxation between graphene and the Cu lattice. Due to the low temperature at which the reconstruction takes place, the crystallization precedes such that the overall surface morphology of graphene-covered areas is preserved. In the case of graphene-covered hills, the shape is therefore approximated through the formation of low energy graphene-copper interfaces and step bunches[57]. Accordingly, different reconstructions are observed on differently oriented grains (see **Figure 5-12**). However, the copper surface reconstruction does not change the orientation of the already grown graphene lattice. This explains why Rasool *et al.*[58] found that different facets, steps and edges of the copper substrate are overgrown with a perfect graphene honeycomb lattice. Surface reconstruction during cooling has so far not been observed directly, however, it has been postulated on the basis of post-growth observations[59]. Because the reconstruction happens after growth, it can give rise to confusions regarding the relation between graphene and the atomic arrangement at the surface of the substrate during growth.[58, 60]

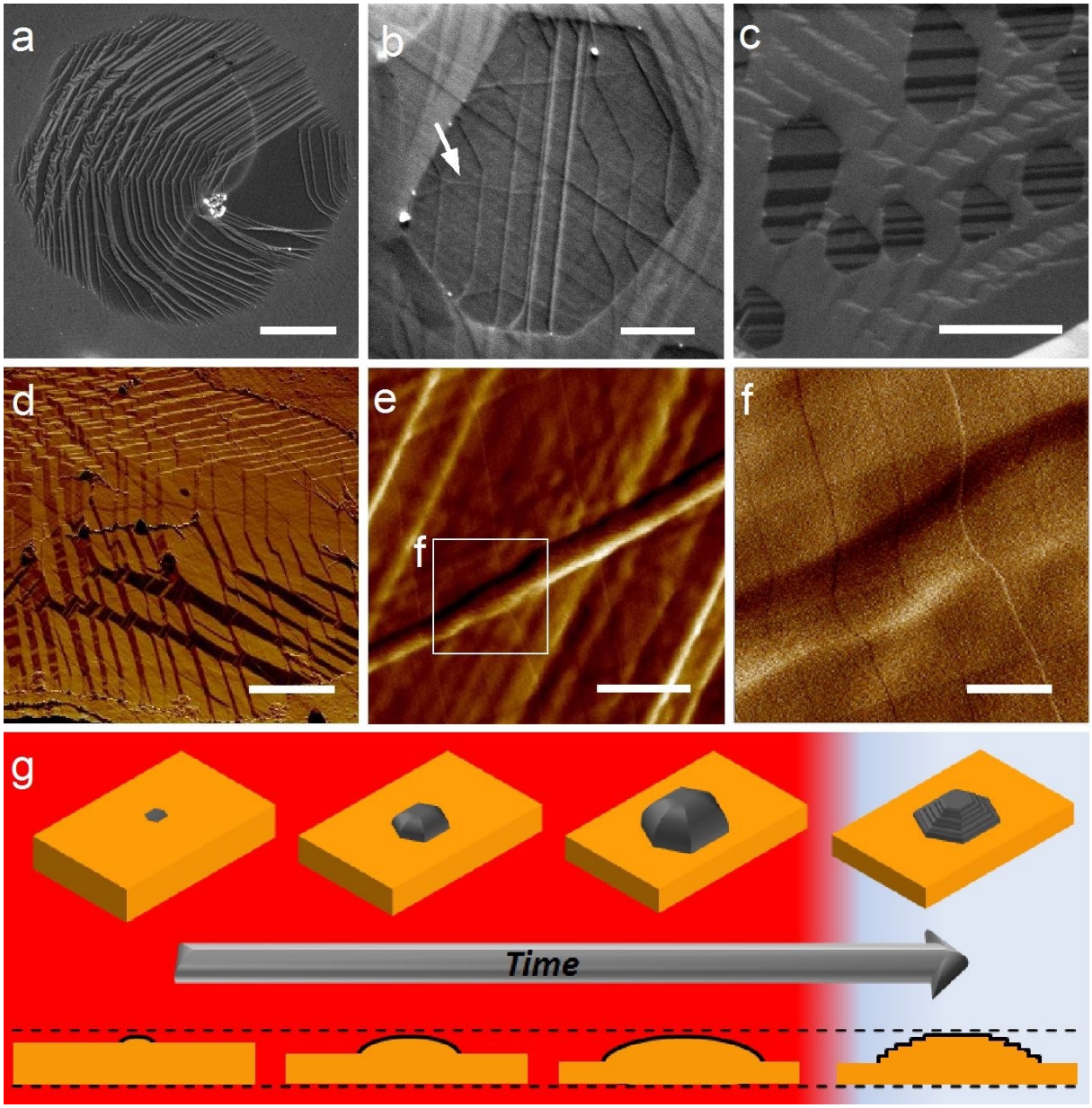

Figure 5-16. Post-growth SEM (a-c) and AFM (d-f) images recorded after growth show graphene induced copper surface reconstruction. In (e) and (f) details of a graphene wrinkle (similar to the one marked with an arrow in (b)) with particular stripes are shown. Note that the copper surface reconstruction is continuous across the wrinkle. (g) schematic illustration showing the sublimation induced hill and valley formation during graphene growth and subsequent surface faceting during cooling. Scales bars measure 2 µm (a), 500 nm (b), 1 µm (c), 10 µm (d), 100 nm (e), and 20 nm (f).

At higher spatial resolution, AFM reveals particular reconstructions in the form of regular steps as show in in Fig. 16f. These stripes are in agreement with graphene-induced Cu surface reconstructions observed by Wilson and Tian *et al.*[61, 62] using STM, who, similarly to Kim *et al.*[57] attributed the formation of regular stripes under graphene to strain release at the copper surface. As can be seen in Fig. 16f, such stripes are continuous even across graphene

wrinkles, indicating a strong coupling between the copper and graphene (**Figure 5-16**, f). The existence of a strong coupling between copper and graphene is in agreement with the findings of Kidambi *et al*.[25] Using *in situ* XPS, they provided evidence for a temperature and atmosphere dependent coupling between film and substrate, which could play a role in the observed surface reconstructions.

However, particular surface reconstructions could also be indicative for the presence of small amounts of adsorbed oxygen.[63, 64] Under conditions of graphene growth in the ESEM, the presence of small amounts of oxygen in the gas phase is confirmed by the MS. The presence of sub-monolayer amounts of oxygen that is dissolved in the surface melt could in fact be a requisite for the catalytic decomposition of the ethylene. Especially, in the case of growth on liquid copper, where the typical high-energy sites, such as step edges and defects, are absent. Indeed, the active catalyst in CVD graphene growth on copper could have similarities to the case of catalytic methanol oxidation on copper: From *in situ* X-ray absorption studies it is known that the active copper phase contains small amounts of dissolved oxygen.[65,66] A possible role of oxygen in the catalytic decomposition of the hydrocarbon on copper is suggested by the successful growth of graphene under conditions of oxidative dehydrogenation.[67] Furthermore, it has been shown that oxygen has an influence on the sticking coefficients and the rate of hydrocarbon precursor decomposition on copper.[68, 69, 70]

According to the Cu-O phase diagram, a transition from stable Cu to Cu_2O can occur at oxygen partial pressures in the range of 10^{-3} Pa at around 830 °C.[71] For lower partial pressures, thermal faceting due to surface oxide formation is observed at lower temperature.[72] The structural changes induced by oxygen adsorption depend on the oxygen coverage and initial crystallography of the faces.[64, 73, 74]

Indeed, our TEM cross-section investigation of samples investigated after growth in the ESEM, confirm the presence of a thin Cu_2O layer on the surface of the copper (see **Figure 5-17**).

Considering the many different CVD set-ups and growth conditions and the published variety of graphene shapes, it can be assumed that the leak tightness and oxygen partial pressure in the atmosphere during growth is an important variable influencing the outcome. Although the role of oxygen in ambient and low pressure CVD graphene growth has been discussed in the

literature,[13, 68] it is clear that its involvement in the catalytic decomposition and the surface chemistry of copper during growth and cooling needs further investigation.

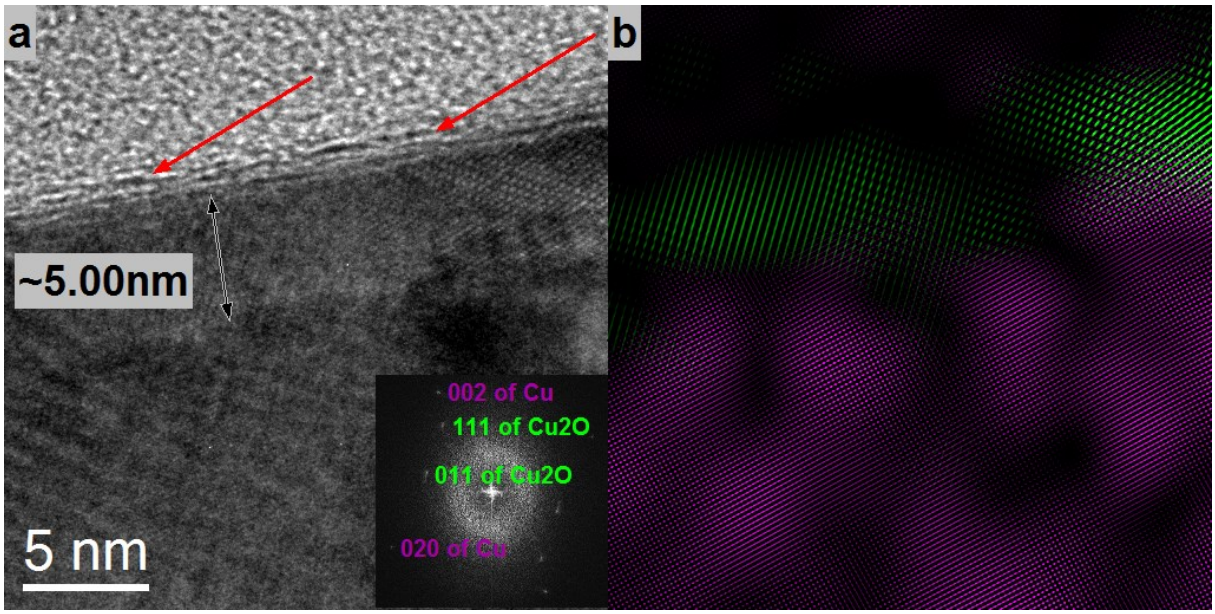

Figure 5-17. (a) TEM cross-section showing a thin Cu_2O layer on the surface of the copper substrate after graphene growth. Arrows indicated the presence of distorted graphene on the surface. The inset in (a) shows a power spectrum with spots due to the lattice of Cu and Cu_2O, respectively. (b) shows a color coded Fourier Filtered version of (a) in which components due to Cu and Cu_2O are colored in violet and green, respectively.

5.5.Conclusion

This chapter demonstrates the potential of an *in situ* technique that enables simultaneous and direct observation of the active catalyst and the forming product. Low pressure CVD growth of graphene inside the chamber of an ESEM reveals the dynamic nature of the copper substrate and demonstrates that growth at high temperature occurs on a pre-melted, highly mobile copper surface. Surface dynamics are strongly depending on the copper grain orientation, temperature and atmosphere and have to be taken into account in the modelling of graphene formation. Real-time observation of graphene nucleation and growth provides relevant insight on the growth mechanism under LP-CVD. It is confirmed that nucleation starts after an induction period during which the surface saturates in growth species. From the growth behaviour, three growth phases can be abstracted. In the first phase, a depletion zone

is built up at the growth front. Once the depletion zone has fully developed, the growth mode changes from attachment to diffusion-limited, and the second growth phase starts. During this phase, the presence of a capturing/diffusion zone at growth fronts is evidenced by the observed mutual influence of neighbouring sheets. Once capturing/diffusion zones of neighbouring sheets overlap, the third phase is reached. Growth at the corresponding growth fronts diminishes until a balance is reached between graphene etching and growth. The contributions of the described phases to the overall growth process certainly depend on the type of hydrocarbon source, the atmosphere pressure, as well as hydrocarbon/hydrogen ratio and should be systematically investigated. However, the ESEM study demonstrates that a correct growth model can only be built on the basis of direct observation of growing sheets and that an integrating analysis of the graphene covered area after growth is insufficient.

In situ growth in the ESEM furthermore demonstrates that the relation between graphene and the copper surface during growth is different to the one observed after cooling in post-growth characterization.[34] This is an important finding that has to be taken into account in the discussion of the influence of the substrate on the graphene growth,[15, 16, 40] specifically concerning preferential alignment[20], growth across grain boundaries[19] and the many different nuclei shapes reported on different facets[8].

The observed surface reconstruction during cooling suggest the presence of small amounts of oxygen which are dispersed as an impurity in the surface melted layer and could convert the Cu metal into a potent catalyst for hydrocarbon dissociation. Further studies will be required to elucidate the role of residual oxygen in CVD growth and it is strongly suggested that the oxygen concentration is monitored and reported in future growth studies.

Finally, this future confirms the high sensitivity of the secondary electron signal to morphological changes at the surface and the presence of atomically thin layers of carbon and furthermore, the instruments capability in terms of *in situ* surface science experiments.

5.6.Methods

In situ CVD growth. *In situ* CVD growth experiments were performed inside the chamber of a commercial ESEM (FEI Quantum 200). The instrument is equipped with a heating stage

(FEI), a gas supply unit (mass flow controllers from Bronkhorst) and a mass spectrometer (Pfeiffer OmniStar) for the analysis of the chamber atmosphere. The vacuum system of the ESEM was upgraded with oil-free pre-vacuum pumps. Polycrystalline copper foils from Alfa Aesar were used as substrate (99.999% purity). Prior to all CVD growth experiments, the chamber of the ESEM was plasma cleaned. All samples were annealed at 1000°C under a hydrogen flow of 8 sccm at a pressure of around 4.4×10^{-2} Pa for 50 min inside the chamber. The temperature was measured *via* a K-type thermocouple that was spot-welded onto the substrate. CVD growth was performed at 1000°C using a flow of 4 sccm H_2 and 0.1 sccm of C_2H_4 at a total chamber pressure of $2\text{-}4\times10^{-2}$ Pa. During the experiments, the microscope was operated at an acceleration voltage of 5.0kV. Images were recorded using the secondary electron signal collected by a standard Everhart Thornley detector (ETD) during sample annealing, CVD growth and cooling. The scan rate was set to one image per 36 s for M1, M2 and M3, respectively. ESEM movies are shown at 7 (M1) and 3 (M2) frames per second. No influence of the electron beam on the growth process could be observed. The imaged regions and their respective surroundings showed similar behaviour, as evidenced by changing the magnification or by moving the sample under the beam. Furthermore, no electron beam induced contamination was observed at elevated temperatures.

Raman. Raman spectroscopy measurements were performed using a Horiba/Jobin-Yvon T64000 spectrometer (Villeneuve D'Ascq, France) with a Coherent Innova 400 (Santa Clara, CA, USA) argon-ion laser operating at 514.5 nm for the excitation. The Raman data were collected with a multi-channel CCD detector. A laser power of 20mW at the sample and an objective with a 100× magnification were used. Confocal approach has been adopted to reduce the background scattering with respect to graphene signal. To obtain a satisfactory signal-to-noise ratio the spectra were recorded with integration times of 60 sec, in total number of 10 accumulations.

EBSD. The EBSD patterns were acquired using the EDAX Digiview detector installed on SEM FEI NovaNanoSEM 230. Analysis of EBSD patterns, including phase identification and generation of orientation maps was performed with EDAX OIM 5.31 Programs.

AFM. Images were taken on a Bruker's Sharp Nitride Lever probe (SNL-10). Imaging was done in tapping mode using a V-shaped cantilever probe B (silicon-tip on Nitride Lever with frequency f_0= 40-75 kHz, and spring constants k=0.32Nm).

STM. Measurements were conducted using a commercial Bruker STM (multimode 8) under ambient pressure at room temperature. A bias voltage of 6 mV was applied at a tunneling current of 3.5 nA. A mechanically cut Pt-Ir tip was used.

TEM. HRTEM image of graphene-copper was taken by a FEI aberration-corrected Titan 80-300 TEM operated at 300 KV.

All the online Movie can be find in this link:

http://pubs.acs.org/doi/suppl/10.1021/nn5059826

Online Movie M1. *In situ* SEM movie showing changes of the Cu surface during annealing in hydrogen from room temperature up to 1000 °C. With rising temperature, restructuring of the surface and grain growth can be observed. Small bright particles start to appear on the surface. They are due to silicon contaminations in the bulk of the foil segregating to the surface. Beyond 850 °C the onset of surface pre-melting can be detected. (Recording time: 3 h 48 min 55 s, 7 fps).

Online Movie M2 *In situ* SEM movie showing CVD growth of graphene on Cu at ~ 1000 ºC. Notice the migration of a grain boundary underneath growing flakes. As a result of sublimation, graphene covered areas form hills that are surrounded by valleys uncovered copper. (Recording time: 25 min 10 s, 3 fps).

Online Movie M3. *In situ* SEM movie showing graphene induced surface reconstruction of the copper during cooling which appears in the temperature range between 750 °C and 520 °C. (Recording time: 54 min, 7 fps).

Online Movie M4 and M5. AFM movies showing surface morphological details of post growth graphene on Cu.

5.7.References

1. Bae, S.; Kim, H.; Lee, Y.; Xu, X. F.; Park, J. S.; Zheng, Y.; Balakrishnan, J.; Lei, T.; Kim, H. R.; Song, Y. I.; *et al.* Roll-to-Roll Production of 30-Inch Graphene Films for Transparent Electrodes. *Nat. Nanotech.* **2010**, *5,* 574–578.

2. Li, X. S.; Cai, W. W.; An, J. H.; Kim, S.; Nah, J.; Yang, D. X.; Piner, R.; Velamakanni, A.; Jung, I.; Tutuc, E.; *et al.* Large-Area Synthesis of High-Quality and Uniform Graphene Films on Copper Foils. *Science* **2009**, *324,* 1312–1314.

3. Sutter, P. Epitaxial Graphene: How Silicon Leaves the Scene. *Nat. Mater*. **2009**, *8,* 171–172.

4. Eswaraiah, V.; Aravind, S. S. J.; Ramaprabhu, S. Top Down Method for Synthesis of Highly Conducting Graphene by Exfoliation of Graphite Oxide using Focused Solar Radiation. *J. Mater. Chem.* **2011**, *21*, 6800–6803.

5. Amini, S.; Garay, J.; Liu, G.; Balandin, A. A.; Abbaschian R. Growth of Large-Area Graphene Films from Metal-Carbon Melts. *J. Appl. Phys.* **2010**, *108*, 094321–094328.

6. Choucair, M.; Thordarson P.; Stride, J. A. Gram-Scale Production of Graphene Based on Solvothermal Synthesis and Sonication. *Nat. Nanotech.* **2009**, *4*, 30–33.

7. Hernandez, Y.; Nicolosi, V.; Lotya, M.; Blighe, F. M.; Sun, Z. Y.; De, S.; McGovern, I. T.; Holland, B.; Byrne, M.; Gun'ko, Y. K.; *et al.* High-Yield Production of Graphene by Liquid-Phase Exfoliation of Graphite. *Nat. Nanotech.* **2008**, *3*, 563–568.

8. Jacobberger, R. M.; Arnold, M. S. Graphene Growth Dynamics on Epitaxial Copper Thin Films. *Chem. Mater.* **2013**, *25*, 871–877.

9. Vlassiouk, I.; Regmi, M.; Fulvio, P. F.; Dai, S.; Datskos, P.; Eres, G.; Smirnov, S. Role of Hydrogen in Chemical Vapor Deposition Growth of Large Single- Crystal Graphene. *ACS Nano* **2011**, *5*, 6069–6076.

10. Wu, B.; Geng, D. C.; Guo, Y. L.; Huang, L. P.; Xue, Y. Z.; Zheng, J.; Chen, J. Y.; Yu, G.; Liu, Y. Q.; Jiang, L.; *et al.* Equiangular Hexagon-Shape-Controlled Synthesis of Graphene on Copper Surface. *Adv. Mater.* **2011**, *23*, 3522–3525.

11. Zhang, Y.; Zhang, L.; Kim, P.; Ge, M.; Li, Z.; Zhou, C. Vapor Trapping Growth of Single-Crystalline Graphene Flowers: Synthesis, Morphology, and Electronic Properties. *Nano Lett.* **2012**, *12,* 2810−2816.

12. Li, X. S.; Magnuson, C. W.; Venugopal, A.; Tromp, R. M.; Hannon, J. B.; Vogel, E. M.; Colombo, L.; Ruoff, R. S. Large-Area Graphene Single Crystals Grown by Low-Pressure Chemical Vapor Deposition of Methane on Copper. *J. Am. Chem. Soc.* **2011**, *133*, 2816–2819.

13. Hao, Y. F.; Bharathi, M. S.; Wang, L.; Liu, Y. Y.; Chen, H.; Nie, S.; Wang, X. H.; Chou, H.; Tan, C.; Fallahazad, B.; *et al.* The Role of Surface Oxygen in the Growth of Large Single-Crystal Graphene on Copper. *Science* **2013**, *342*, 720–723.

14. Piccinin, S.; Zafeiratos, S.; Stampfl, C.; Hansen, T. W.; Havecker, M.; Teschner, D.; Bukhtiyarov, V. I.; Girgsdies, F.; Knop-Gericke, A.; Schlogl, R.; *et al.* Alloy Catalyst in a Reactive Environment: The Example of Ag-Cu Particles for Ethylene Epoxidation, *Phys. Rev. Lett.* **2010**, *104*, 035503.

15. Kandemir, T.; Girgsdies, F.; Hansen, T. C.; Liss, K. D.; Kasatkin, I.; Kunkes, E. L.; Wowsnick, G.; Jacobsen, N.; Schlogl, R.; Behrens, M. *In situ* Study of Catalytic Processes: Neutron Diffraction of a Methanol Synthesis Catalyst at Industrially Relevant Pressure. *Angew. Chem. Int. Ed.* **2013**, *52*, 5166–5170.

16. Behrens, M.; Studt, F.; Kasatkin, I.; Kuhl, S.; Havecker, M; Abild-Pedersen, F.; Zander, S.; Girgsdies, F.; Kurr, P.; Kniep, B. L. The Active Site of Methanol Synthesis over $Cu/ZnO/Al_2O_3$ Industrial Catalysts. *Science* **2012**, *336,* 893–897.

17. Sutter, P.; Flege, J.; Sutter, E. Epitaxial Graphene on Ruthenium. *Nature Mater.* **2008**, *7*, 406–411.

18. Loginova, E.; Bartelt, N. C.; Feibelman, P. J.; McCarty, K. F. Evidence for Graphene Growth by C Cluster Attachment. *New J. Phys.* **2008**, *10,* 093026.

19. Loginova, E.; Bartelt, N. C.; Feibelman, P. J.; McCarty, K. F. Factors Influencing Graphene Growth on Metal Surfaces. *New J. Phys.* **2009**, *11,* 063046.

20. Odahara, G.; Otani, S.; Oshima, C.; Suzuki, M.; Yasue, T.; Koshikawa, T. *In situ* Observation of Graphene Growth on Ni(111). *Surf. Sci.* **2011**, *605,* 1095–1098.

21. Cui, Y.; Fu, Q.; Zhang, H.; Tan, D.; Bao, X. Dynamic Characterization of Graphene Growth and Etching by Oxygen on Ru(0001) by Photoemission Electron Microscopy. *J. Phys. Chem. C*. **2009**, *113,* 20365–20370.

22. Günther, S.; Dänhardt, S.; Wang, B.; Bocquet, M.-L.; Schmitt, S.; Wintterlin, J. Single Terrace Growth of Graphene on a Metal Surface. *Nano Lett.* **2011**, *11,* 1895–1900.

23. Dong,G. C.; Baarle, D. W.; Rost, M. J.; Frenken, J. W. M. Graphene Formation on Metal Surfaces Investigated by *In situ* Scanning Tunneling Microscopy. *New J. Phys.* **2012**, *14,* 053033.

24. Patera, L. Patera, L. L.; Africh, C.; Weatherup, R. S.; Blume, R.; Bhardwaj, S.; Castellarin-Cudia, C.; Knop-Gericke, A.; Schloegl, R.; Comelli, G.; Hofmann, S.; *et al.* In Situ Observations of the Atomistic Mechanisms of Ni Catalyzed Low Temperature Graphene Growth *ACS Nano*. **2013**, *7,* 7901–7912.

25. Kidambi, P. R.; Bayer, B. C.; Blume, R.; Wang, Z. J.; Baehtz, C.; Weatherup, R. S.; Willinger, M. G.; Schloegl, R.; Hofmann, S. Observing Graphene Grow: Catalyst–Graphene Interactions during Scalable Graphene Growth on Polycrystalline Copper. *Nano Lett.* **2013**, *13,* 4769–4778.

26. Wofford, J. M.; Nie, S.; McCarty, K. F.; Bartelt, N. C.; Dubon, O. D. Graphene Islands on Cu Foils: The Interplay between Shape, Orientation, and Defects. *Nano Lett.* **2010**, *10,* 4890–4896.

27. Nie, S.; Wofford, J. M.; Bartelt, N. C.; Dubon, O. D.; McCarty, K. F. Origin of the Mosaicity in Graphene Grown on Cu(111). *Phys. Rev. B* **2011**, *84*, 155425.

28. Takahashi K.; Yamada K.; Kato H.; Hibino H.; Homma Y. *In situ* Scanning Electron Microscopy of Graphene Growth on Polycrystalline Ni Substrate. Surf. Sci. **2012**, *606*, 728-732.

29. Kim, H.; Mattevi, C.; Calvo, M. R.; Oberg, J. C.; Artiglia, L.; Agnoli, S.; Hirjibehedin, C. F.; Chhowalla, M.; Saiz, E. Activation Energy Paths for Graphene Nucleation and Growth on Cu. *ACS Nano* **2012**, *6,* 3614–3623.

30. Celebi, K.; Cole, M. T.; Choi, J. W.; Wyczisk, F.; Legagneux, P.; Rupesinghe, N.; Robertson, J.; Teo, K. B. K.; Park, H. G. Evolutionary Kinetics of Graphene Formation on Copper. *Nano Lett.* **2013**, *13,* 967–974.

31. Seiler, H. Secondary Electron Emission in the Scanning Electron Microscope. *J. Appl. Phys*. **1983**, *54,* R1-R18.

32. Gartland, P. O.; Berge, S.; Slagsvold, B. J. Photoelectric Work Function of a Copper Single Crystal for the (100), (110), (111), and (112) Faces. *Phys. Rev. Lett.* **1972**, *28,* 738–739.

33. Kochat, V.; Pal, A. N.; Sneha, E. S.; Sampathkumar, A.; Gairola, A.; Shivashankar, S. A.; Raghavan, S.; Ghosh, A. High Contrast Imaging and Thickness Determination of Graphene with In-Column Secondary Electron Microscopy. *J. Appl. Phys.* **2011**, *110,* 014315.

34. Robinson Z. R.; Tyagi, P.; Murray, T. M.; Ventrice Jr., C. A. Substrate Grain Size and Orientation of Cu and Cu–Ni Foils used for the Growth of Graphene Films. *J. Vac. Sci. Technol.* **2012**, *30,* 011401.

35. Wood, J. D.; Schmucker, S. W.; Lyons, A. S.; Pop, E.; Lyding, J. W. Effects of Polycrystalline Cu Substrate on Graphene Growth by Chemical Vapor Deposition. *Nano Lett.* **2011,** *11,* 4547–4554.

36. Murdock, A. T.; Koos, A.; Ben Britton, T.; Houben, L.; Batten, T.; Zhang, T.; Wilkinson, A. J.; Dunin-Borkowski, R. E.; Lekka, C. E.; Grobert, N. Controlling the Orientation, Edge Geometry, and Thickness of Chemical Vapor Deposition Graphene. *ACS Nano* **2013**, *7*, 1351–1359.

37. Frenken, J. W. M.; Van der Veen, J. F. Observation of Surface Melting. *Phys. Rev. Lett.* **1985**, *54,* 134–137.

38. Chatterjee, B. Anisotropy of Melting for Cubic Metals. *Nature* **1978**, *275,* 203.

39. Vlassiouk, I.; Smirnov, S.; Regmi, M.; Surwade, S. P.; Srivastava, N.; Feenstra, R.; Eres, G.; Parish, C.; Lavrik, N.; Datskos, P.; *et al.* Graphene Nucleation Density on Copper: Fundamental Role of Background Pressure. *J. Phys. Chem. C*, **2013**, *117,* 18919–18926.

40. Ferrari, A. C.; Meyer, J. C.; Scardaci, V.; Casiraghi, C.; Lazzeri, M.; Mauri, F.; Piscanec, S.; Jiang, D.; Novoselov, K. S.; Roth, S.; *et al.* Raman Spectrum of Graphene and Graphene Layers. *Phys. Rev. Lett.* **2006**, *97,* 187401.

41. Graf, D.; Molitor, F.; Ensslin, K.; Stampfer, C.; Jungen, A.; Hierold, C.; Wirtz, L. Spatially Resolved Raman Spectroscopy of Single- and Few-Layer Graphene. *Nano Lett.* **2007**, *7,* 238–242.

42. Rasool, H. I.; Song, E. B.; Mecklenburg, M.; Regan, B. C.; Wang, K. L.; Weiller, B. H.; Gimzewski, J. K. Atomic-Scale Characterization of Graphene Grown on Copper (100) Single Crystals. *J. Am. Chem. Soc.* **2011**, *133,* 12536–12543.

43. Luo, Z.; Kim, S.; Kawamoto, N.; Rappe, A. M.; Johnson, A. T. C. Growth Mechanism of Hexagonal-Shape Graphene Flakes with Zigzag Edges. *ACS Nano* **2011**, *5,* 9154–9160.

44. Artyukhov, V. I.; Liua, Y.; Yakobson, B. I. Equilibrium at the Edge and Atomistic Mechanisms of Graphene Growth. *PNAS.* **2012**, *109,* 15136–15140.

45. Venables, J. A.; Spiller D. T.; Hanbücken, M. Nucleation and Growth of Thin Films. *Rep. Prog. Phys.* **1984**, *47,* 399–459.

46. Reichelt, K. Nucleation and Growth of Thin Films. *Vacuum* **1988**, *38,* 1083–1099.

47. Meca, E.; Lowengrub, J.; Kim, H.; Mattevi, C.; Shenoy, V. B. Epitaxial Graphene Growth and Shape Dynamics on Copper: Phase-Field Modeling and Experiments. *Nano Lett.* **2013**, *13,* 5692–5697.

48. Eres, G.; Regmi, M.; Rouleau, C. M.; Chen, J. H.; Ivanov, I. N.; Puretzky, A. A.; Geohegare, D. B. Cooperative Island Growth of Large-Area Single-Crystal Graphene on Copper Using Chemical Vapor Deposition. *ACS Nano.* **2014**, *8,* 5657–566.

49. Li, X. S.; Magnuson, C. W.; Venugopal, A.; An, J. H.; Suk, J. W.; Han, B. Y.; Borysiak, M.; Cai, W. W.; Velamakanni, A.; Zhu, Y. W. Graphene Films with Large Domain Size by a Two-Step Chemical Vapor Deposition Process. *Nano Lett.* **2010**, *10,* 4328–4334.

50. Mei, S. Q.; Lu, K. Melting and Superheating of Crystalline Solids: From Bulk to Nanocrystals. *Prog. Mater. Sci.* **2007**, *52,* 1175–1262.

51. Polčik, M., Wilde, L.; Haase, J. Partial Order of the Quasiliquid During Surface Melting of Al (110). *Phys. Rev. Lett.* **1997**, *78,* 491–494.

52. Häkkinen, H.; M. Manninen Computer Simulation of Disordering and Premelting of Low-Index Faces of Copper. *Phys. Rev. B* **1992**, *46,* 1725–1742.

53. Gao, L., Guest, J. R.; Guisinger, N. P. Epitaxial Graphene on Cu(111). *Nano Lett.* **2010**, *10,* 3512–3516.

54. Geng, D. C.; Wu, B.; Guo, Y. L.; Huang, L. P.; Xue, Y. Z.; Chen, J. Y.; Yu, G.; Jiang, L.; Hu, W. P.; Liu, Y. Q. Uniform Hexagonal Graphene Flakes and Films Grown on Liquid Copper Surface. *PNAS*. **2012**, *109,* 7992–7996.

55. DiMasi, E.; Tostmann, H.; Shpyrko, O. G.; Deutsch, M.; Pershan, P. S.; Ocko, B. M. Surface-Induced Order in Liquid Metals and Binary Alloys. *J. Phys.: Condens. Matter* **2000**, *12,* A209–A214.

56. Sidorenko, V. M.; Sidorak, I. I. Boundary and Volume Diffusion of Hydrogen in Copper, Nickel, and Iron. *Mater. Sci.* **1973**, *9,* 372–375.

57. Kim, D. W.; Lee J.; Kim S. J.; Jeon S.; Jung H.T. The Effects of the Crystalline Orientation of Cu Comains on the Formation of Nanoripple Arrays in CVD-Grown Graphene on Cu. *J. Mater. Chem. C,* **2013**, *1*, 7819-7824.

58. Rasool, H. I.; Song E. B.; Allen M. J.; Wassei J. K.; Kaner R. B.; Wang K. L.; Weiller B. H.; Gimzewski J. K. Continuity of Graphene on Polycrystalline Copper. *Nano Lett*. **11,** 251–256 (2011)

59. Paronyan, T. M.; Pigos E. M.; Chen G.; Harutyunyan A. R. Formation of Ripples in Graphene as a Result of Interfacial Instabilities. ACS Nano **2011**, *5*, 12, 9619-9627.

60. Mi, X.; Meunier, V.; Koratkar, N.; Shi, Y. Facet-Insensitive Graphene Growth on Copper. *Phys. Rev. B*. **2012**, *85*, 155436.

61. Wilson, N. R.; Marsden, A. J.; Saghir, M.; Bromley, C. J.; Schaub, R.; Costantini, G.; White, T. W.; Partridge, C.; Barinov, A.; Dudin, P. Weak Mismatch Epitaxy and Structural Feedback in Graphene Growth on Copper Foil. *Nano. Res.* **2013**, *6*, 99–112.

62. Tian, J.; Cao, H.; Wu, W.; Yu, Q.; Guisinger, N. P.; Chen, Y. P. Graphene Induced Surface Reconstruction of Cu. *Nano Lett.* **2012**, *12,* 3893–3899.

63. Guillemot, L.; Bobrov, K. Morphological Instability of the Cu(110)–(2×1)–O Surface under Thermal Annealing. *Phys. Rev. B* **2011**, *83*, 075409.

64. Sotto, M. Oxygen Induced Reconstruction of (h11) and (100) Faces of Copper. *Surf. Sci.* **1992**, *260*, 235–244.

65. Böttger, I.; Schedel-Niedrig, T.; Timpe, O.; Gottschall, R.; Havecker, M.; Ressler, T.; Schlogl, R. Catalytic Methanol Oxidation over Copper: Observation of Reaction-Induced Nanoscale Restructuring by Means of In Situ Time-Resolved X-ray Absorption Spectroscopy. *Chem. Eur. J.* **2000**, *6*, 10, 1870–1876.

66. Schedel-Niedrig, T.; Neisius, T.; Bottger, N.; Kitzelmann, E.; Weinberg, G.; Demuth, D.; Schlogl, R. Copper (sub)Oxide Formation: a Surface Sensitive Characterization of Model Catalysts. *Phys. Chem. Chem. Phys.* **2000**, *2,* 2407–2417.

67. Bernard, L. S.; Spina, M.; Jacimovic, J.; Ribic, P. R.; Walter, A.; Oberli, D. Y.; Horvath, E.; Forro, L.; Magrez, A. Functionalized Graphene Grown by Oxidative Dehydrogenation Chemistry. *Carbon* **2014**, *71*, 11–19.

68. Robinson, Z. R.; Ong E. W.; Mowll, T. R.; Tyagi P.; Gaskill D. K.; Geisler H.; Ventrice C. A. Influence of Chemisorbed Oxygen on the Growth of Graphene on Cu(100) by Chemical Vapor Deposition. *J. Phys. Chem. C* **2013**, *117*, 23919 – 23927

69. Au C. T.; Roberts M. W. Photoelectron Spectroscopic Evidence for the Activation of Adsorbate Bonds by Chemisorbed Oxygen. *Chem. Phys. Lett.* **1980**, *74*, 472-474

70. Alstrup, I.; Chorkendorff I.; Ullmann S. The Interaction of CH, at High Temperatures with Clean and Oxygen Precovered Cu(100), *Surf. Sci.* **1992**, *264*, 95−102

71. Neumann, J. P.; Zhong, T.; Chang, Y. A. The Cu−O (Copper-Oxygen) System. *Bull. Alloy Phase Diagr.* **1984**, *5*, 136–140.

72. Reinecke, N.; Taglauer, E. The Kinetics of Oxygen-Induced Faceting of Cu (115) and Cu (119) Surfaces. *Surf. Sci.* **2000**, *454–456*, 94–100.

73. Simmons, G. W.; Mitchell, D. G.; Lawless, K. R. LEED and HEED Studies of the Interaction of Oxygen with Single Crystal Surfaces of Copper. *Surf. Sci.* **1967**, *8*, 130–164.

74. Boulliard, J. C.; Domange, J. L.; Sotto, M. Structural Changes of Vicinal Copper Surfaces Induced by Oxygen Adsorption. *Surf. Sci.* **1986**, *165*, 434–446.

6. Graphene growth on platinum:

6.1. General

The catalytic growth of graphene on metal surface by chemical vapour deposition (CVD) has emerged as the most versatile and commercially viable technique for manufacturing continuous films to meet the industrial demand for electronic-grade material.[1-6] Among the various catalysts that are used for this process, Pt offers a quite large parameter space for SLG/FLG growth and a much higher catalytic activity for hydrocarbon dissociation. Indeed, the undesired formation of carbon sheets on Pt was a topic of early hydrocarbon catalysis studies, which were aimed on reducing carbon coking of the active phase.[7] Besides the high activity for hydrocarbon dissociation, Pt also exhibits a relatively weak metal-graphene interaction.[8] As a consequence, the synthesized SLG/FLG can be peeled from the Pt surface and transferred onto other substrates without being damaged.[2,8-10] Thus, Pt is considered as ideal catalyst for graphene growth.[11] Here, I briefly summarize graphene CVD formation on Pt from surface cleaning to graphene growth.

1. **Annealing and surface cleaning**

The polycrystalline Pt substrate is first annealed in H_2 (25 Pa) to promote surface grain growth and remove adventitious carbon from the surface. (see **Figure 6−1**) Surface carbon can be completely removed at 910°C. However, there is still carbon in the bulk. In order to effectively clearing dissolved carbon from Pt bulk during annealing, O_2 is co-dosed with H_2 into chamber under a ratio of flow 2sccm: 8sccm at 30-35 Pa until no more carbon appear. We note after dose O_2 into chamber, the carbon continuously comes out from bulk and surface grain boundary. This phenomenon is because that chemical potential of carbon is decreased from surface and then lead to carbon diffuses from bulk to surface. We note a large amount of carbon exudes from grain boundary. (see **Figure 6−2**) This is mainly because grain boundary serves as a more-rapid pathway for carbon diffusing to the surface.[12]

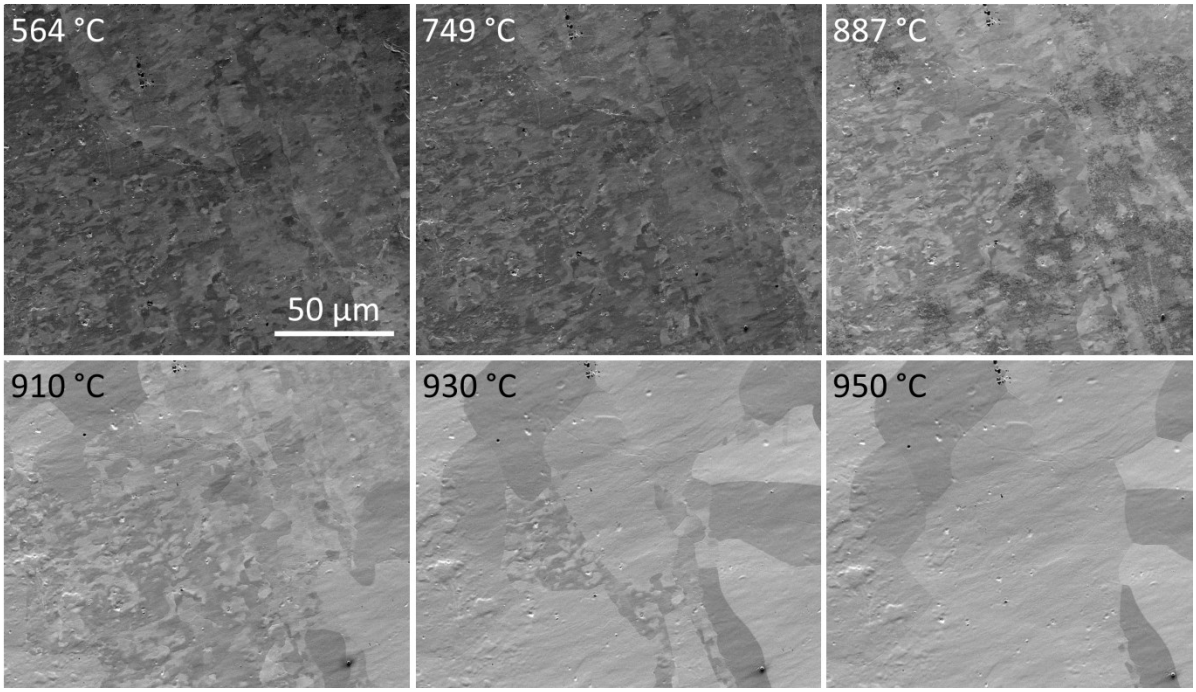

Figure 6−1. Surface grain modifications during an annealing process.

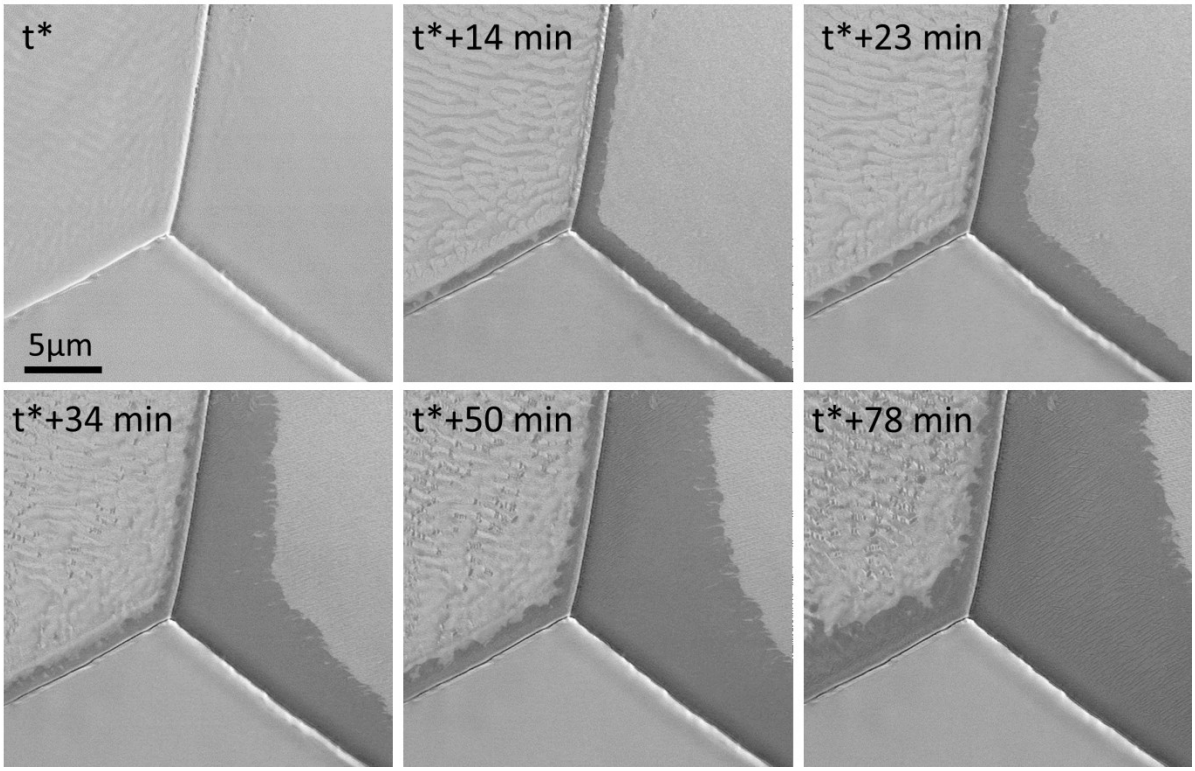

Figure 6−2. Pt surface clean can be seen in snapshots taken during an annealing process at 900°C under H_2 + O_2 (8:2) 35 Pa. Note surface carbon (characterized by darker contrast) comes out from grain boundary and spread to grain face. t* corresponds to the start time of dosing O_2 into the chamber.

2. Graphene growth on Pt.

Due to higher catalytic activity for hydrocarbon dissociation, compared with the Cu and Ni, graphene easily achieved on Pt. At same condition which we grown graphene on Cu (1000°C, 4sccm H_2, 0.1sccm C_2H_4, $4.2 \cdot 10^{-2}$ Pa), induction period before graphene formation on Pt is obviously shorter than growth on Cu. A series of SEM images capturing the appearance and growth of graphene on Pt is presented in **Figure 6−3**. At same condition, formation of graphene on Cu can be observed after an induction period of around 10 min. However, induction period of graphene nucleation on Pt is within 15 s. After the first graphene domain appears, the nucleation of other domains occurs within a relatively short time frame (<60 s). The first nuclei typically form near the centre of a Pt grain away from grain boundaries, and the nucleation density is also observed to be lower close to Pt grain boundaries (see, for example, **Figure 6−3b**). **Figure 6−4** shows plots the areal graphene coverage, A, with time *t* for the entire grain (indicated by the red polygon in **Figure 6−3a**) and for a region close to the centre of the Pt grain (green square in **Figure 6−3b**).

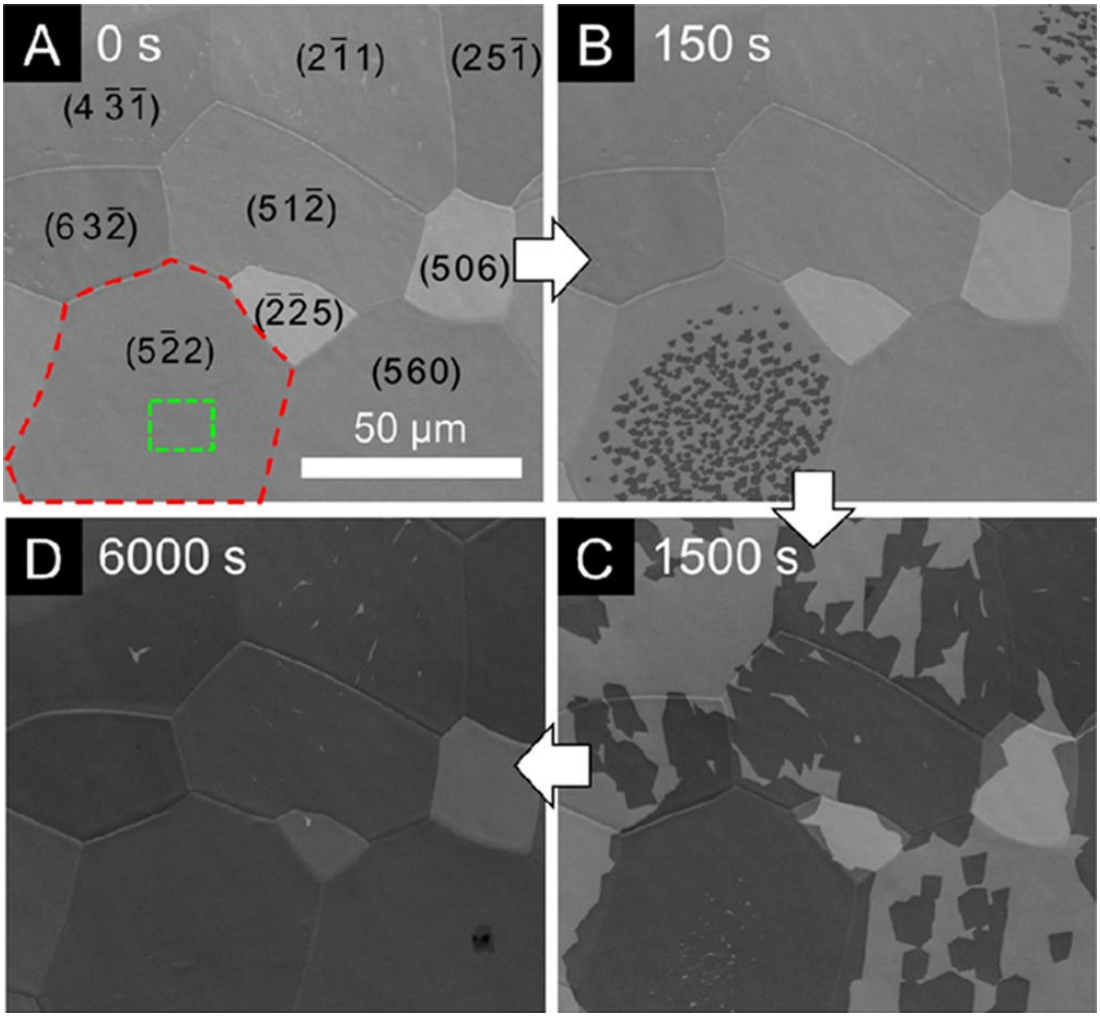

Figure 6−3. Graphene growth evolution on polycrystalline Pt. (A−D) Sequence of in situ SEM images of Pt (25 μm) during C_2H_4 (~10^{-2} Pa) exposure at 900 °C, acquired 0 s (A), 150 s (B), 1500 s (C), or 6000 s (D) after precursor introduction. The approximate orientations of the Pt grains determined by EBSD analysis are indicated within the respective grains in (A).

We note the induction period of different Pt grains vary widely, with graphene domains nucleating on several grains within 90 s of the precursor being introduced, while others show no nucleation events even after >2500 s and only become covered with graphene due to the expansion of domains from adjacent Pt grains across grain boundaries (see **Figure 6−3d**). Furthermore, direct observation reveal that the shape of graphene domain formed on polycrystalline foils is intimately related to that of the underlying surface structure. This phenomenon is attributable to grain orientation dependent variations in the precursor dissociation rate, graphene nucleation barrier, or both, which are likely to be affected by the

density of low coordination sites such as step edges.[13] **Figure 6−4** shows formation of graphene is faster than Cu at same growth condition. We do not obvious the obvious mutual influence between growing flakes on Pt. Graphene flakes easily coalesce along growth propagation direction. (see **Figure 6−5a**) We note approaching rate of neighbouring domains growth front keep constant. (see **Figure 6−5b**) On the contrary, in case of Cu, a capture zone build up at the growth front and induce growing sheets generally do not merge. [14] Moreover, graphene domain growth rate is constant and shape of graphene can be maintained in regular polygon during whole growth process. The evolution of the perimeter and area of the graphene islands during growing is plotted in **Figure 6−5b**. The excellent linear fit for the perimeter and corresponding quadratic fit for the area is consistent with an attachment-limited expansion process, and further prove Pt is better catalyst for graphene growth than Cu.

3. Adlayer graphene growth

Due to the high activity of Pt, the formation of graphene even can happen under highly diluted hydrocarbon/hydrogen ratios of 4/700.[2] The growth of purely single layer graphene appears impossible. Thus, to understand how adlayer form on polycrystalline catalysts and stack sequence of interlayer is very important information for optimizing the growth of graphene.

Above three points raise three issues which are key factors for high quality graphene growth on Pt: 1. Annealing is crucial step to clean dissolved carbon from Pt bulk for graphene growth. 2. Stacking sequence of FLG on Pt need to be understood. 3. The detail of single layer and adlayer graphene growth behaviour on Pt. These questions will be discussed in following chapters.

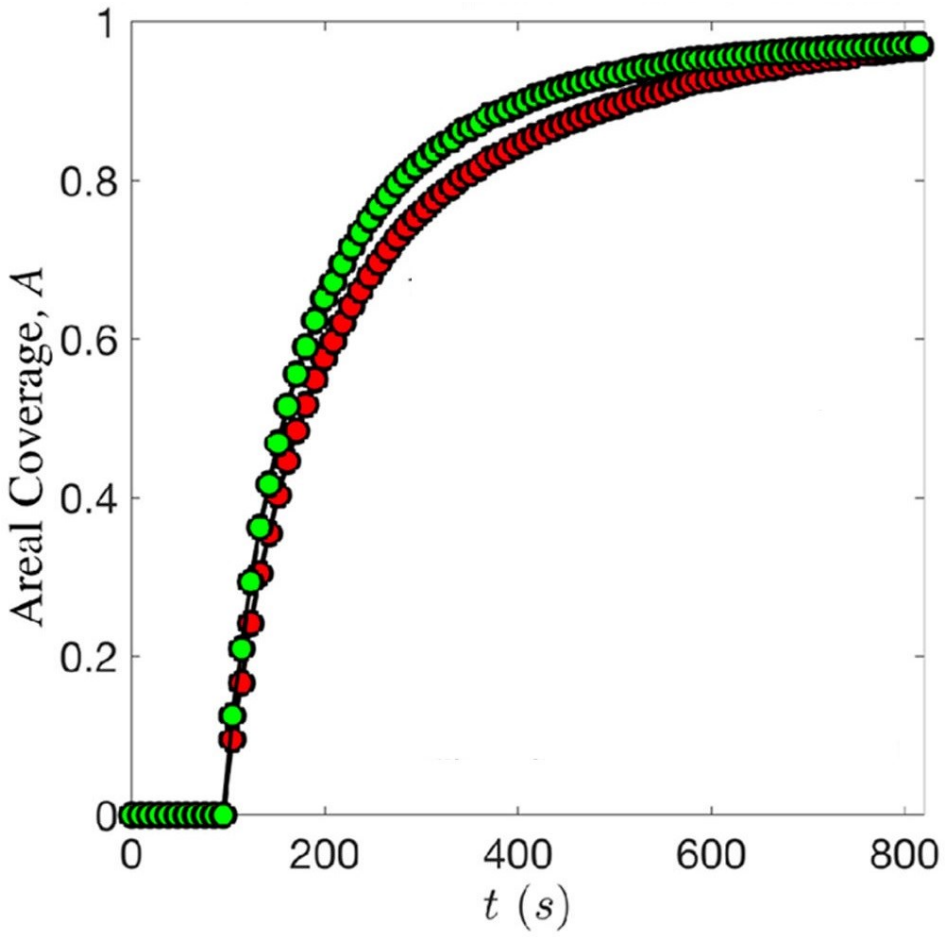

Figure 6−4. Plot of the areal coverage of graphene A with C_2H_4 exposure time *t* for the regions marked with red and green boxes in Figure 6−1 (A).

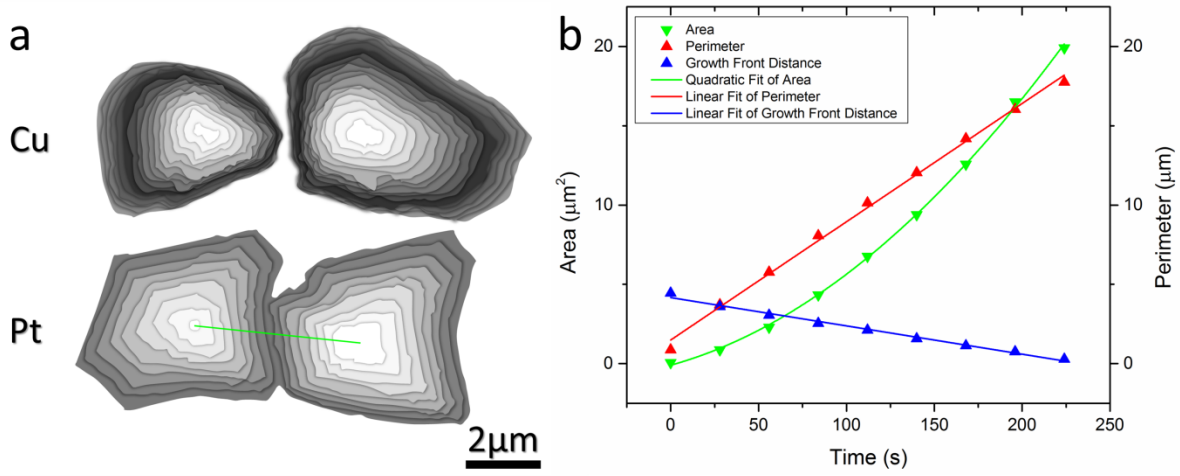

Figure 6−5. (a) Superposition capturing the areal growth of flakes at different times shows graphene expansion behaviours on Cu and Pt. Experiment condition: 1000°C, 4sccm H_2, 0.1sccm C_2H_4, $4.2 \cdot 10^{-2}$ Pa. (interval time 36s) (b) Evolution of perimeter and area of the graphene domain (left island) on Pt shown in (a) with growth time. Note approaching rate of neighbouring domains growth front keep constant on Pt. (Blue line in b)

6.2.References

1. Hao, Y. F.; Bharathi, M. S.; Wang, L.; Liu, Y. Y.; Chen, H.; Nie, S.; Wang, X. H.; Chou, H.; Tan, C.; Fallahazad, B.; Ramanarayan, H.; Magnuson, C. W.; Tutuc, E.; Yakobson, B. I.; McCarty, K. F.; Zhang, Y. W.; Kim, P.; Hone, J.; Colombo, L.; Ruoff, R. S. *Science* **2013**, *342*, 720.

2. Gao, L. B.; Ren, W. C.; Xu, H. L.; Jin, L.; Wang, Z. X.; Ma, T.; Ma, L. P.; Zhang, Z. Y.; Fu, Q.; Peng, L. M.; Bao, X. H.; Cheng, H. M. *Nat. Commun.* **2012**, *3*, 7.

3. Chen, S. S.; Ji, H. X.; Chou, H.; Li, Q. Y.; Li, H. Y.; Suk, J. W.; Piner, R.; Liao, L.; Cai, W. W.; Ruoff, R. S. *Advanced Materials* **2013**, *25*, 2062.

4. Sutter, P. W.; Flege, J. I.; Sutter, E. A. *Nat. Mater.* **2008**, *7*, 406.

5. Pan, Y.; Zhang, H. G.; Shi, D. X.; Sun, J. T.; Du, S. X.; Liu, F.; Gao, H. J. *Advanced Materials* **2009**, *21*, 2777.

6. Iwasaki, T.; Park, H. J.; Konuma, M.; Lee, D. S.; Smet, J. H.; Starke, U. *Nano Letters* **2011**, *11*, 79.

7. Lang, B. *Surf. Sci.* **1975**, *53*, 317.

8. Preobrajenski, A. B.; Ng, M. L.; Vinogradov, A. S.; Martensson, N. *Phys. Rev. B* **2008**, *78*, 4.

9. Sutter, P.; Sadowski, J. T.; Sutter, E. *Phys. Rev. B* **2009**, *80*, 10.

10. Khomyakov, P. A.; Giovannetti, G.; Rusu, P. C.; Brocks, G.; van den Brink, J.; Kelly, P. J. *Phys. Rev. B* **2009**, *79*, 12.

11. Ma, T.; Ren, W.; Liu, Z.; Huang, L.; Ma, L.-P.; Ma, X.; Zhang, Z.; Peng, L.-M.; Cheng, H.-M. *Acs Nano* **2014**, *8*, 12806.

12. Weatherup, R. S.; Shahan, A. J.; Wang, Z. J.; Mingard, K.; Pollard, A. J.; Willinger, M. G.; Schloegl, R.; Voorhees, P. W.; Hofmann, S. *Nano Letters* **2016**, *16*, 6196.

13. Meca, E.; Lowengrub, J.; Kim, H.; Mattevi, C.; Shenoy, V. B. *Nano Letters* **2013**, *13*, 5692.

14. Wang, Z.-J.; Weinberg, G.; Zhang, Q.; Lunkenbein, T.; Klein-Hoffmann, A.; Kurnatowska, M.; Plodinec, M.; Li, Q.; Chi, L.; Schloegl, R.; Willinger, M.-G. *ACS nano* **2015**, *9*, 1506.

7. Stacking sequence and interlayer coupling in few layer graphene by *in situ* imaging

7.1.Abstract

In the transition from graphene to graphite, the addition of each individual layer of graphene modifies the electronic structure and produces a different material with unique properties. Controlled preparation of few-layer graphene is therefore of great interest. Currently, the growth of bilayer and trilayer graphene is performed by trial-and-error methods. In this chapter we combine growth and isothermal etching experiments with *in situ* imaging by scanning electron microscopy to probe the stacking sequence and interlayer coupling strength. Real-time imaging during chemical vapour deposition growth and hydrogen etching conditions allows differentiating between graphene layers forming above or below an already grown layer. The observation of layer-dependent etching rates facilitates the determination of the relative strength of the graphene-graphene and graphene-substrate interaction. Anisotropic etching rates extracted from evolution of the shape of islands and vacancy islands (holes) indicate strong interaction of graphene edges with Pt step edges. We use scanning tunnelling microscopy imaging and density functional theory calculations to confirm strong coupling of the edge atoms of graphene with the Pt substrate, and reproduce the observed shape evolution of islands and vacancy islands during etching by kinetic Wulff constructions. We demonstrate that real-time imaging under controlled atmosphere by *in situ* SEM is a powerful method for designing synthesis protocols for sp^2 carbon nanostructures in between graphene and graphite.

7.2.Introduction

Engineering a band gap without degrading electron mobility is the key to making graphene into a practical electronic material. The two main strategies for opening up a bandgap in graphene rely on size and shape-dependent quantum confinement and charge transfer density modulation. In practice, various approaches such as patterning of graphene nanoribbons (GNR),[1-3] chemical doping or physisorption of various molecules,[3,4] applying uniaxial tensile

strain,[5] or binding the graphene onto substrates,[5,6] have been used to implement these strategies. However, they all compromise the intrinsic properties of graphene either by disturbing the π electrons or by introducing boundaries and defects. In the case of hydrogen plasma etching, incomplete understanding of the underlying reaction mechanisms limits its application to a trial-and-error approach in which the production of well-defined graphene edge structures without disturbance of the basal plane remains an unsolved problem. A control of the electronic states in graphene is also possible by taking advantage of interlayer interactions. Indeed, ordered structures consisting of two or more layers of graphene represent a broad class of materials where the electronic structure and properties uniquely change with each additional layer.[7-10] The coupling between graphene layers and their interaction with the substrate induces charge transfer density modulations. Although the cohesive interaction between graphene sheets is a relatively old topic that has been studied for more than 50 years,[11-14] there remains a lack of experimental data regarding the effect of the substrate on the coupling between few-layer graphene (FLG). Bi-layer graphene (BLG) is of great technological interest because the presence of the second layer creates a semiconductor with a band gap that can be tuned by gating. In contrast, tri-layer graphene (TLG) is a semimetal where gating can be used to change the conductivity. In principle, FLG allows maintaining high electron mobility with only minimal disturbance of the π electron dispersion and without the formation of new boundaries.[7-10]

The growth of BLG and FLG has been achieved on a variety of metal surfaces including Ni, Ni-Cu alloy, Cu, Ru, Ir and Pt catalysts.[15-20] The electronic properties of the FLG structures vary as a function of interlayer spacing, twist angle, and stacking order. Well-known examples of stable staking orders (polytypes) that have distinct electronic properties are the Bernal (AB), and the rhombohedral (ABC) stacking. The formation of a particular stacking order is known to be strongly influenced by the synthesis method and substrate type.[21,22] Specifically, the stacking order can be affected by the vertical stacking sequence of adlayer graphene (ALG). The two vertical stacking sequences in FLG are generally discriminated in the graphene literature as wedding cake (WC) and inverted wedding cake (IWC) models, indicating that the ALG forms either above or inserts below an already grown layer.[23] For substrates that are characterized by a low carbon-solubility and weak graphene-substrate interaction, such as Cu, the stacking sequence of ALG was confirmed to be IWC by isotope labelling and Raman measurements.[24] However, for catalysts that are characterized by higher

carbon solubility than Cu such as Ir, Pt, Rh, Ni, Co and Ru, the stacking sequence is harder to determine unambiguously. Indeed, the ALG can form either by surface in-plane feeding or by carbon segregation from the bulk of the substrate during cooling.[20] In the case of Ru, Sutter *et al.* described the stacking order by the WC model on the basis of combined *in situ* low-energy electron microscopy (LEEM) and charge transport measurements.[19] In contrast, Sun *et al.* using post-growth scanning electron microscopy (SEM) imaging found that multilayer growth on Pt is dominated by carbon precipitation below already formed layers.[25] Real-time imaging is a powerful tool for studying growth kinetics because it enables extracting quantitative data from the changes of the shape and size of graphene islands during their evolution in response to externally controlled environments. In a recent report we demonstrated the effectiveness of *in situ* environmental SEM (ESEM) for studying the mechanistic details of graphene chemical vapour deposition (CVD) on Cu.[26]

In this chapter we take real-time imaging one step further by monitoring isothermal etching of graphene layers on polycrystalline Pt foils to probe the interlayer coupling and reveal the stacking sequence in FLG. We show that etching rates are proportional to the relative coupling strength and that the interaction between two neighbouring graphene layers is significantly weaker than the interaction of SLG with the Pt surface. The observed anisotropic etching behaviour is analysed and related to the interaction of graphene edge atoms with Pt step-edges. Finally, the interpretation of the dynamic data is complemented by post-growth characterization using micro-Raman spectroscopy, scanning probe microscopies (AFM and STM), high-resolution transmission electron microscopy, and theoretical calculations. The ability to probe the interlayer interactions in graphene is important for developing key processing steps such as selecting the ideal substrate for facilitating SLG transfer and the tuning of the properties of FLG by controlling the sequencing of ALG stacking and the number of layers. The broader significance of this work is in demonstrating that etching in combination with direct imaging of in-plane dynamics in response to well controlled experimental environments is a facile approach for deriving information about interlayer coupling that governs the vertical stacking behaviour of 2D materials.

7.3. Results and discussion

7.3.1. Growth and characterization of few layer graphene

The growth and etching of graphene were both performed in the chamber of an ESEM. The ESEM enables real-time imaging of the shape and size evolution of graphene islands in relation to the Pt grain structure and surface features. Observations can be performed as a function of the background atmosphere and temperature during both, growth and etching of graphene.[26] FLG was grown by isothermal CVD using ethene (C_2H_4). After initial growth of FLG islands in a C_2H_4/H_2 atmosphere, the C_2H_4 flow was turned off to perform isothermal etching in pure H_2 at a total pressure of 25 Pa (for experimental details see 7.5. Methods section). We attribute the etching to carbon bond breaking by atomic hydrogen that is produced by dissociation of H_2 on a Pt surface that is known to be a highly efficient catalyst for promoting H_2 dissociation.[27] Post-growth characterization by Raman, STM and high-resolution transmission electron microscopy was used to confirm the high quality of the investigated graphene (**Figure 7─1**).

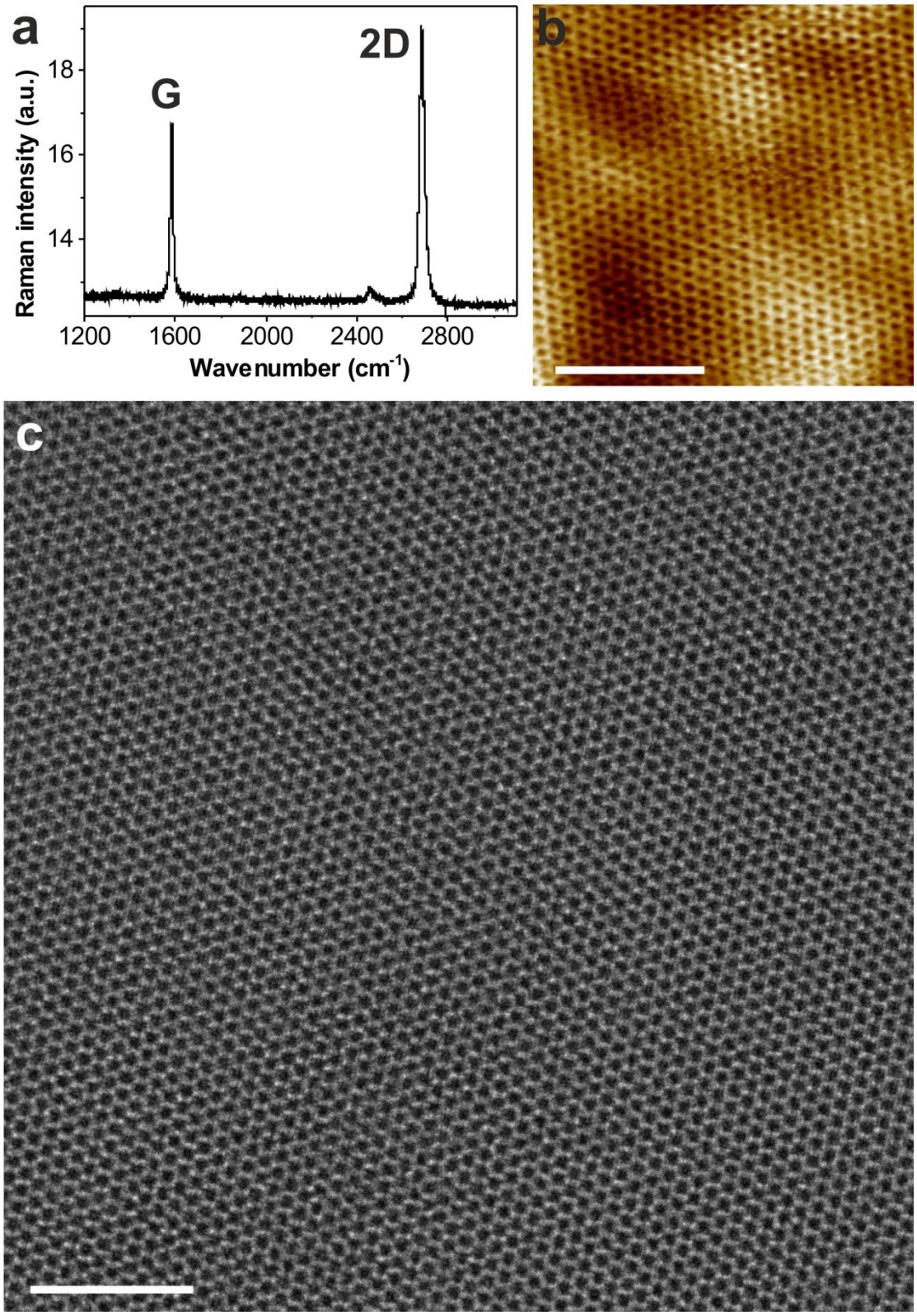

Figure 7—1. Post growth characterization of graphene sheets. a, The Raman spectrum of graphene grown on Pt shows the characteristic G and 2D peaks of single layer graphene. b, STM image showing the carbon honeycomb lattice with no defects. c shows an unprocessed high-resolution TEM image of the

obtained graphene after transfer, without any additional cleaning steps. The scale bar in (c) measures 5 nm.

The key for probing the dynamics of ALG during both growth and etching is the ability to differentiate individual layers stacked on top of each other (see online Movie 1). A wide contrast range is provided by the secondary electron signal, which is sensitive to changes in the surface charge state, electronic structure, work function and variations in secondary electron yield.[28] The *in situ* SEM image in **Fig. 7—2a** and the plot in **Fig. 7—2b** illustrate the stepwise variation of the contrast that allows identification of up to 9 individual graphene layers, starting with the brightest first layer in contact with the substrate.[29] In addition, the *in situ* SEM images of edge misalignment between mutual layers and individual sheets provide real-time information on the evolution of the rotation angle between growing layers and formation of the stacking order.[30] **Fig. 7—2c** illustrates a 30°-30° rotation between successive layers and **Fig. 7—2d** shows ABA or ABC stacked graphene with a hexagonal shape distorted by strong interaction with Pt step edges on the left.

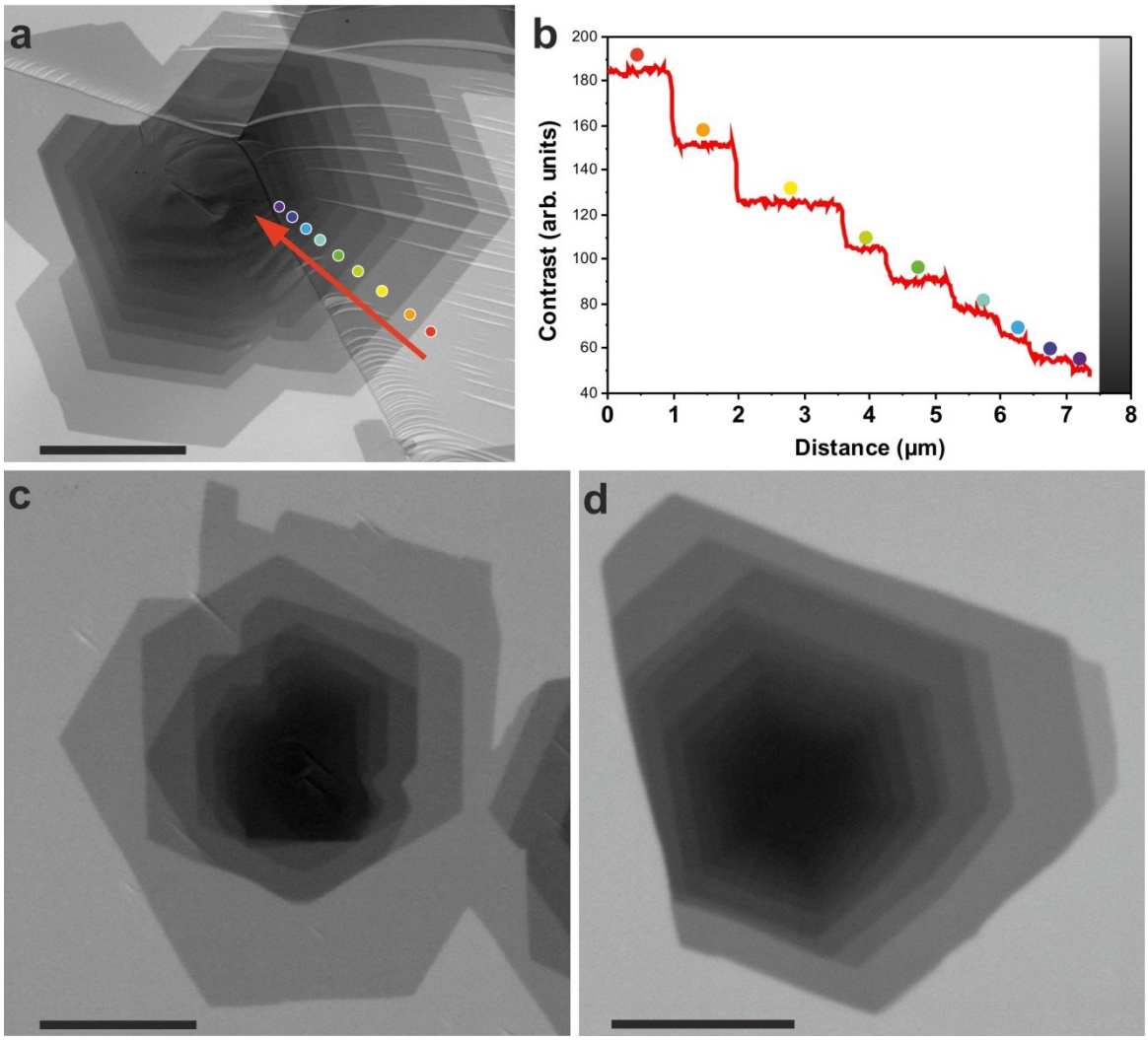

Figure 7—2 Real-time characterization of graphene sheets. a, b, The ESEM image (a)) shows a few-layer graphene stack. Along the red arrow, the brightness in the SE image changes with each additional layer. (b), Line plot showing the change in contrast along the red arrow in (a). Up to 9 layers can be distinguished within the contrast range. The different coloured dots along the arrow are intended to assist the assignment between layer number and grey value. Note that the lightest shade marked by a red dot corresponds to Pt covered by SLG. c, Vertical layer stacking showing a 30° rotation between successive layers. d, Hexagonal shape distorted by interaction with the Pt surface in ABA or ABC stacked FLG. Scale bars in (a), (c), and (d) measure 5 µm, 2 µm and 2 µm, respectively.

7.3.2. Real-time characterization of few layer graphene etching

The shape evolution of single, bi- and tri-layer graphene during hydrogen etching is illustrated in **Fig. 7—3** planes a-d were recorded *in situ* at 900°C in an atmosphere of 25 Pa hydrogen. Designated areas in **Fig. 7—3a** are replotted and compared directly in **Fig. 7—3e**. The time-dependent evolution of the shape and size of the topmost graphene layers in BLG

and TLG during etching is illustrated by colour coded plots and compared to etching of SLG in **Fig. 7─3e**. Individual shapes were extracted from frames of the *in situ* SEM movie provided as Online Movie 2. It is important to note that the etching process is limited to the island edges, while the basal planes remain intact. Indeed, except for the very beginning of the etching process, where some holes appear at grain boundaries, no etching pits appear even after etching for more than 6000s (see **Fig. 7─3 a-d**). This behaviour implies that pure hydrogen etching is less aggressive and more controllable than plasma-assisted hydrogen etching, and that the graphene is of high quality. It can be seen that etching takes place simultaneously at the periphery of each individual layer, indicating that graphene edges in a vertical stack are equally exposed to the reactive hydrogen atmosphere. Also, the out diffusion of etching products from graphene edges in each layer to the surrounding atmosphere is not hindered by the presence of other layers. Thus, the etching behaviour indicates the absence of buried layers. Smaller sheets therefore grow on top of larger ones, indicating that isothermal CVD growth of FLG on Pt substrates follows the WC type stacking. During etching, the smallest topmost layer is the first to disappear in each stack. Hence, in TLG the third layer, and in BLG the second layer are first to disappear, illustrating that removal of layers can proceed in a layer-by-layer fashion.

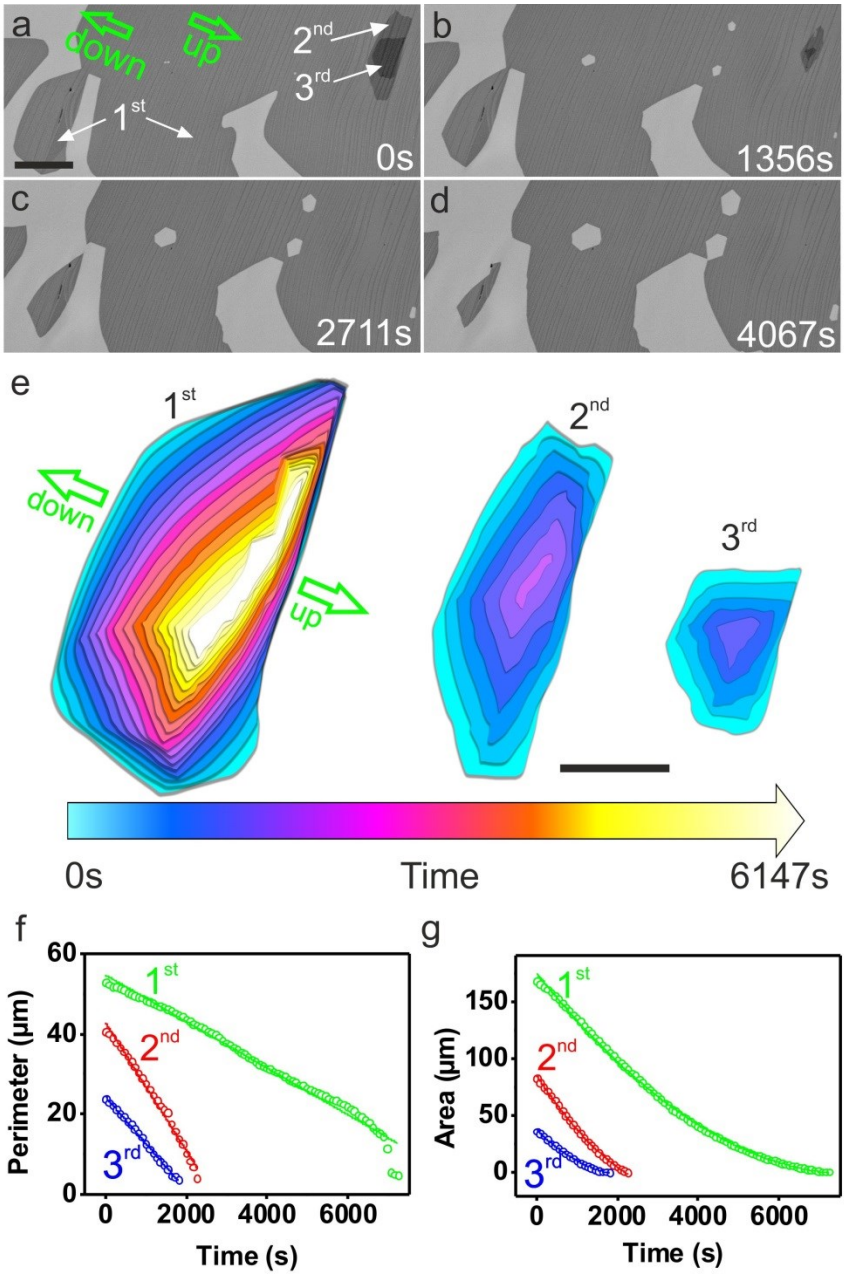

Figure 7–3. Evolution of isothermal CVD grown graphene layers during H_2 etching. a,-d, Time-lapse image series showing the etching of SLG and the topmost layers in BLG and TLG. e, Shape evolution of the respective layers during etching, reproduced as color coded superposition of outlines that were abstracted from images recorded at 3600 s intervals (see online Movie 2). f, Evolution of the perimeters of the first, second and third layer in (a) with corresponding linear fits. g, Evolution of the area of the 1st, 2nd and 3rd layers in (a) with corresponding quadratic fits. The green arrows in (a) and (e) indicate the up-step and down-step directions of Pt terraces. The scale bars in (a) and (e) measure 10 µm and 5 µm, respectively.

The evolution of the perimeter and area of the graphene islands during H_2 etching at 900 °C is plotted in **Figures 7—3 f** and **g**. The excellent linear fit for the perimeter and corresponding quadratic fit for the area is consistent with a detachment-limited etching process following 1st order kinetics.[31] The line slopes in **Fig. 7—3f** correspond to the averaged radial etching rates of the respective layers in **(a)**. They are -5.84 nm·s^{-1} for the 1st, -16.01 nm·s^{-1} for the 2nd and -11.76 nm·s^{-1} for the 3rd layer and are thus different for different layers. With respect to the 1st layer, the etching speed of the 2nd layer is higher by a factor of 2.74 and the one of the 3rd layers by a factor of about 2. This implies different graphene-edge configurations and indicates a WC like stacking. Indeed, in a WC configuration, graphene edge atoms are in direct contact with the Pt substrate only in the case of the 1st layer, while edge atoms of adlayers are located on top of a graphene sheet and are most likely hydrogen terminated.

Under the assumption that the removal of carbon atoms from the perimeter of a graphene sheet can be described by an Arrhenius-type rate $r \sim exp\ (-E_a/k_BT)$, it should be possible to estimate the relative strength of the graphene interlayer coupling.

$$r \sim \exp\left(-\frac{E_a}{k_B T}\right) = \exp\left(-\frac{E_{C-C}+E_{Coupling}+unspecified\ contributions}{k_B T}\right) \qquad (1)$$

The apparent activation energy E_a that is required for removing an edge atom by hydrogen etching contains several contributions. Amongst them, in-plane carbon-carbon bond breaking ($E_{C\text{-}C}$) contributes the largest portion. However, there are also small contributions due to interlayer interactions between edge atoms and the graphene sheet underneath ($E_{Coupling}$). Since edge atoms in the 2nd and 3rd layer are located on top of a graphene sheet in the WC configuration, they face a similar local environment and are exposed to the same hydrogen-rich atmosphere during etching. Thus, the product of the etching process should be the same for both layers. Differences in the activation energy might therefore give a hint on differences in the interlayer coupling strength. By forming the ratio between the experimental etching rates of the 2nd and 3rd layer using eq. (1), identical contributions to the activation energy, which are related to in-plane carbon-carbon bond breaking ($E_{C\text{-}C}$ + *unspecified contributions*) should cancel out, leaving only terms due to different interlayer coupling:

$$E_{(\text{Coupling}-3\text{rd}-2\text{nd})} - E_{(\text{Coupling}-2\text{nd}-1\text{st})} = k_B T \cdot \ln\left(\frac{r_{2\text{nd}}}{r_{3\text{rd}}}\right) \quad (2)$$

Using the experimentally determined etching rates for the 2nd and 3rd layer that are provided in the diagram of **Fig. 7—3f** in eq. (2), we arrive at the estimation that the coupling of 2nd layer edge atoms to the 1st layer is about 31meV weaker than the one between 3rd layer edge atoms and the 2nd layer. Since this value represents the difference in graphene interlayer interaction probed by edge atoms, it cannot directly be translated to the cohesive energy between the graphene sheets. Indeed, compared to the interlayer cohesive energy that is reported for graphite (~ 52 meV),[32] the energy difference determined on the basis of the different etching rates is quite large. Additional etching experiments revealed that the etching rates depend on the etching temperature and are influenced by the surface structure of the Pt grain (see **Figure 7—4** and **Figure 7—5**, Online Movie 3). The slower etching rates shown in **Figure 7—4** compared to the example discussed in the **Figure 7—2** could be a consequence of the full coverage of the Pt grain by a SLG in the case of the adlayer sheets shown in **Figure 7—4**. Since the Pt catalyst is covered, hydrogen activation by Pt is suppressed and etching relies on thermally activated hydrogen.

Anisotropic etching due to irregularities in the morphology of the substrate and resulting anisotropy in the shape of the graphene adlayers should be taken into account. Abstraction of the etching rate based on an integral shrinking perimeter is thus not sufficient for an accurate evaluation of the coupling strength experienced by edge atoms. However, in the case of perfectly flat Pt grains and symmetric hexagonal flakes, etching experiments performed at different temperature should even deliver layer dependent activation energies for etching. Here we refrain from attempting to provide accurate numbers. Instead, we concentrate on the fact that etching experiments performed at different temperatures and on different grains confirmed that the 2nd layer always etches at higher rate than the 3rd layer and that the difference is not related to the size of the etching layers.

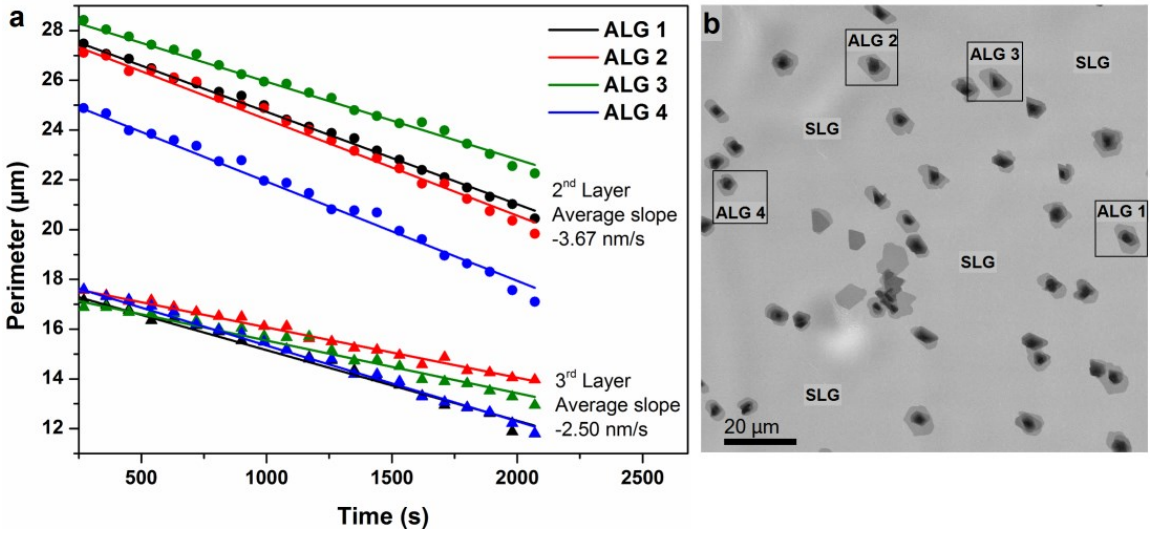

Figure 7–4. Etching rates of 2nd and 3rd layers at 900 °C. a, Plot of the perimeter versus etching time abstracted from 2nd and 3rd adlayers (see online Movie M3). Etching was conducted at 900 °C at 25 Pa H_2. The ratio between the etching rates of the 2nd and 3rd layers are similar to the one discussed in the main text (Average between ALG1-4: 1.5 vs. 1.36 in the main text). b, corresponding overview image of ALG on a continuous SLG. The ALG stacks from which the shrinking perimeters were recorded and plotted in (a) are indicated by rectangular windows and labelled as ALG1-4. For the analysis, regularly shaped ALG domains were selected in which edges of adlayers were not merged.

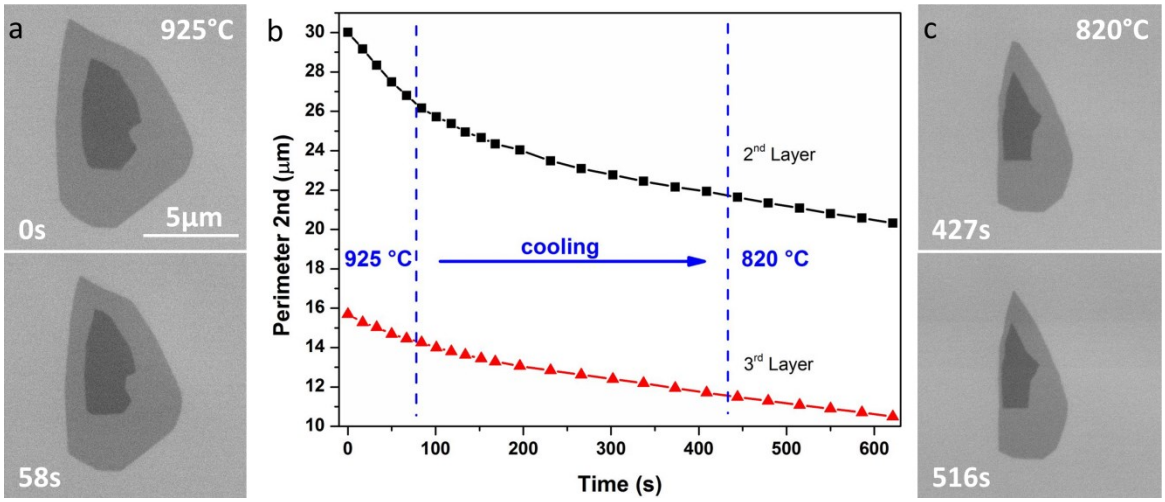

Figure 7–5. Etching of one ALG stack at different temperatures. a, ALG stack showing the 3rd and 2nd layer on a continuous SLG during etching at 925 °C. b, Shrinking of the respective perimeters during etching 925 °C, during cooling to 820 °C and at 820 °C. Throughout the observed temperature regime, the etching rate of the 2nd layer was higher than the one of the 3rd layer by a factor of 2.6 at 925°C and 1.3 at 825 °C. c, The same ALG stack as shown in (a) showing the 3rd and 2nd layer during etching at 820 °C. Anisotropic shape and etching speed are a consequence of the substrate structure and influence the etching rates. Nevertheless, the 2nd layer etches consistently faster than the 3rd layer.

The faster etching speed of the 2nd layer compared to the 3rd layer indicates that the Van der Waals interaction between the 2nd and 1st layer is weakened due to the interaction between the 1st layer and the Pt substrate. In the case of copper substrates, it has previously been shown that coupling between SLG and the substrate induces n-type doping of the graphene sheet, which can be detected by a corresponding shift in the position of the C_{1s} peak in X-ray photoelectron spectra.[33] A similar n-type doping was also observed in the case of ruthenium substrates.[34] The observed weaker coupling between the 2nd and 1st graphene layers that we observe here is thus attributed to a charge imbalance imposed by the strong coupling of the 1st layer to the Pt substrate. The slow etching of the first layer is thus a direct confirmation of a strong interaction between graphene edge atoms and the Pt substrate.

7.3.3. Strong anisotropy revealed by vacancy island etching

A closer scrutiny of **Fig. 7—3e** reveals that etching does not uniformly shrink the islands. Instead, the islands become elongated in a direction along the Pt terraces that run perpendicular to the green up and down arrows. The anisotropy is most visible for the first graphene layer, which is in direct contact with the Pt substrate. This shape evolution indicates that the etching rates are slower in the direction perpendicular to the Pt steps than along the terrace. Asymmetric etching of islands is less pronounced for the second and third graphene layers and is thus another indication of a strong interaction between graphene edge atoms and the Pt surface.

The interaction of graphene with Pt step edges is explored further by measurements of the shape evolution of vacancy islands or holes during isothermal etching of *in situ* grown SLG (see Online Movie 4). In **Figures 7—6 a-c** the size of the vacancy island increases starting after some finite time *t* that is needed to open a small hole at a defect in the SLG. The shape evolution of the vacancy island during etching is plotted in **Fig. 7—6i** from frames recorded at 180 s intervals. The most distinctive feature of this hole is its highly anisotropic shape resulting from the transformation of a hexagon to an elongated polygon. Although atomic scale surface features of the Pt substrate cannot be resolved by ESEM, we can clearly detect the larger steps that are formed by step bunching during growth.[35] Real-time imaging during etching clearly demonstrates that anisotropy of vacancy islands is caused by the alignment of

the etching front with Pt terrace edges, which are discernable as faint lines at roughly 45° in **Fig. 7─6 a-c**. The step edges on the Pt surface are more visible in the AFM image that was recorded on the same Pt grain after the ESEM experiment (**Fig. 7─6d**). Similar to the islands, anisotropic etching of the hole in **Fig. 7─6i** proceeds by rapid elongation along the terraces marked by the blue arrows, while it is suppressed across edges by strong interaction with Pt atoms in the direction of the green arrows. In contrast, **Figures 7─6 e-h** and Online Movie 5 show that if a hole forms on a large terrace devoid of steps, the hexagonal shape is preserved as the hole expands with time. The stability of the hexagonal shape indicates that the edges are zigzag terminated. A comparison of line plots in **Fig. 7─6j** reveals that the overall etch rates change as the shape of the hole evolves. The red symbols correspond to the perimeter and the area of uniformly expanding hexagonal holes on a terrace and thus, represent the intrinsic etching rates of graphene on Pt. The black symbols correspond to the expanding vacancy island on the stepped Pt surface. Initially, the black symbols overlap the red ones. But, they break away from the red ones at a point in time when elongation of the hexagonal shape in **Fig. 7─6i** sets in. This behaviour indicates that the detachment-limited removal of carbon atoms is strongly influenced by changes in the Pt─C interaction at surface steps. There is another small detail hidden in the etching rate of the vacancy island on the flat terrace in **Fig. 7─6j**. Instead of being linear, the rate increases with time. This is because the exposed area of Pt, which acts as catalyst for the production of atomic hydrogen, increases with increasing area of the vacency island.

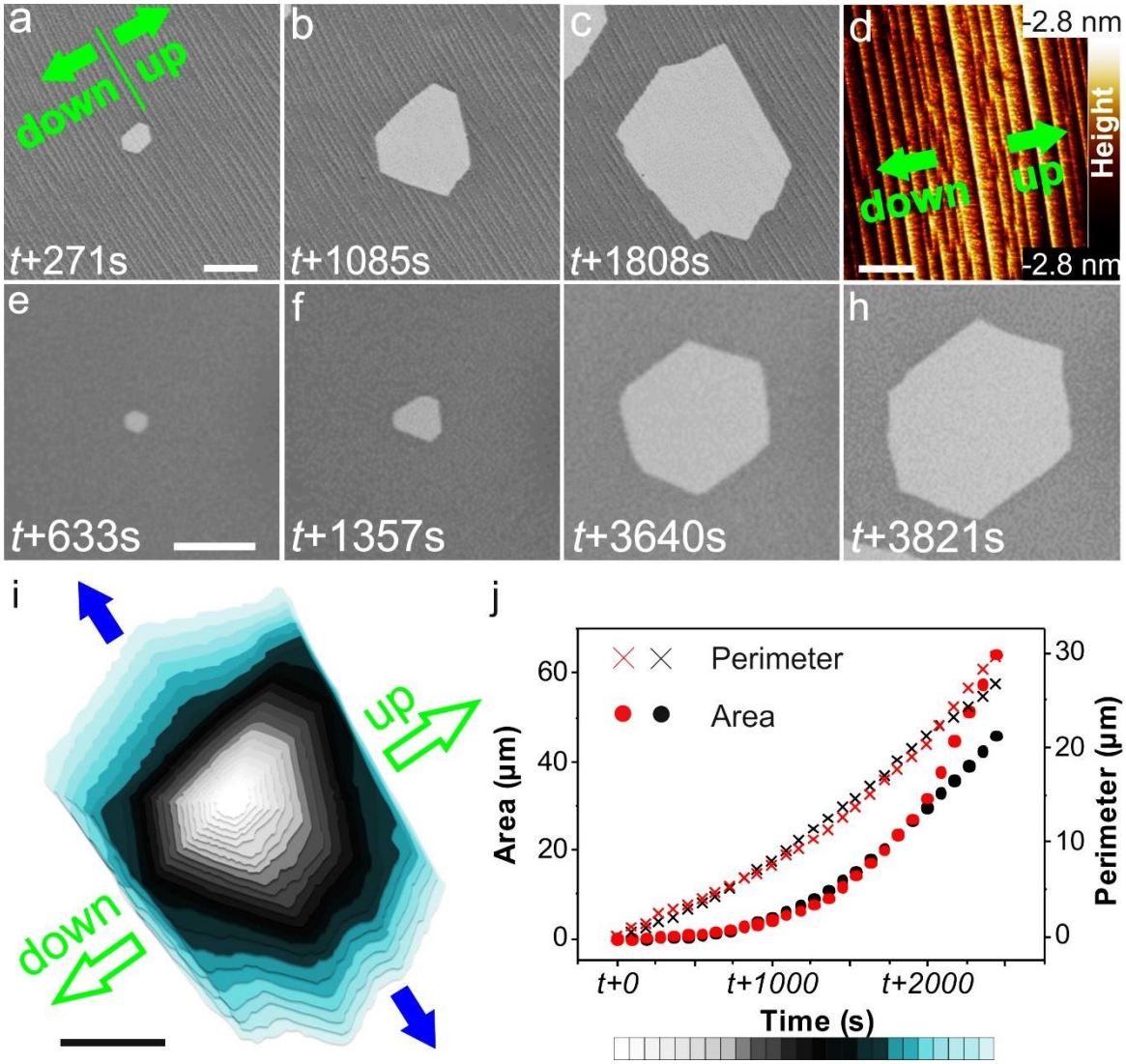

Figure 7—6. The anisotropic etching of vacancy islands. a,-c, *In situ* SEM images recorded at 900 °C during H_2 etching showing the evolution of etch pits on a faceted Pt surface. *t* corresponds to the start time of dosing H_2 into the chamber. d, AFM image recorded from the same Pt grain imaged in a and b. The graphene covered surface is characterized by graphene-induced Pt step bunching and surface reconstruction. e,-h, *in situ* SEM images recorded at 900 °C during H_2 etching showing the evolution of a vacancy island on a flat Pt surface. i, Time-dependent change of the size and shape of the vacancy island shown in a - c. The superimposed shapes were extracted from frames recorded at 180 s intervals. Green arrows indicate the up-/downwards direction of steps. Blue arrows indicate the direction of elongation along the terraces. j, Line plots showing the evolution of the perimeter and area as a function of etching time, black symbols correspond to etching on the stepped Pt surface, red symbols to the case of the flat Pt surface. The scale bars in (a), (d), (e), and (i) measure 2 µm, 200 nm, 5 µm, and 2 µm, respectively.

7.3.4. STM imaging of graphene edge states

The structural information derived from the etching kinetics shows stronger interaction between the first layer and the substrate compared to that between stacked graphene adlayers, and a strong coupling of graphene at step edges of the Pt substrate. Here we describe STM imaging that was performed to explore the electronic structure associated with the edges of graphene sheets. The edges of a graphene island on a flat Pt terrace are shown in the STM image in **Fig. 7—7a**, and those of an ALG grown on a SLG in **Fig. 7—7b**. In contrast to the depressed edges of the SLG on the Pt surface in **Fig. 7—7a**, the ALG edges in **Fig. 7—7b** show clearly elevated features. These apparent height variations in the STM images are attributed to differences in the local electronic density of states in graphene. The high electron density in the STM image in **Fig. 7—7b** localized at the edges of ALG indicates the presence of pronounced edge states. Such a high electron density at edges of graphene sheets has been predicted by DFT calculations to occur at hydrogen terminated zigzag edges.[36] In contrast, the edges of SLG directly in contact with Pt are characterized by depleted electron density, which is attributed to the strong interaction between graphene edge atoms and the flat Pt surface. This observation is in agreement with more recent theoretical descriptions and experimental STM data in the literature, according to which terminal carbon atoms at the graphene edge are either bent down toward the Pt substrate on flat terraces or directly bind to step edges.[37,38] Assuming that this picture holds with increasing domain size, the effect of such strong edge bonding of graphene is to block diffusion, intercalation and transport of reactants and products from and to the growth environment during graphene growth and etching. While it hinders both, growth and etching under the layer, it promotes growth and etching of the topmost layer such as schematically illustrated in **Fig. 7—7d**.

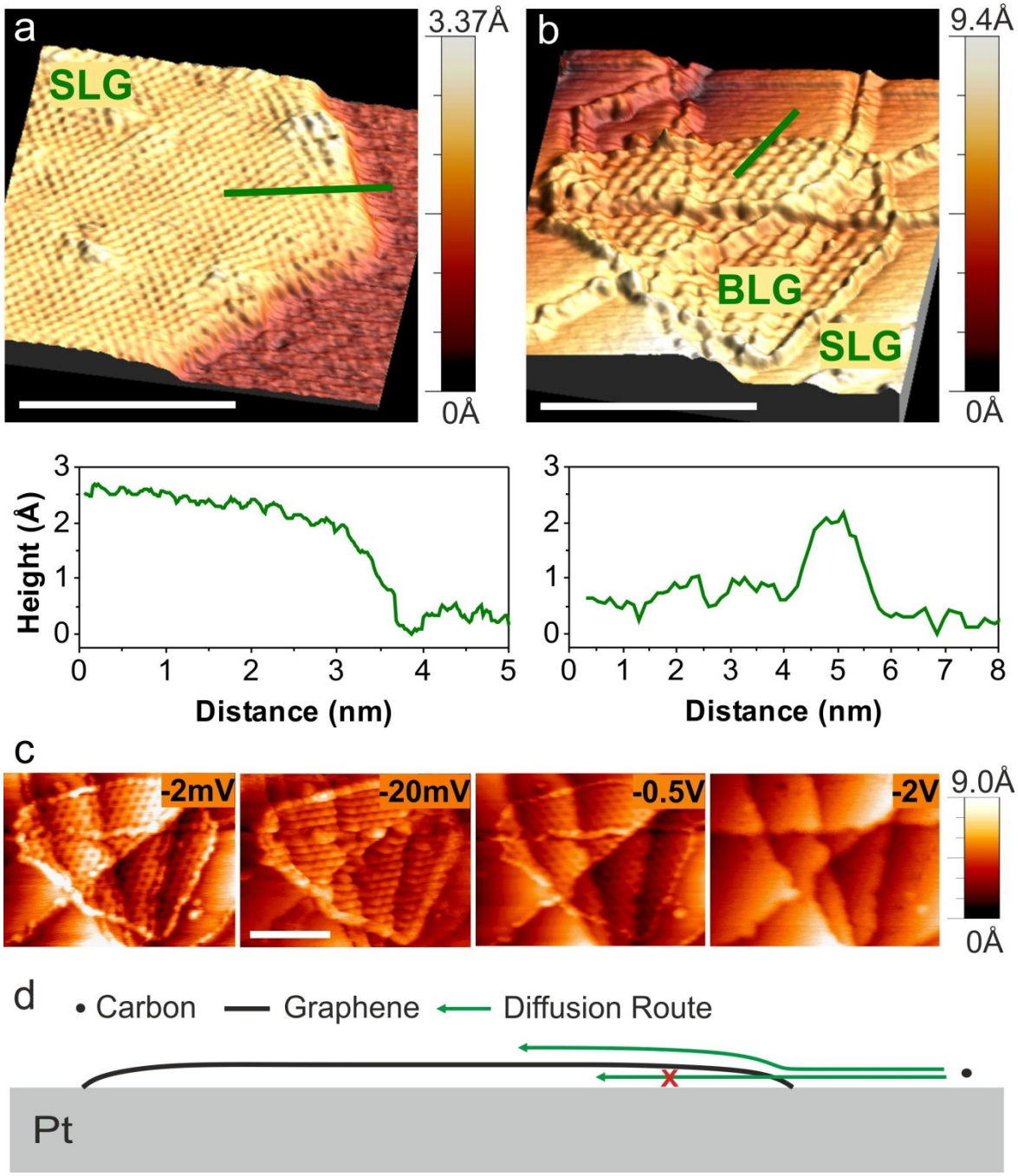

Figure 7–7. STM imaging of graphene edge structures. STM images showing topographic contrast and corresponding height profiles along the green lines are shown in (a) and (b). The images recorded at -2mV bias voltage and 1nA tip current show a reduced signal at the edge of single-layer graphene that is in direct contact with Pt (a) and a higher signal due to increased electron density at edge atoms terminating the top layer in bilayer graphene (b). The dependence of the topologic contrast on tip voltage at a current of 1nA is shown in (c) for the case of bi-layer graphene. A schematic drawing of the bonding of graphene edges and its influence on the diffusion routes of carbon species is shown in (d). Scale bars in (a), (b) and (c) measure 4 nm, 20 nm, and 10 nm, respectively.

7.3.5. Simulation of the shape evolution during graphene etching

To understand the extent to which the graphene-substrate interactions influence the growth and etching behaviour, we performed simulations of graphene shapes during growth and etching on the basis of experimentally obtained growth rates.

It is known that regular shaped graphene domains are enclosed by zigzag edges because of their slow growth rate.[39-42] Assuming that all the edges of the observed domains are zigzag terminated the relative growth rates along different directions were obtained by measuring the distances from the position of the initial nuclei to the respective zigzag edge and dividing it by the growth time (see **Figure 7—8 a-c** and **Table 7—1**). The orientation and the density of steps on the Pt surface breaks up the equal growth rates of the zigzag edges in hexagonally growing graphene into six distinct values.[43,43,44] The largest difference among the six values exists for the up- and down-step directions. However, compared to the 1st layer, the difference in the growth rate in up- and down-step direction is less pronounced in the 2nd and 3rd layers. The reduced influence of the substrate steps is a consequence of the different chemical surrounding and corresponding edge state termination of the adlayers. While the edge of the first graphene layer is attached to the catalyst surface by chemical bonding, both, the 2nd and 3rd layer edge atoms should be H terminated and thus interact only weakly with the graphene layer underneath them.

Anisotropic growth rates.

	0° (up)	60°	120°	180° (down)	240°	300°
First layer	1	>4.5	3.7	3.5	3.9	3.3
Second layer	1	3.3	3.5	1.9	3.7	3.9
Third layer	1	3.5	4.1	1.6	3.9	4.0

Table 7—1. Anisotropic growth rates. The growth rate of graphene zigzag edge as determined from the experiment, plotted as a function of orientation with respect to the up step direction.

Using the experimentally obtained growth rates of the 6 zigzag edges, the growth rates along other directions with different density of kinks were determined under the assumption that growth is controlled by interfacial kinetic processes, using kinetic Wulff construction[39,43,45] (see **7. 5.** Methods). The resulting polar plots of the orientation dependent growth rates for the 1st, 2nd and 3rd layers are shown in **Figure 7─8 d-f**. Applying the obtained growth rates, the steady state shapes of graphene domains during growth were simulated, starting with a dodecagon as the nucleus (see **Figure 7─8 g-i** and Methods). The shapes produced this way are in good agreement with the experimentally observed shapes. Simulations of the etching process were performed simply by reversing the growth process, i.e., by using the determined growth rates along the different directions as etching rates Switching from growth to etching induces a shape change of the graphene islands. While the energetically most stable and slowly growing zigzag edges define the shape during growth (inner six points indicated by red arrows in **Fig. 7─8 d-f**), the shape during etching is determined by the fastest etching ones (indicated by blue arrows in **Fig. 7─9a**). These are edges that are tilted with respect to the zigzag direction by 19.1° and are defined by a maximum densitiy of kinks.[43] The shapes produced during simulated growth were used as the starting point for the simulation of etching. **Figure 7─9** shows that the simulation of the etching process is in excellent agreement with the experimentally observed shape evolution during etching. We conclude that such a good agreement justifies a simulation of etching by inversion of growth. The intrinsic growth and etching behaviour of graphene, which is predominantly determined by the most stable edges during growth and the fastest etching edges during etching is modified by the graphene─Pt coupling to produce the overall rates of carbon attachment and detachment.

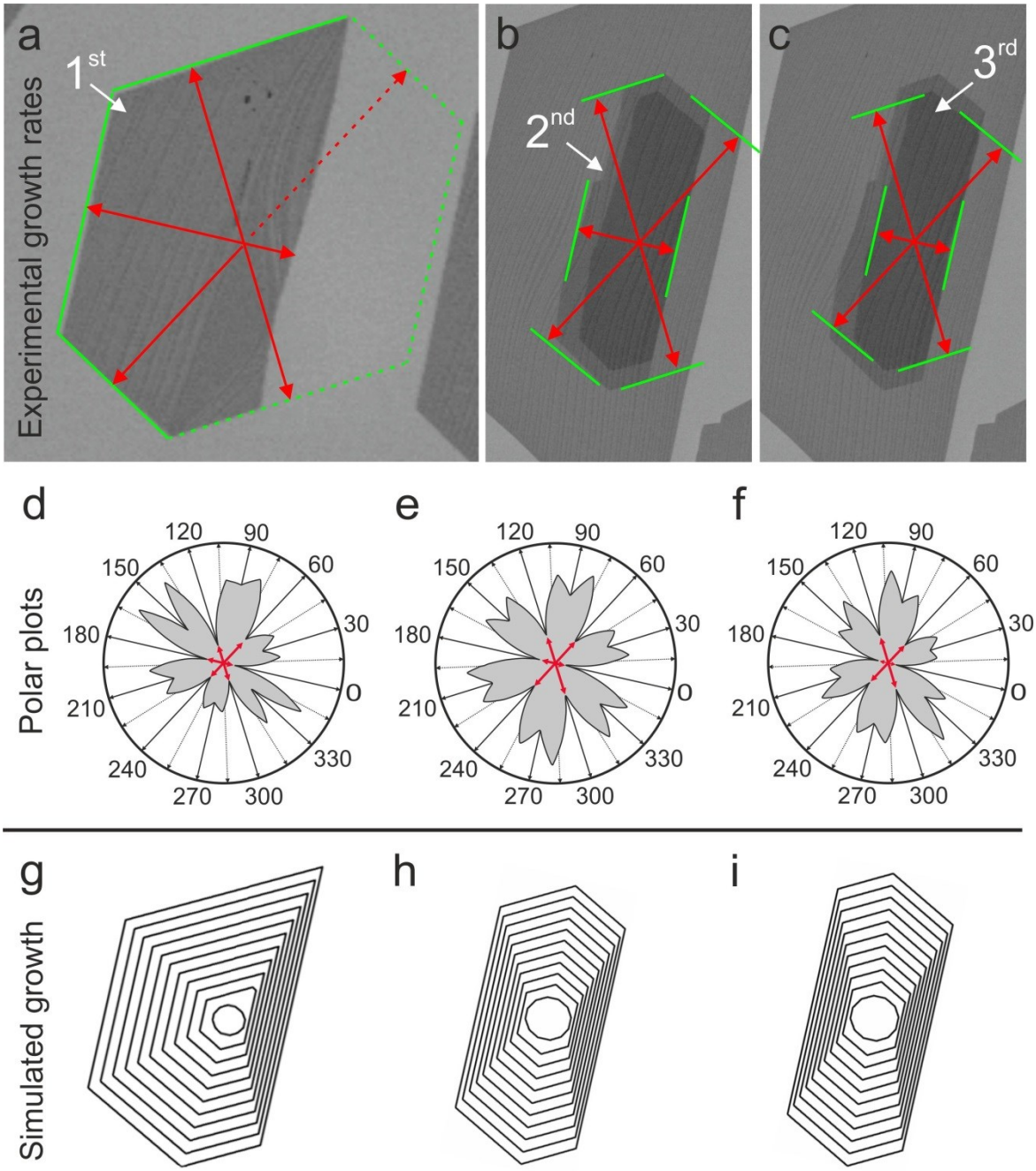

Figure 7─8. | Simulated growth. a,-c, Final shapes of the graphene flakes before initiation of the graphene etching. The outlines of the flakes indicate termination by zigzag edges. d,-f, polar plots obtained using the experimental growth rates (corresponding to the six inner most points in the polar plots). g,-i, simulated kinetic Wulff construction of growth.

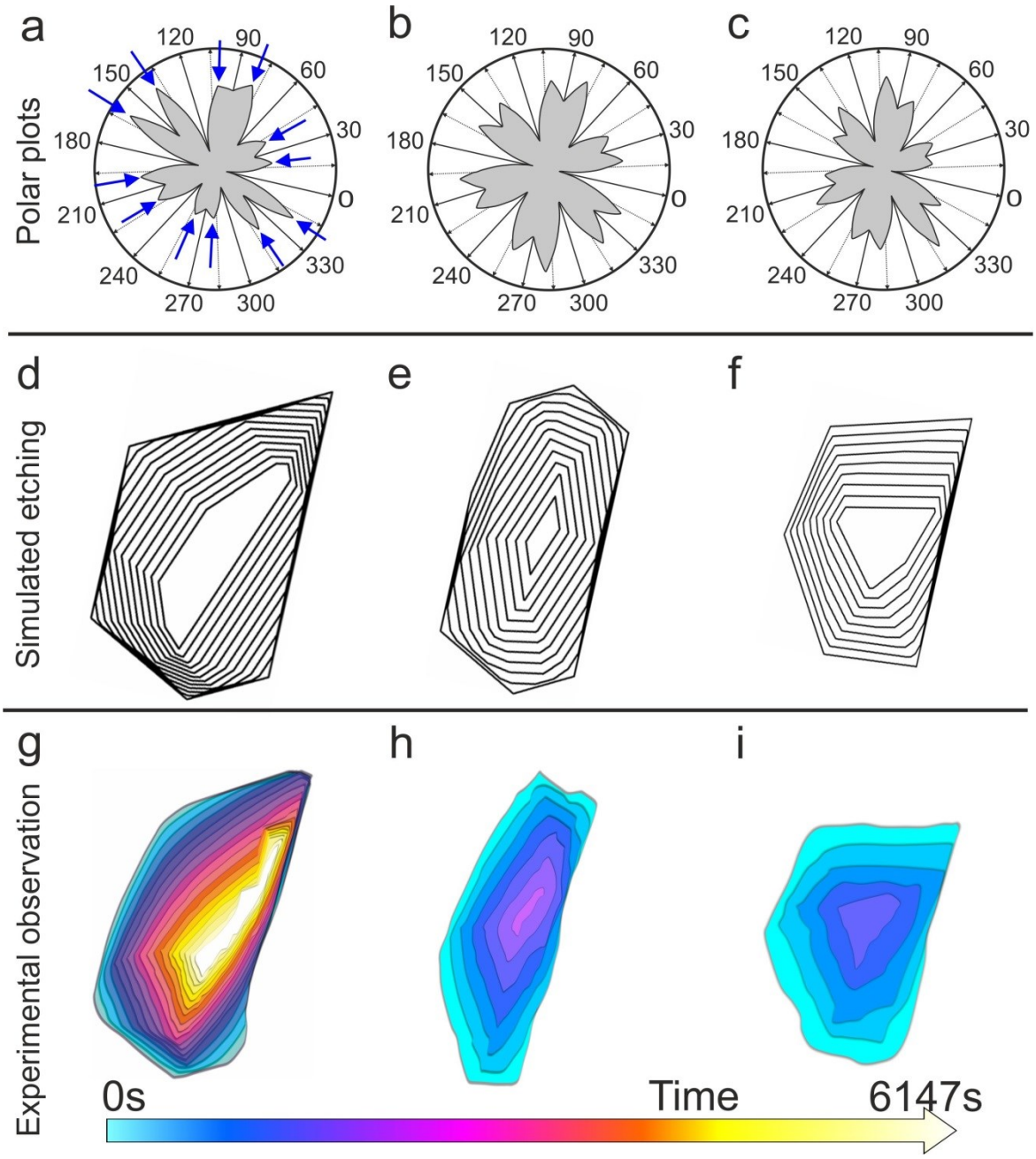

Figure 7—9. Simulated etching. a,-c,. the same polar plots as in Fig. 5, but this time, the fastest directions indicated by blue arrows in (a) determine the shape evolution. d,-f simulated kinetic Wulff construction of the etching process. g,-i, shape evolution of the 1st, 2nd, and 3rd layer during etching as observed in the ESEM.

In order to identify the reason for the pronounced difference in step-up and step-down etching that is observed for the first layer, we performed DFT calculations using the models shown in

Fig. 7—10. The energy required for detaching a C atom from the zigzag graphene edge on the Pt substrate is defined as

$$\Delta E = E_A + \varepsilon_G - E_B \quad (3)$$

where E_A and E_B are the total energy of the structure after and before the detachment of a C atom, ε_G is the energy of a C atom in graphene adsorbed on the Pt (111) surface. From the DFT calculation it follows that down step etching is slower because it requires breaking a 3.2 eV C—Pt bond compared to the up step etching that needs to break only a 1.4 eV C—C bond (for more details about the DFT calculation see Methods section). The large difference in step-up and step-down etching speed is thus a consequence of the different bonding types at the step edges.

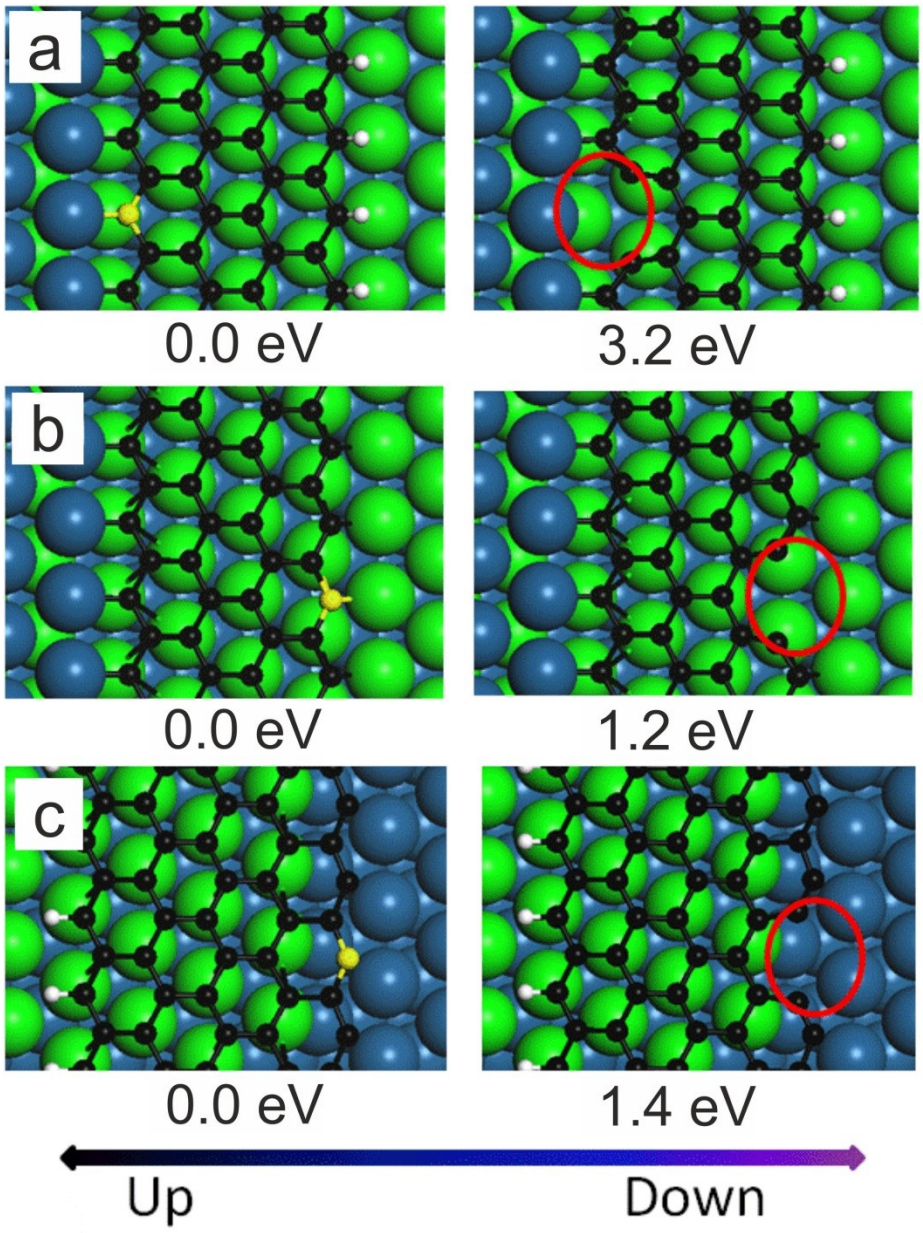

Figure 7—10. DFT models and detachment energies. Models used for the determination of detachment energies for carbon atoms removed from a zigzag graphene edge that is passivated by a substrate step (a), located on the substrate terrace (b), and suspended on a substrate step (c), respectively. The C and H atoms are represented by black and white spheres, respectively. The Pt atoms are coloured in green and blue in order to highlight the step structure. The carbon atom that is removed is represented by a yellow sphere and the location of the formed vacancy is highlighted by red ellipses.

7.3.6. Etching behavior of buried graphene layers

Up to now we have discussed the stacking sequence in few-layer graphene grown by isothermal CVD. However, in the case of Pt, the formation of adlayer graphene can also occur by segregation of dissolved from the polycrystalline Pt foils. We obtained precipitation growth after the termination of an isothermal CVD growth process, during a subsequent cooling step. A typical example for FLG structures that form by segregation during cooling in pure hydrogen atmosphere is shown in Online Movie 6 and illustrated in **Fig. 7—11 a-d**. The sequence of *in situ* SEM images shows that the size of the lighter grey outer layer decreases with time by hydrogen etching, while the size of the smaller darker patch exhibits no detectable change. This behaviour indicates that the large outer layer is being etched because it is a topmost layer that is directly exposed to hydrogen. In contrast, the small darker patch appears to be effectively sealed off from the hydrogen atmosphere. Indeed, closer inspection reveals that it actually grows due to segregation of C from the Pt as shown in **Figures 7—8 e** and **8f**. The second graphene layer corresponding to the small patch therefore grows between the SLG and the Pt substrate by IWC type stacking.[46] Because of the low solubility of C in solid Pt, which is around 0.0711 % at 1000°C,[46] these layers are generally limited to small size. The nucleation of a second layer is suppressed further because the insertion of a new layer underneath the SLG requires work against the coupling of the existing SLG to the substrate.

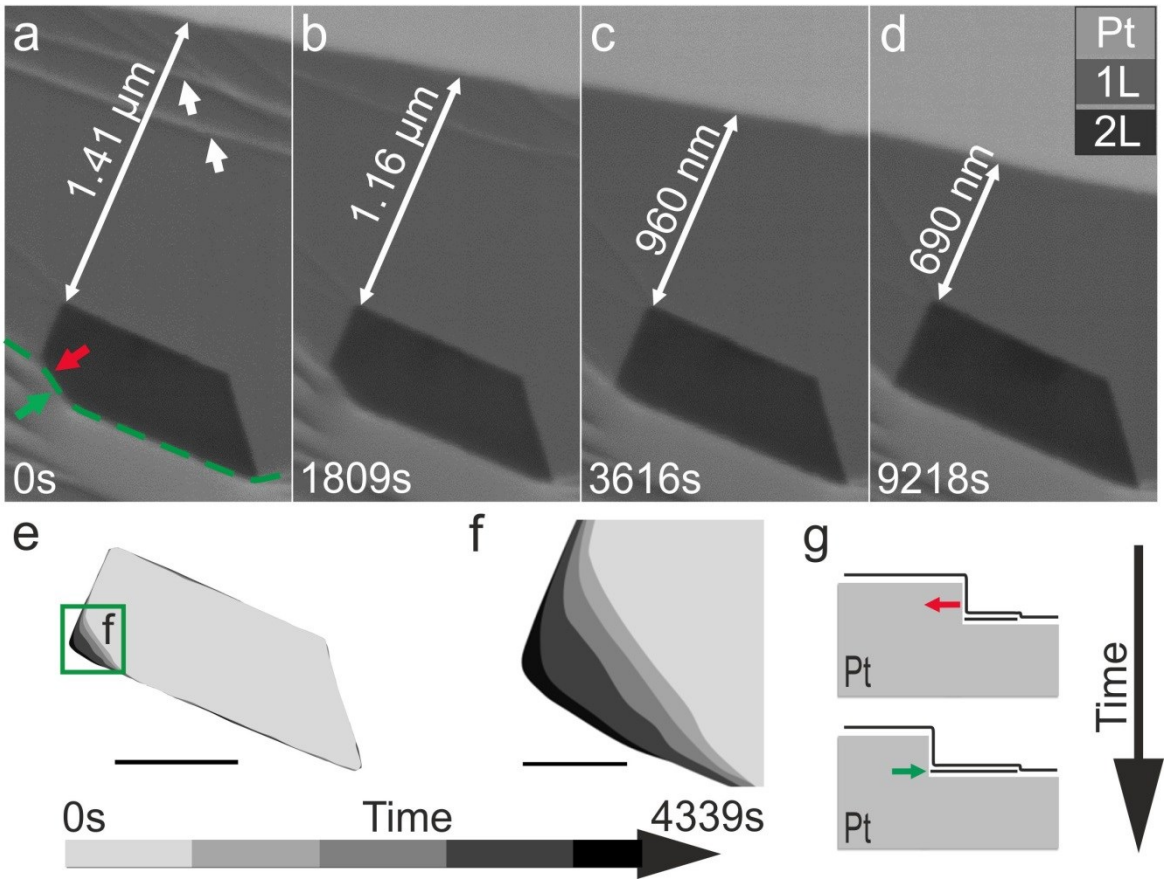

Figure 7—11 | Bilayer growth by C segregation during cooling. a,-d, Time-lapse image series showing simultaneous etching of the topmost layer and growth of the covered layer underneath. e, Contours of the ALG domain at different times. f, Magnified region of (e), showing growth by C segregation from a substrate step edge. g, Schematic view showing the retraction of the Pt step edge and growth of a buried carbon layer. Red and green arrows in (a) and (g) indicate the direction of the Pt step edge movement and C precipitation, respectively. Scale bars in (e) and (f) measure 500 nm and 100 nm, respectively.

The subtle features in **Fig. 7—11e** highlighted by the red and green arrows in vicinity of the dashed green line and magnified in **Fig. 7—11f** provide important clues about the mechanism of the C segregation process. **Fig. 7—11f** reveals that the segregation process occurs at the Pt step edge and involves the gradual sharpening of the corner feature. The surface modification of the Pt is attributed to graphene growth and driven by the Pt—graphene interactions and stabilization of the zigzag edges of graphene.[38] The reconstruction of the Pt step edges involves step bunching through etching and diffusion of the Pt atoms, pushing back the Pt step edges as illustrated by the red arrow, and expansion of the graphene edges marked by the green arrow in the schematic in **Fig. 7—11g**. In **Figure 7—12**, we show that a wrinkle in the

SLG can provide a channel for transporting reactants and products to enable the etching of a buried graphene layer.

Compared to the adlayers on top of the continuous SLG, precipitation layers underneath an existing sheet show a totally different behaviour during hydrogen etching. Because of the high mobility of H on the Pt surface and a high solubility of hydrogen in Pt,[34] H can in principle etch graphene beneath the SLG. Moreover the interplanar spacing between graphene and Pt is close to the interlayer distance of graphite. Normally reactions occurring in nano-sized spaces present novel behaviour due to confinement effects. Indeed, recently Yao et. al. found the space between graphene and Pt could serve as a 2D nano-reactor, in which the activation energy of CO oxidation decreased.[52] However, because the etching products cannot easily diffuse away from the reaction zone, they accumulate until a chemical equilibrium is reached. As a consequence, no substantial etching is observed as long as the precipitated layer is covered by graphene. However, if there is the possibility of exchanging species with the environment—for example through a wrinkle in the top sheet—etching can be observed. In this situation, the wrinkle in the top layer acts as a nano-sized exhaust for the etching products (**Fig. 7—12**). Similarly the graphene wrinkle serves as an inlet for CO to intercalate graphene on Pt.[53] In addition; the evolution behaviour of precipitation layers may give information about edge of top layer.

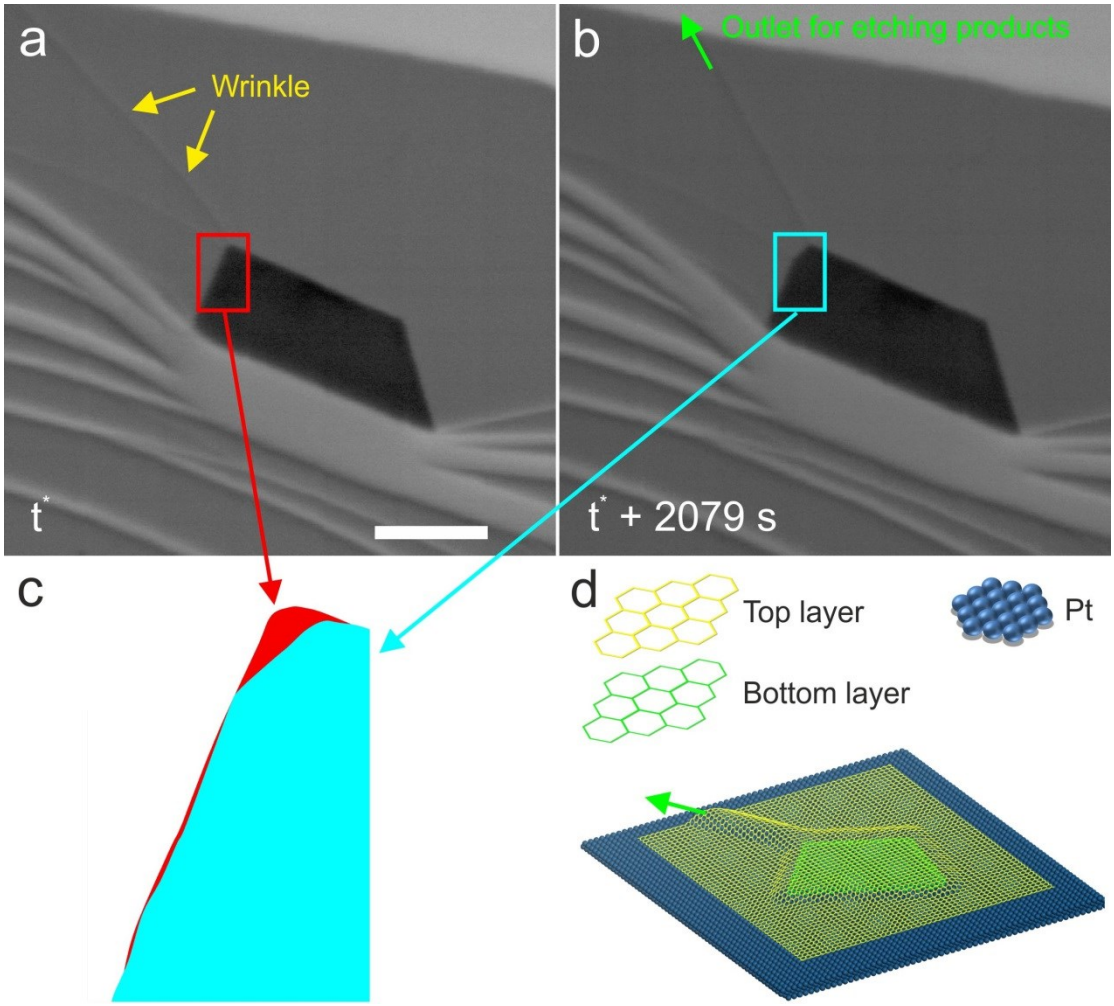

Figure 7—12. Channel formed by a wrinkle. a, b, *In situ* images showing the etching process of IWC graphene. c, Magnified region of (a) and (b), showing etching of the ALG underneath the top layer. Etching is enabled through the channel formed by the wrinkle in the top layer. d, Schematic showing a wrinkle as outlet for etching products. The scale bar in (a) measures 500 nm.

7.4. Conclusion

In this chapter we demonstrate that real-time imaging by ESEM is a versatile and powerful method for the generation of mechanistic insight that is required for the controlled production of few layer graphene with defined number of layers. Direct observation of the shrinking behaviour of individual layers during isothermal etching in pure hydrogen atmosphere

provides the missing clue for unravelling the order of layer stacking in FLG growth. In isothermal CVD growth, new layers grow on the topmost layer, while they are inserted between the substrate and already grown layers by C segregation during cooling. The etching rates reveal that the 1st layer is strongly coupled to the Pt substrate and provides an estimate for the interlayer coupling strength between the 2nd and 3rd layer. By combining theoretical simulations and STM imaging data we show that the coupling of the 1st layer involves C bonding at the graphene edges, where terminal carbon atoms bend down toward a flat Pt surface or attach laterally to Pt step edges.

The etching of vacancy islands exhibits anisotropy that depends on the density and orientation of Pt step edges. Anisotropic etching serves as further evidence for strong interactions with the Pt surface. We conclude that C bonding at the edges is the decisive factor determining the observed layer stacking. It impedes diffusion, intercalation and transport of reactants and products during graphene growth and etching. It hinders both, underlayer growth and etching, but promotes growth and etching of the topmost layer. Moreover, considering the graphene-metal interaction, we propose that the stacking sequence of FLG during isothermal CVD growth is the same on substrates that are characterized by a similar or stronger graphene-metal interaction and comparable carbon solubility such as Pd, Ru, Ir and Rh. In the case of CVD growth on copper in hydrogen rich atmospheres, the reversed stacking sequence might be a consequence of hydrogen terminated edge atoms, as recent DFT calculations have predicted.[23] In this case, diffusion of carbon species into the space between the first layer and the copper substrate and thus, the growth of buried layers is possible. This seems to be in agreement with recently reported statistical analysis of graphene grown on copper,[23] according to which no adlayer growth underneath single-layers is observed for growth at low hydrogen partial pressure. Under such conditions, the graphene edge atoms might be free to interact with the Cu substrate similarly to the case of Pt. Using simulated growth and etching on the basis of growth rates extracted from the experiment, we were able to demonstrate that under attachment and detachment limited conditions, etching can indeed be treated as the inverse of growth. The agreement between simulation and experimental observation confirms that the shape of graphene domains is predominantly determined by the most stable edges during growth and the edges with the highest kink density during etching. Finally, this chapter demonstrates that observation of in-plane dynamics in response to well controlled experimental environments can provide information

about the vertical stacking behaviour of 2D materials and more generally, the capabilities of *in situ* SEM for the study of surface dynamics under controlled environments.

7.5. Methods

7.5.1. *In situ* CVD growth

In situ CVD growth experiments were performed inside the chamber of a commercial ESEM (FEI Quantum 200). The vacuum system of the ESEM was modified and upgraded with oil-free pre-vacuum pumps. The instrument is equipped with a home-made heating stage, a gas supply unit (mass flow controllers from Bronkhorst) and a mass spectrometer (Pfeiffer OmniStar) for the analysis of the chamber atmosphere. The ESEM is not ultra-high-vacuum capable. Due to the use of rubber O-rings for sealing and the fact that the chamber cannot be baked out, the base pressure of the instrument is around $2 \cdot 10^{-5}$ Pa, with a residual gas composition mostly comprising water, N_2 and O_2. In the ESEM chamber, the oxygen partial pressure is thus below $5 \cdot 10^{-6}$ Pa. After each sample loading, the chamber was pumped to around 10^{-3} Pa, purged with nitrogen and pumped again to 10^{-3} Pa successively for several times. Under CVD growth conditions, the pressure is six orders of magnitude higher than the base pressure and constitutes mostly H_2 (99.9995% purity) and C_2H_4 (99.95% purity). Samples of sizes ranging from 3×3 to 5×5 mm were cut from a 0.25 mm thick polycrystalline Pt foil (99.99% purity) purchased from Alpha Aesar. Prior to all CVD growth experiments, the chamber of the ESEM was plasma cleaned. The foils were annealed at 1000 °C under a hydrogen flow of 10 sccm at 25 Pa for 1 hour inside the chamber. The temperature was measured *via* a B-type thermocouple that was spot-welded onto the substrate and simultaneously served to ground the sample. CVD growth was performed at 900 °C using a flow of 10 sccm H_2 and 0.1 sccm of C_2H_4 at a total chamber pressure of 25 Pa. Hydrogen etching was performed under 10 sccm H_2 at 900 °C at 25 Pa. During the experiments, the microscope was operated at an acceleration voltage of 5.0-7.5 kV. Images were recorded by a large field detector (LFD) during CVD growth and etching. No influence of the electron

beam on the growth and etching process could be observed. The imaged regions and their respective surroundings showed similar behaviour, as evidenced by changing the magnification or by moving the sample under the beam. Furthermore, no electron beam induced contamination was observed at elevated temperatures.

7.5.2. Post-growth characterization

Raman spectroscopy was performed using a Horiba/Jobin-Yvon T64000 spectrometer (Villeneuve D'Ascq, France) with a Coherent Innova 400 (Santa Clara, CA, USA) argon-ion laser operating at 514.5 nm for the excitation. The Raman signal was collected with a multi-channel CCD detector. A laser power of 20mW at the sample and an objective with a 100x magnification were used. Measurements were performed in confocal mode in order to reduce the background scattering with respect to the graphene signal. To obtain a satisfactory signal-to-noise ratio, the spectra were recorded with integration times of 60 sec, and a total of 10 accumulations.

AFM images were recorded on a Bruker Sharp Nitride Lever probe (SNL-10). Imaging was done in tapping mode using a V-shaped cantilever probe B (silicon-tip on Nitride Lever with frequency f_0= 40-75 kHz, and spring constants k=0.32 Nm).

STM measurements were conducted under UHV in the microscopic chamber at room temperature (RT) with a constant current mode using a homemade W-tip.

High-resolution transmission electron microscopy was performed using an aberration corrected JEOL ARM electron microscope that is equipped with a cold-field emitter. The image shown in **Figure 7−1** was recorded at an acceleration voltage of 200 kV.

7.5.3. Construction of the polar plots of growth rates

For the 2D graphene, its growth/etching rate can be simply written as $R(\theta)$, where θ is the angle between one graphene edge from the reference edge which is usually chosen to be the

zigzag one. Our previous studies have demonstrated that the growth/etching rate of graphene on Pt (111) substrates has its global minima on zigzag edges, and local minima on armchair edges. In contrast, the growth/etching is fastest when the edge is deviated from the zigzag edge by about 19.1°.[43] Keeping this in mind, we can still qualitatively simulate the growth/etching shape evolution of the graphene flakes in this study, although only the growth rates of zigzag edges can be obtained experimentally. To start with, the growth/etching rates of armchair edges are assumed to be $2.0\times(R_{ZZ\text{-}L}+R_{ZZ\text{-}R})$, where $R_{ZZ\text{-}L}$ and $R_{ZZ\text{-}R}$ are the growth/etching rates of zigzag edges on the left and right sides of the armchair edge. The $R(19.1^{\circ})$ are then given as $1.2\times(R_{ZZ\text{-}R}+R_{AC\text{-}L})$, where $R_{ZZ\text{-}R}$ and $R_{AC\text{-}L}$ are the growth/etching rates of the zigzag and armchair edge on the left and right side of the 19.1° edge. With the above assumptions, the growth/etching rates of all the other edges can be simply obtained by linear interpolation.

7.5.4. The simulation of shape evolution during etching

The simulated etching of the 1st layer graphene domain is initiated from its final growth shape. A minor modification to the final simulated growth shape of the 2nd graphene layer is made to obtain the initial etching state. For the 3rd layer graphene, the simulated etching is started at an intermediate etching state observed in the experiment.

7.5.5. Computational methods.

All the DFT calculations were carried out by using the Vienna ab initio simulation Package (VASP).[47-49] The exchange-correlation functional was treated by local density approximation (LDA).[50] The projected augmented wave (PAW) method was used to describe the interaction between valence electrons and ion cores.[51] To calculate the etching of zigzag graphene edges on the Pt substrate with steps, a 4×1 supercell of the Pt (4 3 3) surface containing three atomic layers was adopted as the substrate, with a zigzag graphene nanoribbon adsorbed on it and the third layer of the Pt substrate fixed during structure optimization. To obtain a commensurate structure, the lattice constants of graphene and Pt are stretched and

compressed to their average value. The size of the orthogonal unit cell is 15.26×10.47×30 Å.49 The k-point grid mesh is sampled by 2×4×1. The force on each atom is converged to 0.01 eV·Å^{-1} during structure optimization, and the energy convergence criterion for the electronic calculation is set to be 10^{-4} eV.

7.6. Online Movie

All the online Movie can be find in this link:

http://www.nature.com/articles/ncomms13256

Online Movie M1. *In situ* SEM movie showing the growth of multi-layer graphene on Pt in a flow of 10 sccm H_2 and 0.1 sccm of C_2H_4 at 25 Pa and a substrate temperature of 900 °C. Images for this movie were recorded at a scan rate of one frame per 10 s.

Online Movie M2 and M3. *In situ* SEM movies showing the shrinking behavior of WC stacked FLG during etching in 25 Pa H_2 at 900 °C. Images for this movie were recorded at a scan rate of one frame per 90 s.

Online Movie M4 and M5. *In situ* SEM movie showing evolution of vacancy islands (holes) during etching on a faceted (**M4**) and smooth (**M5**) substrate grain at 25 Pa H_2 900 °C, respectively. Images for this movie were recorded at a scan rate of one frame per 90 s.

Online Movie M6. *In situ* SEM movie showing the shrinking behavior of IWC stacking FLG during etching in 25 Pa H_2 at 800-900 °C. Images for this movie were recorded at a scan rate of one frame per 90 s.

7.7. References

1. Chen, Z. H.; Lin, Y. M.; Rooks, M. J.; Avouris, P. *Physica E-Low-Dimensional Systems & Nanostructures* **2007**, *40*, 228.

2. Han, M. Y.; Ozyilmaz, B.; Zhang, Y. B.; Kim, P. *Physical Review Letters* **2007**, *98*.

3. Kan, E. J.; Li, Z. Y.; Yang, J. L.; Hou, J. G. *J. Am. Chem. Soc.* **2008**, *130*, 4224.

4. Zanella, I.; Guerini, S.; Fagan, S. B.; Mendes, J.; Souza, A. G. *Phys. Rev. B* **2008**, *77*.

5. Ni, Z. H.; Yu, T.; Lu, Y. H.; Wang, Y. Y.; Feng, Y. P.; Shen, Z. X. *Acs Nano* **2008**, *2*, 2301.

6. Zhou, S. Y.; Gweon, G. H.; Fedorov, A. V.; First, P. N.; De Heer, W. A.; Lee, D. H.; Guinea, F.; Castro Neto, A. H.; Lanzara, A. *Nat. Mater.* **2007**, *6*, 770.

7. Zhang, Y. B.; Tang, T. T.; Girit, C.; Hao, Z.; Martin, M. C.; Zettl, A.; Crommie, M. F.; Shen, Y. R.; Wang, F. *Nature* **2009**, *459*, 820.

8. Castro, E. V.; Novoselov, K. S.; Morozov, S. V.; Peres, N. M. R.; Dos Santos, J.; Nilsson, J.; Guinea, F.; Geim, A. K.; Castro Neto, A. H. *Physical Review Letters* **2007**, *99*, 4.

9. Ohta, T.; Bostwick, A.; Seyller, T.; Horn, K.; Rotenberg, E. *Science* **2006**, *313*, 951.

10. Mak, K. F.; Lui, C. H.; Shan, J.; Heinz, T. F. *Physical Review Letters* **2009**, *102*.

11. Girifalco, L. A.; Lad, R. A. *J. Chem. Phys.* **1956**, *25*, 693.

12. Benedict, L. X.; Chopra, N. G.; Cohen, M. L.; Zettl, A.; Louie, S. G.; Crespi, V. H. *Chemical Physics Letters* **1998**, *286*, 490.

13. Hasegawa, M.; Nishidate, K. *Phys. Rev. B* **2004**, *70*.

14. Spanu, L.; Sorella, S.; Galli, G. *Physical Review Letters* **2009**, *103*.

15. Peng, Z. W.; Yan, Z.; Sun, Z. Z.; Tour, J. M. *Acs Nano* **2011**, *5*, 8241.

16. Yan, K.; Peng, H. L.; Zhou, Y.; Li, H.; Liu, Z. F. *Nano Letters* **2011**, *11*, 1106.

17. Chen, S. S.; Cai, W. W.; Piner, R. D.; Suk, J. W.; Wu, Y. P.; Ren, Y. J.; Kang, J. Y.; Ruoff, R. S. *Nano Letters* **2011**, *11*, 3519.

18. Sutter, P.; Sadowski, J. T.; Sutter, E. *Phys. Rev. B* **2009**, *80*, 10.

19. Sutter, P. W.; Flege, J. I.; Sutter, E. A. *Nat. Mater.* **2008**, *7*, 406.

20. Nie, S.; Walter, A. L.; Bartelt, N. C.; Starodub, E.; Bostwick, A.; Rotenberg, E.; McCarty, K. F. *Acs Nano* **2011**, *5*, 2298.

21. Lu, C. C.; Lin, Y. C.; Liu, Z.; Yeh, C. H.; Suenaga, K.; Chiu, P. W. *Acs Nano* **2013**, *7*, 2587.

22. Wu, Y.; Chou, H.; Ji, H.; Wu, Q.; Chen, S.; Jiang, W.; Hao, Y.; Kang, J.; Ren, Y.; Piner, R. D.; Ruoff, R. S. *Acs Nano* **2012**, *6*, 7731.

23. Zhang, X. Y.; Wang, L.; Xin, J.; Yakobson, B. I.; Ding, F. *J. Am. Chem. Soc.* **2014**, *136*, 3040.

24. Li, Q.; Chou, H.; Zhong, J.-H.; Liu, J.-Y.; Dolocan, A.; Zhang, J.; Zhou, Y.; Ruoff, R. S.; Chen, S.; Cai, W. *Nano Letters* **2013**, *13*, 486.

25. Sun, J.; Nam, Y.; Lindvall, N.; Cole, M. T.; Teo, K. B. K.; Park, Y. W.; Yurgens, A. *Appl. Phys. Lett.* **2014**, *104*, 4.

26. Wang, Z.-J.; Weinberg, G.; Zhang, Q.; Lunkenbein, T.; Klein-Hoffmann, A.; Kurnatowska, M.; Plodinec, M.; Li, Q.; Chi, L.; Schloegl, R.; Willinger, M.-G. *ACS nano* **2015**, *9*, 1506.

27. Christmann, K.; Ertl, G. *Surf. Sci.* **1976**, *60*, 365.

28. Park, M.-H.; Kim, T.-H.; Yang, C.-W. *Surf. Interface Anal.* **2012**, *44*, 1538.

29. Hiura, H.; Miyazaki, H.; Tsukagoshi, K. *Applied Physics Express* **2010**, *3*.

30. Zhao, H. M.; Lin, Y. C.; Yeh, C. H.; Tian, H.; Chen, Y. C.; Xie, D.; Yang, Y.; Suenaga, K.; Ren, T. L.; Chiu, P. W. *Acs Nano* **2014**, *8*, 10766.

31. McLean, J. G.; Krishnamachari, B.; Peale, D. R.; Chason, E.; Sethna, J. P.; Cooper, B. H. *Phys. Rev. B* **1997**, *55*, 1811.

32. Zacharia, R.; Ulbricht, H.; Hertel, T. *Phys. Rev. B* **2004**, *69*.

33. Blume, R.; Kidambi, P. R.; Bayer, B. C.; Weatherup, R. S.; Wang, Z.-J.; Weinberg, G.; Willinger, M.-G.; Greiner, M.; Hofmann, S.; Knop-Gericke, A.; Schloegl, R. *Physical Chemistry Chemical Physics* **2014**, *16*, 25989.

34. Martoccia, D.; Willmott, P. R.; Brugger, T.; Bjorck, M.; Gunther, S.; Schleputz, C. M.; Cervellino, A.; Pauli, S. A.; Patterson, B. D.; Marchini, S.; Wintterlin, J.; Moritz, W.; Greber, T. *Physical Review Letters* **2008**, *101*, 4.

35. Guenther, S.; Daenhardt, S.; Wang, B.; Bocquet, M. L.; Schmitt, S.; Wintterlin, J. *Nano Letters* **2011**, *11*, 1895.

36. Nakada, K.; Fujita, M.; Dresselhaus, G.; Dresselhaus, M. S. *Phys. Rev. B* **1996**, *54*, 17954.

37. Yuan, Q.; Yakobson, B. I.; Ding, F. *J. Phys. Chem. Lett.* **2014**, *5*, 3093.

38. Merino, P.; Rodrigo, L.; Pinardi, A. L.; Mendez, J.; Lopez, M. F.; Pou, P.; Perez, R.; Gago, J. A. M. *Acs Nano* **2014**, *8*, 3590.

39. Artyukhov, V. I.; Liu, Y.; Yakobson, B. I. *Proc. Natl. Acad. Sci. U. S. A.* **2012**, *109*, 15136.

40. Ding, F.; Harutyunyan, A. R.; Yakobson, B. I. *Proc. Natl. Acad. Sci. U. S. A.* **2009**, *106*, 2506.

41. Shu, H.; Chen, X.; Tao, X.; Ding, F. *Acs Nano* **2012**, *6*, 3243.

42. Shu, H.; Chen, X.; Ding, F. *Chemical Science* **2014**, *5*, 4639.

43. Ma, T.; Ren, W. C.; Zhang, X. Y.; Liu, Z. B.; Gao, Y.; Yin, L. C.; Ma, X. L.; Ding, F.; Cheng, H. M. *Proc. Natl. Acad. Sci. U. S. A.* **2013**, *110*, 20386.

44. Artyukhov, V. I.; Hao, Y.; Ruoff, R. S.; Yakobson, B. I. *Physical Review Letters* **2015**, *114*.

45. Sekerka, R. F. *Crystal Research and Technology* **2005**, *40*, 291.

46. Siller, R. H.; Oates, W. A.; McLellan, R. B. *Journal of the Less-Common Metals* **1968**, *16*, 71.

8. Adlayer graphene formation and a processing window for self-terminating single-layer graphene growth

8.1.Abstract

Nucleation processes at surfaces play a crucial role in the growth of crystals and the production of two-dimensional advanced materials. In order to achieve films of high quality, desired crystallinity and precisely controlled thickness, it is crucial to understand the relation between growth kinetics and nucleation behaviour. This is specifically important in the case of two-dimensional materials such as graphene, where in-plane nucleation influences the quality of the film and the addition of each individual layer induces discrete changes in the electronic structure. In this chapter, we use real-time imaging by *in situ* scanning electron microscopy to investigate the growth behaviour of single and adlayer graphene on platinum substrates under controlled chemical vapour deposition conditions. Looking at growth as it happens and in function of growth conditions reveals mechanistic details and provides an undisturbed and real-time insight on the kinetics of two-dimensional growth. It allows us to identify the dominant reasons for adlayer formation and demonstrates that the evolution process of adlayers can be divided into a growth and a decay phase. Finally, we identify conditions for self-limited growth of purely single layer graphene that are suitable for large scale production.

8.2.Introduction

Few-layer graphene (FLG) is either an undesired side-product in the fabrication of wafer-scale monocrystalline single-layer graphene (SLG), or it is the desired product if the aim is to produce a material with a controlled band gap for applications in nano-scaled semiconductor devices. In the latter case, precise control over the alignment between layers and the uniformity of the number of layers over the whole sample is highly desired.

To date, the most widely applied method for SLG and vertically stacked FLG growth is the chemical vapour deposition (CVD) on a metal catalyst surface.[1-6] Among the various

catalysts that are used for this process, platinum offers a quite large parameter space for SLG/FLG growth and a much higher catalytic activity for hydrocarbon dissociation. Indeed, the undesired formation of carbon sheets on platinum was a topic of early hydrocarbon catalysis studies, which were aimed on reducing carbon coking of the active phase.[7] Besides the high activity for hydrocarbon dissociation, Pt also exhibits a relatively weak metal-graphene interaction. As a consequence, the synthesized SLG/FLG can be peeled from the Pt surface and transferred onto other substrates without being damaged.[2,8-10] However, due to the high activity of Pt, the growth of purely single layer graphene appears impossible. Formation of FLG has been reported even under highly diluted hydrocarbon/hydrogen ratios of 4/700.[2] For industrial scale production, control over the formation of adlayers is crucial. Hence, a mechanistic insight on adlayer formation during CVD growth has to be derived. Methods that enable spatially- and time-resolved observation of graphene growth provide a link to the underlying kinetics and have dramatically accelerated our understanding of 2D growth. [4,9,11-19,20 21-23 24 25 26 18]

However, up to date, there is a lack of information regarding the surface morphology and graphene growth dynamics on Pt under relevant catalytic CVD conditions. We have recently demonstrated the potential of *in situ* SEM in the study of graphene growth.[27-29] This technique enables a direct and real-time observation of complete CVD growth processes at millimetre to nanometre-scale resolution under controlled atmosphere. Building on our previous report on the stacking sequence of graphene on Pt, we now present real-time observations with a focus on the formation, growth and shrinking behaviour of adlayers under isothermal conditions. We identify three dominant modes of adlayer formation on clean surfaces and show that they either nucleate simultaneously with SLG on surface steps or defects, or form during the coalescence of domains. It will be demonstrated that the growth of adlayers is limited by the diffusion of growth species from the surface of the active Pt catalyst to the respective growth fronts and that the initial phase of expansion is followed by an etching phase. We reveal that adlayer growth on Pt is a self-terminating process and provide a simple recipe for the growth of self-limited SLG on Pt substrates.

8.3.Results and discussion

Prior to CVD growth, polycrystalline Pt foils were annealed under 25 Pa H_2 atomsphere at 900°C for up to 24 hours in order to remove surface contaminations and to increase the size of the platinum grains. The long annealing time is required in order to remove bulk dissolved carbon to a degree at which no more precipitation of carbon from the bulk can be observed during cooling. After annealing, CVD graphene growth was induced by adding C_2H_4 to the H_2 flow (see chapter 7. Methods. *In situ* CVD growth).

Formation of graphene can generally be observed after an induction period, during which the surface of the metal catalyst supersaturates in growth species.[26,27] For a given temperature, the nucleation density is strongly depending on the C_2H_4 dosing rate and can be adjusted by the C_2H_4/H_2 ratio. During growth, each graphene domain expands through the attachment of carbon species at the growth front,[9] until adjacent domains start coalescing and a continuous graphene sheet is formed. For growth at 900°C on polycrystalline Pt, a grain dependent growth behaviour is observed. It is characterized by a variation in the induction period, nucleation density and growth speed, and is a consequence of the grain orientation dependent catalytic properties of Pt. (see chapter 7). Furthermore, a characteristic grain orientation dependent growth of similarly shaped and aligned domains is observed. During the experiment, the formation and growth of FLG is easily recognizable in the secondary electron images through a step-wise increase of the contrast for each individual adlayer (as discussed in Chapter 7). Depending on the growth conditions, we are able to identify different predominant mechanisms for adlayer formation.

8.1.1. Graphene growth under quasi- and non-equilibrium conditions

Film growth is an inherently non-equilibrium process, which is intimately intertwined with thermodynamics and kinetics. In the case of metal catalysed CVD, the production of growth species varies with time and depends on the availability of free active catalyst suface. Furthermore, graphene growth is constantly accompanied by carbon etching due to the co-feeding of hydrogen.[27] Overall, film growth can be described from three different viewpoints. The thermodynamic view evaluates the deviation of the system from the equilibrum state and

considers nucleation and growth as quasi-equilibrium processes. In the case of the atomistic view, a molecular-kinetic concept of the interaction between atoms adsorbed on the substrate and between the adatoms and the substrate is used. Finally, the kinetic viewpoint considers the lifetime conditions of atoms on the substrate and describes successive states of adatom clusters of different sizes with a set of linear differential coupling equations. Since we are limited by the temporal and spatial resolution of the ESEM, we are not able to directly address atomic scale details and direct information about the growth species. In the following, we are thus describing film growth mainly from the viewpoint of the deviation from the equilibrium and try to link thermodynamic with kinetic considerations.

Under equilibrium conditions, the rate of growth species production through catalytic hydrocarbon decomposition on the substrate is balanced by the rate of their loss from the surface due to desorption and gasification. Thus, supersaturation of growth species on the substrate will not be reached and no nucleation and film growth can occur. Equilibrium conditions can also be established once graphene islands have formed. In that case, no growth is observed because graphene growth and etching are in balance.

Quasi-equilibrium growth is reached under critical flow conditions: It describes the minimal hydrocarbon feeding that is required in order to break the equilibrium and achieve supersaturation, nucleation and film growth within a finite time. Under quasi-equilibrum growth conditions, only a single initial nucleation phase is observed and graphene growth is very slow. In our set-up, quasi-equilibrum growth was achieved at C_2H_4/H_2 flow ratios of around 1:100 at a total pressure of 25 Pa. The resulting radial growth speed of graphene domains was below 0.01µm/s.

Further increase of the hydrocarbon concentration leads to an extended nucleation phase and faster growing graphene domains (> 0.5µm/s in our experiments) and will be referred to as non-equilibrium growth.

Due to its high catalytic activity and the low formation energy, there is a large process window in which graphene growth on platinum proceeds in the attachment limited regime. In this case, the net number of carbon atoms that are attached at the growth front of a sheet per time is proportional to its perimeter and the radial growth along different directions is constant (**Figure 8−1a**). Consequently, the areal growth curves of individual domains follow

a square function (see **Figure 8−1b**). A clear sign of attachment limited growth is that the growing sheets maintain their specific polygon-shape with smooth edges and sharp vertexes throughout the growth.[27,30] The anisotropic growth behaviour that is frequently observed is induced by graphene edge attachment at Pt steps and thus a consequence of the grain dependent surface structure of the substrate (**Figure 8−1 a-b**). Similar anisotropic growth behaviour has previously been observed in graphene grown on ruthenium[4] and associated with orientation dependent diffusion processes.[31] Due to the limited resolution of the ESEM (around 2-3 nm), we are not able to provide direct evidence for nucleation at steps. However, approximately half-hexagon shaped sheets that are observed on some grains, provide indirect confirmation for nucleation at Pt substrate steps (see **Fig 8−1b**). Indeed, low-coordinated surface step sites are distinctly more active than terrace sites and may serve as nucleation site on clean surfaces.[9,15] Once attached to an edge, graphene domains extend faster along terraces than down- and upwards across steps, which explains the elongated half-hexagon or polygon-shapes of the graphene domains.[4]

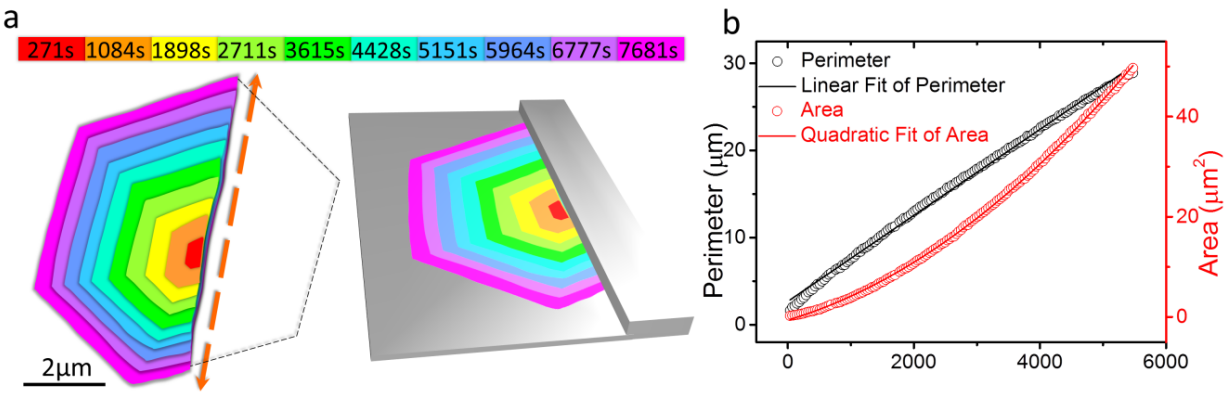

Figure 8−1. Domain growth under quasi-equilibrium growth conditions. (a) color-coded shape evolution of a SLG according to the growth time provided in the color legend. The SEM images of the color-coded domain are shown in Figure 8−2 (a) and 8−3 (a). Orange arrows indicate faster growth along terraces and the black dotted line indicates the missing half of the quasi-hexagon shape. The attachment of domain edges to a Pt step-site is schematically shown in (a). (b) Evolution of perimeter and area of the graphene domain shown in (a) with growth time.

8.1.2. Adlayer growth

In situ growth under different conditions enables us to identify three principal mechanisms for adlayer formation. They can be distinguished on the basis of the growth stage at which they are observed and the respective growth conditions under which they dominate.

Under quasi-equilibrium growth conditions, the formation of FLG was only observed in the initial phase, simultaneously with the appearance of the first SLG domains. FLG stacks can be identified on the basis of their strong contrast in the early stage of growth. When they first appear in the SEM image as a small dark dot after nucleation, the outline of the individual layers cannot be distinguished due to the small size. With time of growth, however, the individual sheets become visible due to an apparent difference in their growth rates. It leads to a splitting of the growth fronts and gives rise to a distinct contrast step in the SEM image for each individual layer (see **Figure 8−2 a-d**). The growth behaviour of the different layers can be analysed on the basis of the recorded images as shown in **Figure 8−2a**. The image stack recorded during growth is represented by one frame in (**a**) and the corresponding orthogonal views through the image stack are shown in (**b**) and (**c**). The orthogonal views correspond to cuts through planes containing the time axis. In (**d**), a three-dimensional view of the image stack is shown. The orthogonal views reveal the evolution of the contrast due to the first and second layer and indicate that both layers nucleated simultaneously. Interestingly, the individual layers of such a stack grow self-similar, indicating that each adlayer is co-oriented and similarly attached to a Pt surface step. Thus, substrate structure and associated barriers along and across steps seem to have similar influence on the growth behaviour of all layers (**Figure 8−2 a- c**).

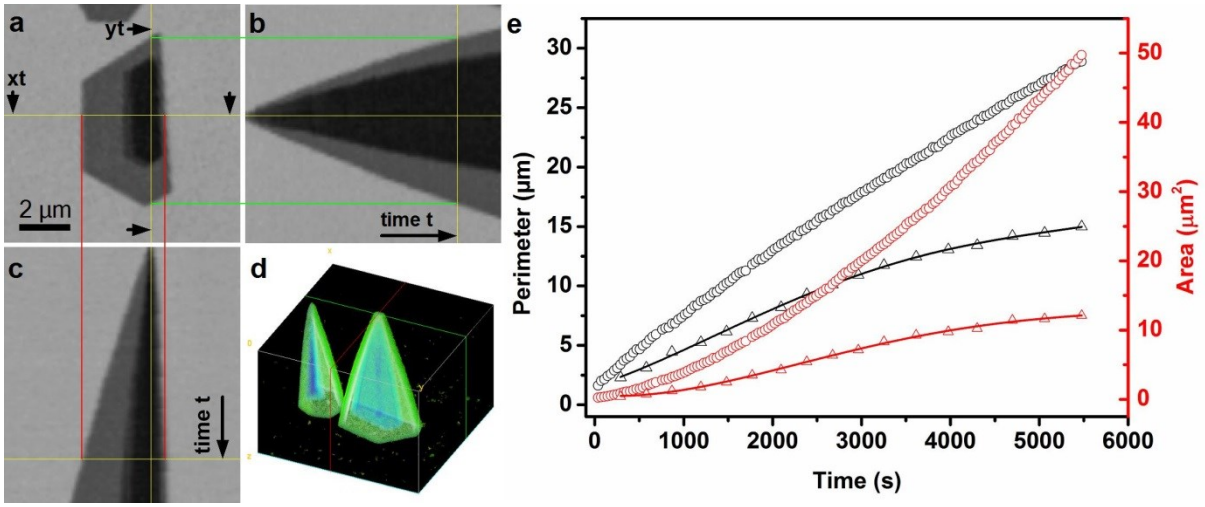

Figure 8−2: Orthogonal views through an image stack recorded during the growth of a FLG at a Pt step edge (not visible). The yellow lines in (a), (b), and (c) indicate the cutting planes and position in the 3D stack, respectively. The time axis runs from 0 sec to 2h. (d) shows a three dimensional representation of the temporal evolution. In (e) the corresponding perimeter and areal growth of the first (circle) and second (triangle) layer are plotted.

Adlayer nucleation at surface steps is the first mechanism of adlayer formation (see **Figure 8−3a**). It is the only mechanism we could observe under quasi-equilibrium growth conditions. Furthermore, under quasi-equilibrium growth, no multilayer formation was observed during growth, i.e., after the initial nucleation phase. In the case of non-equilibrium growth conditions, however, two additional mechanism of adlayer formation were occasionally observed. They are both related to processes that can occur during the merging and coalescence of adjacent SLG domains. The latter implies that the catalyst in the local surrounding is already covered by graphene. For this reason, adlayer formation at grain boundaries is only observed under non-equilibrium growth conditions, where carbon growth species are highly abundant. In the case of co-oriented single layer domains growing on the same Pt grain, the merging of parallel growth fronts can give rise to the formation of a single adlayer. The fact that only one adlayer is formed, which grows concentrically in all directions indicates that it nucleates from a defect at the grain boundary. This is the second mechanism and exemplified in **Figure 8−3b**. Alternatively, the adlayer could be formed through a continued growth of either of the two sheets if one of them locally overgrows the other one. Depending on the details of the merging process, one or more screw dislocations would then be induced, giving rise to the initiation of a single or double spiral and thus, the formation of

multiple adlayers. This is the third mechanism and exemplified by *in situ* observations as shown **Figure 8−3c**.

Since surface steps on a Pt grain can have different orientations, nucleation at steps and growth along step edges can give rise to variations of the in-plane orientation between different graphene islands growing on the same Pt grain.[32,33] In the case of domains that are slightly rotated with respect to one another, the merging of growth fronts seems to preferentially lead to screw-dislocation induced growth of several adlayers, while events in which only a single adlayer is formed, are relatively rare.

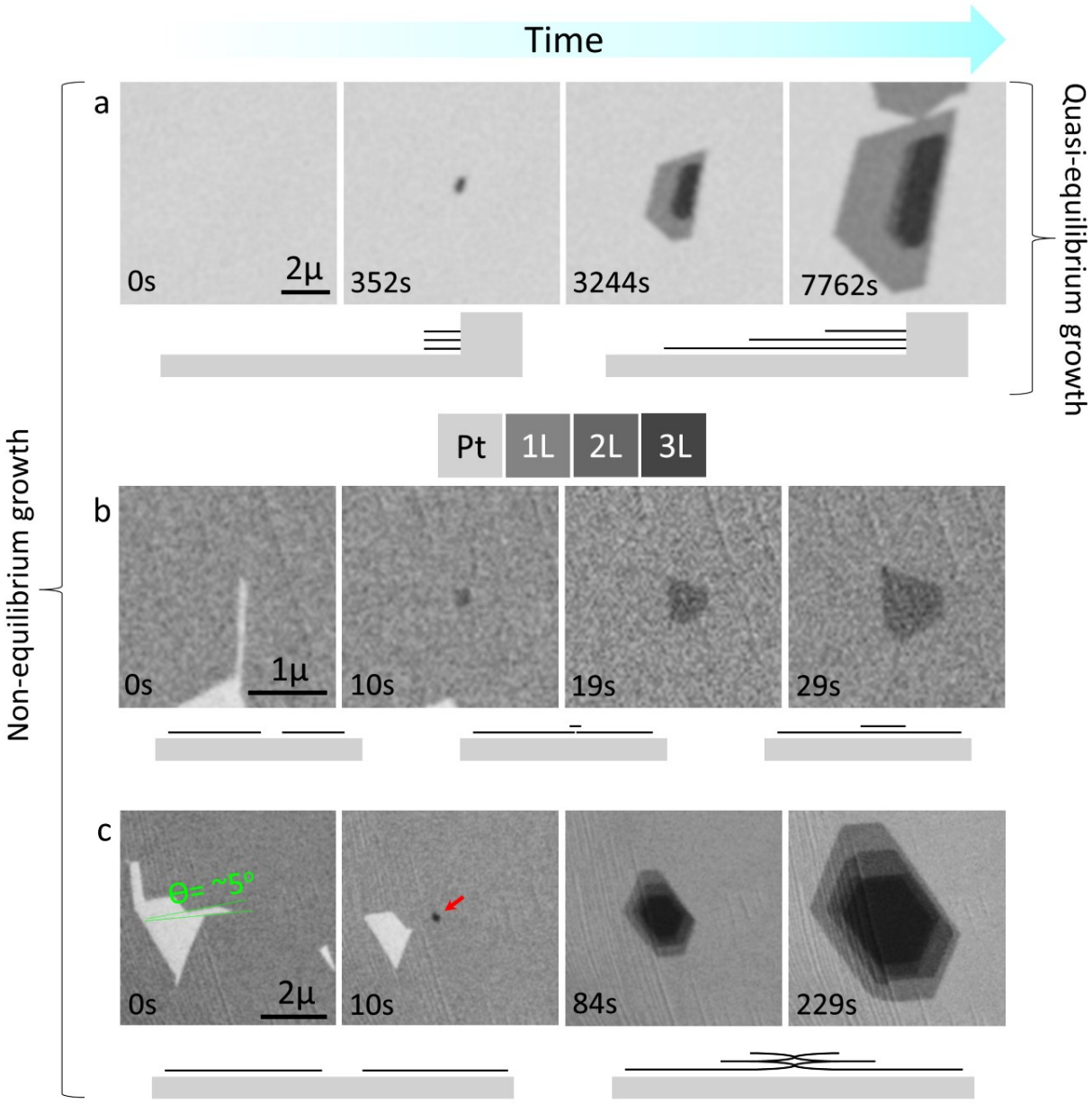

Figure 8−3: Observed mechanisms of adlayer formation: top: quasi-equilibrium growth, bottom 2 rows, non-equilibrium growth. (a) *In situ* SEM images of MLG formed by adlayer nucleation at a Pt step. (b-c): *In situ* SEM images recorded during non-equilibrium growth show an example for the nucleation of a single adlayer during the merging of two parallel growth fronts and a screw-dislocation induced formation of several adlayers, respectively. The angle between the approaching growth fronts before merging is highlighted by green lines in (c).

8.1.3. Adlayer evolution

Direct observation of FLG growth reveals an interesting behaviour that further helps understanding the underlying growth mechanism. During experiments in which the temperature, pressure and gas feeding were kept constant, we found that the initial growth phase of adlayers is followed by a phase during which the adlayers are shrinking (see **Figure 8−4**). Under both, quasi- and non-equilibrium growth conditions, the evolution of adlayers can thus be divided into a growth and a decay phase. It is important to note that the switching from growth to etching occurs while the SLG continues expanding.

The moment at which the switching between growth and etching occurs, depends on the growth conditions. In the case quasi-equilibrium growth, it is observed once the lateral distance between the adlayer growth front and the growth front of the first layer reaches around 2-5 µm (**Figure 8−4a-c**). This distance is related to the lifetime of carbon growth species and their associated diffusion length on the surface of graphene and depends on the surface structure of the respective Pt grain. In the case of non-equilibrium growth, where the abundance of growth species is much higher, the switching from ALG growth to shrinking occurs only once most of the catalyst surface is coated by graphene (**Figure 8−4d-f**).

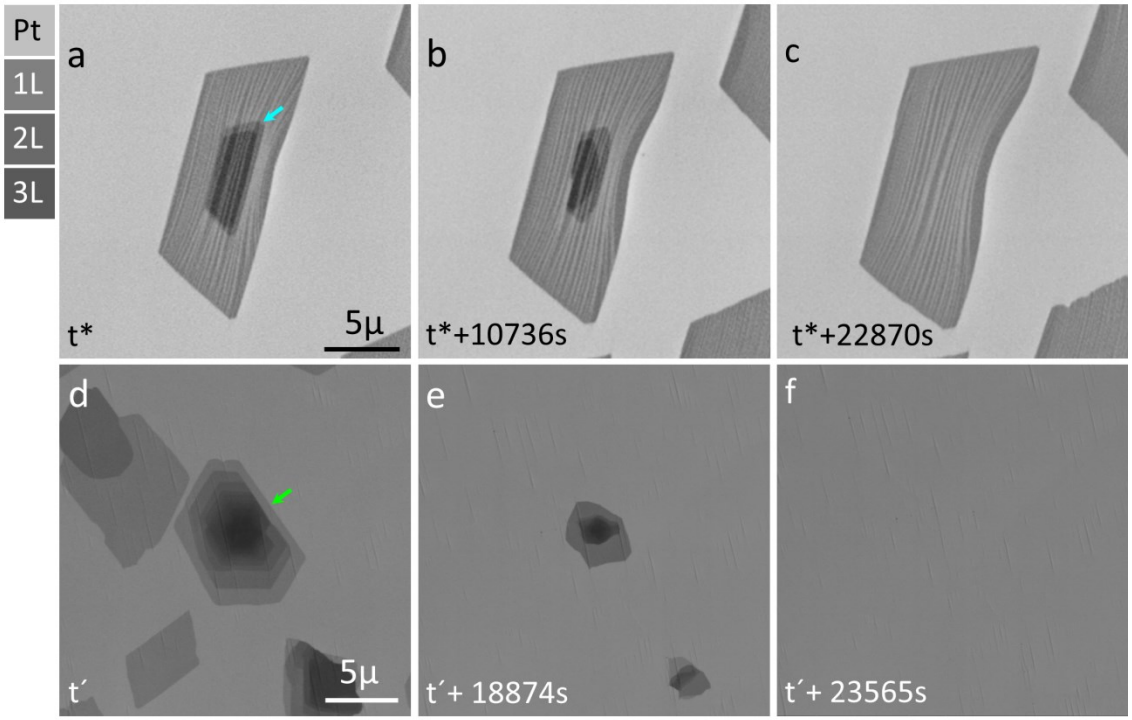

Figure 8−4 Shape evolution of adlayers during the shrinking phase: (a-c): Quasi-equilibrium growth: While the SLG continues expanding at constant rate, the adlayers only grow up to a certain point and then start shrinking until they disappear. (d-f): Non-equilibrium growth: Once most of the Pt surface is covered by SLG, FLG domains start shrinking. The number of layers can be abstracted by comparing the contrast in the images with the contrast legend.

In chapter 7, on the stacking sequence of graphene grown by isothermal CVD, we have already demonstrated that adlayers form on top of the initial layer on platinum. The stacking sequence is thus such that edges of all layers in a layer stack are similarly exposed to the surrounding atmosphere. The shrinking can therefore be related to the hydrogen in the gas phase and a reduced support of the adlayers with growth species. The diagrams in Figure 5a and 5b show the typical evolution of the perimeter and area of a second-layer graphene island during extended exposure to quasi-equilibrium growth conditions (C_2H_4:H_2 of 0.1:10 sccm, total pressure of 25Pa at 900 °C). Throughout the growth, the adlayer grows attachment limited, as indicated by the linear increase of the perimeter and the square-function like onset of the areal growth curve (**Figure 8−5a**). After the initial phase, the growth rate of the second layer starts to decrease and the growth curve develops a sigmoidal shape. The root for the different growth behaviour of the first and the adlayer sheets lies in their different initial growth speed. The first layer is in direct contact with the catalyst and grows significantly faster than the adlayers (see **Figure 8−2**). As a consequence, the distance between the adlayer growth front and the active Pt catalyst increases with growth time. Thus, the number of growth species that reach the adlayer growth-front by diffusion across the surface of the SLG decreases with time. This conclusion is underlined by the fact that the size difference between the adlayers decreases with adlayer number, pointing towards an exponential decay of growth species concentration with radial distance from the uncovered Pt substrate (see **Fig. 8−2a and Fig. 8−4a**). The diffusion and lifetime of growth species on the surface of graphene is thus the rate limiting factor for the growth of adlayers, while the upwards hopping of growth species from one layer onto the next one does not seem to play a relevant role. Since the competing hydrogen etching proceeds at constant rate, there is a point at which etching compensates the growth of adlayers. With further expansion of the SLG, the net etching speed of ALG increases until it finally reaches the detachment limited rate. Thus, a constant reduction of the perimeter is observed towards the end of the etching process (black line in **Figure 8−4b**).

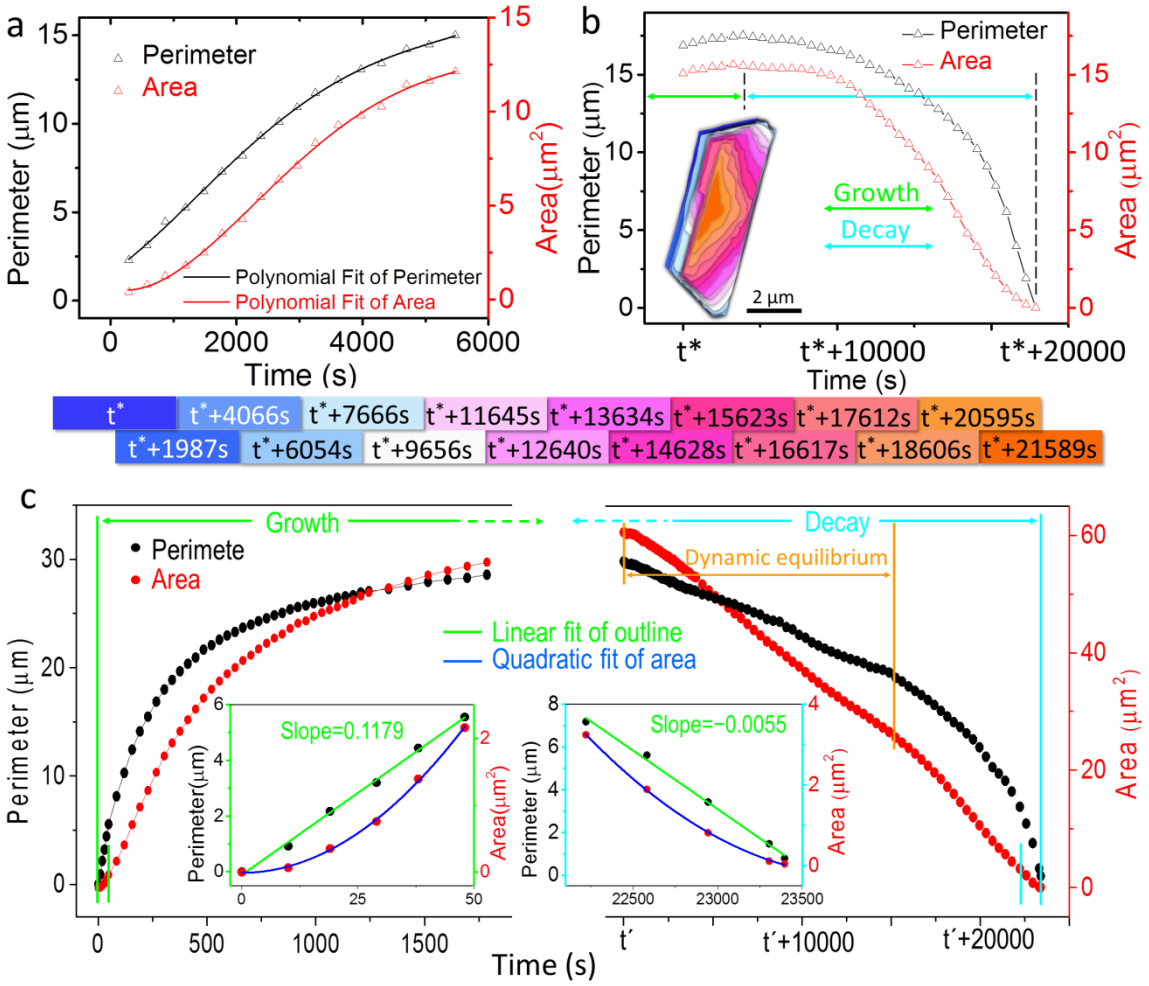

Figure 8−5: Evolution of ALG exemplified by the behaviour of second layer graphene. (a,b): Diagrams showing the growth (a) and shrinking (b) phase of a second layer sheet under quasi-equilibrium growth. (c, d) show growth and etching under non-equilibrium growth. Insets in (c) and (d) show that initial growth is attachment limited and final etching is detachment limited, similar to the case of quasi-equilibrium growth.

The evolution of the perimeter and area during growth and etching under non-equilibrium growth (C_2H_4:H_2 of 1.2sccm :10 sccm at a total pressure of 25Pa at 900 °C) is shown in Figure 5c and 5d for a second layer sheet. Similar to the case above, ALG growth proceeds in the attachment limited regime during the initial growth phase (**Figure 8−5c** and inset in **Figure 8−5c**). With time of growth, the combined effect of a reduced active Pt surface area and a longer diffusion distance of growth species to the adlayer growth fronts leads to a reduction of the growth speed and thus, to a sigmoidal growth curve. Switching from growth

to etching occurs once a significant portion of the catalyst surface is covered by graphene and the associated catalytic production rate of growth species drops below the level that is required to sustain ALG growth. As can be seen in Figure 5d, the etching rate in terms of the areal change of the adlayer sheet and thus, the number of carbon atoms gasified from the ALG per time, is roughly constant. Under continued feeding of C_2H_4 and H_2, a dynamic equilibrium will be established between the gas phase and the carbon species on the surface. The dynamic equilibrium is maintained until etching starts to be detachment limited. This happens as a consequence of the reduction of the integrated perimeter of all adlayers, once the combined etching falls below the value required to maintain the dynamic equilibrium. With time, all adlayers gradually fade away until finally, the whole Pt surface is covered by a SLG (see **Fig. 8−5e**).

8.1.4. Self-termination mechanism and a receipt to extended SLG

With the above understanding, we are ready to explain various experimental observations. Under the near-equilibrium growth condition, where μ_{Gas} must be very close to μ_{SLG} and μ_{SLG}, the ALG is hardly to be nucleated during the continuous growth of the ALG because of the lack of the driving force. In contrast, under the high hydrocarbon pressure, the growth condition was shifted to be far-equilibrium, where μ_{Gas} may be signicantly larger than both μ_{SLG} and μ_{ALG}, the nucleation of ALG during SLG domain growth becomes possible.

The above discussion indicates that the simultaneous SLG growth and ALG etching is possible and therefore we may tune the growth condition into a narrow chemical potential window to form 100% SLG on Pt surface only (as shown in **Figure 8−4f**). While it doesn't explain the kinetic process of SLG growth on the Pt surface. Experimentally we have observed the simultaneous growth of both SLG and ALG on Pt surface and then the shrinkage of ALG when the Pt surface is fully covered by SLG or when the ALG is far from the edge of the SLG under the exact controllable experimental parameters. To further understand the growth kinetics, we need to recall the concept of self-limiting graphene growth. In precious studies, especially for the graphene growth from Cu surface, it is well known that the coverage of the catalyst surface by SLG will greatly reduce the catalyst's accessible area that can catalyse the decomposition of the feedstock and therefore the growth

of graphene will gradually become slower and slower. This indicates that, during the graphene CVD growth under the gas flow, μ_{Gas} actually depends on the coverage of graphene on the catalyst surface and large graphene coverage will lower the μ_{Gas}. At atomic level, it might be caused by the variation of the concentration of carbon radicles (such as CH_3 or CH_2 etc.) in the gas phase due to the reduction of the available catalyst surface. So here we can see that during SLG growth, the driving force $\mu_{Gas} - \mu_{SLG}$ actually will become smaller and smaller during. This is in agreement with the observations shown in **Figure 8−1** and **8−2**, where the rate of SLG domain size increase becomes slower and slower during growth.

Based on the above understanding, the evolution of ALG shown in **Figure 8−4** can be properly explained by considering the diffusion of the Pt decomposed radicles on the graphene domain covered Pt surface. At the initial stage of the growth, the ALG is not far from the edge of the SLG and therefore the radicles decomposed by the Pt surface can easily access the edge of ALG and leads to a fast growth of ALG, although the growth rate of ALG can't be faster than that of the SLG because SLG, which is directly bond to the Pt surface, can be accessed by radicles in higher concentration. During further growth, the edge of ALG becomes far and far from the edge of SLG and therefore the radicles decomposed by the Pt surface must diffuse a longer distance through the gas phase to reach the ALG and then it growth rate becomes slower and slower gradually. At a certainly stage, the rate of radicles reached to the ALG edge is less than the rate of hydrogen etching, then the ALG will be gradually etched away gradually and eventually disappear from the vision. The disappearance of such ALG under the near-equilibrium growth may occur before the full coverage of the Pt with the SLG. While, for the growth with high hydrocarbon concentration, the reduction of the concentration of radicles to the window of ALG etching is hardly to be achieving before the full coverage of Pt surface with SLG. So the disappearance of the ALG can be only seen after the full coverage of the Pt surface with the SLG.

Based on the discussion, we can ascribe the formation of 100% SLG on Pt surface as a self-limiting process. The mechanism of self-limited SLG growth on Pt surface is presented in **Figure 8−6c**, where μ_{Gas} in the initial growth stage can be higher than the SLG window and therefore both SLG and ALG growth are observed. While, during the growth, the increased SLG coverage reduced the accessible catalyst surface and the average radicle concentrations in the gas phase, which leads to a gradually dropping of the μ_{Gas} and the slow growth of both

SLG and ALG. When the μ_{Gas} dropped to the narrow SLG window, the SLG can keep growing while the ALG will be etched away until all disappear. It's important to note that the further reduction of the μ_{Gas} to less than μ_{SLG}, which allow the etching away of the SLG cannot happen for the same reason. Because the etching of the SLG will expose more catalyst area and the greatly increase the μ_{Gas} around the local area of the etched SLG, so it will not occur under the condition of SLG growth.

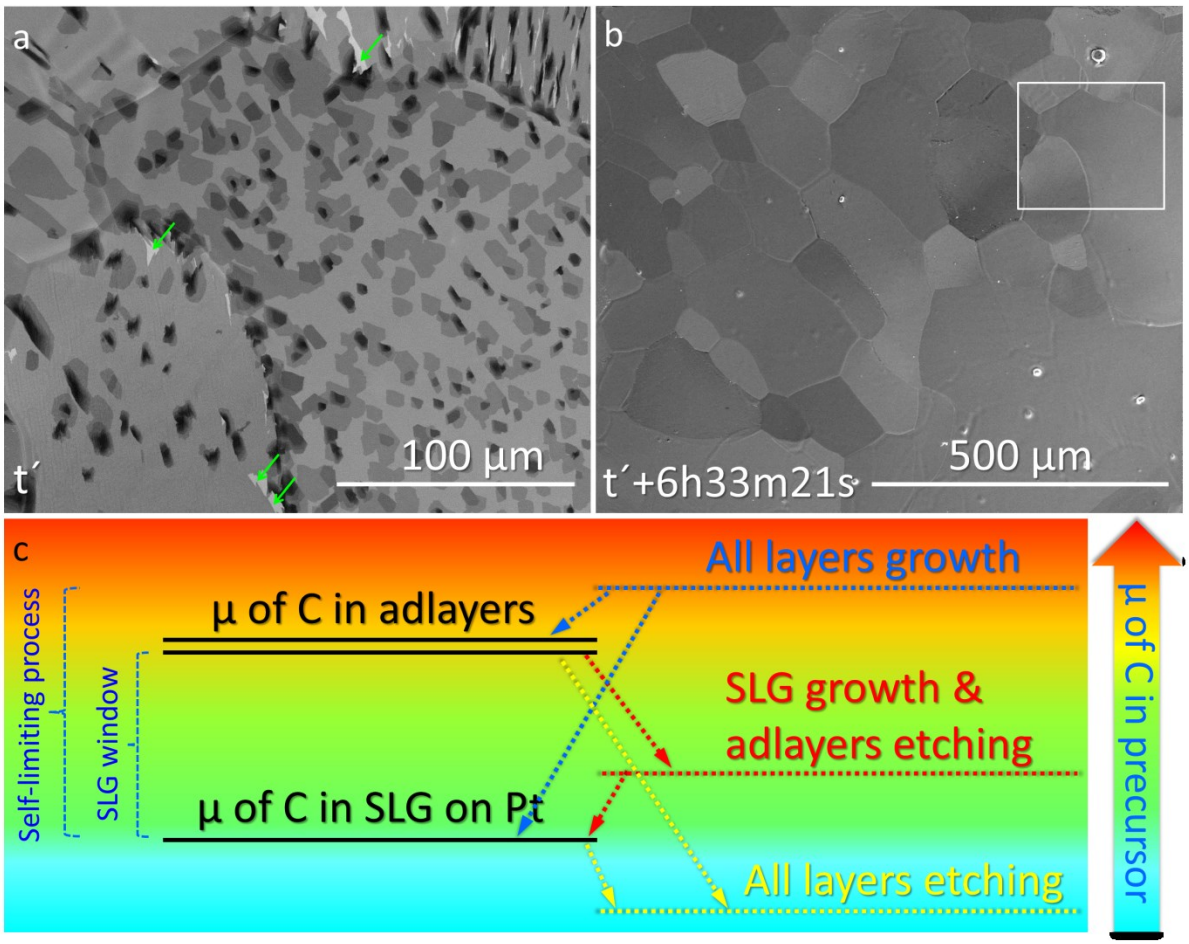

Figure 8−6. Disappearance of adlayers during SLG growth condition. (a) Graphene grown on polycrystalline platinum foil with FLG patches. The image was recorded moments before the catalyst was completely covered by graphene. The green arrows indicate bare Pt surface (b) Shows a large scale SLG covering the whole catalyst surface after annealing for 6.5h at 900 °C. The white square in (b) indicates the region where image (a) was recorded earlier. t' corresponds to the time when the catalyst surface was completely covered. All the *in situ* SEM images were taken under 1.2 sccm C_2H_4+10 sccm H_2 at 900 °C. (c) Schematic showing the mechanism of all layers growth, FLG etching & SLG growth and all layers etching on Pt surface.

8.4.Conclusions

Here, the growth of graphene by Pt catalysed CVD was studied in real-time by *in situ* SEM. Direct observation of graphene growth behaviour under relevant conditions provides insight on the mechanism of single and adlayer graphene on Pt surface. In isothermal growth, FLG growth under different conditions enables to identify three principal mechanisms for adlayer formation. 1. Adlayer nucleation at surface steps can only occur in the initial phase, simultaneously with the appearance of the first SLG domains. 2. The merging of aligned growth fronts can induce defect for formation of a single adlayer. 3. In the case of adjacent domains that are not aligned with each other, the coalescing of edges lead to screw-dislocation induced growth of several adlayers. Under quasi-equilibrium growth conditions, only the mechanism that adlayers form at surface edge could be observed. Under non-equilibrium growth conditions, all of three principal mechanisms for adlayer formation can happen. *In situ* observations and analysis thus indicate that the adlayer formation on Pt is intimately linked to catalyst surface steps, the way of growth fronts merging and precursor partial pressure.

Direct observation of the evolution behaviour of FLG during isothermal growing under controlled atmosphere provides the adequate details for unravelling growth model of each individual layer in FLG growth. In situ observations show shape of SLG keep in regular polygon-shape with smooth edges and sharp vertex throughout whole growth process, and reveal the areal growth curves of SLG always follow a square function. Thus we conclude the high activity of precursor dissociation on Pt lead to the SLG, which directly couple on catalyst surface, growth in the attachment limited regime. Moreover, with coverage of SLG increasing, available catalyst surface decreases which lead to the concentration of carbon radicles is not able to maintain in growth. The areal growth curves of adlayers can thus be divided into a growth and a decay phase under both, quasi- and non-equilibrium growth conditions, and FLG graphene on Pt can be self-terminated into SLG. Considering the C bonding at the edges which is the decisive factor determining stacking sequence in FLG and the graphene-metal interaction, we propose that the self-terminating process of adlayer expansion during isothermal CVD growth could occur on substrates that are characterized by a similar or stronger graphene-metal interaction and comparable carbon solubility such as Pd, Ru, Ir and Rh. Therefore, we can either tune growth atmosphere to render adlayer stay in

self-limiting window to produce pure SLG, or maintain adlayer continuous growth to get large-area FLG. This work provides receipts for the production of high-quality SLG.

8.5. References

1. Hao, Y. F.; Bharathi, M. S.; Wang, L.; Liu, Y. Y.; Chen, H.; Nie, S.; Wang, X. H.; Chou, H.; Tan, C.; Fallahazad, B.; Ramanarayan, H.; Magnuson, C. W.; Tutuc, E.; Yakobson, B. I.; McCarty, K. F.; Zhang, Y. W.; Kim, P.; Hone, J.; Colombo, L.; Ruoff, R. S. *Science* **2013**, *342*, 720.

2. Gao, L. B.; Ren, W. C.; Xu, H. L.; Jin, L.; Wang, Z. X.; Ma, T.; Ma, L. P.; Zhang, Z. Y.; Fu, Q.; Peng, L. M.; Bao, X. H.; Cheng, H. M. *Nat. Commun.* **2012**, *3*, 7.

3. Chen, S. S.; Ji, H. X.; Chou, H.; Li, Q. Y.; Li, H. Y.; Suk, J. W.; Piner, R.; Liao, L.; Cai, W. W.; Ruoff, R. S. *Advanced Materials* **2013**, *25*, 2062.

4. Sutter, P. W.; Flege, J. I.; Sutter, E. A. *Nat. Mater.* **2008**, *7*, 406.

5. Pan, Y.; Zhang, H. G.; Shi, D. X.; Sun, J. T.; Du, S. X.; Liu, F.; Gao, H. J. *Advanced Materials* **2009**, *21*, 2777.

6. Iwasaki, T.; Park, H. J.; Konuma, M.; Lee, D. S.; Smet, J. H.; Starke, U. *Nano Letters* **2011**, *11*, 79.

7. Lang, B. *Surf. Sci.* **1975**, *53*, 317.

8. Preobrajenski, A. B.; Ng, M. L.; Vinogradov, A. S.; Martensson, N. *Phys. Rev. B* **2008**, *78*, 4.

9. Sutter, P.; Sadowski, J. T.; Sutter, E. *Phys. Rev. B* **2009**, *80*, 10.

10. Khomyakov, P. A.; Giovannetti, G.; Rusu, P. C.; Brocks, G.; van den Brink, J.; Kelly, P. J. *Phys. Rev. B* **2009**, *79*, 12.

11. Nie, S.; Walter, A. L.; Bartelt, N. C.; Starodub, E.; Bostwick, A.; Rotenberg, E.; McCarty, K. F. *Acs Nano* **2011**, *5*, 2298.

12. Nie, S.; Wofford, J. M.; Bartelt, N. C.; Dubon, O. D.; McCarty, K. F. *Phys. Rev. B* **2011**, *84*, 7.

13. Sutter, P.; Ciobanu, C. V.; Sutter, E. *Small* **2012**, *8*, 2250.

14. Sutter, P.; Hybertsen, M. S.; Sadowski, J. T.; Sutter, E. *Nano Letters* **2009**, *9*, 2654.

15. Sutter, P.; Sutter, E. *Adv. Funct. Mater.* **2013**, *23*, 2617.

16. Wofford, J. M.; Nie, S.; McCarty, K. F.; Bartelt, N. C.; Dubon, O. D. *Nano Letters* **2010**, *10*, 4890.

17. Mu, R.; Fu, Q.; Jin, L.; Yu, L.; Fang, G.; Tan, D.; Bao, X. *Angewandte Chemie-International Edition* **2012**, *51*, 4856.

18. Yao, Y.; Fu, Q.; Zhang, Y. Y.; Weng, X.; Li, H.; Chen, M.; Jin, L.; Dong, A.; Mu, R.; Jiang, P.; Liu, L.; Bluhm, H.; Liu, Z.; Zhang, S. B.; Bao, X. *Proc. Natl. Acad. Sci. U. S. A.* **2014**, *111*, 17023.

19. Addou, R.; Dahal, A.; Sutter, P.; Batzill, M. *Appl. Phys. Lett.* **2012**, *100*.

20. Cui, Y.; Fu, Q.; Zhang, H.; Tan, D. L.; Bao, X. H. *J. Phys. Chem. C* **2009**, *113*, 20365.

21. Kwon, S. Y.; Ciobanu, C. V.; Petrova, V.; Shenoy, V. B.; Bareno, J.; Gambin, V.; Petrov, I.; Kodambaka, S. *Nano Letters* **2009**, *9*, 3985.

22. Dong, G. C.; Frenken, J. W. M. *Acs Nano* **2013**, *7*, 7028.

23. Patera, L. L.; Africh, C.; Weatherup, R. S.; Blume, R.; Bhardwaj, S.; Castellarin-Cudia, C.; Knop-Gericke, A.; Schloegl, R.; Comelli, G.; Hofmann, S.; Cepek, C. *Acs Nano* **2013**, *7*, 7901.

24. Peng, Z.; Somodi, F.; Helveg, S.; Kisielowski, C.; Specht, P.; Bell, A. T. *J. Catal.* **2012**, *286*, 22.

25. Vlassiouk, I.; Smirnov, S.; Regmi, M.; Surwade, S. P.; Srivastava, N.; Feenstra, R.; Eres, G.; Parish, C.; Lavrik, N.; Datskos, P.; Dai, S.; Fulvio, P. *J. Phys. Chem. C* **2013**, *117*, 18919.

26. Ma, T.; Ren, W.; Liu, Z.; Huang, L.; Ma, L.-P.; Ma, X.; Zhang, Z.; Peng, L.-M.; Cheng, H.-M. *Acs Nano* **2014**, *8*, 12806.

27. Wang, Z.-J.; Weinberg, G.; Zhang, Q.; Lunkenbein, T.; Klein-Hoffmann, A.; Kurnatowska, M.; Plodinec, M.; Li, Q.; Chi, L.; Schloegl, R.; Willinger, M.-G. *ACS nano* **2015**, *9*, 1506.

28. Kidambi, P. R.; Bayer, B. C.; Blume, R.; Wang, Z.-J.; Baehtz, C.; Weatherup, R. S.; Willinger, M.-G.; Schloegl, R.; Hofmann, S. *Nano Letters* **2013**, *13*, 4769.

29. Blume, R.; Kidambi, P. R.; Bayer, B. C.; Weatherup, R. S.; Wang, Z.-J.; Weinberg, G.; Willinger, M.-G.; Greiner, M.; Hofmann, S.; Knop-Gericke, A.; Schloegl, R. *Physical Chemistry Chemical Physics* **2014**, *16*, 25989.

30. Zhang, X.; Li, H.; Ding, F. *Advanced Materials* **2014**, *26*, 5488.

31. Meca, E.; Lowengrub, J.; Kim, H.; Mattevi, C.; Shenoy, V. B. *Nano Letters* **2013**, *13*, 5692.

32. Loginova, E.; Nie, S.; Thuermer, K.; Bartelt, N. C.; McCarty, K. F. *Phys. Rev. B* **2009**, *80*.

33. Starodub, E.; Bostwick, A.; Moreschini, L.; Nie, S.; El Gabaly, F.; McCarty, K. F.; Rotenberg, E. *Phys. Rev. B* **2011**, *83*, 9.

9. Conclusions

In this thesis, graphene formation behaviours have been studied on three metal catalysts - Ni, Cu and Pt by *in situ* SEM:

(1) Real-time surface imaging technique by ESEM

Firstly, I review conventional *in situ* imaging techniques that have been used for the direct observation of graphene growth, and summarize limitations of the existing methods (Chapter 1). Due to the high sensitivity of the secondary electron, graphene on metal surface can be detected as a variation in contrast. Thus, ESEM can be modified to be *in situ* imaging technique for graphene growth behaviour study (Chapter 2). Indeed, graphene CVD growth on metal catalyst is able to be visualized by ESEM and even realize to observe graphene coupling state (Chapter 3). Therefore, real-time imaging by modified ESEM is a novel *in situ* technique for surface-science research. In chapter 2, I have demonstrated how to modify ESEM to achieve directly observing surface processes during a reaction under relevant conditions. Based on the modified ESEM, the sample can be easily observed under reactive atmosphere over a large range of magnifications, revealing surface dynamic information from the mili- to the nanometer scale and provide a better overview of CVD graphene growth behaviours.

(2) Graphene formation behaviours on various metal catalyst

Using real-time imaging technique by ESEM, we are able to *in situ* fingerprint a whole CVD process from substrate annealing to graphene growth and subsequent cooling. The *in situ* observation reveals dynamic nature of the catalyst surface and provides important insights on the graphene growth kinetics and the graphene-substrate interactions at nanometer scale. In chapter 4, to better understand formation of graphene, I apply *in situ* SEM to study the details of graphene CVD growth on three conventional catalysts (Ni, Cu and Pt). The graphene growth behaviours highly depend on carbon solubility of catalyst and surface-film interaction. Due to high carbon solubility of Ni and a bulk reservoir effect, it is hardly to control layer number during growth, and carbon precipitation during cooling makes SLG growth difficultly. On the contrary, the single layer graphene can be nicely grown on Cu and

Pt surface. Therefore, from chapter 5 to chapter 8, I investigated detail of graphene growth on Cu and Pt.

(3) Graphene growth details on Cu (Chapter 5)

Because of low carbon solubility and weak surface-film interaction, Cu is considered as ideal catalyst for graphene CVD growth. *In situ* SEM revealed at growth temperature (beyond 900°C) Cu show a pre-melted, highly mobile surface and surface dynamics are strongly depending on the grain orientation. Throughout complete growth process, three growth phases can be identified. In the first phase, a depletion zone is developing at the growth front. Once the depletion zone has completely build up, the growth mode changes from attachment to diffusion-limited, and the second growth phase starts. In second phase, the presence of a depletion zone at growth fronts is verified by the observed mutual influence of neighbouring graphene islands. Once depletion zones of neighbouring graphene overlap, the third phase is reached in which graphene growth shows competitive relationship.

(4) Graphene growth details on Pt (Chapter 7 and 8)

Due to higher catalytic activity for hydrocarbon dissociation than Cu, Pt offers a large error-tolerant window for graphene growth. Moreover, a weak Pt-graphene interaction allows the synthesized graphene to be easily transferred onto other substrates without being damaged. Thus Pt is also a popular catalyst for graphene CVD growth. Based on *in situ* observation, we found that the growth of graphene can be easily achieved on Pt in comparison to Cu (chapter 6). In order to control production of single layer graphene, stacking sequence of few layer graphene on Pt need to be understood. We combine isothermal growth and etching experiments to probe the stacking sequence and interlayer coupling strength (Chapter 7). The etching rate of individual layers in hydrogen atmosphere reveals the stacking sequence of few layer graphene. Furthermore, by combining theoretical simulations and STM imaging data we conclude that C bonding at the edges of the first layer graphene is the decisive factor determining the stacking sequence in few layer graphene. Finally, we identify two dominant modes of adlayer formation and show that they either nucleate simultaneously with single layer graphene on surface steps or defects, or form during the coalescence of domains (Chapter 8). We reveal that in case of adlayer graphene on the top, adlayer growth is a self-

terminating process on Pt and provide a simple recipe for the growth of single layer graphene on Pt substrates.

In summary, this thesis represents a proof-of-concept for using *in situ* SEM imaging for developing a real-time feedback loop for controlling graphene growth by CVD. Thus, *in situ* SEM will play an important role in the future of graphene and other 2D materials research.